Structural Modulation of Carbazole Derivatives for Triplet State Engineering and Delayed Emission

A thesis submitted for the degree of

Doctor of Philosophy

in

Chemistry

by

Jibin S.

PHD201022

Indian Institute of Science Education and Research
Thiruvananthapuram (IISER TVM),
Thiruvananthapuram – 695551
Kerala, India

April 2026

Declaration

I hereby declare that the Ph.D. thesis entitled **"Structural Modulation of Carbazole Derivatives for Triplet State Engineering and Delayed Emission"** is an independent work carried out by me at the School of Chemistry, Indian Institute of Science Education and Research Thiruvananthapuram (IISER TVM), under the supervision of **Prof. Mahesh Hariharan** and it has not been submitted anywhere else for any other degree, diploma or title. In keeping with the general practice of reporting the scientific observations, due acknowledgements have been made wherever the work described is based on the findings of other investigators.

Place: IISER Thiruvananthapuram **Jibin S.**

Date:

Certificate

This is to certify that the work embodied in the thesis entitled **"Structural Modulation of Carbazole Derivatives for Triplet State Engineering and Delayed Emission"** has been carried out by **Jibin S. (PHD201022)** under my supervision at the School of Chemistry, Indian Institute of Science Education and Research Thiruvananthapuram (IISER TVM), and the same has not been submitted elsewhere for a degree.

Place: IISER Thiruvananthapuram
Date:

Prof. Mahesh Hariharan
(Thesis Supervisor)

Dedicated

To My Beloved

Mother, father and sisters.

“It always seems impossible until it’s done!”

-Nelson Mandela

Acknowledgements

My Ph.D. thesis represents the outcome of years of dedication, research, and personal growth, made possible through the support and guidance of numerous individuals and institutions. I am sincerely grateful to all those who have played a role in shaping this journey.

First and foremost, I am deeply grateful to my thesis advisor, Prof. Mahesh Hariharan, for his unwavering support, expert guidance, and constant encouragement throughout this journey. His thoughtful insights and patient mentorship have been instrumental in shaping my Ph.D. research and overall growth as a scholar.

I sincerely thank Prof. J. N. Moorthy, Director of IISER Thiruvananthapuram, for ensuring access to excellent infrastructure and research facilities. I am also grateful to the current and former Heads of the School of Chemistry for their support of my research through the CIL and IISER TVM facilities. I sincerely appreciate the guidance of my doctoral committee members, Prof. K. George Thomas and Prof. Reji Varghese, whose valuable feedback and continued support have greatly enriched my research journey. I would also like to acknowledge all the School of Chemistry faculty members for their exceptional mentoring during the Ph.D. coursework.

I am also grateful to Prof. Vivek Tiwari, Professor, IISc Bangalore, whose collaboration and discussions have been enlightening and motivating. I particularly appreciate Prof. Vivek Tiwari's constructive suggestions and shared knowledge on understanding the 2D ultrafast spectroscopy to unravel the solvent dependency in the spiro-connected perylenediimide dimer. Additionally, I would like to thank Prof. Frank Wuethner, University of Würzburg, for allowing me to work with him for a short period on understanding the intersystem crossing mechanism in a selenium-annulated perylenediimide. I am also thankful to Dr. Brijith Thomas of New York University for the opportunity to collaborate on an engaging project focused on investigating the solid-state packing and structural properties of disordered organic materials. I would extend my acknowledgement to Dr. Vinayak Bhatt for the quantum chemical calculations to elucidate the hybrid local and charge transfer state in the co-crystals.

I am deeply obliged to all past and present Hariharan group members: Dr. Nanditha G. N., Dr. Bappa G., Dr. Swati D., Dr. Aasif K., Dr. Indrajit G., Dr. Remya R., Dr. Ebin S., Dr. Devika S.,

Dr. Athira T. J., Dr. Lijina M. P., Dr. Swathi Krishna P. E., Mr. Alfy B., Mr. Deepu G., Mr. Dilip P. S., Ms. Kavya V., Mr. Aniruddha Mazumder, Mr. Philip D. M., Ms. Anjana V. M., Ms. Suvarna S. C., Ms. Tessy P., Ms. Raniya P., Mr. Jeswin S., Ms. Akshaya N., Ms. Keerthy P. S., Mr. Vivek V. D., Mr. Akhilesh K. U., Mr. Sohan D. J., Ms. Pallavi P. D., Ms. Hruidya C. B., Ms. Diana T., Mr. Lukhmanul H. K., Mr. Hanock B., Ms. Anitta B., Ms. Anjana S. K., Ms. Agaja K., Ms. Fathima T., Ms. Najuma N., Mr. Sharath D., Mr. Amalnadh T., Mr. Tamizharasan T., Mr. Abhijith M., Ms. Sona S., Mr. Gokul G., Mr. Ariharasudhan R., Ms. Megha S., Ms. Aswathy H., Ms. Greeshma G., Ms. Dhanushya P., Mr. Jagannathan V., Ms. Aarjoo J., Ms. Sujitha S., Mr. Devanath M., B., Mr. Avanindhra, Mr. Anjelo J., Mr. Anzil B. M. and Ms. Meera Jacob for the endless support, care, motivation and joyful moments during my Ph.D. work. On a special note, I would like to thank Ms. Kavya V. and Mr. Amalnadh T. M. for their contributions to the ultrafast transient absorption measurements presented in my doctoral work. I would like to give special thanks to Dr. Ebin S. for being an outstanding mentor. His early guidance, thought-provoking discussions, and foundational lessons in research have impacted my academic journey. I would like to extend my heartfelt thanks to the BS-MS and project students, Ms. Anakha Rajeev, Mr. Arjun S. Nair, Mr. Binil T., and Ms. Navya, for their valuable contributions to the research presented in this thesis. I would like to sincerely thank Mr. Sanjoy Patra, Mr. Vivek N. Bhat, Mr. Atandrita Bhattacharyya, and Mr. Sayan Ghosh for their valuable collaboration and contributions.

I sincerely thank the administrative staff of IISER Thiruvananthapuram for their steadfast support in managing logistics and administrative tasks, which played a vital role in the smooth conduct of my doctoral studies. I am particularly grateful to Mr. Alex for his crystallographic insights, Mr. Adarsh B. for his help with NMR experiments; Mr. Nibith K. for GC-MS, elemental, and FT-IR analyses; Ms. Athira S., and Ms. Ansumol for MALDI-TOF measurements; Mr. Aneesh for SEM analysis; and Mr. Pradeep K. G. and Mr. Prem K. for HRMS support. I also extend my gratitude to all the teaching and non-teaching staff, especially those in the library, IT, purchase, finance, and mess departments, for their timely assistance. I am deeply grateful to UGC for the financial support I received during my doctoral research, and I truly appreciate their continued investment in my academic and professional development.

On a personal note, I am deeply thankful to my friends and peers who have offered moral support and companionship throughout this journey. I thank my PhD 20 batchmates, who have been a constant source of motivation for me. I would also like to thank my Paagal Log friends' group, Ms. Kavya V., Mr. Aniruddha Mazumbder, Mr. Philip D. M., Ms. Megha R., Ms.

Preetika V., Mrs. Ann T. B., and Mr. Prajoy M., who have stood beside me during the entire Ph.D. journey

I am deeply grateful to my family for their unwavering support and boundless love. Their belief in me and the sacrifices they have made have been the foundation of this research journey. I bow with deep gratitude to my beloved parents, Sathyabhama and Sivanarayanan, whose unconditional love, sacrifices, and endless encouragement have been the strongest pillars of my journey. Their unwavering faith in me has been my greatest source of strength, and I dedicate this work to them with all my heart.

I am equally grateful to my dear sisters, Nisha and Jisha, for always being by my side with their love, patience, and unwavering support. Their presence has been a blessing throughout my life. My heartfelt thanks also go to their wonderful children, Akhil Krishna, Aswin Krishna, and Meera Vipin, whose innocence, warmth, and affection have been a source of joy and motivation, bringing light to even my most difficult days.

I would also like to express my heartfelt gratitude to my brother, Prasad, and my dearest friend, Deepak. Their unwavering support, motivation, and encouragement have been invaluable to me. Prasad's constant care as a brother and his belief in my capabilities have given me the strength to endure moments of doubt and struggle.

To all of them, I owe more than words can ever express. This thesis is not just my achievement; it is a reflection of their love, care, and inspiration.

Above all, I am deeply grateful to God for His abundant blessings and for granting me the strength and courage to complete this journey.

- Jibin S.

Preface

The study of organic photophysics has always been guided by the principles of spin statistics, which dictate the fate of electronically excited states. Upon photoexcitation, the probability of forming singlet and triplet excitons is inherently constrained, yet the ability to harvest the long-lived triplet manifold has opened new directions in materials science, ranging from highly efficient organic light-emitting diodes to room-temperature phosphorescent materials and photocatalysts. This central idea, that triplet states are both a challenge and an opportunity, forms the motivation for the present thesis.

This thesis is devoted to monitoring and understanding the population of triplet states in carbazole oligomers with different connectivities. The subsequent chapters detail the design and synthesis of carbazole derivatives, their steady-state and time-resolved photophysical characterisation, and the mechanistic insights obtained from advanced spectroscopic techniques. Particular emphasis is placed on transient absorption and related methods that allow direct observation of triplet formation and dynamics. Each chapter is designed to build on the previous one, gradually connecting the conceptual framework of spin statistics to the molecular design principles that govern triplet harvesting. Through this progression, the thesis aims not only to uncover how connectivity modulates excited-state behaviour in carbazole systems but also to highlight broader strategies for tuning triplet photophysics in organic materials.

In Chapter 1, the fundamental concepts that underpin this thesis are introduced. The discussion begins with the importance of the triplet manifold in organic photophysics, highlighting how long-lived triplet states play a central role in applications ranging from optoelectronics to photocatalysis. Special emphasis is placed on the different mechanisms available for populating the triplet state, including intersystem crossing, sensitisation, and thermally activated processes. These pathways are presented in the context of spin statistics, which governs the distribution of excited states and forms the conceptual foundation for subsequent chapters. The chapter further introduces carbazole as the chromophore of choice for this study. Carbazole is not only a well-known building block in organic materials but also exhibits high triplet energy, structural rigidity, and versatile synthetic tunability. Its diverse photophysical behaviour, spanning fluorescence, delayed fluorescence, phosphorescence, and excimer formation, makes it a model scaffold for exploring excited-state processes. By establishing the rationale for employing carbazole derivatives and outlining the strategies for accessing their triplet states, Chapter 1 sets the stage for the experimental investigations presented in the later chapters.

In particular, the manner in which carbazole units are linked, through the nitrogen atom (N-N), a carbon–nitrogen bond (C-N), or a direct carbon-carbon bond (C-C), can drastically alter the photophysical landscape, modulating processes such as intersystem crossing and thermally activated delayed fluorescence. Despite the wide application of carbazole derivatives in optoelectronic devices, a systematic exploration of how connectivity dictates triplet formation remains underdeveloped.

Chapters 2-4 collectively elucidate structural strategies for controlling triplet harvesting in carbazole-based organic emitters. In Chapter 2, Halogen engineering demonstrates that bromination of a carbazole dimer (BrCz-D) enhances SOC and ISC, enabling robust crystalline-state RTP through halogen-mediated lattice rigidification, in contrast to the TADF-dominant behaviour of the unsubstituted analogue (Cz-D). Chapter 3 shows that efficient RTP can also be achieved without heavy atoms in a planar C–C-connected carbazole dimer, where ultrafast spectroscopy and computations reveal that molecular planarity and extended π-conjugation promote ISC and stabilise triplet excitons. Chapter 4 explores dual delayed emission using heavy-atom-free carbazole oligomers: a trimer (Cz-T) exhibiting balanced TADF/RTP and a hexamer (Cz-H) with phosphorescence-dominated emission. 3D electron diffraction reveals that dense C–H···π interactions in Cz-H generate a rigid supramolecular network, opening a new avenue to the triplet manifold. Ultrafast spectroscopy and quantum-chemical analyses further reveal enhanced ISC, a 7.8-fold increase in SOC, and a reduced ΔE_{ST} in Cz-H, offering a unified picture of how halogenation, planarity, and supramolecular rigidity govern emissive pathways in organic materials.

This body of work represents a journey from fundamental photophysical concepts to the molecular-level understanding of carbazole oligomers, reflecting my deep interest in the interplay between molecular structure and excited-state dynamics. I hope that the insights gained will contribute to the design of next-generation organic emitters and photofunctional materials.

Table of Contents

List of Figures

List of Tables

List of Schemes

Abstract

Triplet states occupy a central role in organic photophysics, governing processes such as delayed fluorescence, room-temperature phosphorescence, and exciton harvesting in optoelectronic devices. Carbazole, with its high triplet energy, rigid molecular framework, and rich excited-state chemistry, serves as a prototypical scaffold for exploring triplet dynamics. Despite its widespread application in organic emitters and photofunctional materials, the manner in which molecular connectivity influences triplet formation in carbazole oligomers remains insufficiently understood. This thesis focuses on monitoring and elucidating the pathways of triplet population in carbazole derivatives with distinct connectivities, N-N, C-N, and C-C, using a combination of steady-state, time-resolved, and ultrafast spectroscopic techniques.

The fundamental importance of triplet harvesting for optoelectronic applications and the pivotal role of carbazole-based systems in this context. The carbazole scaffold, owing to its tunable electronic structure and rigid framework, allows modulation of emission behaviour from fluorescence to delayed fluorescence and room-temperature phosphorescence (RTP). Strategic substitution at different positions within the carbazole core enables fine control over excited-state dynamics and emissive properties.

Chapter 2 explores halogen engineering as an effective tool to modulate emissive pathways from TADF to RTP. We investigated two carbazole dimers: the unsubstituted carbazole dimer (Cz-D) and its brominated analogue (BrCz-D). While Cz-D exhibits TADF under ambient conditions, BrCz-D displays pronounced RTP in the crystalline state. Femtosecond transient absorption spectroscopy confirmed the population of triplet manifolds in both systems. Bromine substitution significantly enhances SOC, facilitating efficient intersystem crossing (ISC) and robust RTP. The enhanced phosphorescence in BrCz-D is attributed to halogen-mediated supramolecular interactions (Br···Br, C···Br, and H···Br) that rigidify the crystal lattice. In contrast, these interactions are absent in solution, explaining the lack of RTP under ambient conditions.

Chapter 3 demonstrates the realisation of RTP without heavy atoms or halogens through a planar C-C-connected carbazole dimer. Ultrafast spectroscopic and quantum chemical analyses reveal efficient triplet formation, supported by singlet oxygen quantum yield measurements. This study highlights how structural planarity and strong π-conjugation can promote ISC and stabilise triplet excitons even in purely organic systems.

Chapter 4 investigates the coexistence of TADF and RTP, dual delayed emission, as a strategy for maximising triplet utilisation in organic emitters. The structural origins of this behaviour are elucidated using three-dimensional electron diffraction (3D ED) combined with time-resolved spectroscopy. Two heavy-atom-free carbazole systems, a trimer (Cz-T) and a hexamer (Cz-H), exhibit distinct dual-emissive behaviours: Cz-T shows balanced TADF and RTP, whereas Cz-H exhibits phosphorescence-dominated emission. Despite its flexible aromatic framework, nanocrystalline Cz-H was successfully resolved by 3D ED, revealing a rigid supramolecular network stabilised by dense C–H···π interactions. This supramolecular likely facilitates efficient triplet harvesting in crystalline Cz-H. Ultrafast transient absorption spectroscopy confirms enhanced ISC in Cz-H compared to Cz-T, while quantum-chemical calculations indicate a 7.8-fold increase in SOC and a reduced ΔE_{ST} from 22.6 meV (Cz-T) to 8.5 meV (Cz-H).

Overall, this thesis establishes clear structure-property correlations in carbazole-based systems and demonstrates how supramolecular design, halogen interactions, and rigid molecular packing can be leveraged to control triplet dynamics. The insights gained provide guiding principles for the rational design of next-generation TADF and RTP materials for high-efficiency, heavy-atom-free OLEDs.

Chapter 1

Introduction to Spin States and Triplet Photophysics: Fundamentals, Techniques, and Applications

1.1. Introduction to Triplet States

The distribution of electrons in atomic and molecular orbitals follows a set of fundamental principles:[1]

❖ Aufbau principle: orbitals are filled sequentially, starting from the lowest to the highest energy levels.

❖ Hund's rule of maximum multiplicity: in degenerate orbitals (e.g., p, d, f sets), electrons occupy orbitals singly with parallel spins before pairing occurs.

❖ Pauli exclusion principle: no two electrons in the same atom can share an identical set of four quantum numbers (n, ℓ, m_ℓ, m_s).

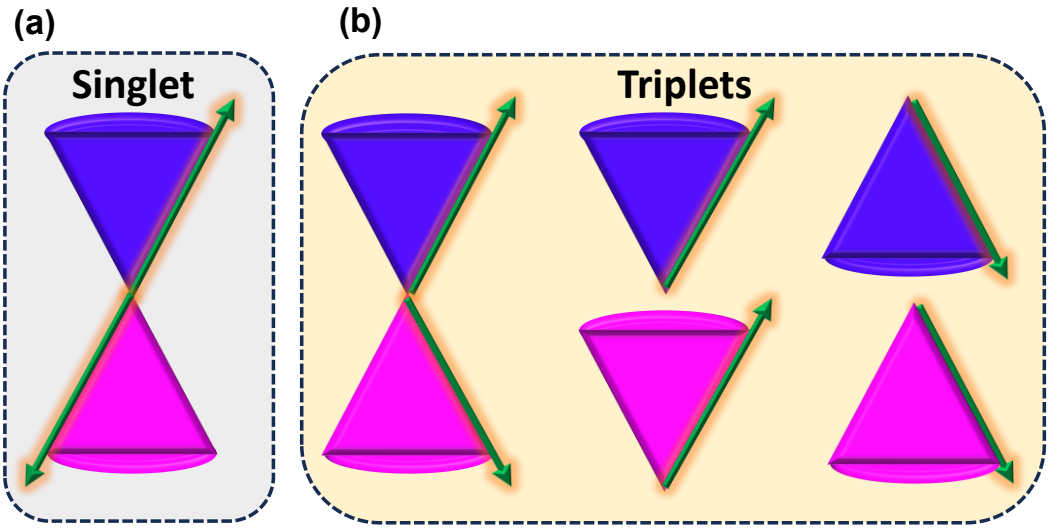

Figure 1.1: Electron spin diagrams of (a) singlet (out-of-phase) and (b) triplet (in-phase) states represented with respect to the direction of the spin vectors.

Uhlenbeck and Goudsmit have introduced the concept of electron spin (m_s = +½, –½), which is crucial for understanding spin multiplicity.[2] Later, Pauli defined spin angular momentum (m_s = 2S+1), which depends on the relative spin orientation, and two electrons can form distinct spin states. The antiparallel configuration results in overall spin angular momentum S = 0, giving rise to a singlet state (Equation 1), where the net spin is zero (Figure 1.1a). Conversely, the parallel spin configurations (Equation 2) correspond to S = 1, producing a triplet state with three degenerate spin sublevels (m_s = –1, 0, +1). Thus, the singlet state is non-degenerate, while the triplet manifold exhibits threefold degeneracy (Figure 1.1b).[3]

$$\frac{1}{\sqrt{2}}((\alpha_1\beta_2) - (\alpha_2\beta_1)) \qquad \text{Equation 1.1}$$

$$\left.\begin{array}{c} \frac{1}{\sqrt{2}}((\alpha_1\beta_2) + (\alpha_2\beta_1)) \\ (\alpha\alpha) \\ (\beta\beta) \end{array}\right\} \qquad \text{Equation 1.2}$$

In most organic molecules, the electronic ground state corresponds to a spin-paired singlet configuration (S_0). Upon photoexcitation, an electron is excited to a higher-energy orbital, generating an excited singlet state (S_n) through an allowed spin-conserving transition.[4] According to Kasha's rule, relaxation from higher singlets occurs rapidly to the lowest singlet excited state (S_1).[5] Importantly, the lowest triplet state (T_1) typically lies below the first singlet state (S_1) in energy. This energy stabilisation of the triplet state arises from the exchange interaction, which lowers the total energy when the two unpaired electrons possess parallel spins (Figure 1.2).[2]

Accessing the triplet manifold from S_1 requires a spin inversion, known as intersystem crossing (ISC), which is a formally spin-forbidden process.[6] However, ISC can be enabled by spin-orbit coupling (SOC), which introduces mixing between singlet and triplet wavefunctions.[3]

$$k_{ISC} \propto \frac{\langle \Psi_s | \hat{H}_{SO} | \Psi_t \rangle}{exp(\Delta E_{ST})^2} \qquad \text{Equation 1.3}$$

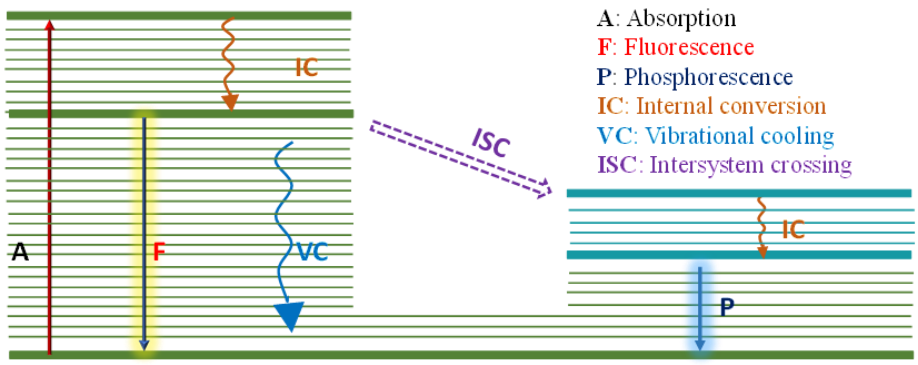

Figure 1.2: Jablonski diagram indicating the various radiative (fluorescence, F; and phosphorescence, P) and non-radiative transitions (ISC, IC, VC).

The efficiency of ISC depends not only on the magnitude of SOC but also on the singlet-triplet energy gap (ΔE_{ST}). According to perturbation theory, the ISC rate (k_{ISC}) is directly proportional to the square of the SOC matrix element and inversely proportional to ΔE_{ST} (Equation 1.3).[7]

1.2. Characterisation methods for triplet excited state

The characterisation of triplet excited states is essential for understanding the fundamental photophysical behaviour of organic chromophores. Triplet states, owing to their long lifetimes and unique spin configurations, play a pivotal role in processes such as phosphorescence,[8] TADF,[9] and exciton dynamics in organic optoelectronic materials.[10] A comprehensive investigation of these states provides valuable insights into non-radiative decay channels, intersystem crossing efficiencies, and excited-state energy transfer mechanisms. To unravel these aspects, a combination of spectroscopic and theoretical techniques has been employed, offering a clear picture of the nature and dynamics of the triplet manifold.

1.2.1. Transient Absorption Spectroscopy (TAS):

Transient absorption spectroscopy is one of the widely used techniques to probe the dynamics of triplet states in organic molecules.[11] In this method, a short pump pulse excites the sample to the singlet manifold, and a subsequent probe pulse monitors the evolution of excited-state populations over time.[12] Triplet states are identified by the appearance of characteristic excited-state absorption bands that are absent in the ground-state spectrum. The long lifetimes of triplets,

typically ranging from nanoseconds to milliseconds, make them distinguishable from singlet excitations, which decay on much shorter timescales.[13] By monitoring the kinetics of these transient signals, information on intersystem crossing efficiency, triplet yield, and decay pathways can be obtained (Figure 1.3). Additionally, global fitting of the kinetic traces allows extraction of rate constants for processes such as ISC and triplet–triplet annihilation, providing a comprehensive picture of triplet dynamics.

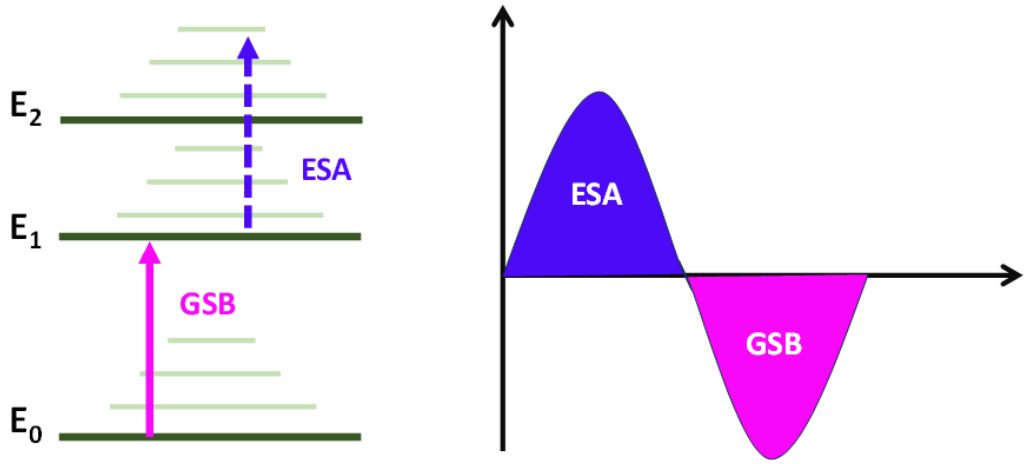

Figure 1.3: A schematic illustrates the photoinduced processes originating from the ground and excited states. The transient absorption spectrum shown alongside features a negative signal attributed to ground-state bleaching (GSB) and positive bands arising from excited-state absorption (ESA).

1.2.2. Electron Paramagnetic Resonance (EPR) Spectroscopy:

EPR spectroscopy provides a direct means of detecting triplet states owing to their unpaired electrons and associated magnetic moments.[14] In particular, time-resolved EPR (TREPR) can capture the formation and evolution of triplet sublevels immediately following photoexcitation. The triplet state gives rise to characteristic zero-field splitting (ZFS) parameters (D and E), which reflect the spatial distribution and anisotropy of the unpaired electron spins. Analysis of these parameters yields valuable insight into the geometry of the triplet exciton and the extent of spin-spin interactions. Unlike optical techniques, EPR does not rely on radiative processes, making it especially powerful for probing “dark” triplet states that are optically forbidden. Thus, EPR

spectroscopy serves as a complementary tool to TAS, providing direct structural and spin-specific information about the triplet manifold.[15]

1.2.3. Singlet Oxygen ((Φ_Δ) Generation Method:

Singlet oxygen generation provides a reliable method to probe the triplet excited states of photosensitizers. The singlet oxygen quantum yields (Φ_Δ) of the photosensitizers were determined using Rose Bengal (RB) as the reference standard (Φ_Δ = 0.80 in methanol, Figure 1.4). The absorbance of the singlet oxygen scavenger, 1,3-diphenylisobenzofuran (DPBF), was adjusted to approximately 1.0 in aerated dimethylformamide (DMF). Subsequently, a photosensitizer was introduced into the cuvette, and its absorbance was maintained in the range of 0.2-0.3. The sample was then irradiated with monochromatic light at the absorption maximum of the photosensitizer for 20 seconds, followed by multiple absorbance measurements after each irradiation cycle. The rate of DPBF bleaching was quantified by plotting the decrease in its characteristic absorption band at 414 nm against time, and the slope of this plot was used to calculate ΦΔ according to a modified Equation 4.[16]

$$\Phi_\Delta^{Sam} = \Phi_\Delta^{ref} \times \frac{k_{Sam}}{k_{ref}} \times \frac{F_{ref}}{F_{Sam}} \qquad \text{Equation 1.4}$$

where k is the slope of the difference in the change in the absorbance of DPBF (at 414 nm) with irradiation time, and F is the absorption correction factor, which is given by F = $1–10^{OD}$ (OD at the irradiation wavelength).[17]

The quantification of singlet oxygen is a powerful approach for assessing the efficiency of intersystem crossing and exploring the triplet manifold of chromophoric systems. Due to its high reactivity, singlet oxygen ($^1\Delta_g$) is of great significance in photodynamic therapy, where it plays a crucial role in selectively destroying affected cells. Mechanistically, during singlet oxygen generation, the triplet excitation energy of the photosensitizer is transferred to ground-state molecular oxygen ($^3\Sigma_g$), producing the excited singlet oxygen species ($^1\Delta_g$).

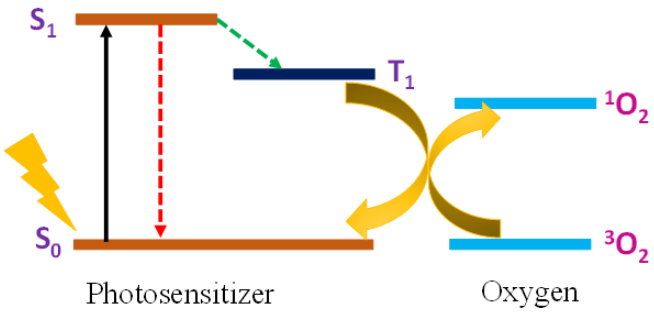

Figure 1.4: Mechanism of singlet oxygen generation by the TTE method.

1.3. Methods to Populate Triplet States

Understanding the methods by which triplet states are populated is crucial for elucidating their role in the excited-state processes of organic molecules. Triplets can be generated through various pathways, most commonly via intersystem crossing (ISC) from the singlet manifold, as well as through mechanisms such as charge recombination, energy transfer, or photoexcitation under specific conditions. The efficiency and nature of these population routes directly influence the photophysical properties of the system, including delayed fluorescence, phosphorescence, and exciton harvesting in optoelectronic applications.

1.3.1. Heavy Atom Effect

SOC arises from the interaction between the magnetic moment generated by an electron's orbital motion and that originating from its intrinsic spin. As the nuclear charge (atomic number, Z) increases, the electrons are accelerated to higher velocities, which enhances the orbital magnetic moment.[3] This orbital contribution couples with the spin magnetic moment, leading to spin reorientation or inversion. The magnitude of SOC scales approximately with the fourth power of the nuclear charge (Z^4), a phenomenon commonly known as the heavy-atom effect (HAE, Figure 1.5). The HAE was first reported in 1949 by McClure, who demonstrated that the direct incorporation of heavy atoms into π-conjugated systems enhances SOC, which is referred to as the internal heavy-atom effect. Subsequently, in 1952, Kasha introduced the concept of the external heavy-atom effect, where SOC enhancement arises from orbital interactions between a molecule and a proximate heavy atom in its environment.[18]

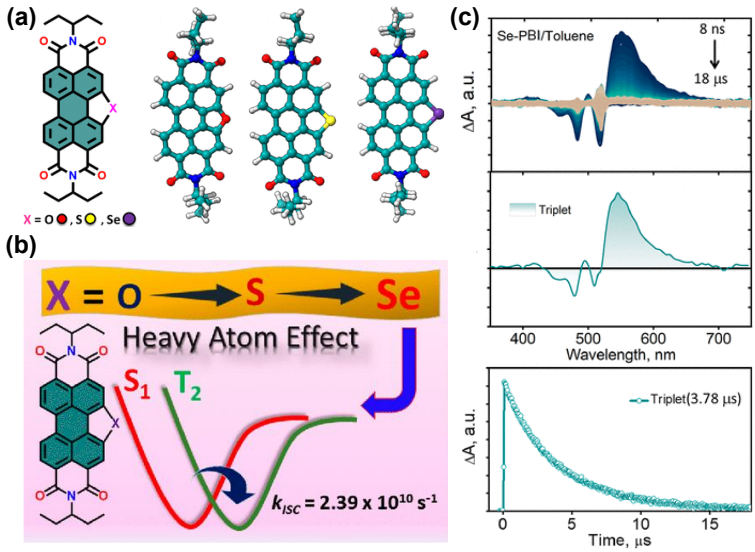

Figure 1.5: (a) Molecular structure of a series of chalcogen annulated PDIs, (b) The Jablonski diagram showing faster ISC in Se-PDI and (c) The nsTA measurement of Se-PDI in TOL.[19]

1.3.2. Vibronically Assisted ISC

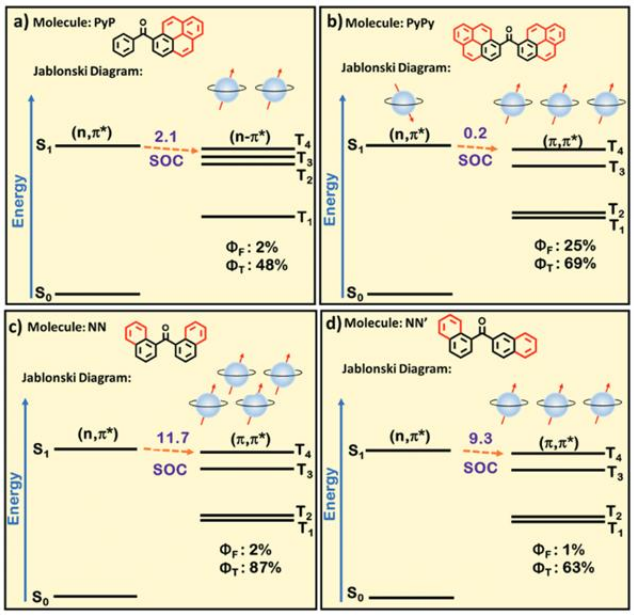

Figure 1.6: Jablonski diagrams for (a) PyP, (b) PyPy, (c) NN and (d) NN_0. The unit for SOC is cm^{-1}, and one blue sphere represents a B20% singlet/triplet quantum yield. *Reproduced from ref. 20 with permission from the PCCP Owner Societies, copyright 2025.*

Vibronically assisted intersystem crossing refers to the transition of a molecule between its singlet and triplet excited states, facilitated by molecular vibrations.[20] In this mechanism, the vibrational modes couple with the electronic states, effectively bridging the energy gap and enabling transitions that are otherwise spin-forbidden. The vibrational contribution provides the necessary pathway for conserving both energy and momentum, thereby enhancing the probability of ISC. As a result, access to triplet states, normally restricted by spin selection rules, is significantly improved (Figure 1.6). This vibronic assistance plays a pivotal role in dictating the photophysical behaviour of molecules, particularly in materials that exhibit thermally activated delayed fluorescence (TADF) or room-temperature phosphorescence (RTP).

1.3.3. Singlet Fission Mediated Triplet Formation

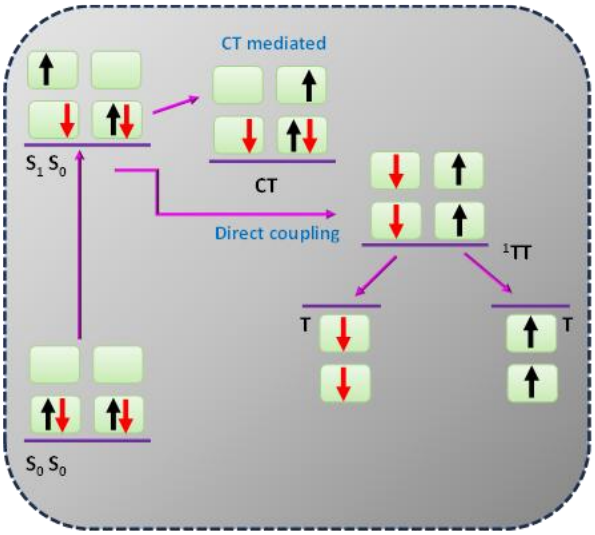

Figure 1.7: General representation of singlet fission and two modes of forming triplet-triplet correlated pair.

Singlet fission is a phenomenon in molecular systems where an optically excited singlet state (S_1) generates two triplet excited states (T_1) localised on adjacent molecules.[21] For this process to be energetically favourable, the energy of the singlet state must be greater than or approximately equal to twice that of the triplet state, i.e., $E(S_1) \geq 2E(T_1)$. This criterion ensures thermodynamic feasibility, allowing the conversion of one high-energy singlet exciton into two lower-energy triplet excitons. Importantly, singlet fission is a spin-allowed process, as the overall spin multiplicity of the system remains conserved.[22] Due to its ability to generate multiple

excitons from a single photon, singlet fission has garnered considerable attention for enhancing the efficiency of organic photovoltaic devices and for the design of advanced optoelectronic materials (Figure 1.7).

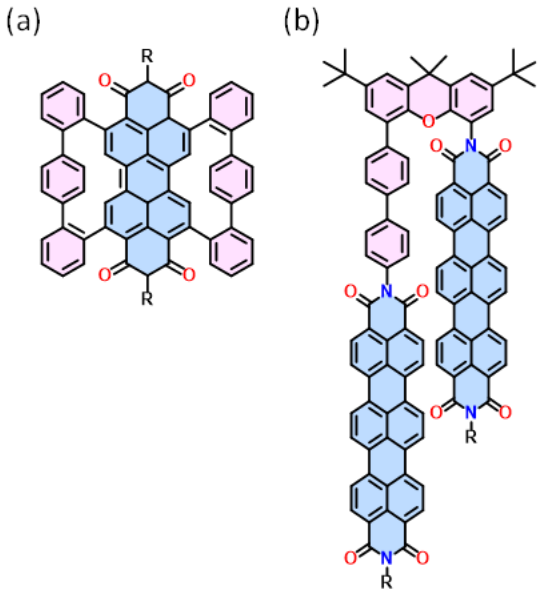

Figure 1.8: Chemical structures of molecules showing Singlet Fission (SF).*[23,24]*

1.3.4. Triplet Formation via Charge Recombination

Charge recombination-mediated triplet formation refers to the generation of triplet excited states through the recombination of charge-separated pairs (Figure 1.9).[3] Two principal mechanisms are commonly recognised.

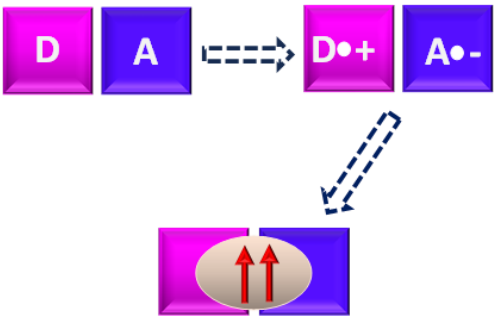

Figure 1.9: A schematic depicts triplet-state formation through charge recombination. D and A denote the donor and acceptor, respectively. Charge recombination between the donor radical cation and acceptor radical anion results in the population of triplet states.

❖ ***Spin-Orbit Coupled Charge Transfer (SOCT):*** In this mechanism, the charge-transfer (CT) state is coupled to a triplet state via spin–orbit coupling (SOC). SOC enables mixing between singlet and triplet manifolds, thereby allowing triplet exciton formation during charge recombination (Figure 1.10). This process is frequently observed in donor–acceptor systems where the CT state exhibits significant SOC, facilitating intersystem crossing (ISC) to triplets. Efficient SOCT-mediated triplet generation typically requires the donor and acceptor to adopt a nearly orthogonal arrangement, which minimises electronic overlap between frontier orbitals and stabilises the CT state, thereby enhancing SOC effects.[25]

❖ ***Radical Pair Mechanism (RPM):*** In this pathway, the spin dynamics of the radical pair (the charge-separated state) govern the eventual spin state of the recombined exciton.[26] Depending on the spin correlation, recombination can yield either singlet or triplet excitons.[27] Under certain conditions, particularly when the radical pair evolves into or maintains a triplet spin configuration, the RPM favours the generation of triplet excitons.[28]

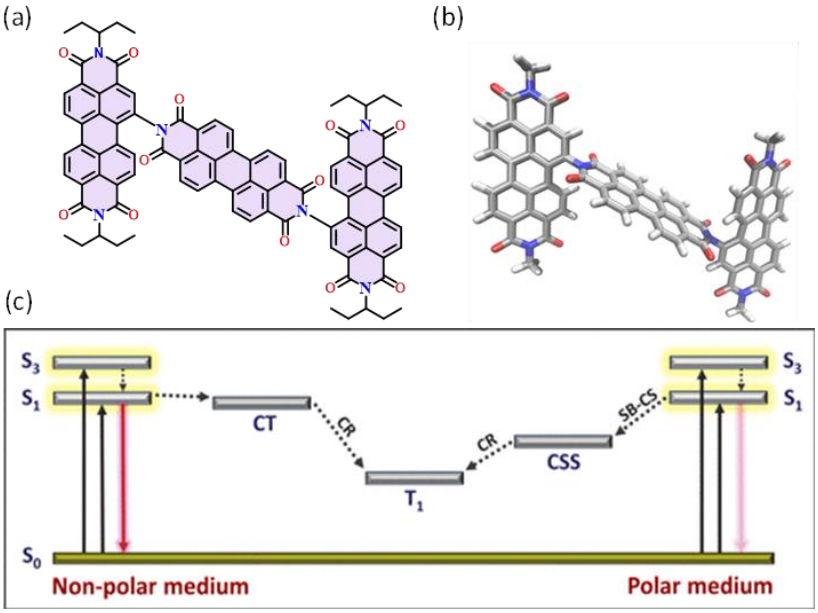

Figure 1.10: (a) Molecular structure of PDI trimer, (b) Optimised structure of the PDI-T and (c) The proposed Jablonski diagram showing CR based triplet formation in PDI-T. *Reproduced from ref. 28 with permission from the JPC Letters Owner Societies, copyright 2025.*

1.3.5. Twist-Induced Triplet Population

Twist-induced triplet population describes a process in which molecular twisting or curvature promotes the formation of triplet excited states.[29] In systems such as fullerenes,[30] the nonplanar, curved geometry reduces molecular symmetry and facilitates mixing between singlet and triplet states, thereby enhancing ISC (Figure 1.11).[31] This effect is often associated with the increased spin-orbit coupling (SOC) that arises from structural distortion and orbital mixing within the twisted framework. By contrast, highly planar systems, such as graphene, preserve higher symmetry and exhibit weaker singlet-triplet mixing, resulting in less efficient triplet generation.[32] Thus, the intrinsic curvature or twisting of fullerenes and related molecules plays a key role in governing their photophysical behaviour, particularly the dynamics of triplet state population.

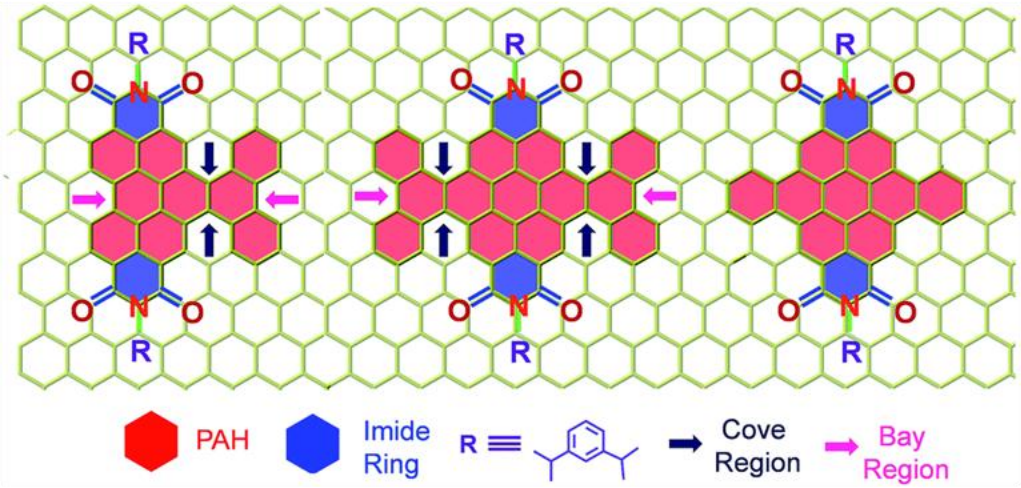

Figure 1.11: (a) Schematic representations of PDI-a and PDI-b indicating the point of twisting in the cove region and planar PDI-c. *Reproduced from ref. 29 with permission from the Chemical Science Owner Societies, copyright 2025.*

1.3.6. Aromaticity Driven Triplet Population

Aromaticity-driven triplet population refers to the role of aromatic stabilisation or destabilisation in governing the accessibility of triplet excited states. According to Hückel's rule, cyclic conjugated systems with (4n + 2) π-electrons exhibit aromatic stabilisation in the ground state, whereas systems with 4n π-electrons are antiaromatic.[33] In contrast, Baird's rule predicts that this relationship is reversed in the lowest triplet excited state: 4n π-electron systems gain aromatic stabilisation, while (4n + 2) π-electron systems become antiaromatic.[34] This change in aromatic character upon excitation directly influences the relative energetics of singlet and triplet states. When the triplet state is stabilised by Baird aromaticity, the singlet–triplet energy gap (ΔE_{ST}) is reduced, thereby facilitating ISC and enhancing triplet population (Figure 1.12). Conversely, when the singlet state is strongly stabilised by Hückel aromaticity, ISC is less efficient due to the larger ΔE_{ST}. Thus, the interplay between Hückel and Baird aromaticity provides a design principle for tuning triplet formation in conjugated molecules and polycyclic aromatic hydrocarbons, with profound implications for their photophysical behaviour and applications in optoelectronic materials.

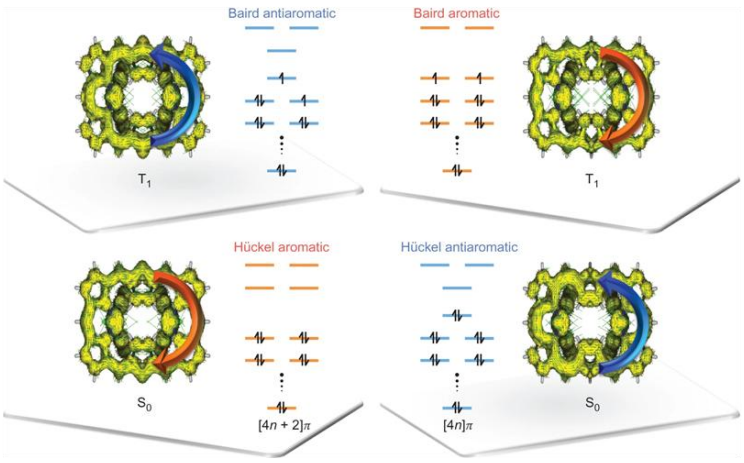

Figure 1.12: ACID plots for R26H (left) and R28H (right) in the ground state and lowest triplet state. *Reproduced from ref. 34 with permission from the Nature Chemistry Owner Societies, copyright 2025.*

1.4. Molecular Design Strategies to Harness the Triplet Manifold

Upon photoexcitation, organic chromophores undergo the formation of an exciton, which represents a Coulombically bound electron-hole pair. The radiative recombination of these excitons results in the emission of photons. Based on spin statistics, the initial exciton population in singlet and triplet excited states is 1:3 in ratio.[35] The latter are predominantly formed through the process of ISC, in which an excited-state species undergoes a transition between electronic states of different spin multiplicities. This spin-forbidden transition is enabled by spin-orbit coupling (SOC) and is governed by El-Sayed's rule, which stipulates that ISC is most efficient when it involves a change in the type of orbital (e.g., π–π^* ↔ n–π^*) between the participating states.[36] Once generated, singlet excitons typically relax radiatively through fluorescence, a process characterised by relatively short lifetimes on the order of nanoseconds. Triplet excitons, in contrast, decay radiatively via phosphorescence, a much slower process due to the spin-forbidden nature of the triplet-singlet transition.[37] However, the triplet manifold is also prone to competing non-radiative decay pathways, such as internal conversion and vibrational relaxation, which often dominate at ambient temperatures and suppress phosphorescence. At cryogenic temperatures (e.g., 77 K), thermal vibrations are significantly quenched, thereby reducing non-radiative losses. Under such conditions, phosphorescence can effectively compete with non-radiative channels, allowing for its more efficient observation.

The first-generation organic light-emitting diodes (OLEDs) primarily utilised only singlet excitons for light emission, which fundamentally restricted the internal quantum efficiency (IQE) to 25% according to spin statistics (Figure 1.13a). In practical devices, the EQE of such systems has been reported to be below 5%, due to additional optical losses and non-radiative decay pathways.[38,39] This significant limitation prompted researchers to explore strategies to effectively harvest triplet excitons, which constitute the majority of the exciton population. Early efforts to exploit the triplet manifold involved incorporating heavy metal complexes containing elements such as iridium (Ir), osmium (Os), ruthenium (Ru), platinum (Pt), palladium (Pd), silver (Ag), and gold (Au).[40] These atoms exhibit strong spin-orbit coupling (SOC), which facilitates efficient intersystem crossing (ISC) and enables radiative triplet emission, also known as phosphorescence (Figure 1.13b). Although this approach markedly enhanced device efficiencies,

it was soon recognised that reliance on noble metals introduced challenges related to high cost, limited resource availability, and potential environmental toxicity upon disposal.[41]

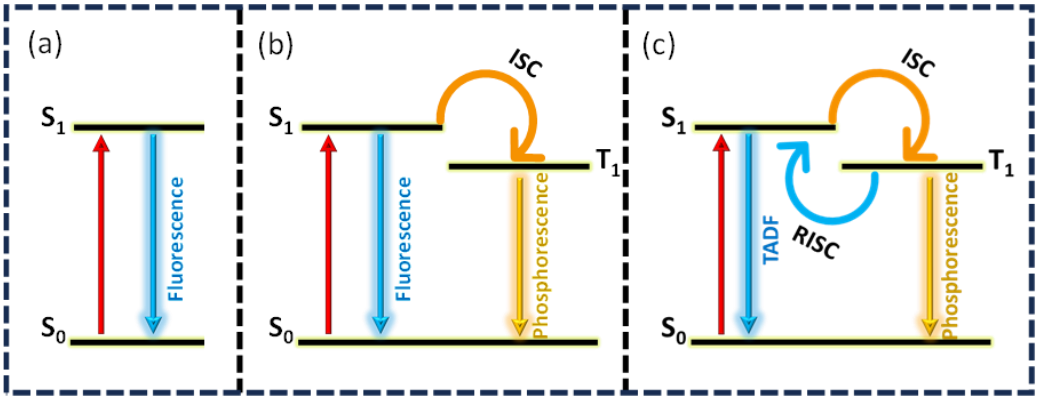

Figure 1.13: Schematic representations of (a) First-generation OLEDs, (b) Second-Generation OLEDs and (c) Third-generation OLEDs.

In response to these concerns, a third-generation OLED strategy was developed, which introduced the concept of converting non-emissive triplet excitons back into emissive singlets through reverse intersystem crossing (RISC).[42] This process results in photon emission from the singlet state, but with a delayed temporal profile, leading to what is known as TADF (Figure 1.13c).[43] Since ISC is a non-radiative spin-conversion process, RISC requires an input of thermal energy to overcome the energetic barrier, making it inherently endothermic. Consequently, the efficiency of RISC, and hence TADF, increases with thermal activation. For efficient TADF, two critical conditions must be satisfied:[44]

❖ The singlet-triplet energy gap (ΔE_{ST}) between the lowest excited singlet (S_1) and triplet (T_1) states should be sufficiently small (typically < 0.1 eV) to enable efficient thermal upconversion.

❖ The spin-orbit coupling should be adequately strong to facilitate spin-flip transitions between T_1 and S_1.

When both criteria are fulfilled, TADF materials can achieve near-unity internal quantum efficiencies, as they are capable of harvesting both singlet and triplet excitons for light emission.

This makes them highly promising candidates for practical device applications, bridging the gap between efficiency, cost-effectiveness, and environmental sustainability.

One of the most widely adopted molecular design strategies for realising TADF is the donor-acceptor (D-A) architecture.[45] In this approach, electron-donating and electron-accepting moieties are covalently linked within a single molecular framework. Such an arrangement promotes spatial separation of the frontier molecular orbitals: the highest occupied molecular orbital (HOMO) is predominantly localised on the donor unit, whereas the lowest unoccupied molecular orbital (LUMO) is largely concentrated on the acceptor unit. This spatial segregation of electron density reduces the overlap between the HOMO and LUMO wavefunctions. Consequently, the exchange integral (J_{exc}), which quantifies the electron-hole exchange interaction, is minimised. Since the singlet-triplet energy gap (ΔE_{ST}) is directly related to this exchange integral according to the relation:[9]

$$J_{exc} = \frac{1}{2}\Delta E_{ST} \qquad \text{Equation 1.5}$$

A smaller orbital overlap results in a smaller ΔE_{ST}. The reduction of ΔE_{ST} is a fundamental prerequisite for efficient RISC, as it allows thermal energy at room temperature to overcome the energy barrier between the triplet and singlet states. Therefore, the D-A molecular design has become a conventional and highly effective methodology for achieving TADF-active emitters.[46]

1.5. Utilisation of Triplet Excitons

1.5.1. Room Temperature Phosphorescence (RTP)

Upon photoexcitation, singlet excitons can undergo intersystem crossing (ISC) to populate the triplet manifold. The radiative decay from these triplet states is referred to as phosphorescence.[47] Observation of phosphorescence at 77 K was a routine phenomenon reported several decades ago; however, realising the same under ambient conditions posed a significant challenge. At room temperature, thermal vibrations efficiently deactivate the triplet excitons non-radiatively, thereby suppressing their radiative decay.

In the early stages, achieving room-temperature phosphorescence (RTP) was primarily realised through the incorporation of heavy-metal atoms, which enhanced spin-orbit coupling and promoted ISC. Although effective, this strategy was costly and raised environmental concerns due to issues with disposing of metal. The first documented example of pure organic RTP was reported in 1939 by Clapp, who observed green-to-blue afterglow from tetraphenyl methane and tetraphenyl silane derivatives.[47] Subsequently, Bilen and co-workers demonstrated RTP in crystalline dibenzothiophene, dibenzofuran, and triphenylene.[48] After a long hiatus, research on purely organic RTP re-emerged, and numerous reports have since established its feasibility (Figure 1.14). A landmark contribution was made by Adachi and co-workers, who recently demonstrated ultralong-lived RTP with lifetimes exceeding one hour, marking a major advance in the field.[49]

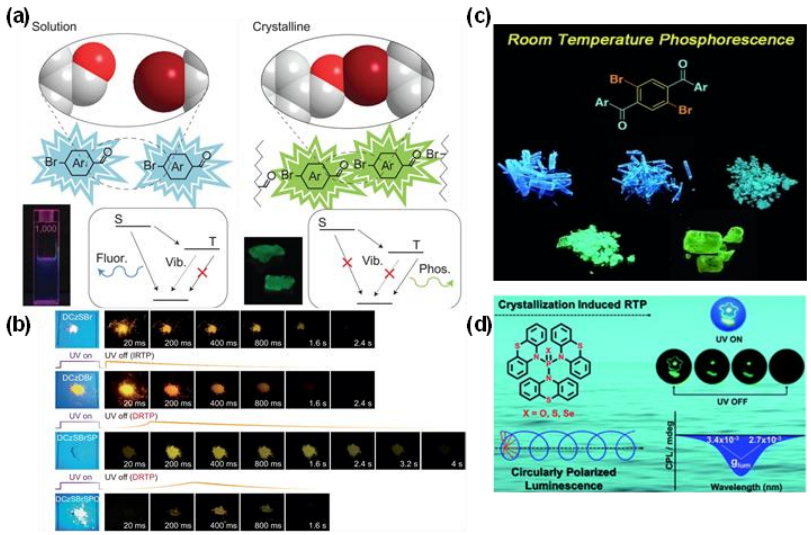

Figure 1.14: (a) Crystallisation-induced RTP, *Reproduced from ref. 50 with permission from the Nature Owner Societies, copyright 2025*, (b) Host-guest interaction induced RTP, *Reproduced from ref. 51 with permission from the Wiley Owner Societies, copyright 2025*, (c) Supramolecular aggregation induced RTP, *Reproduced from ref. 52 with permission from the Nature Owner Societies, copyright 2025* and (d) *Reproduced from ref. 53 with permission from the Chemical Science Owner Societies, copyright 2025*

Organic chromophores can display RTP when specific structural and environmental factors effectively suppress non-radiative deactivation pathways. A rigid molecular framework or a confined environment can restrict intramolecular motions, thereby favouring radiative decay of triplet excitons.[50] Incorporation of heteroatoms or heavy atoms enhances spin-orbit coupling, which facilitates intersystem crossing and increases the probability of triplet-state population. In addition, supramolecular organisation,[51] such as molecular aggregation, crystallisation,[52] or host-guest complexation,[53] can stabilise the triplet state and further minimise non-radiative loss channels. The interplay of these factors enables organic chromophores to achieve efficient RTP, establishing them as attractive candidates for applications ranging from optoelectronic devices to bioimaging.

RTP has diverse applications across various fields. In bioimaging, RTP materials enable high-contrast imaging due to their long-lived emission.[54] They are also used in optical sensing to detect oxygen, temperature, and other analytes.[55] Additionally, RTP materials are being explored for use in display and lighting technologies, such as OLEDs, due to their efficient and stable emission properties.[56] Furthermore, RTP's unique properties make it suitable for security features like anti-counterfeiting marks and authentication tags.[57] RTP materials also show promise in photodynamic therapy, where the long-lived triplet state can generate reactive oxygen species for cancer treatment.[58] These applications leverage RTP's distinct characteristics, making it a valuable technology across multiple domains.

1.5.2. Thermally Activated Delayed Fluorescence

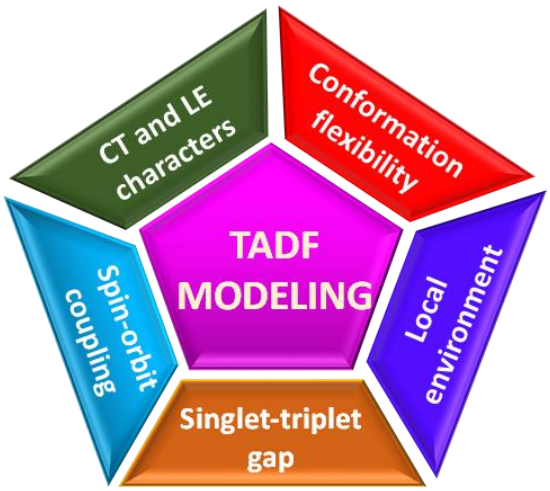

TADF is a non-trivial photophysical process in which non-emissive triplet excitons (T_1) are thermally promoted to the lowest singlet excited state (S_1) through reverse intersystem crossing (RISC).[59] Once in S_1, these excitons undergo radiative decay to the ground state (S_0), resulting in delayed fluorescence. Unlike conventional fluorescence, which only utilises singlet excitons, TADF effectively recycles both singlet and triplet excitons, thereby achieving near-unity internal quantum efficiency in organic light-emitting diodes (OLEDs).[60–63] Adachi and co-workers provided a seminal demonstration of TADF in a carbazole-based donor–acceptor system, wherein the interplay of the aforementioned parameters was systematically realised;[64–68]

The efficiency of TADF is governed by several interdependent molecular and environmental parameters:

❖ ***Charge Transfer (CT) vs. Locally Excited (LE) Character***

The relative contributions of CT and LE states are crucial in defining TADF behaviour.[69–72] CT states, originating from donor-acceptor electron transfer, reduce the singlet-triplet energy gap (ΔE_{ST}), which facilitates RISC.[73] LE states, on the other hand, retain strong oscillator strength, ensuring high radiative emission efficiency. An optimal balance between CT and LE character is therefore essential: too little CT results in a large ΔE_{ST} (inefficient RISC), while excessive CT diminishes emission efficiency due to weak radiative transitions.

❖ ***Spin-Orbit Coupling (SOC)***

SOC mediates the mixing between singlet and triplet manifolds, thereby enabling both forward ISC and the RISC.[62] Incorporation of heteroatoms, heavy atoms, or specific molecular geometries can enhance SOC, accelerating triplet-singlet upconversion.[44,59] However, excessive SOC may introduce non-radiative decay channels (triplet quenching), underscoring the need for fine-tuned molecular design.

❖ ***Singlet-Triplet Energy Gap (ΔE_{ST})***

A small ΔEST (generally < 0.2 eV) is the most critical prerequisite for efficient TADF. This energy gap can be minimised by spatial separation of frontier orbitals (HOMO localised on donor, LUMO on acceptor). Rational molecular engineering, such as twisting donor and acceptor units or introducing steric constraints, is widely employed to reduce orbital overlap and hence lower ΔE_{ST}.[74]

❖ ***Local Environment***

The photophysical response of TADF materials is highly sensitive to their medium. Solvent polarity or host matrix properties can stabilise CT states, altering ΔE_{ST} and the efficiency of RISC.[75] Rigid environments, such as crystalline states or well-designed host materials, restrict molecular vibrations, suppress non-radiative decay, and thereby improve emission intensity and lifetime.[72]

❖ ***Conformational Rigidity and Flexibility***

Structural rigidity is advantageous as it suppresses vibrational relaxation pathways that deactivate excited states non-radiatively. Flexible donor-acceptor linkages may lead to torsional motions, which broaden ΔE_{ST} and quench delayed fluorescence.[76] Strategies such as steric hindrance, rigid scaffolds, or intramolecular locking are often employed to restrict conformational motion, thereby stabilising CT states and enabling efficient TADF (Figure 1.15).[77]

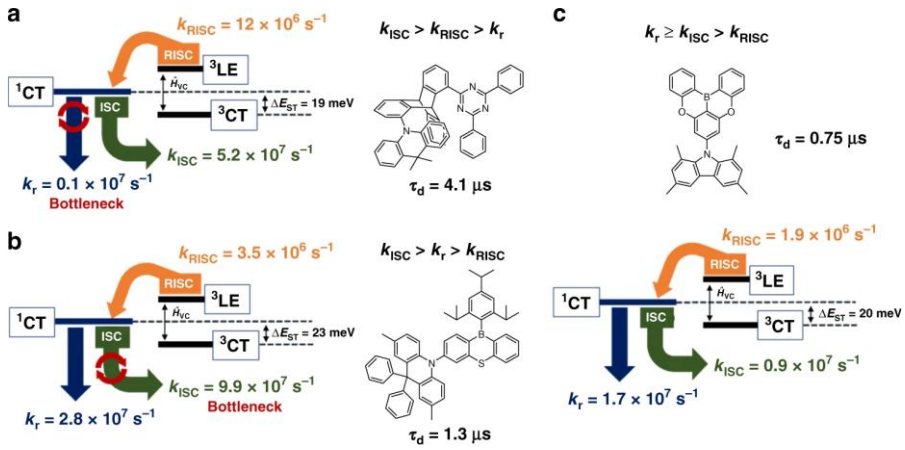

Figure 1.15: (a) TpAT-tFFO, (b) MPAc-BS, and (c) TMCz-BO. k, k_{ISC}, k_{RISC}, CT, LE, and ΔE_{ST} represent the rate constants of fluorescence radiative decay, ISC, RISC, charge transfer, localised excited states, and the energy gap between the lowest singlet and triplet excited states, respectively. *Reproduced from ref. 77 with permission from the Nature Communications Owner Societies, copyright 2025.*

1.5.3. Dual Emission or Biluminescence

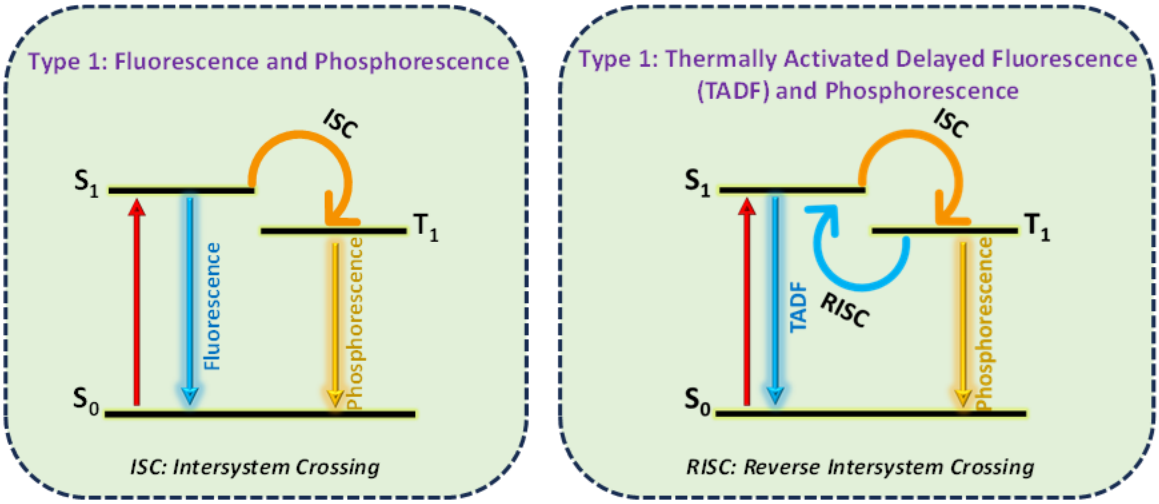

Figure 1.16: Schematic representation of types of dual emissions.

Dual emission (DE), also referred to as biluminescence, originates from the simultaneous radiative decay of two or more excited states within a single molecular framework (Figure 1.16). This multifaceted phenomenon can arise through distinct mechanisms. For instance, non-Kasha type emission from higher singlet states ($S_2 \rightarrow S_0$) coexisting with conventional S_1 emission has been observed in molecules such as porphyrins[78–80] and azulenes.[81,82] Alternatively, dual fluorescence and phosphorescence from the S_1 and T_1 states, respectively, is exemplified in Cu(I)-based organometallic complexes.[83] In contrast, the manifestation of S_1/T_1 dual emission in purely organic systems remains rare, with the first well-characterised example reported only in 2013. Lu and co-workers have recently demonstrated the coexistence of TADF and ultralong room-temperature phosphorescence (URTP) in a D-A system.[84] In their study, a phenanthroline-triphenylamine architecture was employed as the D-A framework. Interestingly, the pristine D-A system exhibited URTP as the dominant emissive pathway. However, upon coordination of a silver atom with an appropriate ligand, the resulting metal-organic complex (denoted as complex 1) displayed markedly different photophysical behaviour. The presence of the Ag centre enhanced SOC and reduced the singlet-triplet energy gap (ΔE_{ST}), thereby facilitating efficient

RISC (Figure 1.17). This synergistic effect enabled the simultaneous manifestation of TADF and URTP in complex 1, highlighting the crucial role of metal coordination in modulating the excited-state dynamics of organic emitters (Figure 1.17).

The photophysical origin of S_1/T_1 DE relies on a subtle interplay among the competing rate processes of fluorescence, ISC, phosphorescence, and non-radiative decay.[85] Notably, many reported organic S_1/T_1 DE systems exhibit a combination of prompt fluorescence and TADF, where the efficiency critically depends on the relative rates of RISC versus other radiative and non-radiative pathways.

Rational molecular design for achieving DE requires finely tuned singlet-triplet energy gaps (ΔE_{ST}) and SOC strengths. These parameters must be optimised to promote efficient competition between fluorescence/TADF and RTP, while suppressing energy loss through non-radiative channels. The resulting dual-emissive materials often display distinct emission bands, characteristic lifetimes, oxygen sensitivity, and temperature-dependent photophysics. Such features make DE systems particularly attractive for applications in ratiometric sensing, security encryption, and the development of white-light organic light-emitting diodes (OLEDs). Continued exploration of the mechanistic underpinnings and design strategies of DE is therefore essential to harness its full technological potential.[86–88]

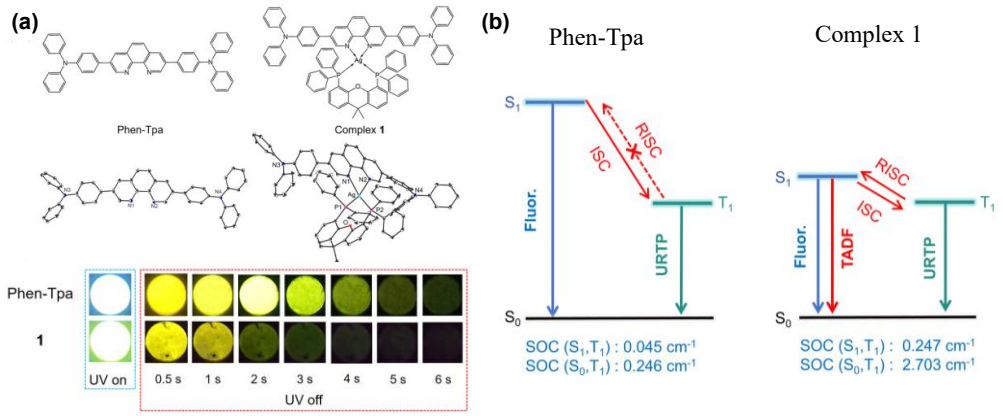

Figure 1.17: (a) Molecular structure of the ligand and the coordinating complex with silver and its URTP images, and (b) the proposed Jablonski diagram for the proposed chromophore. *Reproduced from ref. 84 with permission from the Chemical Science Owner Societies, copyright 2025.*

1.6. Carbazole

Carbazole ($C_{12}H_9N$) is a tricyclic aromatic heterocycle that was first identified in 1872 by Graebe and Glaser during coal tar investigations.[89] Historically, its primary source was the anthracene fraction of coal tar, where carbazole occurred as a minor component. Due to the close similarity in physical properties between carbazole and anthracene, particularly their crystalline characteristics, their separation required extensive recrystallisation procedures. This fraction thus served as the earliest industrial source of carbazole, which subsequently found utility as a precursor for synthetic dyes, pigments, pharmaceuticals, and functional materials (Figure 1.18).[90] However, the limited availability of carbazole from coal tar prompted the development of synthetic routes, which remain the predominant method of production to this day.

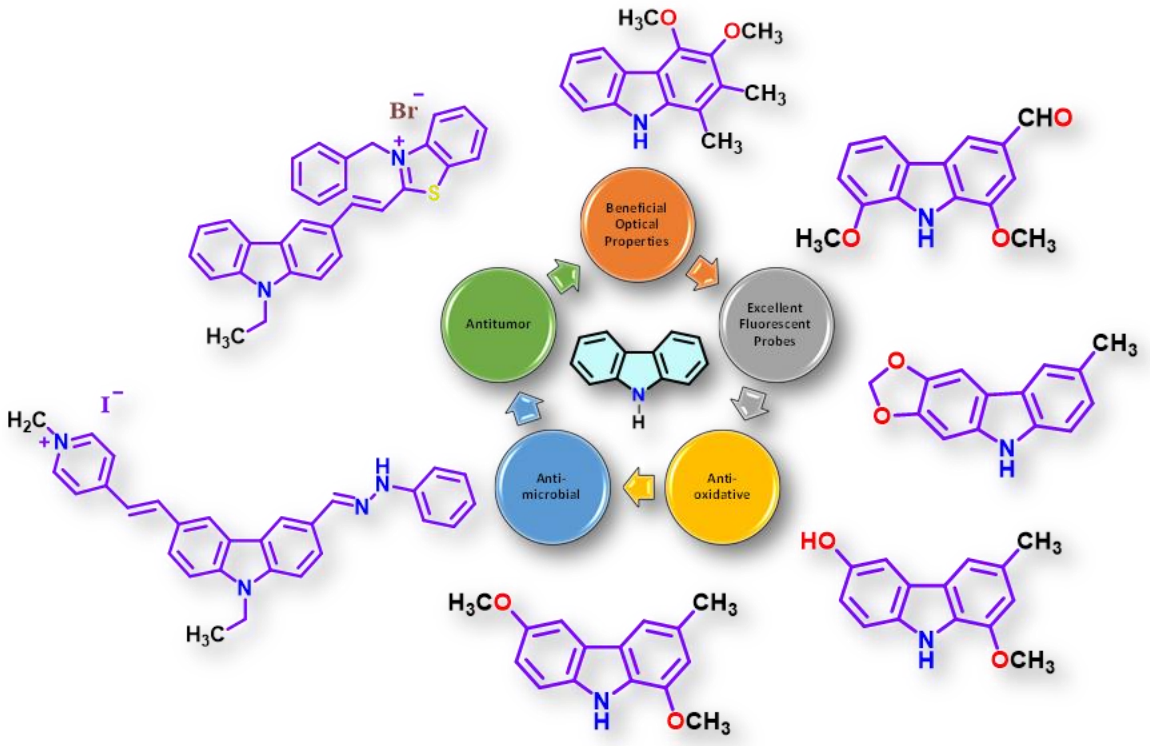

Figure 1.18: Carbazole and its role in the biological and chemical fields.[91]

Due to their distinctive optical and electronic properties, carbazoles and their derivatives have attracted considerable research interest. These properties underpin their widespread application in advanced organic electronic devices, including organic light-emitting diodes (OLEDs), organic photovoltaics (OPVs), and organic field-effect transistors (OFETs), where they serve as efficient charge-transport and emissive components.[92] Beyond optoelectronics, carbazole-based systems are actively investigated for applications in bioimaging and chemical sensing, capitalising on their strong photoluminescence (Scheme 1.1).[93] Moreover, the inherent structural versatility of the carbazole scaffold permits extensive chemical modification and functionalization, thereby enabling the rational design of tailored materials for targeted technological and biomedical applications.[94]

In 1965, Chakraborty and co-workers reported the isolation of murrayanine (3-formyl-1-methoxycarbazole) from Murraya koenigii Spreng., marking the first identification of a naturally occurring carbazole alkaloid.[95] This species, commonly known as the curry-leaf tree and widely distributed in India, a region renowned for its rich diversity of medicinal plants, was shown to yield a compound with notable antibiotic activity. The findings of Chakraborty and colleagues sparked significant interest in carbazole-based natural products, subsequently opening new avenues for exploring the pharmacological and biological potential of the carbazole framework.

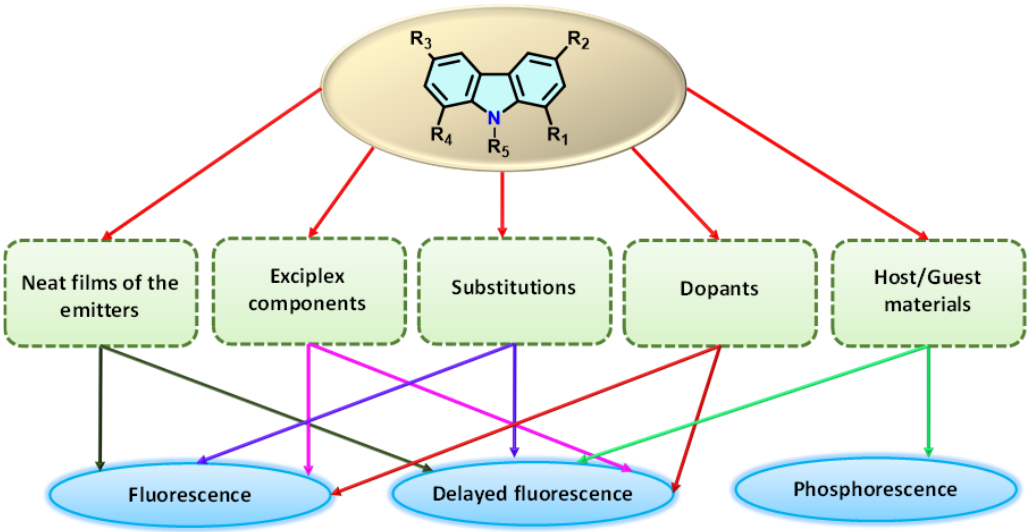

Scheme 1.1: Tuning pathways in carbazole to have variable emission.[96]

Carbazole derivatives are among the most versatile and widely employed chromophores in organic light-emitting diode (OLED) applications. Owing to their unique electronic and structural characteristics, carbazole-based compounds can serve multiple functions within device architectures.[97] They can act as the emissive species in neat films or function as host or guest components within host-guest emissive systems. Importantly, by judicious structural modification of the carbazole framework, their photophysical properties can be finely tuned, enabling transitions across fluorescence, TADF, and even phosphorescence.

In conventional D-A molecular architectures, carbazole frequently serves as the donor moiety. Its strong electron-donating ability facilitates intramolecular charge transfer (ICT) states when coupled with suitably electron-deficient acceptors, thereby modulating the emission colour. For instance, integration with highly electron-accepting units can shift the emission into the red or even near-infrared (NIR) spectral regions. Triarylborane represents a particularly notable acceptor in this context. Possessing a low-lying LUMO, triarylborane readily forms ICT states with carbazole. Moreover, the intrinsic electron-deficient nature of the boron centre not only enhances charge-transfer emission but also promotes aggregation-induced emission (AIE) in the solid state. Consequently, carbazole-triarylborane conjugates emerge as efficient fluorescent emitters.[98]

The D-A motif can be further elaborated through conjugated bridges, forming D-π-A-π-D type structures, where the extended π-conjugation offers additional avenues for fine-tuning emission characteristics across the visible spectrum.[99] A landmark example was reported in 2008 by Kuo, Chen, Jeng, and co-workers, who demonstrated carbazole-arylborane conjugates as efficient blue-emitting fluorophores.[100] Their design achieved an external quantum efficiency (EQE) of 6.9%, marking a significant breakthrough in fluorescent OLED research of that era. Since then, extensive efforts have been devoted to diversifying the acceptor components in carbazole-based systems, resulting in progressively higher device efficiencies and reinforcing the pivotal role of carbazole in the design of advanced OLED materials.[96]

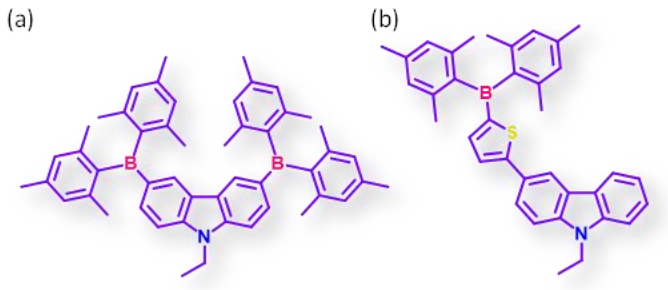

Figure 1.18: Chemical structures of the D-A system to have TADF emission.[101]

A breakthrough in the field of OLEDs was achieved in 2012 by Adachi and co-workers, who were the first to demonstrate highly efficient devices based on the principle of TADF.[45] Their pioneering work established carbazole-based donor-acceptor (D-A) systems as a new class of TADF emitters, fundamentally expanding the design strategies for next-generation emissive materials.

In their study, the authors systematically engineered carbazole derivatives by coupling the donor fragment with various electron-accepting units. This molecular design enabled a wide spectral tunability of emission, spanning from sky-blue to orange regions. Importantly, they demonstrated that the emission colour could be finely adjusted not only by the intrinsic electronic properties of the chosen acceptors but also by modulating the donor-acceptor connectivity within the molecular scaffold. Such structural variations directly influenced the degree of charge transfer, the singlet-triplet energy gap (ΔE_{ST}), and consequently the efficiency of RISC, which is central to the TADF mechanism.

Through careful optimisation of molecular design and device architecture, Adachi's group reported record EQEs at that time: 19.3% for green-emitting devices, 11.2% for orange-emitting devices, and 8.0% for sky-blue devices.[45,64,67,68,102] These remarkable results clearly established TADF as a viable and highly promising alternative to phosphorescent OLEDs, with the added advantage of utilising purely organic materials without the need for heavy-metal complexes. This seminal work not only highlighted the versatility of carbazole as a donor unit in D-A systems but also laid the foundation for a new era of OLED research. It inspired extensive efforts

toward the rational design of TADF emitters, where emission colour, efficiency, and device stability could be systematically tuned through molecular engineering strategies.

Figure 1.19: D-A systems, which are composed of carbazole as donor and -CN substitution as acceptor for OLEDs fabrications.[45]

Carbazole derivatives not only function as intrinsic TADF emitters in D-A molecular systems but can also participate in ICT processes, resulting in exciplex-based emission. An exciplex is formed at the interface between an electron-donating and an electron-accepting material, where photoexcitation induces charge transfer across the D-A boundary. This intermolecular charge-transfer excited state can efficiently undergo RISC, thereby producing TADF. Grazulevicius and co-workers were among the first to report exciplex-type TADF emission originating from carbazole-based donor systems.[103] In their pioneering work, the carbazole-acceptor exciplex exhibited an EQE of 3.15% in OLED devices, an important early demonstration of exciplex-mediated TADF, albeit with modest performance compared to intramolecular emitters.[104] Subsequent research efforts have focused on optimising exciplex-based systems by carefully tailoring the acceptor moieties, D-A energy alignment, and the host matrix environment. These advances significantly improved the photophysical processes governing exciplex emission, including better overlap of frontier molecular orbitals and reduced singlet-triplet energy gaps, which facilitated more efficient RISC. As a result of these molecular and device-level optimisations, the EQE of carbazole-based exciplex OLEDs has been remarkably enhanced, reaching values as high as ~20%. This progression, from the initial proof-of-concept by Grazulevicius et al. to the subsequent high-efficiency exciplex systems, underscores the potential

of carbazole as a versatile donor unit. It also highlights the broader significance of exciplex formation as a powerful strategy for achieving efficient TADF in OLEDs through intermolecular design, complementing the more conventional intramolecular D-A emitter approach.[105]

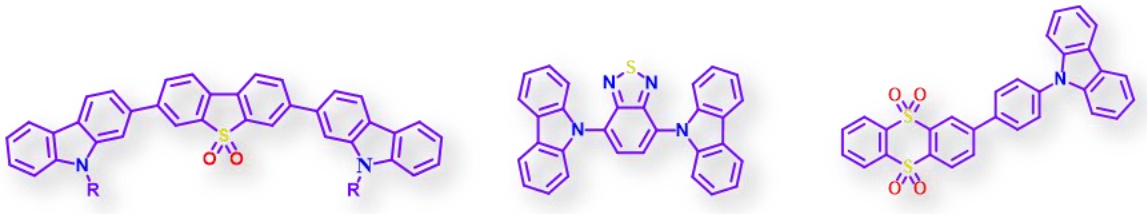

Figure 1.20: Triad systems (D-A-D) exhibiting TADF emission.*[106]*

A fundamental understanding of the photoexcited-state dynamics of carbazole and its derivatives is crucial, particularly in the context of their widespread application in OLEDs.[107] While carbazole has long been recognised as a versatile chromophore and a building block for functional materials, the detailed photophysical mechanisms that govern its excited-state behaviour remain only partially understood. In my thesis work, I have sought to address this gap by systematically probing the excited-state processes in carbazole-based systems.

Early pioneering efforts, such as the transient spectroscopic studies reported by Takahashi and co-workers in 2003, provided valuable insight into the intrinsic excited-state pathways of carbazole in isolation.[108] These investigations revealed the fundamental processes of singlet and triplet population dynamics, laying the groundwork for understanding their role in optoelectronic applications. However, once carbazole is incorporated into more complex molecular architectures, such as D-A systems, oligomers, or conjugated polymers,[109] the situation becomes significantly more intricate.[110] The introduction of electronic coupling between donor and acceptor fragments, or the extended conjugation present in oligomeric and polymeric frameworks, can drastically alter excited-state relaxation pathways.[111]

Even in homo-oligomeric carbazole systems, without the presence of strong acceptor units, the excited-state behaviour deviates markedly from that of the monomer. These differences are often evident in steady-state photophysical measurements, where spectral shifts, changes in emission

lifetimes, and altered quantum yields suggest the presence of new deactivation channels or excited-state interactions. Such phenomena indicate that the evolution from monomer to higher analogues introduces new degrees of freedom in exciton dynamics that remain poorly resolved.

Disentangling these mechanisms is essential, as carbazole-based systems can manifest a diverse range of emissive processes, including prompt fluorescence, TADF, and RTP. Each of these processes is governed by distinct excited-state pathways, involving competition between radiative and non-radiative decay, ISC, and RISC. A deeper photophysical understanding will not only shed light on the intrinsic behaviour of carbazole but also provide design principles for tailoring its derivatives to achieve specific emission properties in OLEDs and related optoelectronic devices.

1.7. Aim and Objectives of the Thesis

Harnessing the triplet manifold is central to advancing next-generation optoelectronic materials. This thesis focuses on accessing and controlling triplet states in carbazole-based chromophores through systematic structural modulation and design of connectivity.

❖ First, the role of halogen engineering in dictating crystal packing and promoting RTP is explored. In the N-N-bonded carbazole dimer, the heavy-atom-induced spin-orbit coupling of bromine effectively switches the emissive pathway from TADF in the unsubstituted dimer (Cz-D) to RTP in its brominated analogue (BrCz-D). This demonstrates halogen engineering as a powerful strategy for tailoring photophysical behaviour.

❖ Next, the challenge of achieving RTP in the absence of heavy atoms or strong halogen effects is addressed. A purely organic C–C-connected carbazole dimer was synthesised, wherein pronounced π–π interactions in the crystal lattice rigidify the molecular framework. This rigidity facilitates efficient RTP, yielding a lifetime of τ_{RTP} = 481 μs, and represents a significant step toward the design of metal-free RTP.

❖ Finally, the thesis investigates simultaneous emission from singlet and triplet states, a rare and emerging phenomenon known as dual emission. A C-N-linked carbazole trimer (Cz-T) and its N-N-connected hexameric analogue (Cz-H), comprising six carbazole units without spacers, were developed. Both structures exhibit delayed dual emission involving TADF and RTP. Moreover, the structure of Cz-H was resolved using three-dimensional electron diffraction, a technique essential for its micron-sized crystals (1.1 μm^3).

Overall, the work establishes how precise structural modifications in carbazole frameworks can effectively tune emissive pathways and enable the generation and utilisation of the triplet manifold. These investigations collectively define the aims and objectives of the thesis.

Chapter 2

Unlocking the Room Temperature Phosphorescence through Halogen Engineering in Carbazole Dimers

Abstract

RTP in purely organic, metal-free systems holds considerable promise for next-generation optoelectronic technologies. Nevertheless, the deliberate design of RTP-active molecules remains nontrivial due to the intricate interplay between molecular structure, ISC dynamics, and excited-state interactions. In this work, we systematically investigate how ISC efficiency, SOC, and halogen-mediated intermolecular interactions govern the emissive behaviour of a brominated carbazole dimer (BrCz-D). Unlike its unsubstituted counterpart, Cz-D, which displays TADF under ambient conditions, BrCz-D exhibits pronounced RTP in the crystalline state. The fsTA spectroscopy reveals an effective population of the triplet excited states in both dimers, confirming that triplet formation is operative in each system. However, bromine incorporation substantially amplifies SOC (V_{SOC} = 23.22 cm^{-1}), thereby promoting more efficient ISC and favouring phosphorescent decay pathways in BrCz-D. The robust RTP observed in crystalline BrCz-D originates from specific halogen-driven intermolecular contacts, Br···Br, C···Br, and H···Br, that rigidify the molecular environment, suppress nonradiative decay, and stabilise triplet excitons. These interactions are largely absent in solution, explaining the disappearance of RTP under ambient, non-crystalline conditions. Overall, this work highlights the pivotal roles of enhanced surface order and halogen-directed crystal packing in facilitating efficient RTP. These insights provide a rational design framework for developing high-performance organic phosphorescent materials through targeted crystallo-chemical engineering.

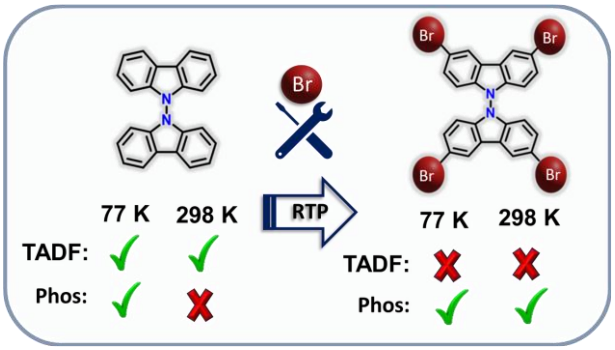

2.1. Introduction

Recycling/retrieving the triplet manifold is fundamental to achieving high internal quantum efficiencies (IQE), as dictated by spin-statistics.[112] The transition from a singlet to a triplet state, known as intersystem crossing (ISC), is typically spin-forbidden but can be facilitated through spin-orbit coupling (SOC),[113,114] including metal-free alternatives.[3] By leveraging thermally activated delayed fluorescence (TADF) and phosphorescence, singlet and triplet excitons can be harvested, thereby attaining a theoretical 100% IQE.[65] Dual-emission (DE; TADF and phosphorescence) has garnered significant interest as one of the most fascinating photophysical phenomena.[115] TADF and phosphorescence, as distinct mechanisms, play pivotal roles in applications such as organic light-emitting diodes (OLEDs),[35,45,116,117] memory storage devices,[11] and biological imaging.[118–120] The rational design of such processes hinges on reducing the singlet-triplet energy gap (ΔE_{ST}), a critical parameter influencing their efficiency. Adachi and co-workers pioneered the development of metal-free organic luminescent molecules with remarkably low ΔE_{ST}, promoting efficient spin-up conversion from non-radiative triplet states to radiative singlet states.[45] Furthermore, Monkman and co-workers elucidated the spin-vibronic coupling mechanism, highlighting the role of charge transfer states in facilitating TADF.[15]

Tailoring functional groups in organic chromophores has emerged as a viable strategy to develop DE materials. The intricate interplay between delayed emission and phosphorescence is a cornerstone in designing high-performance luminescent systems.[76,121,122] Feng et al. introduced a novel approach to selectively switching between fluorescence and phosphorescence using a push-pull effect.[123] Bryce and co-workers have highlighted the significance of dihedral angle control around the donor-acceptor connectivity in regulating the interplay between TADF and phosphorescence.[71] However, achieving precise control over TADF and phosphorescence remains a formidable challenge. Halogen engineering, leveraging the distinctive properties of halogens, provides a promising avenue to address such hurdles.[124] By strategically incorporating halogens, we can fine-tune photophysical properties,[125] thereby opening up avenues for advancements in photovoltaics, nanoelectronics, and sustainable materials science.

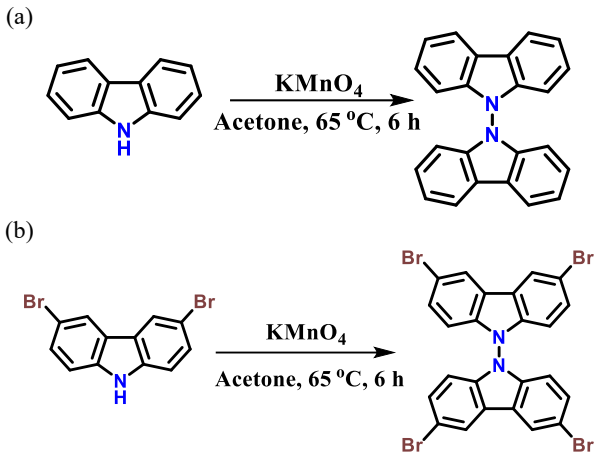

Scheme 2.1: Synthesis scheme of (a) **Cz-D** and (b) **BrCz-D**

Herein, we synthesised and explored the photophysics of N–N–linked carbazole homodimers, **Cz-D** and the brominated analogue **BrCz-D**. **Cz-D** exhibited TADF in the crystalline state, whereas **BrCz-D** activated room-temperature phosphorescence (RTP). Bromine incorporation into **Cz-D** amplifies SOC and induces unique non-covalent halogen interactions, culminating in the emergence of robust and efficient RTP in the crystalline **BrCz-D**. The findings highlight halogen-based molecular engineering as a powerful strategy for rationalising functional materials.[50]

2.2. Results and Discussion

2.2.1. Dimer Molecules and the Crustal Structures

The covalently connected symmetric carbazole dimer (**Cz-D**) and tetrabrominated carbazole dimer (**BrCz-D**) were synthesised following established literature procedures (Scheme 2.1, Figures A2.1 and A2.2).[126,127] High-quality single crystals suitable for diffraction analysis were obtained by slow evaporation of **Cz-D** in acetone and **BrCz-D** in a chloroform-hexane mixture at room temperature (Figure A2.3). Crystallographic analysis revealed that **Cz-D** crystallises in the monoclinic crystal system with a *Cc* space group, while BrCz-D adopts the orthorhombic *Pccn* space group (Table A2.1). The structural analysis revealed that the carbazole dimers exhibit

non-planar orientations, with a rotational angle of 72.11° for **Cz-D** (Figure 2.1c) and a nearly orthogonal angle of 86.64° for **BrCz-D** (Figure 2.1d). Additionally, halogenation enhances face-to-face π-π interactions, resulting in a packing transition from a herringbone motif in **Cz-D** to a γ motif in **BrCz-D** (Figures 2.2 and 2.3).

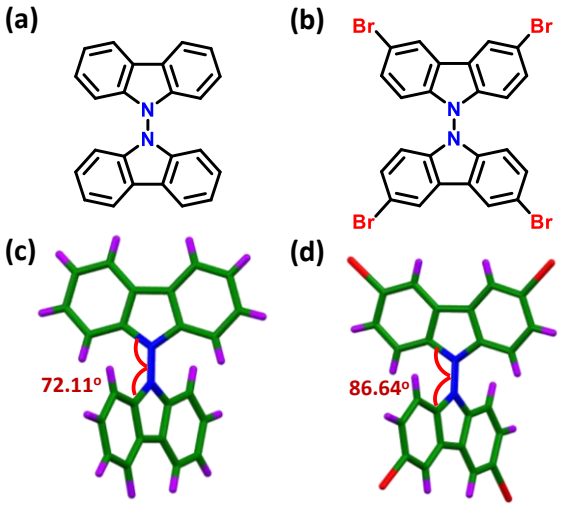

Figure 2.1: (a) Molecular structure of **Cz-D**, (b) Molecular structure of **BrCz-D**, (c) Crystal structure of **Cz-D**, and (d) Crystal structure of **BrCz-D**.

Truncated symmetry-adapted perturbation theory (SAPT) provides a computational framework for quantifying interaction energies between two monomers by decomposing the total energy into distinct components, including electrostatic, exchange, induction, and dispersion interactions.[128] For SAPT(0) calculations, various dimeric arrangements in the three-dimensional crystal packing were analysed. In the case of **BrCz-D**, three distinct dimers were identified, while **Cz-D** exhibited one dimeric arrangement (Figures A2.4 and A2.5). Notably, all identified dimers for **Cz-D** and **BrCz-D** underscored the dominant role of dispersion energy in stabilisation, resulting in a negative total SAPT(0) energy (Tables A2.2 and A2.3). Hirshfeld surface analysis provided a statistical overview of intermolecular interactions within the crystal assembly.[129,130] The two-dimensional fingerprint plots for **Cz-D** revealed that C···H interactions contributed predominantly (49.8%), followed by H···H (49.1%) and C···C (1.1%)

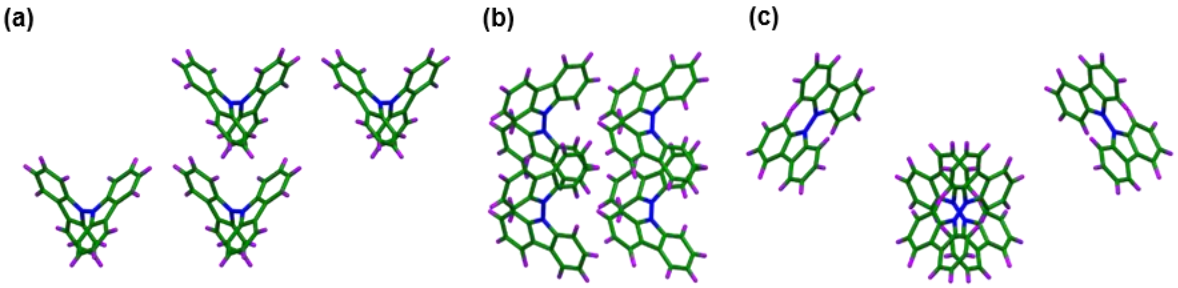

Figure 2.2: Crystal packing of Cz-D along (a) X-axis, (b) Y-axis and (c) Z-axis

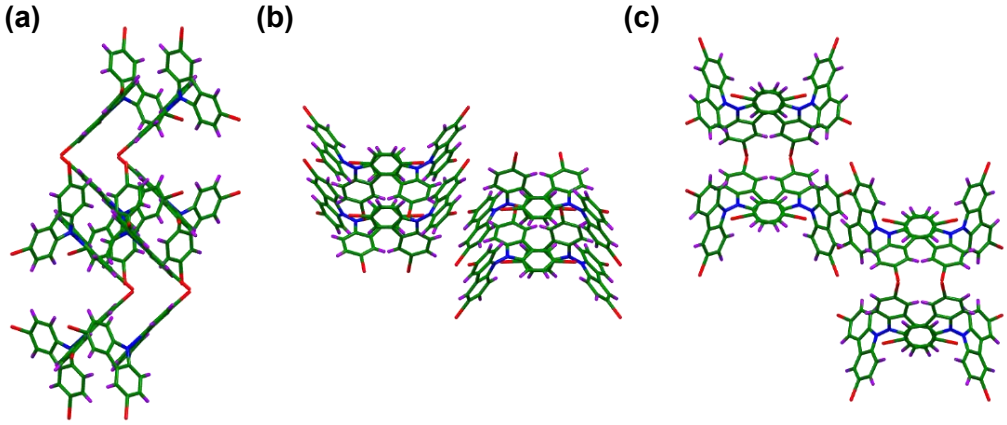

Figure 2.3: Crystal packing of **BrCz-D** along (a) X-axis, (b) Y-axis and (c) Z-axis

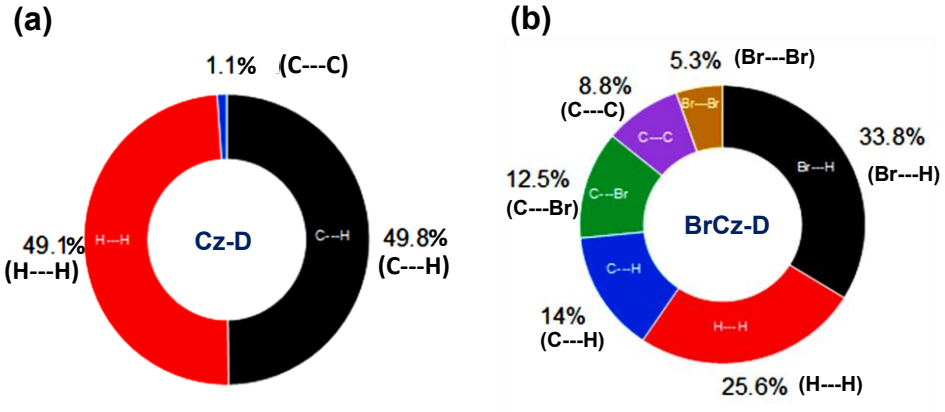

Figure 2.4: Percentage of intermolecular interactions in (a) Cz-D and (b) BrCz-D.

interactions. Conversely, **BrCz-D** displayed a significantly altered interaction profile due to the presence of bromine, with Br···H interactions being the most prominent (27.00%), followed by H···H (20.4%), C···H (11.2%), Br···C (10.00%), C···C (7.00%), and Br···Br (4.20%) interactions (Figure 2.4 and Table A2.4). The incorporation of bromine thus markedly influenced the crystal packing arrangement in **BrCz-D** (Figures A2.6 and A2.7).

2.2.2. Steady-State Photophysical Properties of the Dimers in Solution-state

The UV-vis absorption and fluorescence emission spectra of **Cz-D** and **BrCz-D** are depicted in Figures 2.5 and A2.8 and summarised in Table A2.5. The electronic absorption spectra of **Cz-D** and **BrCz-D** in toluene (TOL) exhibit peaks within the range of 290 to 350 nm.

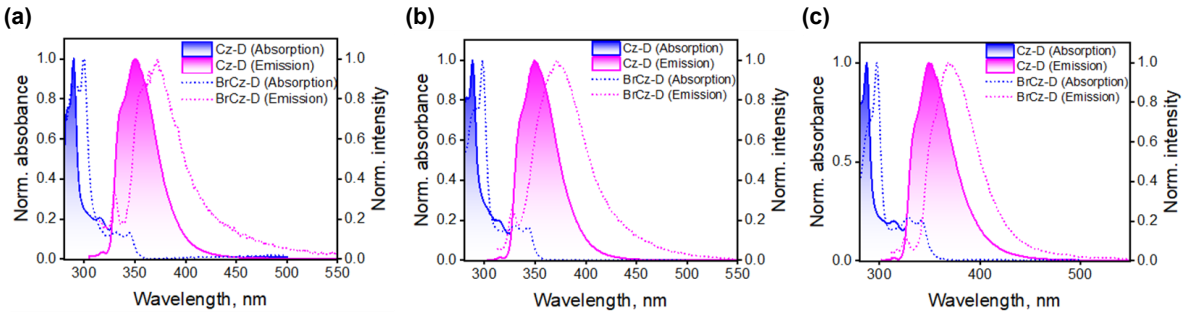

Figure 2.5: Steady state UV-vis absorption and fluorescence emission spectra of **Cz-D** and **BrCz-D** in (a) Toluene, (b) Tetrahydrofuran and (c) Acetonitrile.

The absorption peak at 290 nm for **Cz-D** and 300 nm for **BrCz-D** can be attributed to π→π* transitions, while the shoulder peaks spanning from 330 to 350 nm for both dimers correspond to n→π* transitions.[131–133] The 10 nm bathochromic shift observed in the UV-vis absorption spectrum of **BrCz-D** relative to **Cz-D** in TOL is likely attributed to the enhanced conjugation facilitated by the electronegative bromine atom.[2] The UV-vis absorption spectra of both **Cz-D** and **BrCz-D** exhibit negligible dependence on solvent polarity. The fluorescence emission spectra for **Cz-D** in TOL and acetonitrile (ACN) show variations in intensity, with emission maxima centred around λ_{Max}^{Fl}= 370 nm. Conversely, **BrCz-D** demonstrates a 20 nm bathochromic shift in its fluorescence emission maximum, shifting from 372 nm in TOL to 392 nm in ACN, indicating a substantial stabilisation of the excited state with polarity.[134,135] The

significant reduction in fluorescence quantum yields (for Cz-D, φ_f = 28.13%, in TOL, φ_f = 12.88% in ACN, and for BrCz-D, φ_f = 1.30% in TOL, and 0.18% in ACN) observed in high dielectric environments for both dimers provides strong evidence for activating non-radiative deactivation pathways (Table S4).[136–139] **Cz-D** exhibits a notably large Stokes' shift of 5985 cm^{-1} in TOL, while **BrCz-D** demonstrates an enhanced Stokes shift, attaining 7920 cm^{-1} in the same dielectric environment (Figures S8a and S8b). The substantial Stokes' shift observed in TOL, which further increases in ACN, indicates a significant enhancement in charge transfer/excitonic coupling within the dimers.[140]

2.2.3. Steady-state Photophysical Properties of Dimers on Solid-state

The photophysical properties of **Cz-D** and **BrCz-D** in the crystalline state were further investigated. The Kubelka-Munk transformed absorption spectra of the dimers spanned the

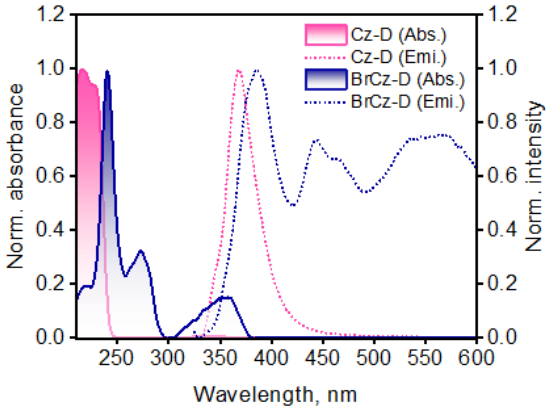

Figure 2.6: Solid-state UV-vis absorption spectra of **Cz-D** and **BrCz-D**

range of 200–380 nm, with absorption maxima observed at λ_{Max}^{Abs} = 340 nm for **Cz-D** and λ_{Max}^{Abs} = 360 nm for **BrCz-D** (Figures 2.6 and A2.10). Compared to their solution states, the π→π* transition in the crystalline state exhibited a blue shift, while the n→π* transition showed a red shift. The restricted π-electron delocalisation in the crystalline environment leads to a blue shift in the π→π* transition. Conversely, the red shift in the n →π* transition can be attributed to the stabilisation of the excited state, which reduces the energy gap between the ground and excited states.[4,5] In the crystalline state, fluorescence emission spectra of **Cz-D** on excitation at 310 nm

revealed a narrow emission profile spanning 330-460 nm with an emission maximum at λ_{Max}^{Fl} = 368 nm, compared to its monomeric state. In contrast, **BrCz-D** exhibited a broad emission spectrum, extending from 340 to 750 nm. The broadening in fluorescence emission spectra of **BrCz-D** can be attributed to bromine atoms, which may engage in halogen interactions within the crystal lattice. Such non-covalent interactions create a more diverse electronic environment, contributing to spectral broadening**.**

2.2.4. Delayed Emission Measurements of Dimers

A comprehensive understanding of the triplet excited state's properties necessitated the employment of gated emission measurements. Accordingly, we performed the spectroscopic analysis on **Cz-D** and **BrCz-D** under ambient conditions in N_2-purged TOL (Figure 2.7). **Cz-D** exhibited a delayed emission maximum at λ_{Max}^{Dl} = 370 nm, while **BrCz-D** displayed no detectable signal under ambient conditions. At 77 K, gated emission spectra revealed a prominent red-shifted peak centred at λ_{Max}^{Dl}= 450 nm for both dimers, along with a shoulder peak at 370 nm that was exclusive to **Cz-D** (Figure A2.13). The presence of the red-shifted peak in both **Cz-D** and **BrCz-D** confirms the manifestation of phosphorescence in the solution state at 77 K. Furthermore, the 370 nm emission for **Cz-D** is attributed to TADF.[9,66] Gated emission measurements were conducted in the presence of oxygen at 298 K, revealing a pronounced reduction in emission intensity compared to the N_2-purged solution. The observation conclusively confirmed the TADF behaviour of the **Cz-D** dimer, with its emission centred at 370 nm.[71,141] An increase in solvent polarity induced a bathochromic shift in the delayed emission peak of **Cz-D**, progressing from 370 nm in TOL to 377 nm in THF and further to 383 nm in ACN. Similarly, **BrCz-D** also exhibited a pronounced red shift in its phosphorescence peak with the dielectric, suggesting a charge-transfer (CT) character of the T_1 state (Figure A2.14).[142] Analysis of the decay profiles for the dimers across varying solvent polarities revealed an increase in photoluminescence lifetimes with increasing polarity (τ_{TOL}^{Dl}, τ_{THF}^{Dl} = within pulse width, τ_{ACN}^{Dl} = 153 ms), further supporting the involvement of a CT state in the observed delayed emission behaviour (Figure S13).

To investigate the nature of the triplet excited state in crystalline assemblies, gated emission measurements were performed on crystalline dimers **Cz-D** and **BrCz-D** at room temperature

under excitation at 310 nm. Crystalline **Cz-D** exhibited a gated emission peak centred at 375 nm with a delay time of 50 µs, corresponding to TADF. In contrast, crystalline **BrCz-D** displayed a gated emission peak at 520 nm, attributed to RTP with a lifetime of 275.9 µs, characterised by its extended phosphorescence lifetime and significant Stokes shift.[125,143,144] The crystallisation process rigidifies the chromophores through various non-covalent interactions, including halogen bonding, hydrogen bonding, H···H interactions, and π-π stacking.[50] Both **Cz-D** and **BrCz-D** possess C···H and H···H interactions in their crystalline states; however, RTP is observed exclusively in **BrCz-D**.[50] Crystallographic analysis highlights the critical role of bromine in crystal packing, indicating that halogen interactions (Br···Br = 4.2%), (H···Br = 27%), and (C···Br = 10.1%) particularly those involving bromine, are essential for enabling RTP, which is operational only in the crystalline state of **BrCz-D**.[145,146]

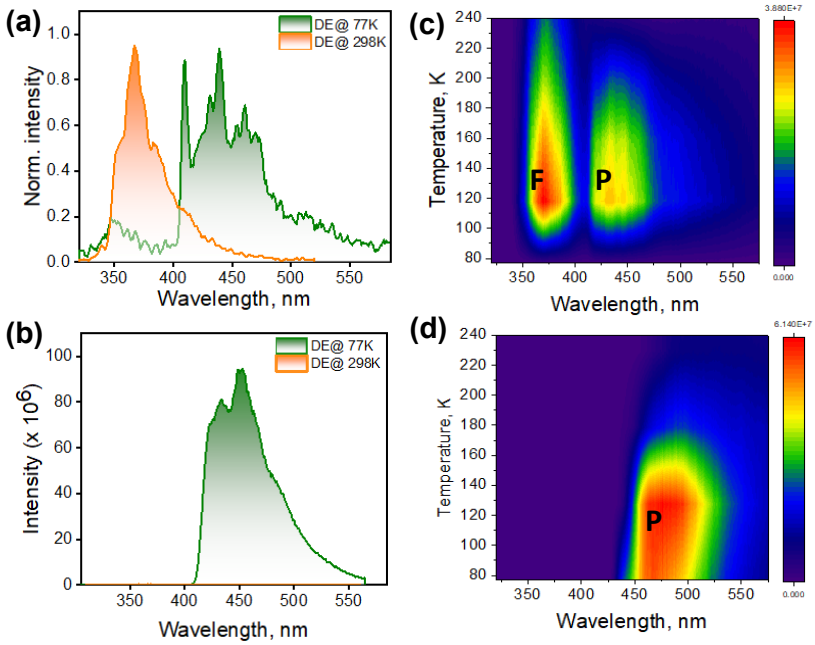

Figure 2.7: Delayed emission spectra of (a) **Cz-D** and (b) **BrCz-D** (Normalised delayed emission as inset), at RT and 77K in toluene, temperature-dependent delayed emission of (c) **Cz-D**, (d) **BrCz-D** in solid-state (3D-contour plot). F indicates delayed fluorescence (TADF).

Temperature-dependent delayed emission measurements in the crystalline state were employed for **Cz-D** and **BrCz-D** to elucidate the underlying photophysical mechanisms governing the delayed emission behaviour (Figures A2.15 and A2.16). The experiments were conducted over a temperature range of 77 K (cryogenic conditions) to 240 K for both **Cz-D** and **BrCz-D**. At 77

K, **Cz-D** exhibited distinct emission peaks at 370 nm and 444 nm with varying intensities. Upon increasing the temperature, the intensity of the 370 nm band decreased gradually; in contrast, the 444 nm band diminished more rapidly. Decay profile fitting at the delayed emission peak centred at 370 nm revealed negligible changes in lifetime, with minimal variation observed across the temperature range. Artem'ev and co-workers have highlighted the significance of short-lifetime TADF materials in OLED applications to mitigate saturation effects.[147] The transition from the triplet to the singlet state involves an activation energy barrier, with thermal energy playing a critical role in facilitating the particular transition. This process ultimately leads to delayed emission originating from the singlet state (^{1}CT or ^{1}S).[148] In contrast, lifetime analysis for the 444 nm peak revealed significant changes, with lifetimes decreasing from 7 ms at 77 K to 250 µs at 240 K, indicating that the emission originates from the triplet state (Table 2.1).

Table 2.1: Decaying wavelength from decay profile plots and its corresponding lifetime for **Cz-D.**

Temperature	Lifetime at 370 nm	Lifetime at 444 nm
77 K	τ_1 = 181.8 µs	τ_1 = 613.8 µs
		τ_2 = 7.1 ms
120 K	τ_1 = 126.0 µs	τ_1 = 455.0 µs
		τ_2 = 6.4 ms
160 K	τ_1 = 125.0 µs	τ_1 = 530.5 µs
		τ_2 = 5.3 ms
200 K	τ_1 = 118.2 µs	τ_1 = 319.8 µs
		τ_2 = 2.1 ms
240 K	τ_2 = 81.9 µs	τ_1 = 47.4 µs
		τ_2 = 251.85 µs

Table 2.2: Decaying wavelength from decay profile plots and its corresponding lifetime for **BrCz-D.**

Decaying wavelength (nm)	Lifetime
470@ 77K	τ_1 = 1.97 ms
	τ_2 = 63.78 ms
490@ 160K	τ_1 = 1.95 ms
	τ_2 = 28.90 ms
526@ 200K	τ_1 = 1.17 ms
	τ_2 = 23.56 ms
528@ 240K	τ_1 = 1.12 ms
	τ_2 = 21.07 ms

For crystalline **BrCz-D**, gated emission measurements across various temperatures, using 310 nm excitation and a delay time of 50 μs, revealed a single broad emission band spanning 430–650 nm. The particular band exhibited progressive red-shifting and broadening with increasing temperature, accompanied by significant intensity changes, strongly indicative of phosphorescence. The decay profile comprises two components with long lifetimes (τ_1= 63.8 ms at 77 K to 275.8 μs at 298 K and τ_2= 2.0 ms at 77 K to 1.1 ms at 298 K, Table 2.2) and pronounced temperature dependence, possibly corresponding to a locally excited triplet state (^{3}LE) and a charge-transfer triplet state (^{3}CT).[72,149] The observed red shift and broadening of the delayed emission at elevated temperatures result from enhanced vibronic coupling and an increased population of higher vibrational energy levels.[134,148,150]

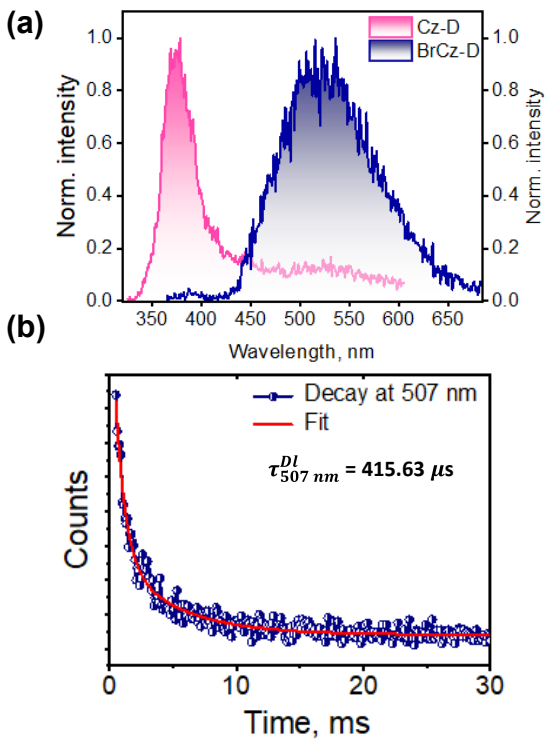

Figure 2.8: (a) The solid-state gated emission measurements of **Cz-D** and **BrCz-D** at room temperature, (b) The decay profile of **BrCz-D** at room temperature (gating 40 ms) in the crystalline state.

2.2.5. Femtosecond Transient Absorption Measurements of Cz-D & BrCz-D

To elucidate the excited-state dynamics of **Cz-D** and **BrCz-D**, femtosecond transient absorption (fsTA) spectroscopy was performed in various dielectric environments: toluene (TOL, $\varepsilon = 2.40$), tetrahydrofuran (THF, $\varepsilon = 7.60$), and acetonitrile (ACN, $\varepsilon = 37.50$). Evolution-associated spectra (EAS) for **Cz-D** and **BrCz-D** in these solvents were derived through global fitting of the three-dimensional fsTA spectral data (time vs. wavelength) using an A→B→GS kinetic model. The fsTA spectra of **Cz-D** and **BrCz-D** in TOL are illustrated in Figure 2.9.

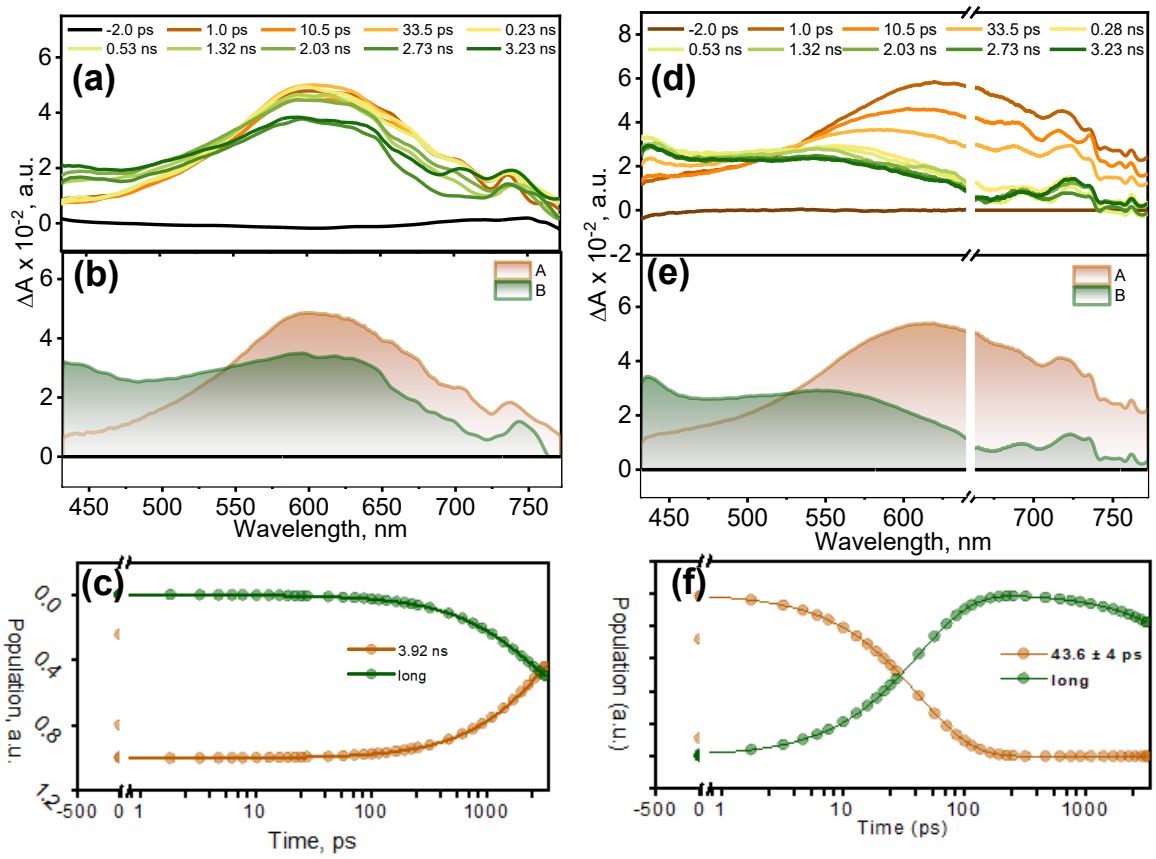

Figure 2.9: (a) Femtosecond transient absorption spectra of **Cz-D** in TOL, (b) Evolution associated spectra (EAS) of **Cz-D** obtained using the sequential A→B→GS model of **Cz-D** in TOL, (c) Kinetic evolution of EAS for **Cz-D** in TOL; (d) Femtosecond transient absorption spectra of **BrCz-D** in TOL, (e) Evolution associated spectra (EAS) of **BrCz-D** in TOL obtained using the sequential A→B→GS model, (f) Kinetic evolution of EAS for **BrCz-D** in TOL.

Upon photoexcitation of **Cz-D** in TOL at 330 nm, using a ~100 fs laser pulse, a prominent excited-state absorption (ESA) feature emerged at 610 nm, indicative of the singlet excited-state signature of carbazole (Cz, Figure 2.9).[108,151,152] Within a few nanoseconds (~3 ns), a new absorption band emerged in the 440-500 nm range. Spectral deconvolution of the total spectra identified two sequential components: the singlet excited state (component A) with a lifetime of 3.92 ± 0.002 ns, and a long-lived species (component B) persisting beyond 4 ns. Spectral deconvolution determined the decay constants of component A in **Cz-D** as 3.70 ± 0.008 ns in THF and 3.40 ± 0.006 ns in ACN. Upon photoexcitation of **BrCz-D**, spectral features resembling those of **Cz-D** were observed; however, the decay time of the singlet state differed significantly

with respect to **Cz-D**. The excited state of **BrCz-D** in TOL decayed within 43.6 ± 4 ps (component A), resulting in the formation of a new, long-lived transient species characterised by excited-state absorption (ESA) spanning 420–500 nm (component B). The long-lived species could be triplet excited states, formed on ultrafast timescales in **BrCz-D** compared to **Cz-D**, likely influenced by the heavy-atom effect due to bromine atoms in **BrCz-D**. Previous reports on brominated carbazoles also corroborate the assignment of the excited-state absorption (ESA) signature at approximately 450 nm to triplet excited states, as observed in both **Cz-D** and **BrCz-D**.[108] **BrCz-D** exhibited solvent-dependent variations in the decay kinetics of its initial excited state. Spectral deconvolution revealed decay constants for component A as 33.8 ± 4 ps in THF and 24.6 ± 3 ps in ACN for **BrCz-D**. The decrease in ESA decay time constants with increasing solvent polarity, accompanied by the emergence of triplet-excited states, can be attributed to the dielectric influence of the solvent on the dynamics of the excited state. Solvent polarity is known to modulate the relaxation pathways of the singlet state, thereby facilitating ISC to the triplet-excited states observed was consistent with the previously reported results.[153,154]

2.2.6. TDDFT Calculations of Cz-D and BrCz-D

The vertical excitation energies (VEEs) calculated at the CAM-B3LYP-D3/6-311G+(d,p) level of theory in vacuum reveal the presence of multiple bright singlet states with significant oscillator strengths (*f*) and low-lying triplet states in **Cz-D** and **BrCz-D** (Tables A2.6-A2.9). The existence of several singlet states with considerable oscillator strengths likely accounts for the multiple absorption peaks (n→π* and π→π*) of varying intensities observed in the UV-vis absorption spectra of **Cz-D** and **BrCz-D** (*vide supra*).[7] Additionally, natural transition orbitals (NTOs) for the $S_0 \rightarrow S_n$ transitions (n = 1–5) of **Cz-D** and **BrCz-D** are depicted in Figures S24 and S25, indicating localised electron density within a single carbazole unit of the dimers during the $S_0 \rightarrow S_1$ to S_4 transitions, consistent with their locally excited (LE) nature.[155] Conversely, the $S_0 \rightarrow S_5$ transitions exhibit a dominant CT character, supported by the spatially disjoint electron density distribution between the highest occupied natural transition orbitals (HO-NTOs) and the lowest unoccupied natural transition orbitals (LU-NTOs) on distinct monomer units within the dimers (Figure 2.10).

2.2.7. Fragment-Based Excited-State Analysis

Further analysis of the excited-state characteristics was conducted using fragment-based approaches implemented in TheoDORE, following Plasser's methodology.[156,157] The dimers **Cz-D** and **BrCz-D** were partitioned into two fragments, each corresponding to a carbazole/dibromo carbazole unit, respectively (Tables A2.10 and A2.11). The S_1 state of **Cz-D** (PR = 1.40, CT = 0.09) and **BrCz-D** (PR = 1.07, CT = 0.06), confirms the partial charge-transfer character of these transitions. In contrast, the S_5 states of **Cz-D** (PR = 1.48, CT = 0.894) and **BrCz-D** (PR = 1.22, CT = 0.869) exhibit pronounced CT character. The corresponding hole-electron isosurfaces demonstrate that the hole is localised on one fragment while the electron resides on the other, further substantiating the inter-fragment charge-transfer nature of the particular excitations. Solvent effects critically influence the S_5 state energetics, stabilising its charge-transfer nature in polar environments. This stabilisation facilitates ISC, impacting the photophysical properties of **Cz-D** and **BrCz-D**.[158]

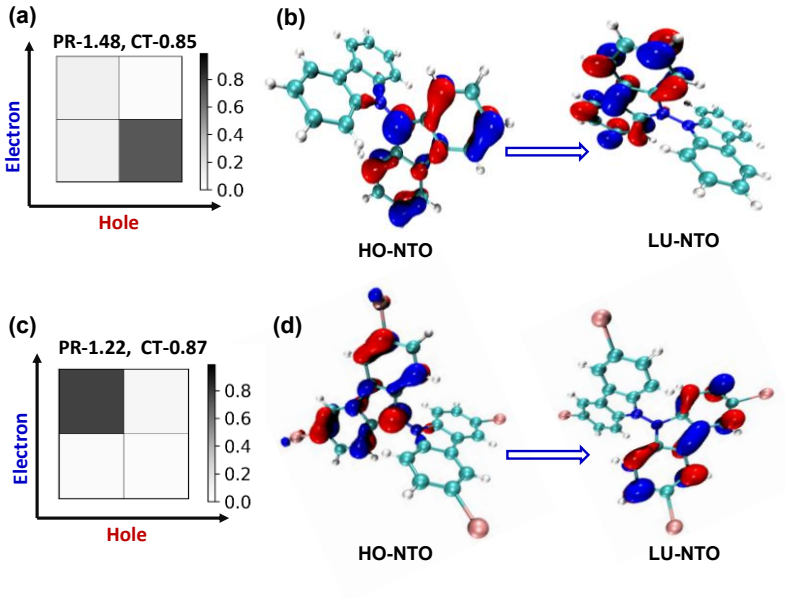

Figure 2.10: Hole-electron correlation plots showing the localised or delocalized Frenkel exciton or charge transfer nature for the S5 excited-states of (a) **Cz-D**, (c) **BrCz-D** and TD-DFT calculated natural transition orbitals (NTOs) of the S5 state of (b) **Cz-D**, (d) **BrCz-D**.

2.2.8. Spin-Orbit Coupling calculation

To investigate the influence of bromine substitution on the enhancement of spin-orbit coupling (SOC), we employed time-dependent density functional theory (TD-DFT) to compute the vertical excitation energies for singlet states, while triplet states were calculated using the Tamm-Dancoff approximation (TDA). Furthermore, the associated SOC constants between singlet and triplet states were evaluated using the PySOC package at the CAM-B3LYP-D3/6-311G+(d,p) level of theory, providing a quantitative understanding of the bromine substitution effect on SOC (Table A2.12 and A2.13). The geometries of the relaxed S_1 state for **Cz-D** and **BrCz-D** were optimised through density functional theory (DFT) calculations at the same level of theory. To assess the ISC efficiency between energetically accessible singlet and triplet states, we computed the SOC values across different singlet-triplet pairs. Theoretical calculations reveal that the isoenergetic states in **Cz-D** are S_1 and T_7, separated by 0.03 eV, whereas in **BrCz-D**, the corresponding isoenergetic states are S_1 and T_5, with an energy gap of 0.14 eV. Notably, the SOC constant undergoes a 65-fold increase from 0.23 cm^{-1} in **Cz-D** to 14.96 cm^{-1} in **BrCz-D**. The substantial enhancement in SOC, coupled with the reduced singlet-triplet energy gap, synergistically facilitates efficient ISC in both dimers, highlighting the critical role of these factors in modulating the photophysical properties. The experimentally estimated ISC of the molecule is supported by the large magnitude of the V_{SOC} between S_1 and T_5 in **BrCz-D** and between S1 and T7 in Cz-D, following El Sayed's rule.[36] The calculated SOC value between the triplet state (T_1) and the singlet ground state (S_0) is 14.76 cm^{-1}. This significant SOC facilitates ISC from the triplet state (T_1) to the singlet ground state (S_0), ultimately leading to phosphorescence emission as the excited molecule relaxes to its ground state.[13] The VEE analysis reveals a minimal energy gap of 0.03 eV between the T_7 and S_1 states of **Cz-D**, facilitating intersystem crossing (ISC). Following ISC, the T_7 state undergoes non-radiative internal conversion (IC), populating the T_1 state, which subsequently engages in the rISC process to the S_1 state. The energy gap between the S_1 and T_1 states ($\Delta E_{S1\text{-}T1}$) in **Cz-D** is 0.83 eV, representing a comparatively large separation. Despite the substantial ΔE_{ST}, previous studies by Monkman and co-workers have demonstrated that rISC can proceed efficiently between S_1 and T_1, regardless of the magnitude of the energy gap.[159] Additionally, Adachi and coworkers have developed carbazole-based blue TADF emitters exhibiting ΔE_{ST} values in the range of 0.5 to 1

eV.[160] Consistent with the reports, the present findings indicate that **Cz-D** possesses a high-energy singlet-triplet manifold that actively participates in the rISC process, ultimately contributing to TADF emission.[76,161]

2.2.9. Proposed Jablonski Diagram

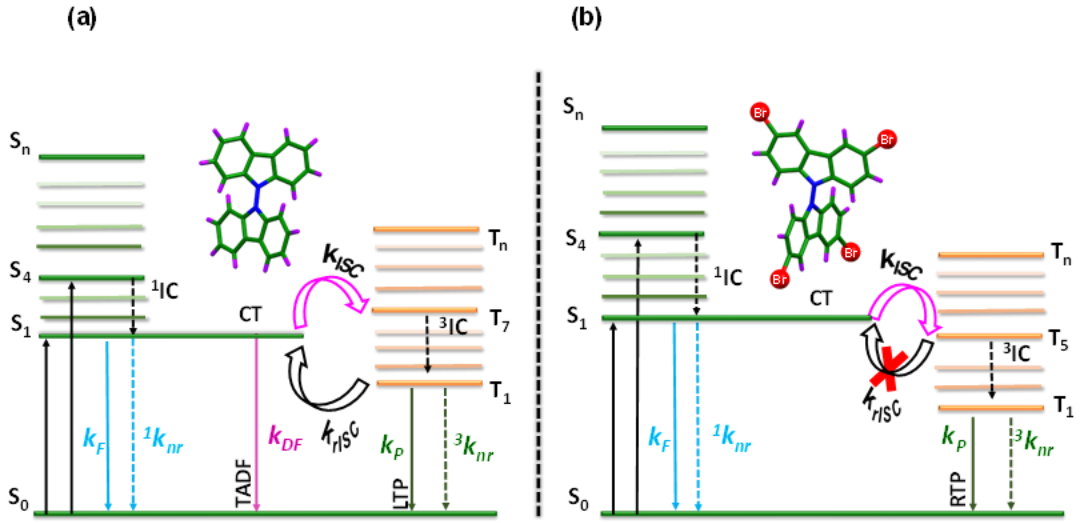

Figure 2.11: The proposed Jablonski diagram for (a) **Cz-D** showing TADF and low-temperature phosphorescence (LTP), and (b) **BrCz-D** showing RTP.

Figure 2.11 presents a schematic energy-level diagram summarising the excited-state dynamics of **Cz-D** and **BrCz-D**. Upon photoexcitation, **Cz-D** initially populates the S_1 state, from which intersystem crossing (ISC) occurs to an isoenergetic triplet state, T_7 (ΔE_{ST} = 0.03 eV). Subsequent internal conversion (IC) brings the population to T_1, followed by reverse intersystem crossing (rISC) from T_1 back to S_1 (ΔE_{ST} = 0.83 eV), ultimately giving rise to TADF in **Cz-D**. In contrast, **BrCz-D** populates higher singlet excited states after photoexcitation, followed by ISC from S_1 to T_5 (ΔE_{ST} = 0.14 eV). After IC to T_1, the rISC pathway is effectively suppressed due to the significantly enhanced spin–orbit coupling (SOC) between S_0 and T_1 (V_{SOC} = 14.9 cm^{-1}). In combination with halogen-induced modulation of the crystal packing, this suppression of rISC facilitates efficient RTP in crystalline **BrCz-D** (Figure 2.11).

2.3. Conclusion

The present work underscores the tunability of TADF and phosphorescence properties in carbazole-based dimers (**Cz-D** and **BrCz-D**) via strategic halogen substitution. At ambient temperature, crystalline **Cz-D** exhibits TADF, whereas dual emission is observed at cryogenic temperature, comprising TADF (370 nm) and phosphorescence (444 nm) components. Lifetime decay analysis reveals microsecond-scale (125 μs) and millisecond-scale (7 ms) lifetimes for TADF and phosphorescence, respectively. In contrast, **BrCz-D** displays a single, red-shifted emission band at 470 nm, characterised by prolonged lifetimes of 63 ms (77 K) and 415.63 μs (298 K), indicative of radiative transitions (phosphorescence) from the triplet state in the crystalline environment. Steady-state delayed emission measurements, NTO analysis, and TheoDORE calculations collectively confirm the intermediary of a CT state during the ISC in both dimers. Notably, bromine substitution enhances the SOC constant (V_{SOC} = 14.94 cm^{-1}) in **BrCz-D**, thereby augmenting ISC efficiency relative to the unsubstituted analogue **Cz-D**. The halogen-specific interactions in **BrCz-D**, such as Br···Br, Br···C, and Br···H, facilitate RTP in the crystalline state. Our investigations elucidate a paradigm shift from TADF in **Cz-D** (crystalline) to pure phosphorescence in **BrCz-D** (crystalline) at ambient conditions, providing a rational framework for designing advanced optoelectronic materials with tailored photophysical properties.

2.4. Experimental Section

2.4.1. Syntheses and Characterisation

Synthesis of Cz-D: To a solution of carbazole (500 mg, 2.99 mmol) in acetone (20 mL) was added KMnO4 (1.2 g, 7.48 mmol) at room temperature. The reaction mixture was warmed up to 65 °C with a reflux condenser. The reaction was stirred for 6 hours at 65 °C and then cooled to room temperature. After evaporation of acetone under reduced pressure, the reaction mixture was suspended in chloroform, filtered through a glass funnel, and washed with chloroform. The filtrate was washed with saturated aqueous $Na_2S_2O_3$ solution, brine, dried over Na_2SO_4, filtered, and concentrated under reduced pressure. The crude product was purified by chromatography

(Petroleum ether/chloroform) to afford a white powder (50 mg, 20% yield).

^{1}H NMR *(400 MHz, $CDCl_3$): δ 8.23-8.19 (m, 4H), 7.38-7.31(m, 8H), 6.93-6.89(m, 4H) ppm.*

Synthesis of BrCz-D: To a solution of 3, 6-dibromo-carbazole (500 mg, 1.54 mmol) in acetone (20 mL) was added KMnO4 (608 mg, 3.85 mmol) at room temperature. The reaction mixture was warmed up to 65 °C with a reflux condenser. The reaction was stirred for 6 hours at 65 °C and then cooled to room temperature. After evaporation of acetone under reduced pressure, the reaction mixture was suspended in chloroform, filtered through a glass sintered funnel, and washed with chloroform. The filtrate was washed with saturated aqueous $Na_2S_2O_3$ solution, brine, dried over Na_2SO_4, filtered, and concentrated under reduced pressure. The residue was purified by recrystallisation from chloroform/hexane to give a white needle-like crystal (400 mg, 80% yield).

^{1}H NMR *(500 MHz, 298 K, $CDCl_3$): δ 8.27(d, 4H, J=1.7 Hz), 7.47(dd, 4H, J=8.6, 1.8 Hz), 6.75(d, 4H, J=8.6 Hz) ppm.*

2.5. Additional Figures and Tables

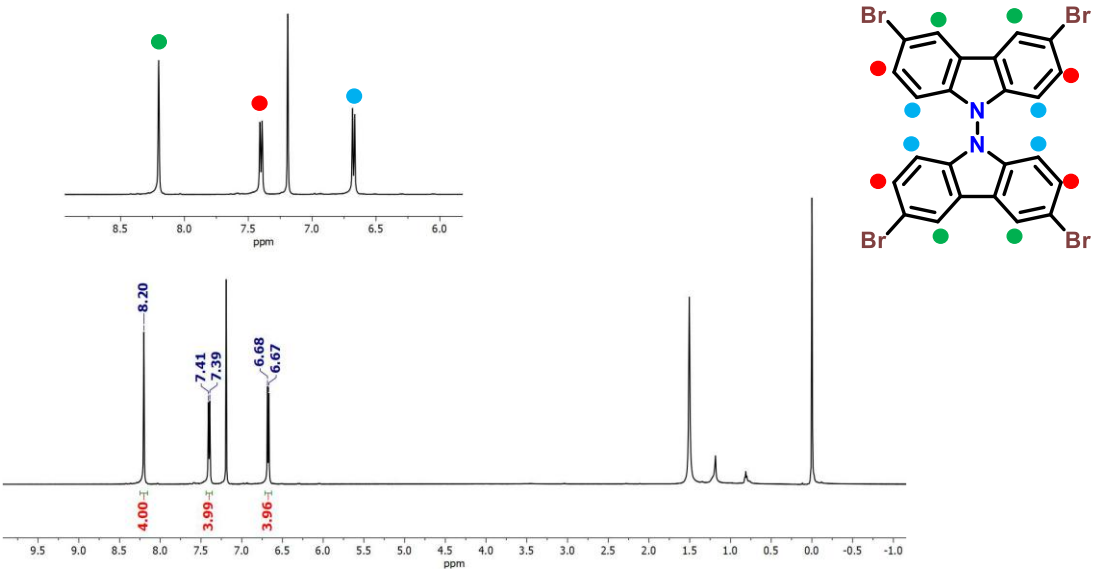

Figure A2.1: ^{1}H-NMR spectrum of **BrCz-D** in $CDCl_3$

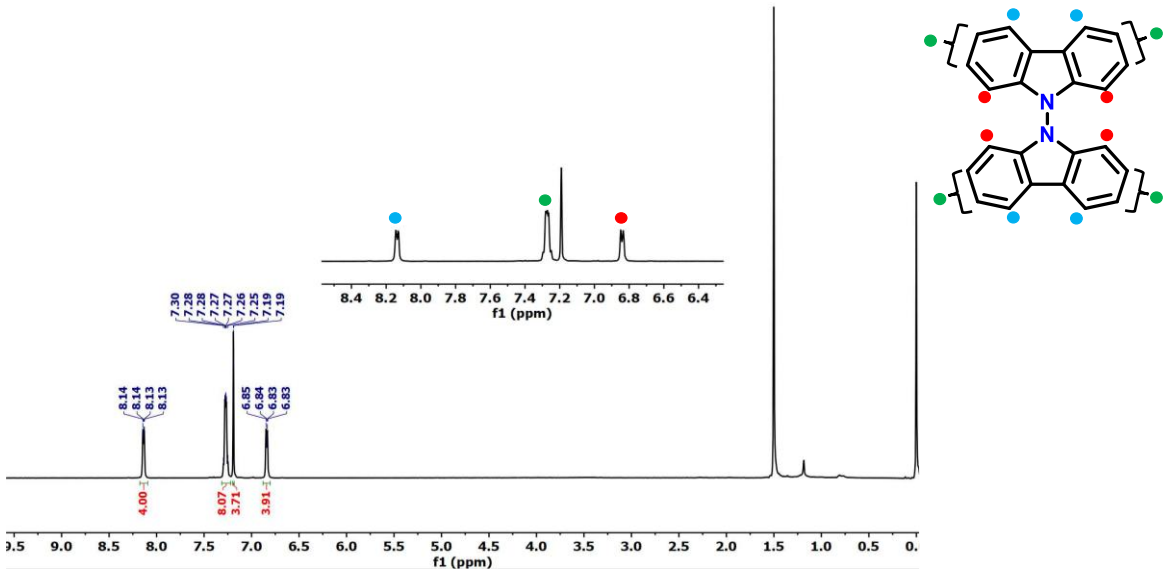

Figure A2.2: ^{1}H-NMR spectrum of Cz-D in $CDCl_3$.

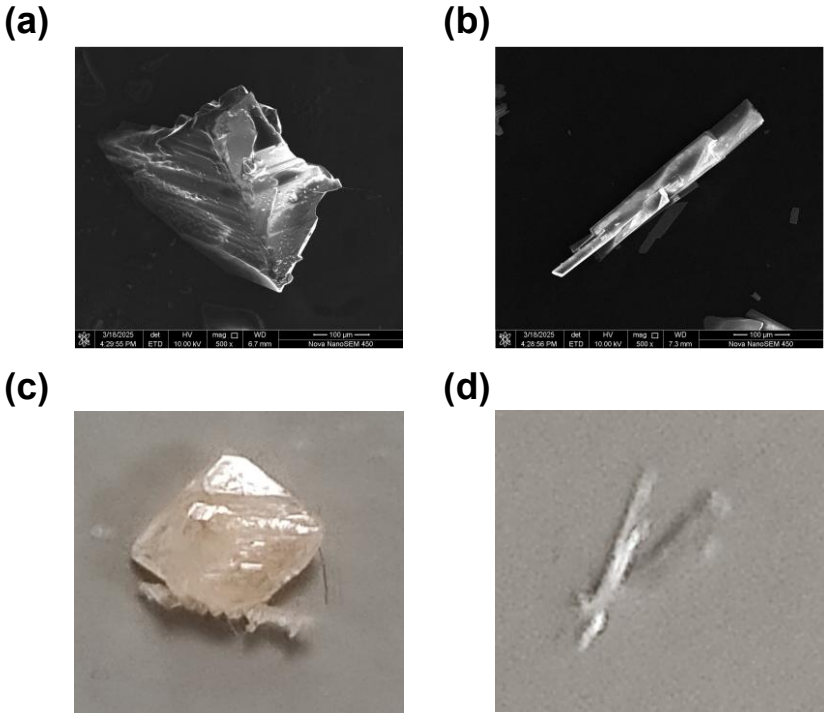

Figure A2.3: SEM images of crystalline (a) **Cz-D** and (b) **BrCz-D** and photographic images of crystalline (c) **Cz-D** and (d) **BrCz-D**.

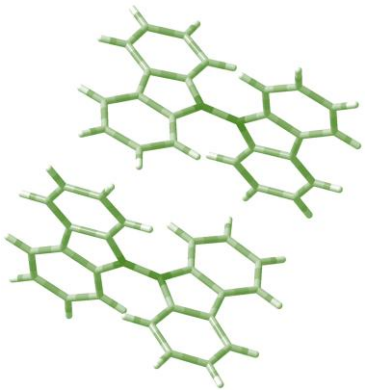

Figure A2.4: The dimeric arrangement in the **Cz-D** for SAPT(0) analysis.

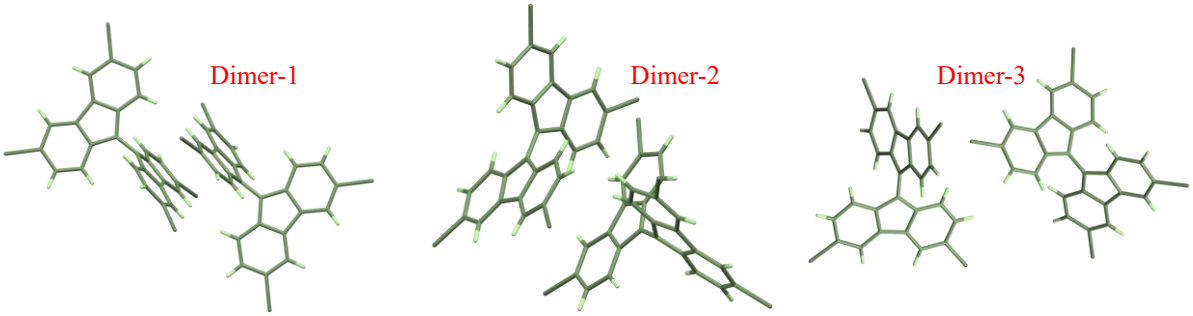

Figure A2.5: The possible dimeric arrangements in the crystal packing of **BrCz-D** for the SAPT(0) analysis.

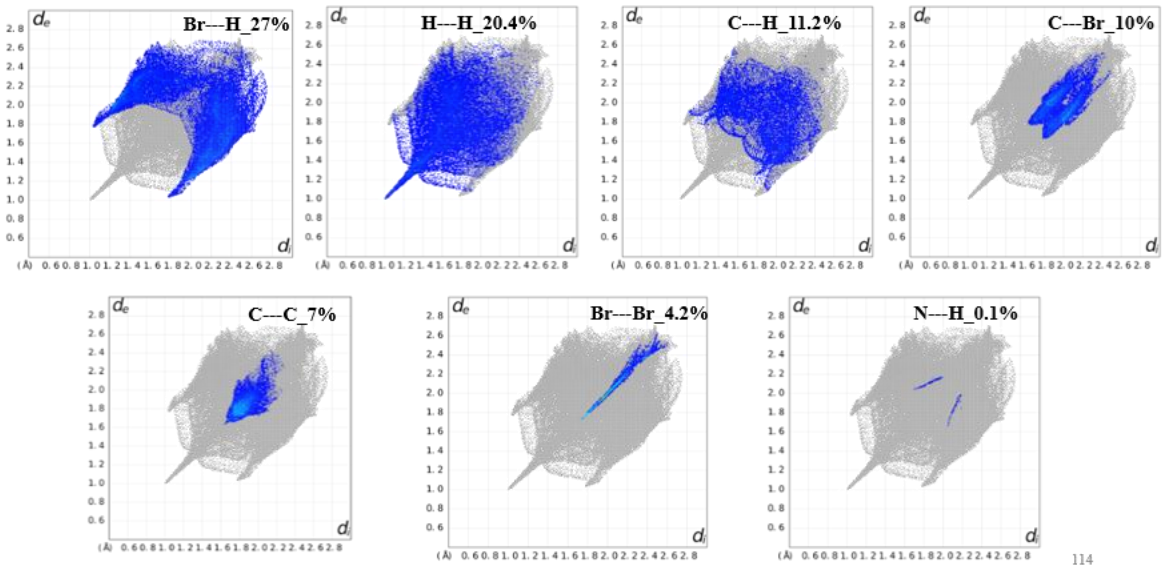

Figure A2.6: Hirshfeld 2D fingerprint plots of **BrCz-D** with different intermolecular interactions.

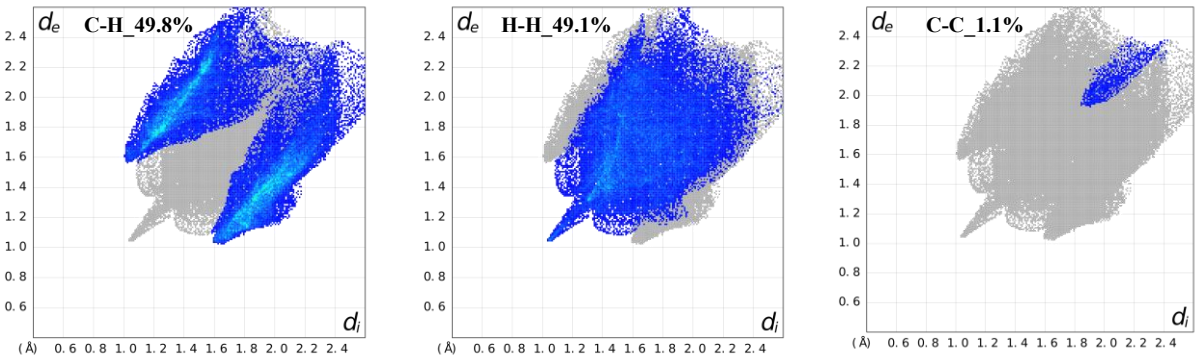

Figure A2.7: Hirshfeld 2D fingerprint plots of **Cz-D** with different intermolecular interactions.

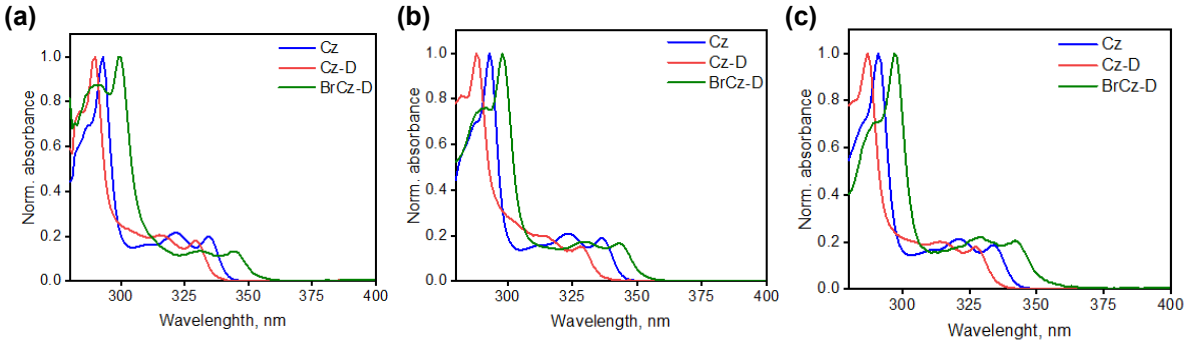

Figure A2.8: UV-vis absorption of carbazole (Cz), **Cz-D** and **BrCz-D** in (a) TOL, (b) THF and (c) ACN.

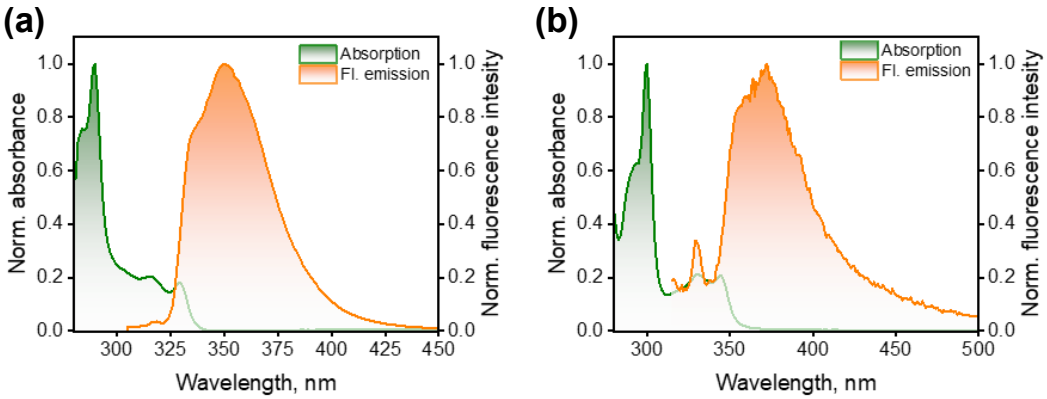

Figure A2.9: The UV-vis absorption and fluorescence emission spectra of (a) **Cz-D** and (b) **BrCz-D** in TOL.

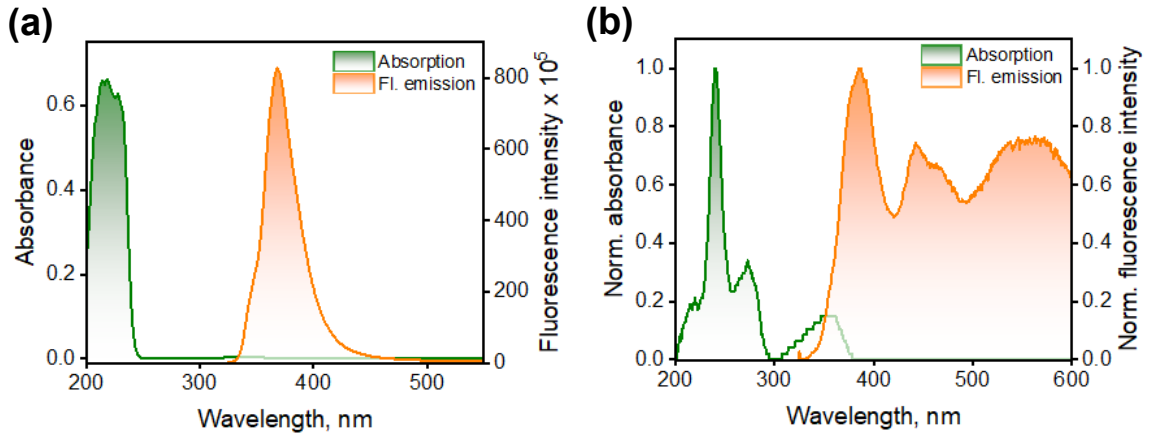

Figure A2.10: Solid-state UV-vis absorption and fluorescence emission spectra of (a) **Cz-D** and (b) **BrCz-D**.

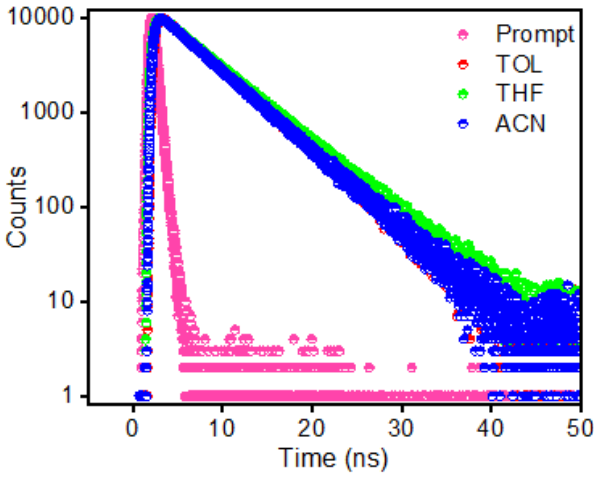

Figure A2.11: Fluorescence lifetime measurements of **Cz-D** in different solvents.

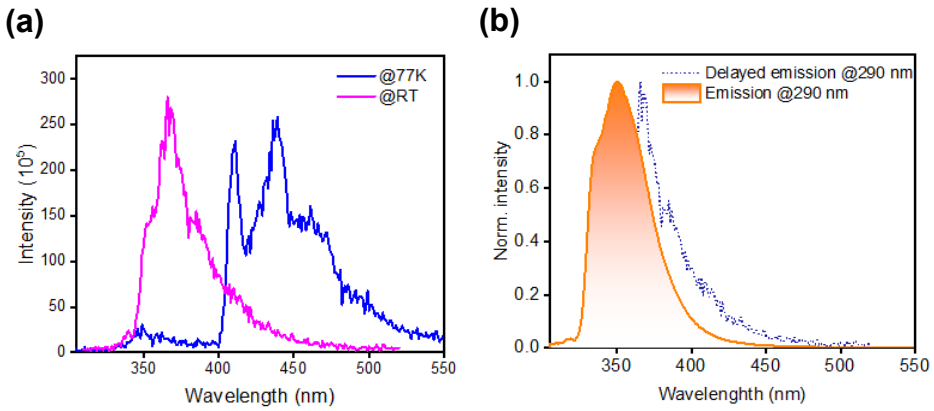

Figure A2.12: Delayed emission measurements of **Cz-D** (a) at 298 K and 77 K and (b) Fluorescence emission at 298 K and delayed emission at 298 K in crystalline state.

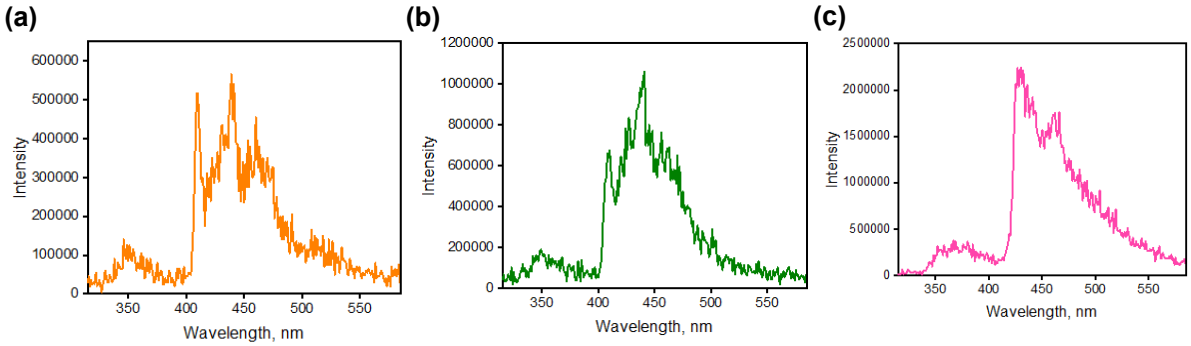

Figure A2.13: Delayed emission measurements of **Cz-D** at 77 K (a) TOL, (b) THF and (c) ACN.

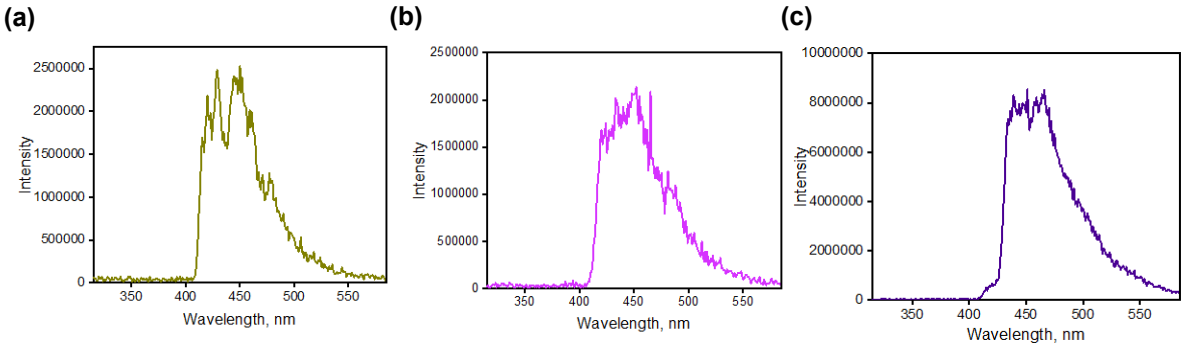

Figure A2.14: Delayed emission measurements of **BrCz-D** at 77 K (a) TOL, (b) THF and (c) ACN.

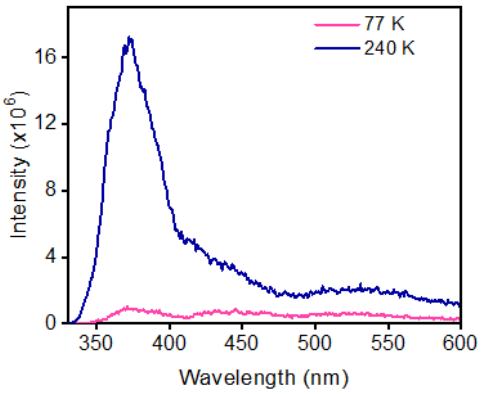

Figure A2.15: Temperature-dependent delayed emission measurements of **Cz-D** in its crystalline state.

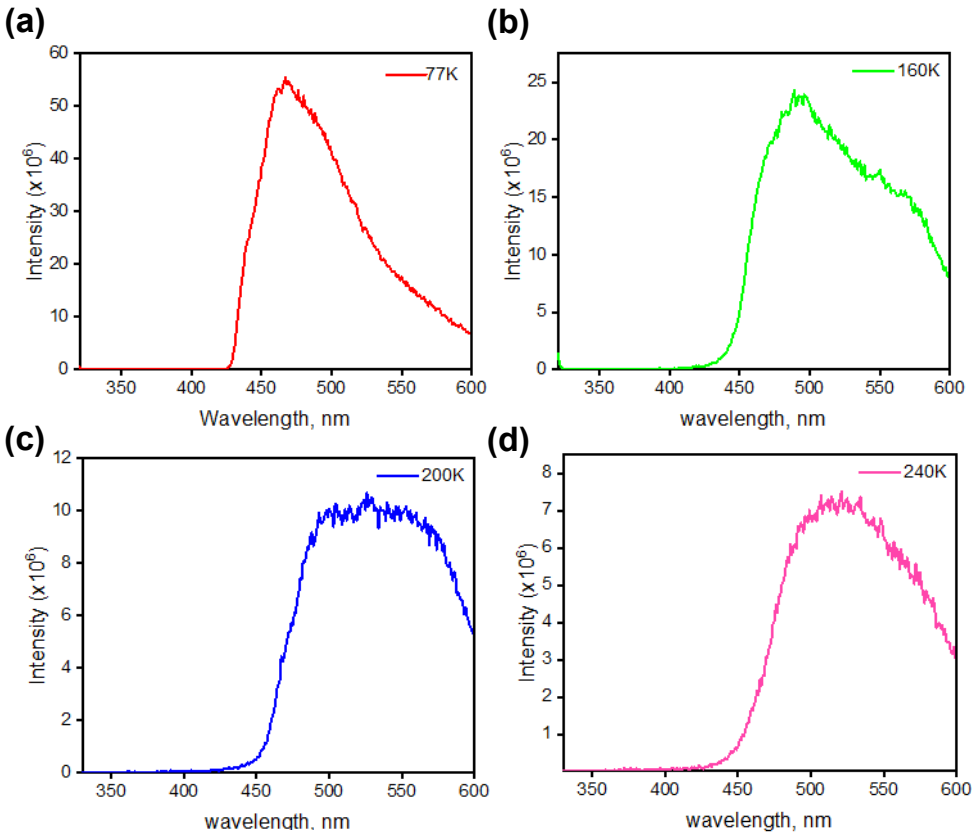

Figure A2.16: Temperature-dependent delayed emission measurements of BrCz-D in its crystalline state.

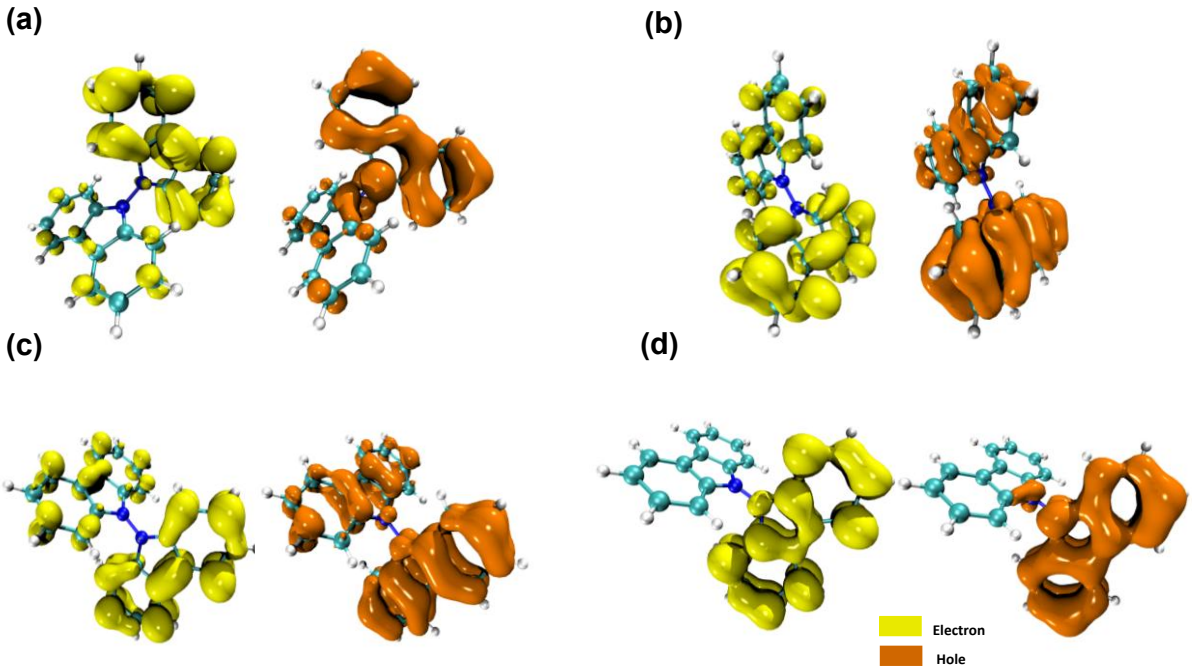

Figure A2.17: Hole-electron analysis of **Cz-D** (a) S1, (b) S2, (c) S3 and (d) S4 transition.

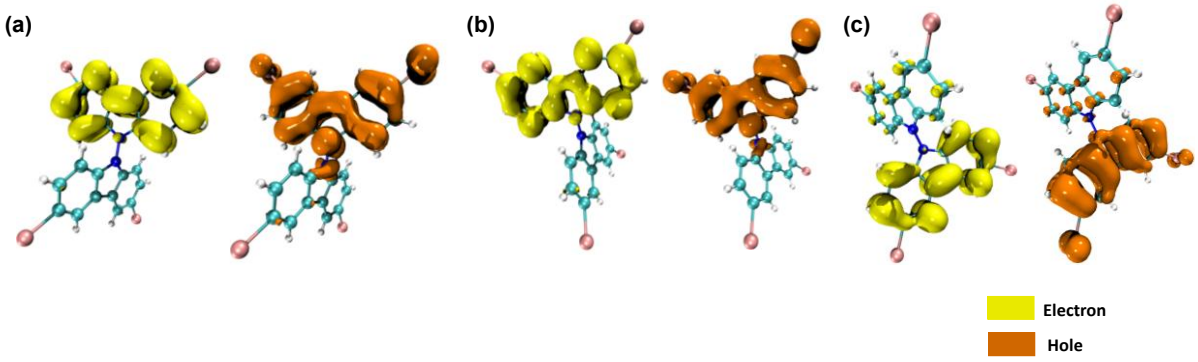

Figure A2.18: Hole-electron analysis of **BrCz-D** (a) S1, (b) S2 and (c) S3 transitions.

Table A2.1: Crystallographic data and refinement parameters for **Cz-D** and **BrCz-D**.

Parameters	**Cz-D**	**BrCz-D**
Formula	$C_{24}H_{16}N_2$	$C_{24}H_{12}Br_4N_2$
Formula weight	332.41	647.99
Crystal system	monoclinic	orthorhombic
Space group	*Cc*	*Pccn*
a, Å	11.80	21.61
b, Å	20.04	26.33
c, Å	14.48	9.15
α, deg	90.00	90.00
β, deg	90.64	90.00
γ, deg	90.00	90.00
V, $Å^3$	3429.49	5211.23
R-factor (%)	8.17	4.87

Table A2.2: Interaction energies in selected dimers determined by SAPT(0)/6-311G+(d,p) calculations and SAPT(0) energy components for **Cz-D** crystals.

Energy components (KJ/mol)	**Dimer**
Electrostatic	-18.4550
Exchange	38.5652
Induction	-4.7542
Dispersion	-61.1099
Total Energy	-45.7539

Table A2.3: Interaction energies in selected dimers determined by SAPT(0)/6-311G+(d,p) calculations and SAPT(0) energy components for **BrCz-D** crystals.

Dimer	Electrostatic KJ/mol	Exchange KJ/mol	Induction KJ/mol	Dispersion KJ/mol	Total Energy KJ/mol
1	-26.7340	78.0034	-7.7943	-137.6168	-94.1418
2	-32.2415	78.4211	-6.9601	-116.4559	-77.2365
3	-13.2404	30.1879	-3.4119	-40.5333	-27.0176

Table A2.4: Relative % intermolecular interactions of **Cz-D** and **BrCz-D** obtained from Hirshfeld analysis.

Interaction	%H•••H	%C•••H	%C•••C
Cz-D	49.1	49.8	1.1

Interaction	%Br•••H	%H•••H	%C•••H	%C•••C	%Br•••Br	%N•••H
BrCz-D	27	20.4	11.2	7	4.2	0.1

Table A2.5: Absorption maxima, emission maxima, fluorescence quantum yield and lifetime of **Cz-D** and **BrCz-D**.

Solvents	Cz-D				BrCz-D			
	λ_{abs} (nm)	λ_{emi} (nm)	Φ_f (%)	τ (ns)	λ_{abs} (nm)	λ_{emi} (nm)	Φ_f (%)	τ (ns)
Toluene	290	350	28.13	5.21	300	372	1.30	---
Tetrahydrofuran	288	350	23.90	5.55	298	373	0.46	---
Acetonitrile	287	350	12.88	5.22	297	392	0.18	---

Reference: Quinine sulphate in 0.5 M H_2SO_4.

Table A2.6: TD-DFT Vertical excitation energies of singlets of **Cz-D** computed at CAMB3LYP-D3/6-311-G+(d,p) level of theory.

States	Energy (eV)	Oscillator Strength (f)
S1	4.3413	0.0166
S2	4.4013	0.0816
S3	4.7652	0.1574
S4	4.7799	0.2202
S5	5.2883	0.0019
S6	5.3362	0.0001
S7	5.3739	0.1511
S8	5.3880	0.1132
S9	5.6912	0.0117
S10	5.7269	0.0385

Table A2.7: TD-DFT Vertical excitation energies of singlets of **BrCz-D** computed at CAMB3LYP-D3/6-311-G+(d,p) level of theory.

Singlet	Energy (eV)	Oscillator Strength (f)
S1	4.1696	0.0261
S2	4.2308	0.0630
S3	4.6560	0.1698
S4	4.6934	0.2153
S5	5.0742	0.0034
S6	5.1546	0.1677
S7	5.1622	0.0124
S8	5.1788	0.1481
S9	5.5220	0.0164
S10	5.5289	0.0388

Table A2.8: TDA Vertical excitation energies of triplet of **Cz-D** computed at CAMB3LYP-D3/6-311-G+(d,p) level of theory.

Triplet	Energy (eV)
T1	3.5117
T2	3.5161
T3	3.6589
T4	3.6927
T5	4.2227
T6	4.2381
T7	4.3796
T8	4.4213
T9	4.6763
T10	4.6973

Table A2.9: TDA Vertical excitation energies of triplet of **BrCz-D** computed at CAMB3LYP-D3/6-311-G+(d,p) level of theory.

Triplet	Energy (eV)
T1	3.4789
T2	3.4868
T3	3.5008
T4	3.5557
T5	4.0252
T6	4.0600
T7	4.2137
T8	4.2299
T9	4..5825
T10	4.5943

Table A2.10: Vertical excitation energy, oscillatory strength (f), mean position (POS), participation ratio (PR) and charge transfer character (CT) of excited states in **Cz-D** at CAMB3LYP-D3/6-311-G+(d,p) level of theory.

State	dE (eV)	POS	PR	CT
S_1	4.343	1.826	1.403	0.092
S_2	4.401	1.177	1.410	0.064
S_3	4.764	1.276	1.665	0.025
S_4	4.779	1.725	1.664	0.024
S_5	5.288	1.461	1.477	0.849
S_6	5.337	1.536	1.455	0.814
S_7	5.376	1.954	1.097	0.082
S_8	5.389	1.047	1.099	0.084
S_9	5.692	1.533	1.989	0.333
S_{10}	5.728	1.466	1.991	0.111

Table A2.11: Vertical excitation energy, oscillatory strength (f), mean position (POS), participation ratio (PR) and charge transfer character (CT) of excited states in **BrCz-D** at CAMB3LYP-D3/6-311-G+(d,p) level of theory.

State	dE (eV)	POS	PR	CT
S_1	4.170	1.072	1.154	0.064
S_2	4.231	1.925	1.160	0.056
S_3	4.656	1.117	1.260	0.025
S_4	4.693	1.880	1.268	0.025
S_5	5.074	1.516	1.217	0.869
S_6	5.155	1.063	1.134	0.099
S_7	5.162	1.462	1.217	0.839
S_8	5.179	1.959	1.085	0.070
S_9	5.522	1.067	1.144	0.026
S_{10}	5.529	1.868	1.298	0.047

Table A2.12: S_1-optimised SOC calculation of **Cz-D** at CAMB3LYP-D3/6-311-G+(d,p) level of theory.

Transitions	cm-1	Transitions	cm-1	Transitions	cm-1
<S0|Hso|T1>	0.08728	<S2|Hso|T1>	0.59379	<S4|Hso|T1>	0.03945
<S0|Hso|T2>	0.02622	<S2|Hso|T2>	0.93022	<S4|Hso|T2>	0.04786
<S0|Hso|T3>	0.18715	<S2|Hso|T3>	0.04967	<S4|Hso|T3>	0.68800
<S0|Hso|T4>	0.12301	<S2|Hso|T4>	0.17570	<S4|Hso|T4>	0.66845
<S0|Hso|T5>	0.11860	<S2|Hso|T5>	0.03562	<S4|Hso|T5>	0.14339
<S0|Hso|T6>	0.29792	<S2|Hso|T6>	0.16199	<S4|Hso|T6>	0.04959
<S0|Hso|T7>	1.02058	<S2|Hso|T7>	0.10884	<S4|Hso|T7>	0.04251
<S0|Hso|T8>	1.15485	<S2|Hso|T8>	0.20760	<S4|Hso|T8>	0.06205
<S0|Hso|T9>	0.25824	<S2|Hso|T9>	0.11401	<S4|Hso|T9>	0.31742
<S0|Hso|T10>	0.18802	<S2|Hso|T10>	0.08876	<S4|Hso|T10>	0.47245
<S0|Hso|T11>	1.09455	<S2|Hso|T11>	0.17068	<S4|Hso|T11>	0.05981
<S0|Hso|T12>	1.04652	<S2|Hso|T12>	0.43471	<S4|Hso|T12>	0.06229
<S0|Hso|T13>	0.28118	<S2|Hso|T13>	0.09884	<S4|Hso|T13>	0.59387
<S0|Hso|T14>	0.16353	<S2|Hso|T14>	0.14325	<S4|Hso|T14>	0.37933
<S0|Hso|T15>	0.64407	<S2|Hso|T15>	1.33383	<S4|Hso|T15>	0.22514
<S0|Hso|T16>	0.48017	<S2|Hso|T16>	1.65711	<S4|Hso|T16>	0.19212
<S0|Hso|T17>	0.75861	<S2|Hso|T17>	0.22135	<S4|Hso|T17>	0.09895
<S0|Hso|T18>	0.22492	<S2|Hso|T18>	1.56173	<S4|Hso|T18>	0.50254
<S0|Hso|T19>	1.02046	<S2|Hso|T19>	0.07259	<S4|Hso|T19>	0.04432
<S0|Hso|T20>	0.34525	<S2|Hso|T20>	0.09674	<S4|Hso|T20>	0.02365
<S1|Hso|T1>	0.95616	<S3|Hso|T1>	0.02103	<S5|Hso|T1>	0.11699
<S1|Hso|T2>	0.55003	<S3|Hso|T2>	0.04293	<S5|Hso|T2>	0.28073
<S1|Hso|T3>	0.08559	<S3|Hso|T3>	0.61594	<S5|Hso|T3>	1.69897
<S1|Hso|T4>	0.34399	<S3|Hso|T4>	0.62103	<S5|Hso|T4>	1.07078
<S1|Hso|T5>	0.10846	<S3|Hso|T5>	0.15211	<S5|Hso|T5>	0.43484
<S1|Hso|T6>	0.09165	<S3|Hso|T6>	0.15613	<S5|Hso|T6>	1.38245
<S1|Hso|T7>	0.23237	<S3|Hso|T7>	0.04722	<S5|Hso|T7>	0.36654
<S1|Hso|T8>	0.13438	<S3|Hso|T8>	0.09391	<S5|Hso|T8>	0.69729
<S1|Hso|T9>	0.02488	<S3|Hso|T9>	0.46475	<S5|Hso|T9>	0.29779
<S1|Hso|T10>	0.07981	<S3|Hso|T10>	0.28960	<S5|Hso|T10>	0.16761
<S1|Hso|T11>	0.43125	<S3|Hso|T11>	0.04556	<S5|Hso|T11>	0.41466
<S1|Hso|T12>	0.16942	<S3|Hso|T12>	0.07391	<S5|Hso|T12>	0.07141
<S1|Hso|T13>	0.06994	<S3|Hso|T13>	0.34031	<S5|Hso|T13>	0.32447
<S1|Hso|T14>	0.06752	<S3|Hso|T14>	0.57763	<S5|Hso|T14>	0.17309
<S1|Hso|T15>	0.68816	<S3|Hso|T15>	0.30486	<S5|Hso|T15>	0.18208
<S1|Hso|T16>	1.50371	<S3|Hso|T16>	0.28772	<S5|Hso|T16>	0.07753
<S1|Hso|T17>	0.47235	<S3|Hso|T17>	0.09119	<S5|Hso|T17>	0.10494
<S1|Hso|T18>	2.17002	<S3|Hso|T18>	0.24810	<S5|Hso|T18>	0.32207
<S1|Hso|T19>	0.07100	<S3|Hso|T19>	0.02269	<S5|Hso|T19>	0.13030
<S1|Hso|T20>	0.49649	<S3|Hso|T20>	0.08991	<S5|Hso|T20>	0.22621

Table A2.13: S_1-optimised SOC calculation of **BrCz-D** at CAMB3LYP-D3/6-311-G+(d,p) level of theory.

Transitions	cm-1	Transitions	cm-1	Transitions	cm-1
<S0|Hso|T1>	14.76114	<S2|Hso|T1>	0.37387	<S4|Hso|T1>	0.31400
<S0|Hso|T2>	7.49451	<S2|Hso|T2>	2.54428	<S4|Hso|T2>	0.59287
<S0|Hso|T3>	4.85085	<S2|Hso|T3>	0.40884	<S4|Hso|T3>	0.50953
<S0|Hso|T4>	4.81141	<S2|Hso|T4>	0.70375	<S4|Hso|T4>	2.99115
<S0|Hso|T5>	11.93960	<S2|Hso|T5>	0.80672	<S4|Hso|T5>	1.08329
<S0|Hso|T6>	16.79232	<S2|Hso|T6>	0.54510	<S4|Hso|T6>	0.58631
<S0|Hso|T7>	12.92493	<S2|Hso|T7>	0.05736	<S4|Hso|T7>	0.22507
<S0|Hso|T8>	7.96346	<S2|Hso|T8>	0.38265	<S4|Hso|T8>	0.68797
<S0|Hso|T9>	19.03033	<S2|Hso|T9>	0.48005	<S4|Hso|T9>	1.08711
<S0|Hso|T10>	38.35536	<S2|Hso|T10>	1.06977	<S4|Hso|T10>	1.91091
<S0|Hso|T11>	22.19939	<S2|Hso|T11>	0.37577	<S4|Hso|T11>	0.28219
<S0|Hso|T12>	13.00065	<S2|Hso|T12>	1.13619	<S4|Hso|T12>	0.42642
<S0|Hso|T13>	72.77471	<S2|Hso|T13>	1.79277	<S4|Hso|T13>	1.06768
<S0|Hso|T14>	88.64405	<S2|Hso|T14>	1.64758	<S4|Hso|T14>	1.79792
<S0|Hso|T15>	618.29535	<S2|Hso|T15>	5.01086	<S4|Hso|T15>	7.29102
<S0|Hso|T16>	564.67627	<S2|Hso|T16>	9.90007	<S4|Hso|T16>	21.7890
<S0|Hso|T17>	699.02582	<S2|Hso|T17>	8.15409	<S4|Hso|T17>	17.81782
<S0|Hso|T18>	618.25354	<S2|Hso|T18>	4.04946	<S4|Hso|T18>	7.43478
<S0|Hso|T19>	278.46677	<S2|Hso|T19>	8.93130	<S4|Hso|T19>	4.86298
<S0|Hso|T20>	30.69970	<S2|Hso|T20>	1.51392	<S4|Hso|T20>	1.64954
<S1|Hso|T1>	1.31352	<S3|Hso|T1>	0.84556	<S5|Hso|T1>	0.40335
<S1|Hso|T2>	0.58304	<S3|Hso|T2>	0.23736	<S5|Hso|T2>	1.05114
<S1|Hso|T3>	0.74129	<S3|Hso|T3>	1.48733	<S5|Hso|T3>	1.63865
<S1|Hso|T4>	0.64194	<S3|Hso|T4>	0.71703	<S5|Hso|T4>	6.26495
<S1|Hso|T5>	14.93966	<S3|Hso|T5>	0.34390	<S5|Hso|T5>	2.24672
<S1|Hso|T6>	0.68301	<S3|Hso|T6>	0.90501	<S5|Hso|T6>	2.29637
<S1|Hso|T7>	0.68785	<S3|Hso|T7>	0.67081	<S5|Hso|T7>	0.56399
<S1|Hso|T8>	23.21818	<S3|Hso|T8>	0.18981	<S5|Hso|T8>	2.12248
<S1|Hso|T9>	0.34735	<S3|Hso|T9>	1.60643	<S5|Hso|T9>	1.43980
<S1|Hso|T10>	0.19289	<S3|Hso|T10>	1.15455	<S5|Hso|T10>	0.20605
<S1|Hso|T11>	1.05651	<S3|Hso|T11>	1.07450	<S5|Hso|T11>	1.60623
<S1|Hso|T12>	0.40747	<S3|Hso|T12>	0.28467	<S5|Hso|T12>	0.48103
<S1|Hso|T13>	1.95696	<S3|Hso|T13>	1.04322	<S5|Hso|T13>	0.13211
<S1|Hso|T14>	0.35186	<S3|Hso|T14>	2.09159	<S5|Hso|T14>	3.92638
<S1|Hso|T15>	10.15331	<S3|Hso|T15>	18.30008	<S5|Hso|T15>	3.62656
<S1|Hso|T16>	0.36500	<S3|Hso|T16>	6.39408	<S5|Hso|T16>	2.06463
<S1|Hso|T17>	1.23391	<S3|Hso|T17>	5.81568	<S5|Hso|T17>	3.05110
<S1|Hso|T18>	9.32443	<S3|Hso|T18>	18.04069	<S5|Hso|T18>	0.71047
<S1|Hso|T19>	4.29012	<S3|Hso|T19>	4.33049	<S5|Hso|T19>	0.54707
<S1|Hso|T20>	9.00671	<S3|Hso|T20>	3.03793	<S5|Hso|T20>	1.56758

2.6. Appendix

2.6.1. Materials and Methods

All reagents were obtained from commercial sources and used directly without additional purification. Reactions were performed in oven-dried glassware. Solvents were purified and dried following standard laboratory procedures before use. Thin-layer chromatography (TLC) was carried out on pre-coated silica gel 60 F254 aluminium plates (0.25 mm, Merck), with visualisation under UV light at both short and long wavelengths. Column chromatography was performed on silica gel (200-400 mesh) using solvent systems selected based on the TLC mobility of the target compounds. Reported yields correspond to products confirmed to be both chromatographically and spectroscopically pure. Melting points were determined using a capillary melting point apparatus. ^{1}H and ^{13}C NMR spectra were recorded on a Bruker Advance DPX 500 MHz spectrometer with tetramethylsilane (TMS) as the reference standard. Mass spectra were obtained using a Bruker UltrafleXtreme MALDI-TOF/TOF instrument equipped for matrix-assisted laser desorption/ionisation (MALDI). Photophysical studies were performed in quartz cuvettes with a 10 mm path length. UV-vis-NIR absorption spectra were collected on a Shimadzu UV-3600 spectrophotometer, and fluorescence measurements were recorded using a Horiba Jobin Yvon Fluorolog system. Fourier transform infrared (FT-IR) spectra were acquired on a Shimadzu IR Prestige-21 spectrometer with samples prepared as KBr pellets.

2.6.2. X-ray Crystallography

High-quality crystals of **Cz-D** and **Br-CzD** with appropriate dimensions were selected for the X-ray diffraction experiments. The crystallographic data collected are presented in the Supporting Information, Table S1. A single crystal was mounted using oil (Infineum V8512) on a glass fibre. All measurements were made using a CCD area detector with graphite-monochromated Mo Kα radiation. The data was collected using a Bruker APEXII detector and processed using APEX2 from Bruker. The structure was solved by the direct method and expanded using the Fourier technique. The non-hydrogen atoms were refined anisotropically. Hydrogen atoms were included in idealised positions, but not refined. Their positions were constrained relative to their parent atom using the appropriate HFIX command in SHELX-97.3. All programs used during the

crystal structure analysis are incorporated in the WINGX software. 4, 5 The full validation of the CIF and structure factor was performed using the checkCIF utility and found to be free of major alert levels. 3D structure visualisation and the exploration of the crystal packing were carried out using Mercury 3.10.1.

2.6.3. Kubelka-Munk transformed absorption

We employed barium sulfate ($BaSO_4$) as the dispersing agent, leveraging its exceptional optical properties, including high transmittance and nearly 100% reflectance in the UV-Vis range. To preserve the structural integrity of the dimer crystals, we carefully embedded them in $BaSO_4$, avoiding full pulverisation into a fine powder. Subsequently, diffuse reflectance measurements were performed on the crystalline samples, ensuring accurate characterisation of their optical properties.

2.6.4. Computational Analysis

All the computational investigations were carried out in the Gaussian 16 software package.[162] Geometry optimisations for the ground-state were carried out in the gas phase at the B3LYP-D3/6-311+G(d,p) level of theory. Vertical excitation energies along with oscillator strengths were obtained using time-dependent density functional theory (TDDFT) calculations at the CAM-B3LYP-D3/6-311+G(d,p) level. Long-range Coulombic coupling values were determined via the electronic energy transfer (EET) module implemented in Gaussian 16. Hole-electron distributions and natural transition orbital (NTO) isosurfaces for the **Cz-D** and **BrCz-D** model compounds were analysed using Multiwfn 3.8. The resulting visualisations were prepared with VMD version 1.9.3.[155]

2.6.5. TheoDORE Analysis[156]

The nature of the excited states in Cz-D and BrCz-D was analysed by fragment-based excited-state analysis using TheoDORE at the ground-state optimised geometry. Each carbazole monomer was considered as a fragment in both dimers. To analyse the excited-state properties, three parameters were employed: the participation ratio (PR), the mean position (POS) of the initial (hole) and final (electron) orbitals, and the charge transfer character (CT). The PR

indicates the number of molecular fragments involved in a given excitation and, in this study, spans values between 1 and 2. The POS denotes the average spatial location of the hole and electron for each excitation event. The CT parameter quantifies the extent of charge separation by measuring the contribution of transitions where the initial and final orbitals reside on different fragments. A CT value of 1 represents a fully charge-separated state, while a CT of 0 corresponds to a Frenkel-type excitation. Additionally, electron-hole correlation plots were created to provide a visual and qualitative understanding of the nature of each excited state in both dimer systems.

2.6.6. Noncovalent interaction (NCI) Plot

NCI analysis employs an index based on electron density and its derivatives to identify noncovalent interactions. A two-dimensional plot of reduced electron density(s) against electron density (ρ) and the critical points is associated with the troughs appearing in the plot. Reduced electron density is given by

$$S = \frac{1}{2(3\pi^2)^{1/3}} \frac{|\nabla_\rho|}{\rho^{4/3}}$$

Noncovalent interactions occur at the real-space points where these troughs appear. The sign of the second derivative of ρ(∇2ρ) is analysed to distinguish attractive and repulsive interactions. The noncovalent interaction regions are represented in the plot as discs with colour ranging from blue (attractive) to red (repulsive) as in the VIBGYOR spectrum.

2.6.7. Hirshfeld Analyses[129]

Important intermolecular interactions within the crystal structure of Cz-D and BrCz-D were identified through Hirshfeld surface analyses using Crystal Explorer 3.1. The Hirshfeld surface is defined as a set of points in 3D space where the ratio of pro molecule and pro crystal electron densities is equal to 0.5. The exploration of intermolecular contacts is provided by mapping normalised contact distances (d_{norm}), which is a function of the closest distance from the point to the nuclei interior (d_i) and exterior (d_e) to the surface, as well as on the van der Waals radii (r^{vdw}). 2D fingerprints that were generated by deriving from the Hirshfeld surface by plotting the fraction of points on the surface as a function of d_i and d_e, which provide a visual summary of

intermolecular contacts within the crystal.

2.6.8. Symmetry Adapted Perturbation Theory (SAPT)[128]

SAPT(0) analysis was employed to determine the non-covalent interaction energies of dimer molecules. The SAPT module of the psi4 code was employed, with 6-311G+(d,p) basis set. SAPT(0) calculations provide the contributing components of interaction energy. The results obtained from SAPT(0) analysis are a second-order perturbation expansion, comprising first-order electrostatic and exchange energy terms, and second-order dispersion, induction, and their exchange counterparts as perturbation terms.

$$E_{int}^{SAPT(0)} = E_{elec.}^{(1)} + E_{ex.}^{(1)} + E_{ind.}^{(2)} + E_{ind-ex}^{(2)} + E_{dis-ex}^{(2)} + E_{dis.}^{(2)}$$

2.6.9. Femtosecond Transient Absorption (fsTA) Measurement

Femtosecond transient absorption (fsTA) experiments were performed using a setup seeded by a Spectra-Physics Mai Tai SP mode-locked laser (86 MHz, 800 nm), which pumped a Spectra-Physics Spitfire Ace regenerative amplifier operating at 1 kHz with an output energy of 5.5 mJ. Part of the amplified beam was directed to a TOPAS optical parametric amplifier to generate the 440 nm pump pulses, while the remaining 800 nm light was sent through an optical delay line within an ExciPro pump-probe spectrometer. A sapphire crystal placed in this path produced a white-light continuum, which was then split into a probe and reference beam. Detection was carried out using a dual diode array detector, offering a spectral coverage of 200 nm and a maximum time delay of 3.6 ns. Sample solutions were held in a 1.2 mm path length rotating cuvette. The instrument response function (IRF), determined from the two-photon absorption of a 10% benzene/methanol mixture, was ~110 fs at 530 nm. An 80% neutral density filter was employed to control the excitation fluence, and the samples were photoexcited with 200 nJ, 100 fs pulses. The polarization between the pump and probe pulses was kept at ~54.7° magic angle, to maintain an isotropic signal for the sample. **Cz-D and BrCz-D** were excited at 355 nm and , for the fsTA measurements. Upon variations in laser intensity, the detected kinetic components remained unaffected, excluding singlet-singlet annihilation.

2.6.10. Global Analysis[163]

A global analysis of the fsTA data was performed using Glotaran software. This involved evaluating the instrument response function and accounting for group velocity dispersion of the white light continuum, which facilitated accurate determination of decay lifetimes and dispersion-corrected spectra. A sequential kinetic model was applied during the global fitting process, enabling the simultaneous examination of all wavelengths to obtain the EAS.

Time-resolved spectroscopic measurements are recorded with respect to two variables: the spectral parameter, wavelength (λ), and the temporal delay (t) following the moment of photoexcitation. The model underlying the data matrix is a superposition of n_{comp} components given by the equation,

$$\Psi(\lambda, t) = \sum_{l=1}^{n_{comp}} c_l(t)\varepsilon_l(\lambda)$$

where c_l and ε_l are the unknown concentration profile and spectrum of the component, respectively.

An initial step in analysing such datasets generally entails performing singular value decomposition to gain insights into the underlying spectral and kinetic components. Singular value decomposition (SVD) serves as a matrix decomposition method that assists in identifying the number of distinct spectral and temporal contributions within the dataset, providing crucial insight for constructing an appropriate initial kinetic model (Golub GH, Van Loan CF, 1996, Matrix Computations. 3rd edition. The Johns Hopkins University Press, Baltimore).

By applying a sequential fitting model to the fsTA dataset within the Glotaran platform, one obtains the SVD of the residual matrix, along with the extracted kinetic parameters, EAS, their normalised counterparts, and corresponding concentration profiles through an interactive graphical interface. In a sequential or unbranched unidirectional model, the associated spectra are called evolution-associated spectra (EAS), and the model of equation 2.3 then reads as,

$$\Psi(\lambda, t) = \sum_{l=1}^{n_{comp}} c_l^{EAS}(t, \theta)EAS_l(\lambda)$$

With successively increasing lifetimes, the EAS visualises the spectral evolution. It is essential to emphasise that the EAS reflects how spectral features evolve over time and do not directly correspond to distinct chemical or physical entities. Rather, EAS captures the dynamic spectral

variations linked to specific kinetic time constants.

Chapter 3

Structural Planarization of a Carbazole Dimer Enabling Heavy-Atom-Free Room-Temperature Phosphorescence

Abstract

Purely organic room-temperature phosphorescence (RTP) remains challenging due to intrinsically weak spin-orbit coupling and efficient non-radiative deactivation of triplet excitons. Herein, we report a heavy-atom-free carbazole dimer in which two carbazole units are covalently linked through a 3,3′-C-C bond, forming an unusually planar and rigid π-conjugated framework. Single-crystal X-ray diffraction reveals complete planarization of the dimer, enabling extended π-electron delocalisation and strong intermolecular interactions in the crystalline state. As a result, the material exhibits pronounced RTP with a lifetime of 490 µs under ambient conditions, without the need for heavy atoms or external rigid hosts. Quantitative photophysical analysis reveals a high triplet quantum yield of 42.3%, accompanied by an efficient intersystem crossing rate constant of k_{ISC} = 1.0 x 10^8 s^{-1}, indicating rapid and effective singlet-triplet conversion facilitated by structural planarization and electronic coupling between the carbazole units. Temperature-dependent gated photoluminescence measurements reveal a clearly blue-shifted phosphorescence band at 77 K, accompanied by an extended lifetime of 980 µs, indicating enhanced excitonic coupling arising from the reduced interchromophoric distances in the dimers within the unit cell at 77 K. This work demonstrates that structural planarization achieved through a simple C-C linkage is an effective molecular design strategy for realising efficient RTP in purely organic chromophores.

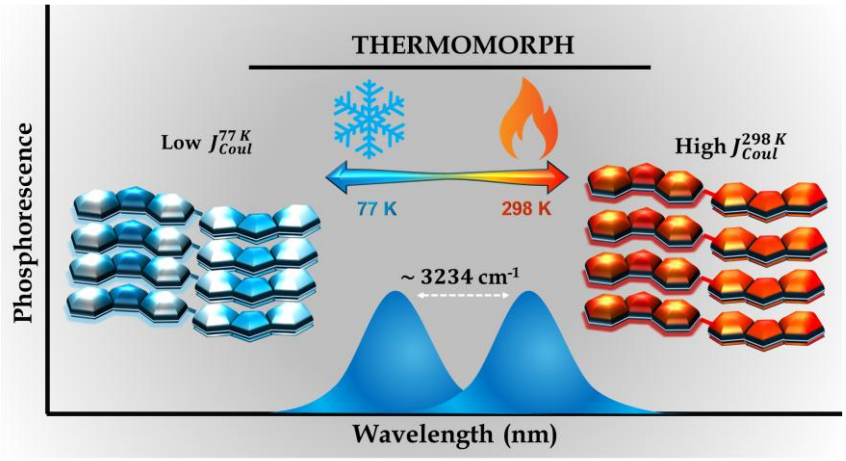

3.1. Introduction

Room-temperature phosphorescence (RTP) from purely organic molecules has garnered considerable interest due to its fundamental significance and potential applications in optoelectronics,[99] sensing, biomedicine,[101] and information security. Unlike fluorescence, phosphorescence originates from spin-forbidden triplet-singlet transitions, which are intrinsically inefficient in organic systems owing to weak spin-orbit coupling (SOC) and rapid non-radiative deactivation of triplet excitons.[2] Consequently, efficient RTP has traditionally relied on heavy-metal complexes, where strong SOC facilitates ISC and phosphorescent decay. However, the use of heavy metals raises concerns related to cost, toxicity, and environmental sustainability, motivating the development of heavy-atom-free organic RTP systems.

In recent years, significant progress has been achieved in enabling RTP in purely organic chromophores by suppressing non-radiative decay pathways and stabilising triplet excitons.[164] Strategies such as rigidification through crystallisation,[8] host-guest encapsulation, polymer matrices, hydrogen-bonding networks, and molecular aggregation have been widely explored.[38,48,49,165] These approaches primarily function by restricting molecular motions, reducing vibrational coupling, and shielding triplet states from quenching by oxygen or thermal fluctuations. Nevertheless, achieving long-lived and efficient RTP in simple, structurally minimal organic molecules remains challenging, particularly without relying on external matrices or heteroatom-induced spin-orbit coupling enhancement.[166]

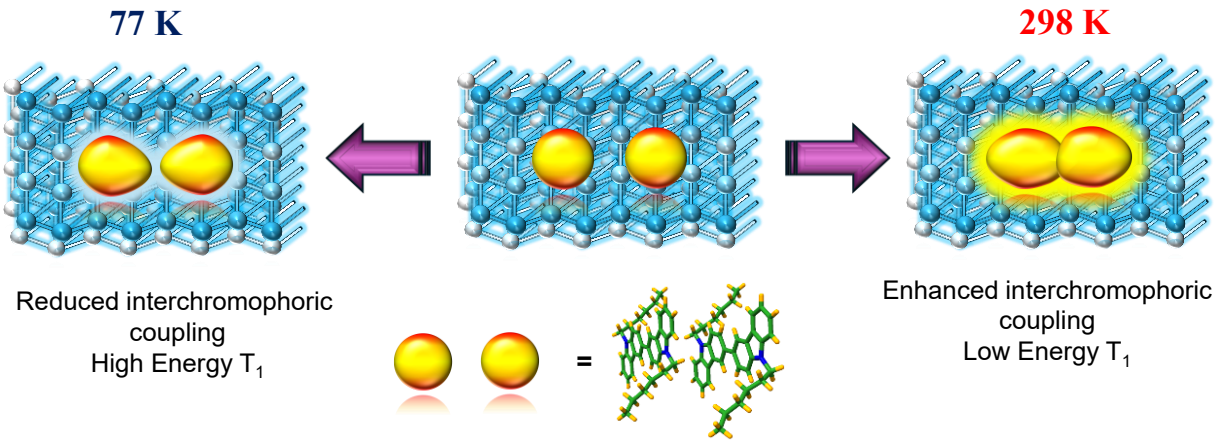

Scheme 3.1: Schematic illustration of interchromophoric excitonic coupling modulating the triplet state energy

Carbazole derivatives have emerged as an attractive platform for organic RTP owing to their rigid aromatic framework, relatively small singlet-triplet energy gaps (ΔE_{ST}), and versatile structural tunability.[93,94,98,99,109,167–169] Most reported carbazole-based RTP systems rely on heavy-atom substitution, donor-acceptor architectures, or host-assisted crystallisation to induce phosphorescence.[10,170,171] In contrast, RTP arising from purely hydrocarbon-linked carbazole assemblies, without heteroatom perturbation or external rigid hosts, remains comparatively underexplored.

Herein, we report a purely organic, heavy-atom-free carbazole dimer in which two carbazole units are covalently connected through a 3,3′-C-C bond, forming an unusually planar and rigid π-conjugated framework. Single-crystal X-ray diffraction reveals complete planarization of the dimer, enabling extended π-electron delocalisation and strong intermolecular interactions in the crystalline state. This structural motif facilitates efficient triplet formation and stabilisation, giving rise to pronounced RTP in the absence of heavy atoms or external matrices. Furthermore, temperature-dependent spectroscopic studies reveal distinct triplet-emissive regimes, providing mechanistic insight into triplet relaxation and kinetic trapping in organic RTP systems. This work highlights molecular planarization as an effective design principle for achieving RTP in structurally simple organic chromophores.

3.2. Results and Discussion

3.2.1 Dimer Molecule and the Crustal Structure

A 3,3′-linked N-hexyl carbazole dimer (C-C D) was synthesised following previously reported procedures.[172] Single crystals suitable for X-ray diffraction were obtained by slow evaporation from a 1:1 mixture of dichloromethane and hexane. Single-crystal X-ray diffraction (SCXRD) analysis revealed that C-C D crystallises in a monoclinic lattice with the $P2_1/c$ space group (Figure 3.1). The unit-cell parameters were determined to be a = 9.10 Å, b = 13.85 Å, and c = 11.07 Å, with α = 90°, β = 98.71°, and γ = 90°. Notably, the two carbazole units connected through the C-C bond adopt a fully planar conformation, exhibiting a dihedral angle of 180°. Such an unusual planar arrangement for a single-bond-linked dimer facilitates extended π-electron delocalisation across both carbazole units, enhancing conjugation and predisposing the molecule to unique excited-state behaviour. The intrinsic rigidity and conjugation are expected to play a decisive role in governing the observed photophysical properties, particularly in the solid state (Figure 3.2).

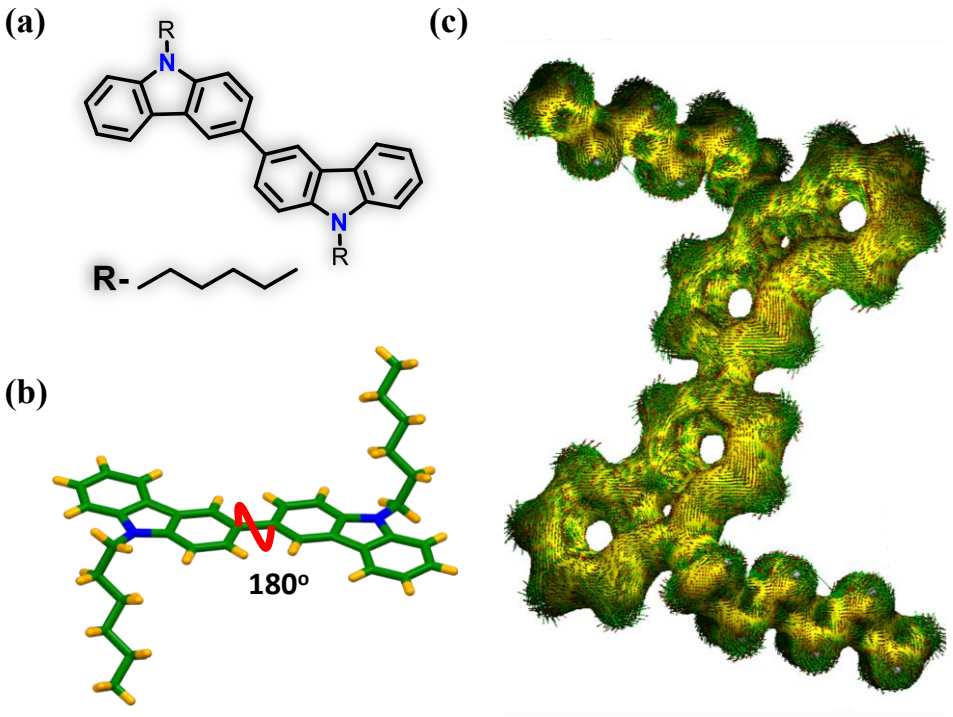

Figure 3.1: (a) Molecular structure of C-C D, (b) Crystal structure of C-C D showing planar geometry and (c) AICD plot showing efficient electronic communication between two monomeric units.

Temperature-dependent single-crystal X-ray diffraction analysis was performed at 298 K and 77 K to investigate potential structural changes in the ground state (Tables A3.1 and A3.2). Upon cooling from 298 K to 77 K, the unit-cell volume decreases from 1437 Å^3 to 1387 Å^3, corresponding to an absolute contraction of ~50 Å^3 (≈3.5%).[173,174] The estimated volumetric thermal expansion coefficient ($\beta \approx 1.6 \times 10^{-4}$ K^{-1}) and the corresponding effective linear expansion coefficient ($\alpha \approx 5.3 \times 10^{-5}$ K^{-1}) are consistent with values typically reported for the organic molecular crystals.

Notably, a non-negligible change in molecular conformation or intermolecular connectivity parameters indicates that the crystal structure remains essentially invariant in the electronic ground state across this temperature range. However, even such a modest lattice contraction can have pronounced consequences for excited-state behaviour. The reduced free volume and enhanced lattice rigidity at low temperature are expected to restrict intramolecular and intermolecular structural relaxation in the excited state, thereby reshaping the excited-state potential energy surfaces.

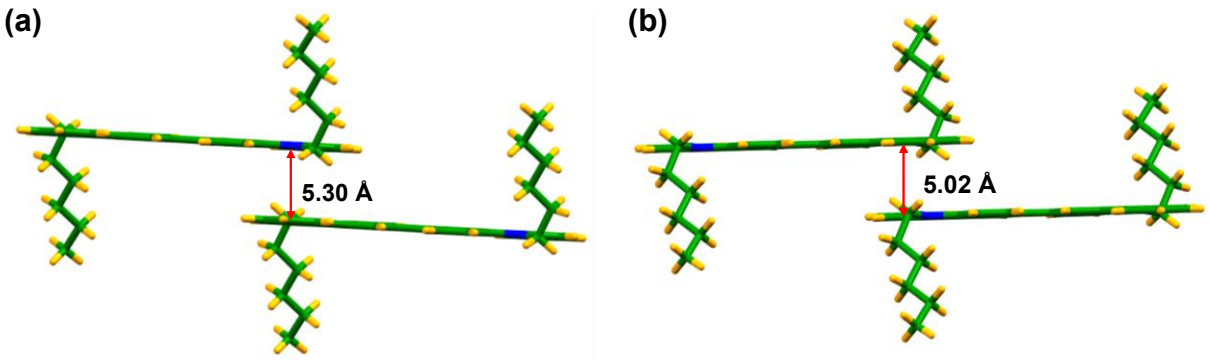

Figure 3.2: The interchromophoric distance of C-C D measured (a) at 298 K and (b) 77 K.

Crystallographic analyses performed at two different temperatures reveal a clear temperature-dependent modulation of intermolecular proximity. At 298 K, the interchromophoric distance between the most stable dimeric units within the crystal lattice is 5.30 Å. Upon cooling to 77 K, this separation decreases to 5.02 Å, corresponding to an approximate compression of ~4%, which is consistent with the overall lattice contraction observed at low temperature.

This reduction in interchromophoric distance is expected to enhance π-π interactions at 77 K, thereby strengthening intermolecular excitonic coupling. Such increased electronic coupling at lower temperatures is likely to play a crucial role in modulating the excited-state electronic structure and, consequently, the material's temperature-dependent optical properties.

As a result, thermally driven differences in excited-state conformational relaxation, excitonic coupling, and the accessibility of aggregate- or excimer-like excited states are likely operative, despite the invariance of the ground-state structure. These effects provide a plausible structural basis for the distinct temperature-dependent optical responses observed at 77 K and 298 K, underscoring the critical role of subtle lattice contraction in governing excited-state dynamics in the solid state.

To elucidate the intermolecular interactions stabilising the crystal packing, truncated symmetry-adapted perturbation theory [SAPT(0)] calculations were performed on the dominant dimeric motifs identified in the crystal lattice (Table A3.3).[128] Two distinct dimeric arrangements were observed, both exhibiting negative total interaction energies dominated by dispersion contributions, underscoring the importance of van der Waals forces in stabilising the molecular assembly (Figure A3.4). Complementary Hirshfeld surface analysis further confirmed the prevalence of H···H (55.9%) and C···H (32.9%) contacts, with minor contributions from N···H

interactions (0.9%), collectively contributing to the structural integrity of the crystalline framework (Figure A3.5).[129]

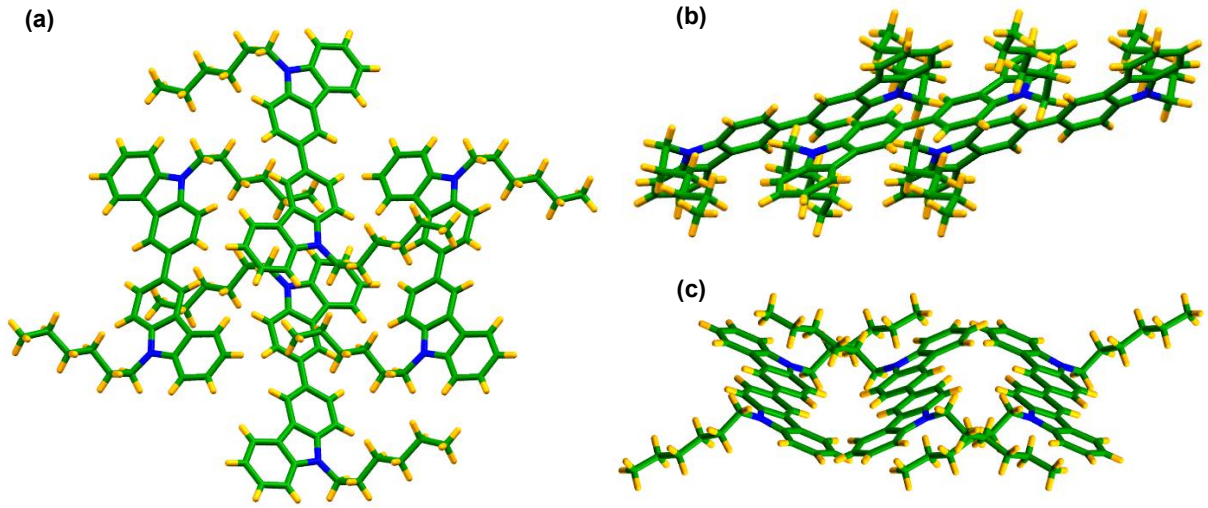

Figure 3.3: The molecular packing of C-C D along (a) X-axis, (b) Y-axis and (c) Z-axis.

3.2.2. Temperature-dependent NMR analysis

Temperature-dependent solid-state ^{1}H and ^{13}C NMR measurements were conducted on the C-C D system at 298 K and 248 K to probe thermally induced changes in the local electronic environment. Upon cooling, the aromatic resonances exhibit noticeable spectral broadening and a systematic deshielding relative to spectra recorded at ambient temperature (Figure 3.4).

The observed line broadening at lower temperature is indicative of reduced molecular mobility and increased lattice rigidity in the solid state, while the downfield shift of the aromatic signals suggests enhanced π-π intermolecular interactions. This deshielding effect can be rationalised by the decreased interchromophoric distances at reduced temperature, which intensify ring-current effects and modify the local magnetic environment of the aromatic nuclei. Collectively, these NMR signatures provide complementary evidence for strengthened intermolecular electronic interactions at low temperature, consistent with the structural contraction observed from temperature-dependent crystallographic analysis.

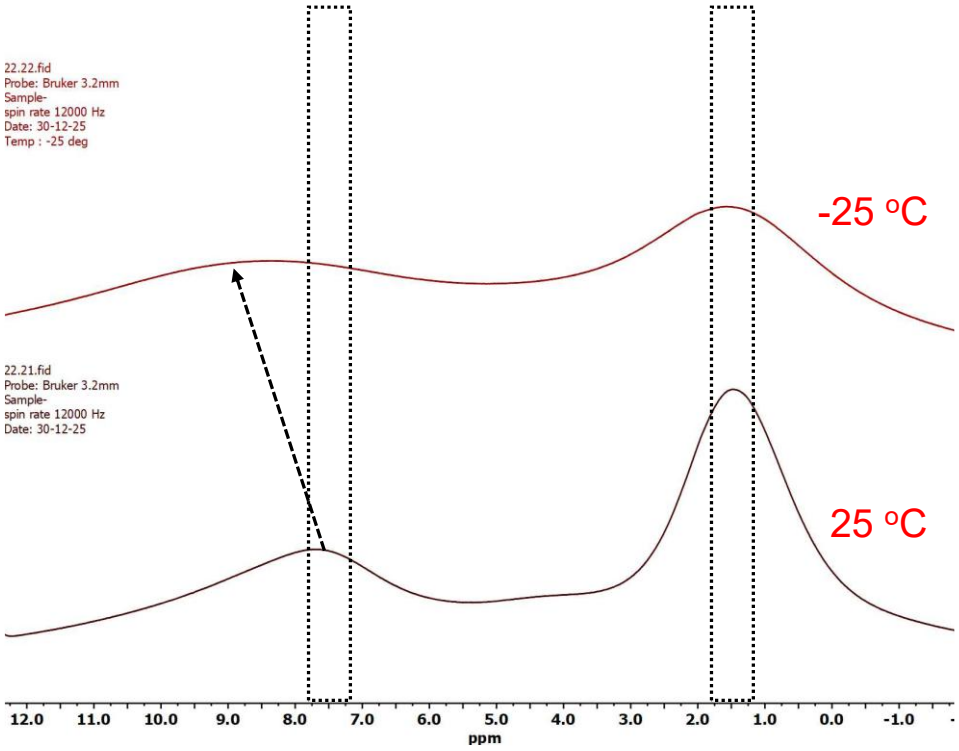

Figure 3.4: Temperature-dependent ^{1}H NMR measurements of C-C D in the solid state.

3.2.2 Steady-State Photophysical Properties of C-C D

The steady-state optical properties of C-C D were first investigated in solution. UV-vis absorption and fluorescence spectra were recorded in tetrahydrofuran (THF) and acetonitrile (ACN) (Figures 3.3 and A3.6). The absorption spectra span 280-380 nm, with a maximum at 300 nm, and display negligible dependence on solvent polarity, indicating the absence of significant ground-state charge-transfer character.[175] The observation suggests that the lowest-energy electronic transition is predominantly of a locally excited (LE) nature, with minimal change in dipole moment upon excitation.

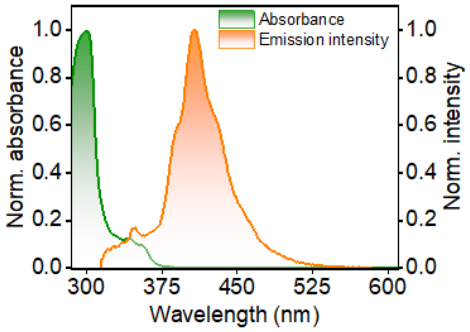

Figure 3.5: Steady-state UV-vis absorption and fluorescence emission spectra of C-C D in THF.

In THF, C-C D exhibits a broad, vibronically unresolved fluorescence band with an emission maximum at 408 nm, a fluorescence quantum yield of 25.1%, and a singlet excited-state lifetime of 4.09 ns. In ACN, the fluorescence quantum yield decreases to 12.8%, while the lifetime remains nearly unchanged (3.9 ns). The reduction in quantum yield without a corresponding decrease in lifetime indicates enhanced non-radiative decay pathways in more polar environments, consistent with increased solvent-induced vibrational relaxation.[72]

In the crystalline state, the Kubelka-Munk-transformed absorption spectrum extends from 200 to 410 nm, with a maximum at 305 nm. The solid-state fluorescence spectrum exhibits a sharp emission band centred at 419 nm (Figure 3.4). Compared to the solution, the absorption and emission maxima are red-shifted by approximately 5 nm and 11 nm, respectively. These bathochromic shifts arise from intermolecular interactions and excitonic coupling in the closely packed crystal lattice, which stabilise the singlet excited state.[50,144,176]

To probe triplet-state behaviour, gated photoluminescence measurements were conducted. In solution at room temperature, the delayed emission overlaps with the prompt fluorescence, indicating the presence of TADF (Figure A3.9).[43] At 77 K, however, the delayed emission spectrum becomes broader and red-shifted, spanning 378-577 nm, reflecting the efficient population of the triplet manifold due to the suppression of RISC at low temperatures.[19]

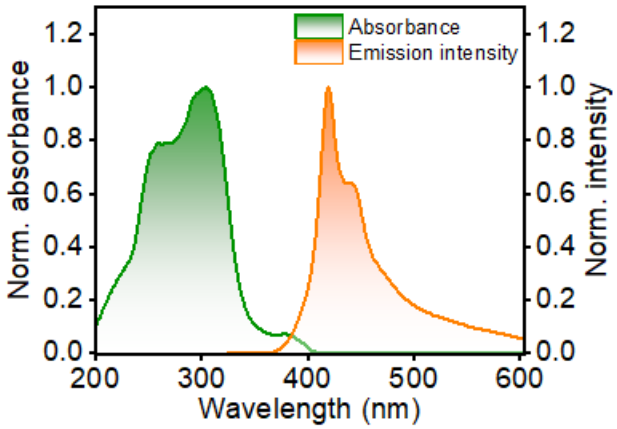

Figure 3.6: Steady-state UV-vis absorption and fluorescence emission spectra of C-C D in the crystalline state.

In the crystalline state, gated-emission measurements at 298 K reveal a broad emission band with a maximum at 513 nm and a lifetime of 490 µs (Figures 3.5a and b). The long-lived emission is attributed to RTP, which is enabled by the rigid molecular framework and dense crystal packing.

Such crystal engineering suppresses non-radiative decay and facilitates spin-forbidden radiative transitions in the absence of heavy atoms.[8,42,52]

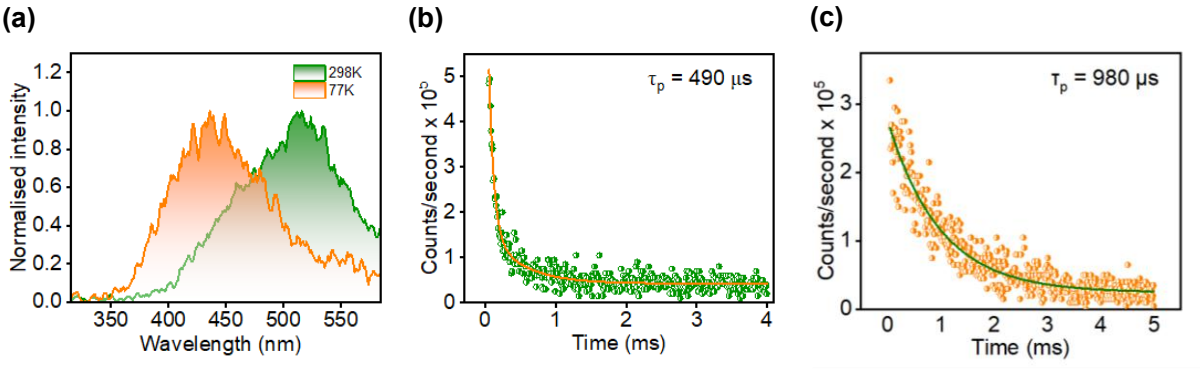

Figure 3.7: (a) Delayed emission spectra of C-C D at ambient temperature and cryogenic temperature, (b) Decay profile of C-C D at 298 K and (c) Decay profile of C-C D at 77 K.

At 77 K, the gated-emission spectrum of crystalline C-C D exhibits a pronounced blue shift, with an emission maximum at approximately 460 nm, accompanied by an extended lifetime of 980 µs (Figures 3.5a and c). Importantly, the longer lifetime at lower temperature does not imply emission from a lower-energy triplet state. Instead, it reflects the strong suppression of vibrational and lattice-assisted non-radiative decay pathways at cryogenic temperatures. The blue-shifted emission is therefore attributed to the enhancement in the excitonic coupling, which arises due to the closer proximity of chromophores in the crystal packing at 77 K.

Singlet-oxygen quantum yield measurements further corroborate efficient triplet formation, yielding a value of 22% using Rose Bengal as a reference, confirming the significant involvement of triplet excitons in the photophysics of C-C D (Figure A3.11).

3.2.3 Femtosecond Transient Absorption Measurements of C-C D

Femtosecond transient absorption (fsTA) spectroscopy was employed to elucidate the ultrafast excited-state dynamics of C-C D in THF (Figure 3.6). Upon photoexcitation at 330 nm with a 100-fs pump pulse, C-C D displayed a pronounced excited-state absorption (ESA) band centred at 643 nm, attributable to the excited-state absorption of the carbazole-based chromophores.[133] Over the course of a few picoseconds, a systematic blue shift of the ESA maximum to 620 nm was observed, indicative of rapid excited-state relaxation. On the nanosecond timescale, a new absorption band emerged at 480 nm, which persisted throughout the entire experimental window of 3.8 ns. Global analysis of the fsTA data using a sequential A → B → C → GS kinetic model revealed three distinct excited-state components. The initial component (A) corresponds to a vibrationally hot

singlet excited state, which relaxes to component B, assigned to the thermally relaxed singlet state, with a time constant of 4.67 ps. Subsequently, this relaxed singlet state evolves into a long-lived species (C) within 1.2 ns, which persists beyond the temporal resolution of the fsTA measurements.

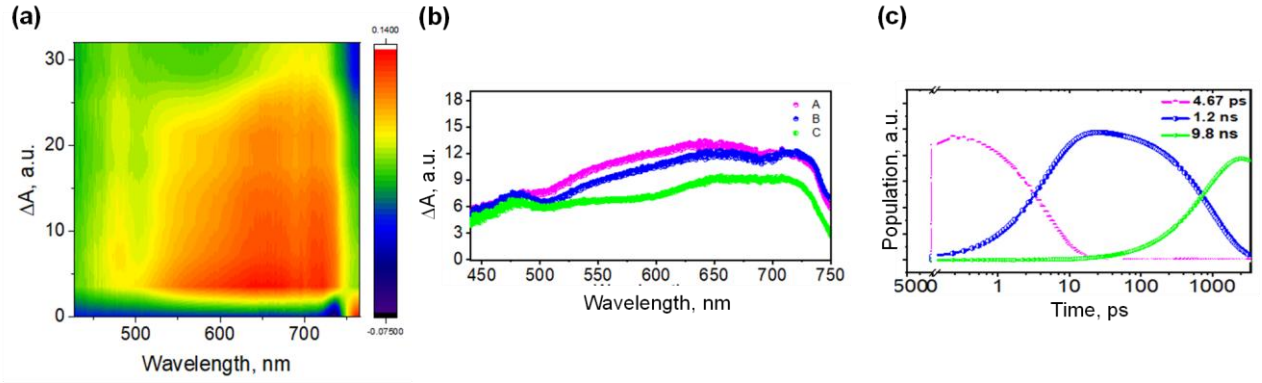

Figure 3.8: (a) Femtosecond transient absorption contour spectra of C-C D in THF, (b) Evolution associated spectra (EAS) of C-C D obtained using sequential A→B→C → GS model in THF, and (c) Kinetic evolution of EAS for C-C D in THF.

3.2.4 Nanosecond Transient Absorption Measurements of C-C D

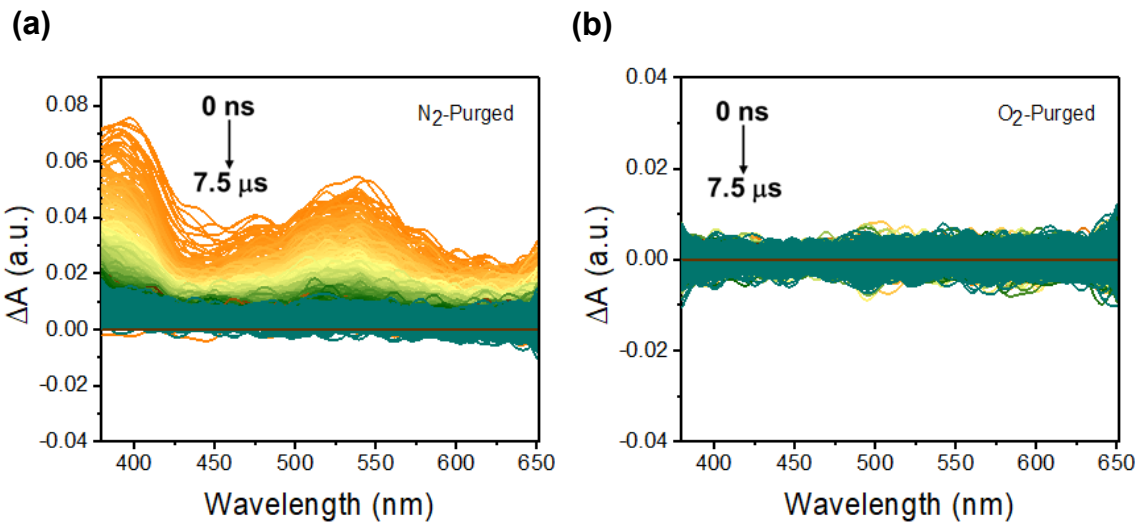

Figure 3.9: Nanosecond transient absorption measurements of C-C D in THF (a) N_2-purged solution and (b) O_2-purged solution.

Nanosecond transient absorption (nsTA) spectroscopy was employed to probe the long-lived excited-state species associated with the triplet manifold of C-C D (Figure 3.7). The measurements were carried out in THF at a concentration of 20 μM using 355 nm excitation with a pulse width of approximately 10 ns. Under nitrogen-purged conditions, C-C D exhibited two prominent

excited-state absorption (ESA) bands centred at 380 nm and 530 nm, with lifetimes of 0.42 μs and 3.99 μs, respectively. Upon increasing the solvent polarity by switching to acetonitrile, the lifetime of the 380 nm ESA band showed only a marginal decrease (0.11 μs), indicating that this transition is largely insensitive to solvent polarity and is therefore attributed to a localised triplet state.[108] In sharp contrast, the ESA band at 530 nm exhibited a pronounced reduction in lifetime (0.10 μs), indicating a strong solvent polarity dependence.[136,139,177] The triplet nature of these absorption features was further confirmed by quenching experiments under oxygen-saturated conditions, where rapid decay of the ESA signal was observed due to efficient deactivation by molecular oxygen. Collectively, the negligible solvent effect on the 390 nm band and the significant lifetime shortening of the 535 nm band in a highly polar medium strongly support the assignment of the latter to a triplet charge-transfer (^{3}CT) state (Figure A3.14).[64,175,177] To determine the triplet quantum yield (Φ_T) of C-C D, triplet-triplet energy transfer (TTET) experiments were carried out using $[Ru(bpy)_3]^{2+}$ as the reference sensitiser ($\Phi_T \approx 100\%$ in methanol) and β-carotene as the triplet energy acceptor.[178] Under these conditions, C-C D exhibited a substantial triplet population, with a triplet quantum yield of 42.3% in THF (Figure A3.13). Using the experimentally determined triplet quantum yield and prompt fluorescence lifetime, the intersystem crossing rate constant was estimated to be $k_{ISC} = 1.0 \times 10^8$ s^{-1}, indicating highly efficient singlet-triplet conversion facilitated by electronic coupling between the carbazole units.

3.2.5 Quantum computational analysis of C-C D

Vertical excitation energy calculations performed at the CAM-B3LYP-D3/6-311+G(d,p) level reveal the presence of multiple low-lying triplet excited states in **C-C D** (Tables A3.4 and A3.5). Notably, a small singlet-triplet energy gap (ΔE_{ST} = 0.13 eV) between the lowest singlet excited state (S_1) and a higher-lying triplet state (T_5) is observed, which is expected to promote efficient and rapid ISC (Figure A3.14).

In addition, SOC calculations yield a relatively large coupling constant of 0.5713 cm^{-1} for the S_1-T_5 transition, which is remarkable for a purely organic, non-heavy-atom system. The enhanced SOC strength provides further support for the experimentally observed fast ISC process in **C-C D** (Table A3.6). Following ISC, the population in the T_5 state is expected to undergo rapid internal conversion (IC) to the lowest triplet state (T_1). Subsequently, radiative decay from T_1 to the ground state (S_0) gives rise to room-temperature phosphorescence (RTP). Consistent with this assignment, the calculated SOC matrix element for the T_1-S_0 transition (V_{SOC} = 0.1575 cm^{-1}) is sufficiently

large to enable spin-forbidden radiative decay, thereby supporting the experimentally observed RTP emission in **C-C D**.

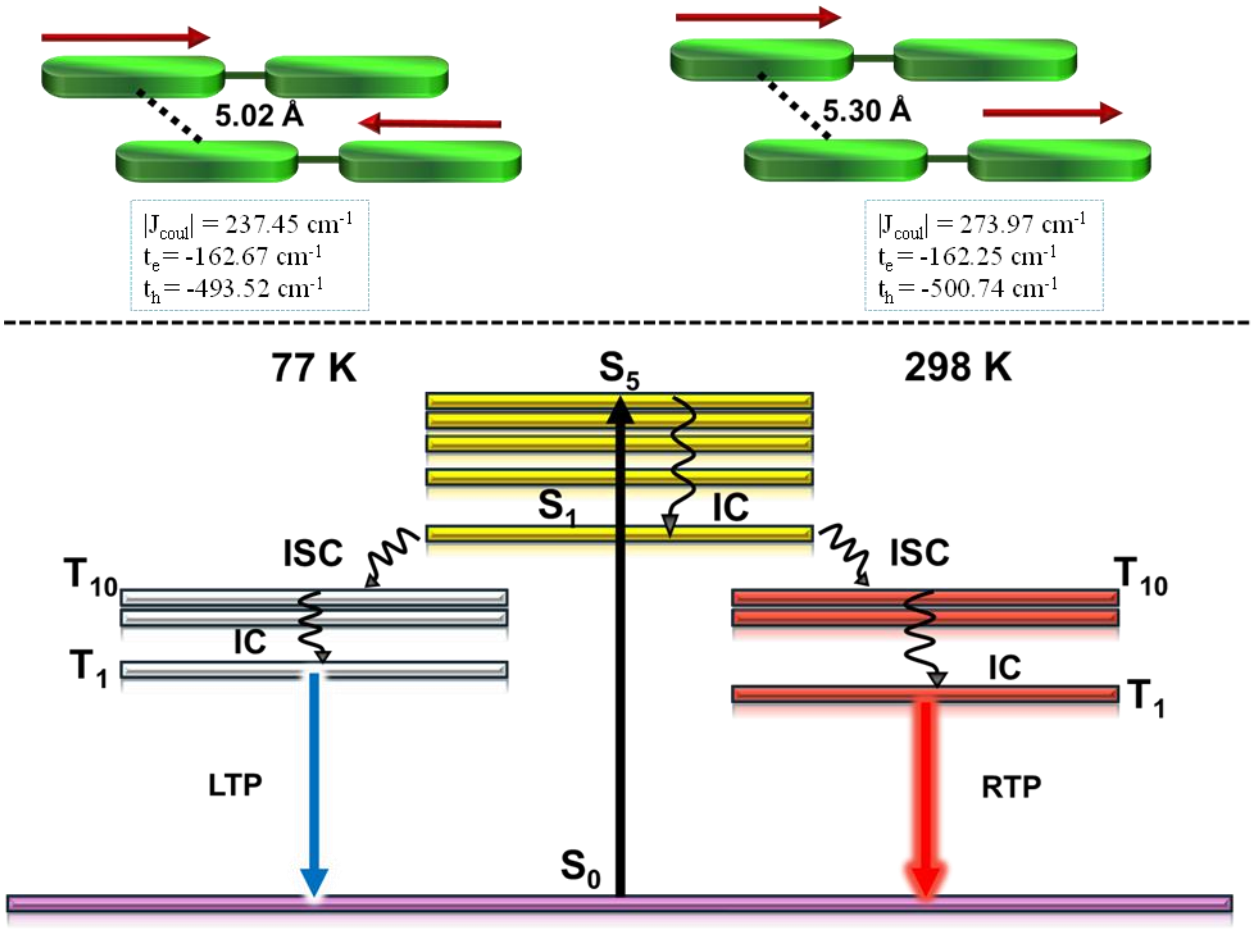

Figure 3.10: (Top) The interchromophoric separation and the calculated excitonic coupling values, (Bottom) Jablonski diagram representing the possible deactivation pathways of CD@77 K (left) and at CD@298 K (right).

3.3. Conclusion

This work establishes that enforcing complete molecular planarization in a 3,3′-linked carbazole dimer fundamentally reshapes its excited-state landscape, enabling access to both delayed fluorescence in solution and efficient phosphorescence in the solid state without reliance on heavy atoms. The unusually high triplet population, quantified by a triplet quantum yield of 42.3%, together with a rapid intersystem crossing rate constant of k_{ISC} = 1.0 x 10^8 s^{-1}, underscores the effectiveness of planar C-C linkage in promoting singlet-triplet conversion through enhanced electronic coupling. In the crystalline phase, temperature-dependent structural analysis reveals non-negligible lattice variations, as evidenced by a relatively large linear thermal expansion

coefficient of 5.3×10^{-4} K^{-1}. Such thermally induced structural modulation is expected to influence intermolecular interactions and molecular conformations within the crystal, leading to corresponding changes in the excited-state potential energy landscape. These temperature-driven structural adjustments likely govern the observed evolution of phosphorescence, with higher temperatures permitting greater excited-state relaxation and lower temperatures restricting structural reorganisation. Consequently, the pronounced temperature dependence of the RTP emission can be attributed to changes in excited-state structural dynamics rather than intrinsic stabilisation of the triplet energy levels. This insight underscores the pivotal role of crystal lattice flexibility and thermally accessible structural relaxation pathways in regulating heavy-atom-free organic phosphorescence.

3.4. Experimental Section

3.4.1. Syntheses and Characterisation

Synthesis of N-hexyl carbazole: 190 mg of carbazole was dissolved in 25 ml of DMSO, and 50% NaOH solution was added dropwise until the colour of the solution changed to yellow. Add iodohexane, approximately 100 mL, to the reaction mixture and heat the solution for 12 hours at 90 °C.

^{1}H NMR *(500 MHz, 298K, CDCl3): δ 8.02 (d, 2H), 7.14-7.41 (m, 6H), 4.21-4.24 (m, 2H), 1.76-1.82 (m, 2H), 1.22 (t, 6H), 0.77-0.81 (t, 3H).*

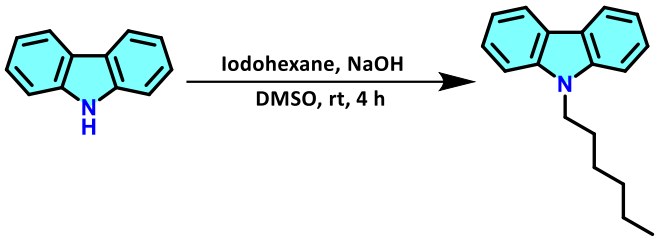

Scheme A3.1: Synthesis of N-hexyl carbazole

Synthesis of C-C D: To a stirred solution of 3.23 g of carbazole in 50 mL of CHCl3 under an Ar atmosphere, was added. 3.75 g of FeCl3 was added immediately under Ar conditions. After stirring at room temperature for 16 h, pour the reaction mixture into water and collect the organic layer. The organic layer is concentrated and purified using column chromatography (Hex/DCM/triethylamine = 80/20/1). Recrystallise the pure product using a hexane/dichloromethane mixture.

^{1}H NMR *(500 MHz, 298K, CDCl3): δ 8.34 (s, 2H), 8.11-8.13 (d, 2H), 7.75-7.77 (d, 2H), 7.35-7.44 (m, 8H), 4.26-4.29 (t, 4H), 1.83-1.86 (t, 4H), 1.24-1.28 (m, 12H), 0.80-0.81 (t, 3H).*

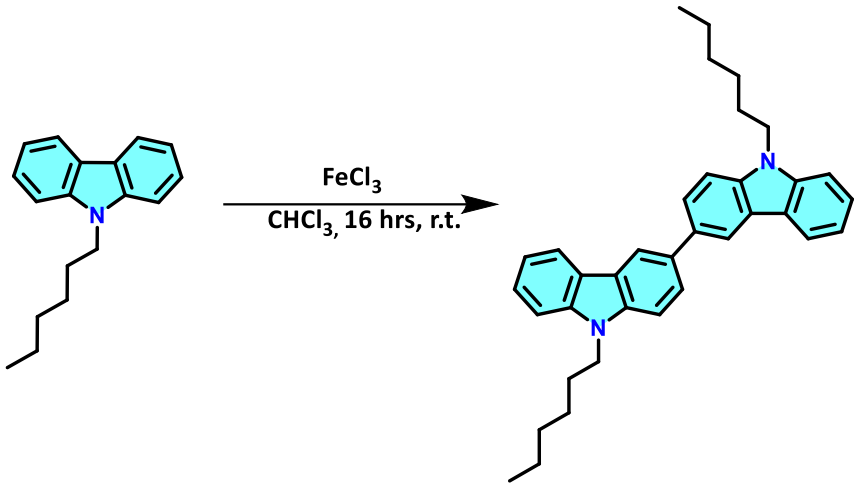

Scheme A3.2: Synthesis of C-C D.

3.5. Additional Figures and Tables

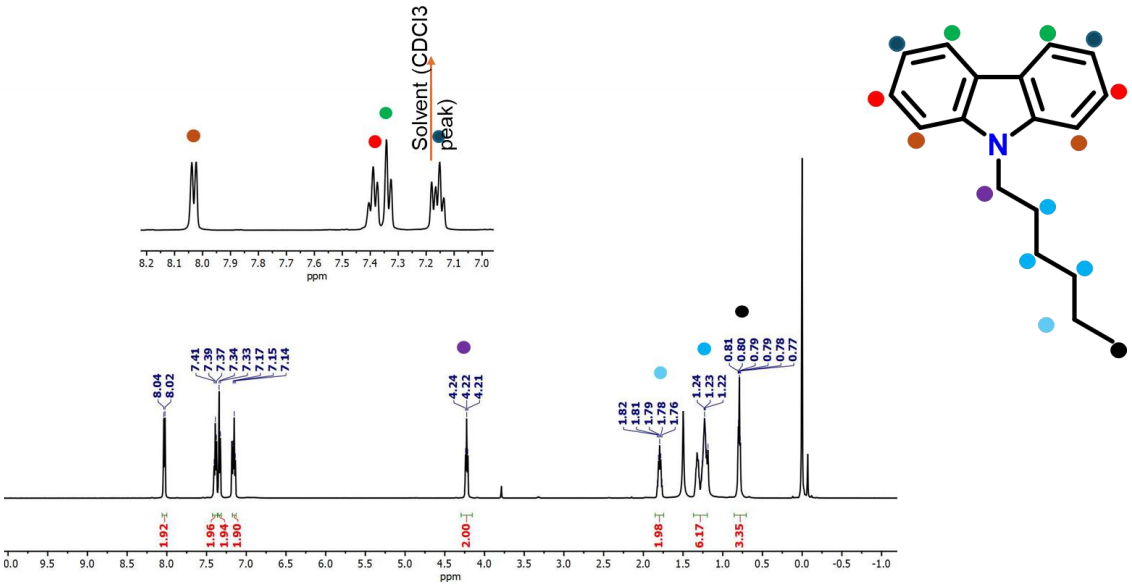

Figure A3.1: ^{1}H-NMR spectrum of N-hexyl **Cz** in $CDCl_3$.

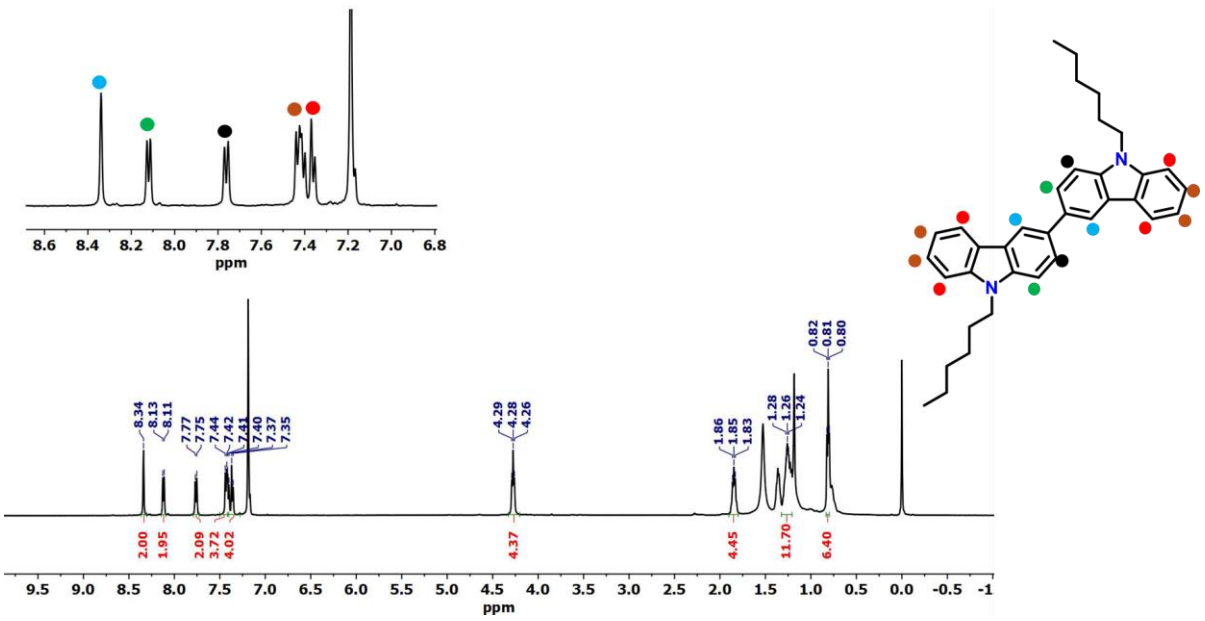

Figure A3.2: ^{13}H-NMR spectrum of **C-C D** in $CDCl_3$.

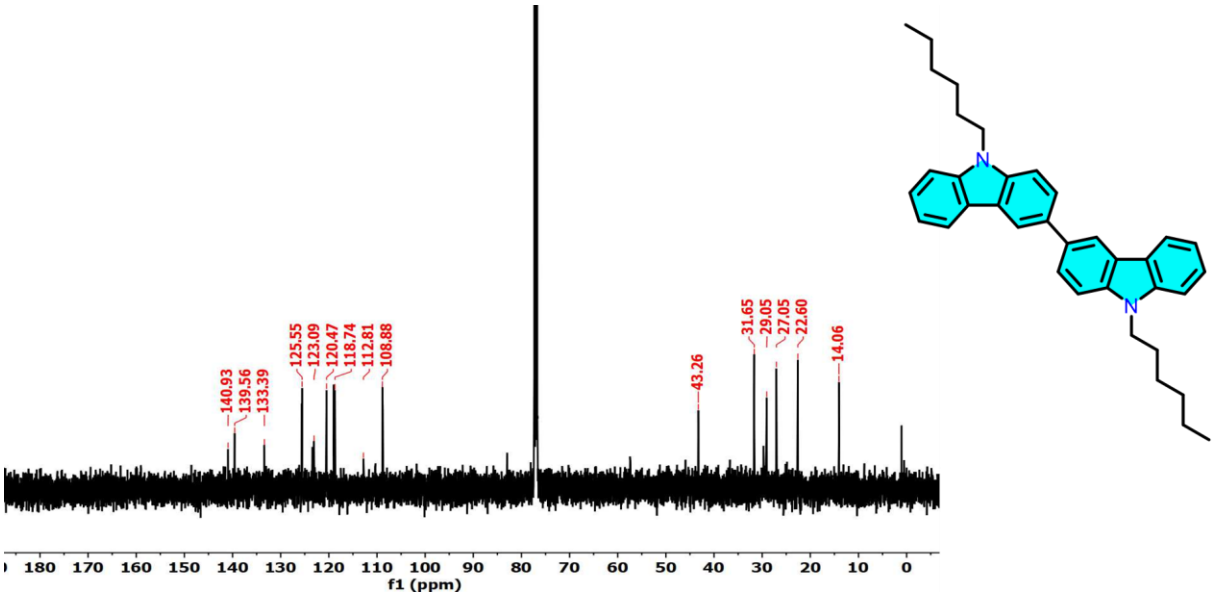

Figure A3.3: ^{13}C-NMR spectrum of **C-C D** in $CDCl_3$.

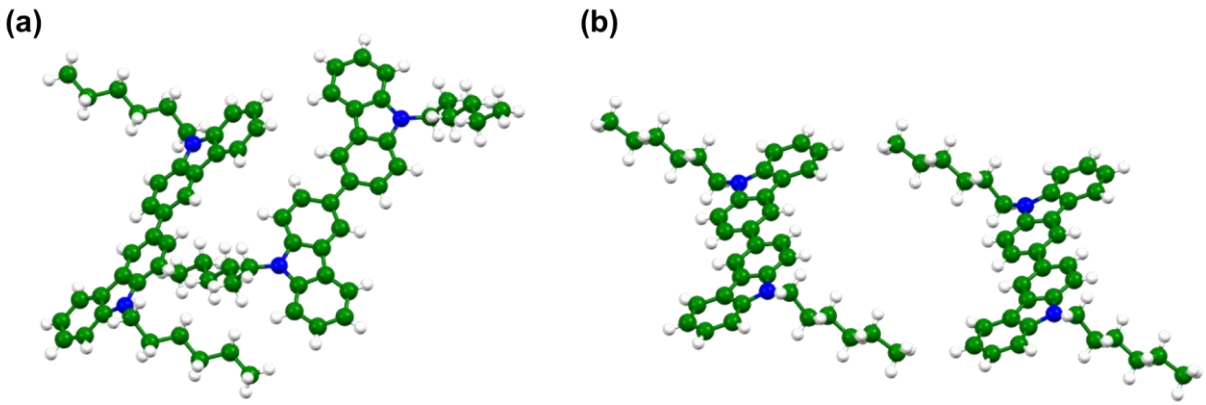

Figure A3.4: Isolated dimers of C-C D in the crystal packing (a) Dimer 1 and (b) Dimer 2**.**

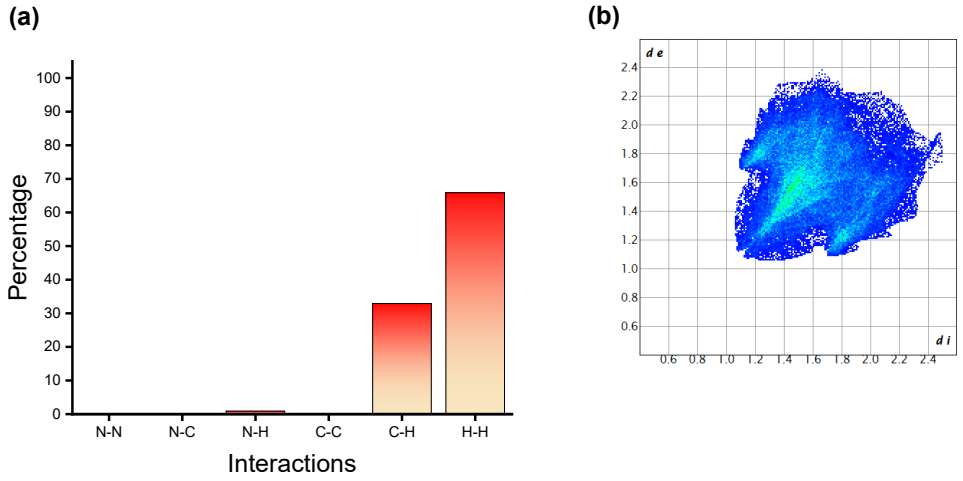

Figure A3.5: Hirshfeld surface analysis of C-C D (a) Percentage of interactions and (b) 2D fingerprint plot**.**

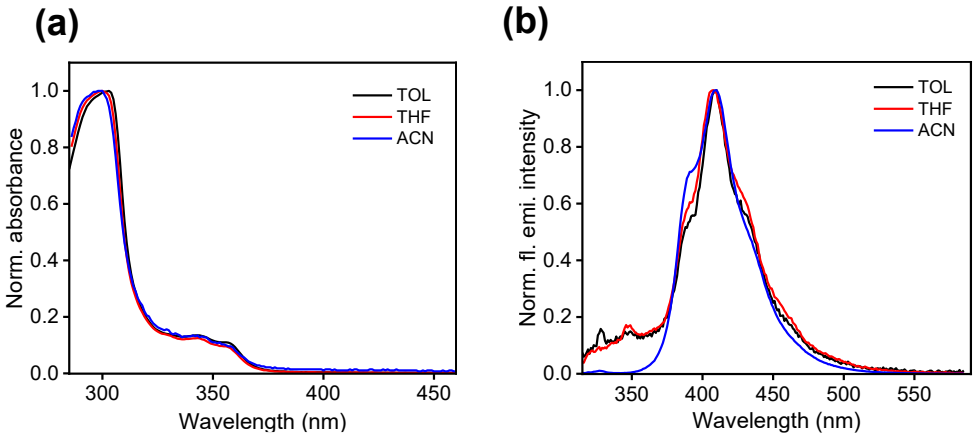

Figure A3.6: (a) Solvent-dependent UV-vis absorption spectra of C-C D (b) Solvent-dependent fluorescence emission spectra of C-C D.

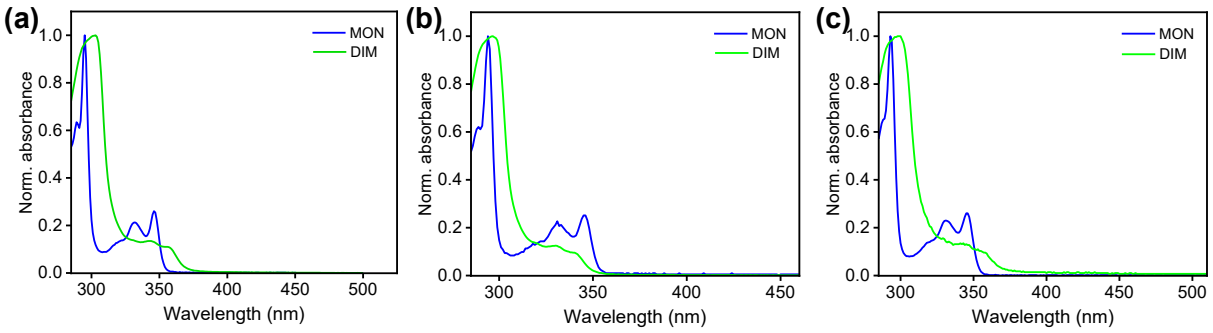

Figure A3.7: A comparison of UV-vis absorption spectra of monomer, N-hexyl Cz and C-C D in (a) TOL, (b) THF and (c) ACN.

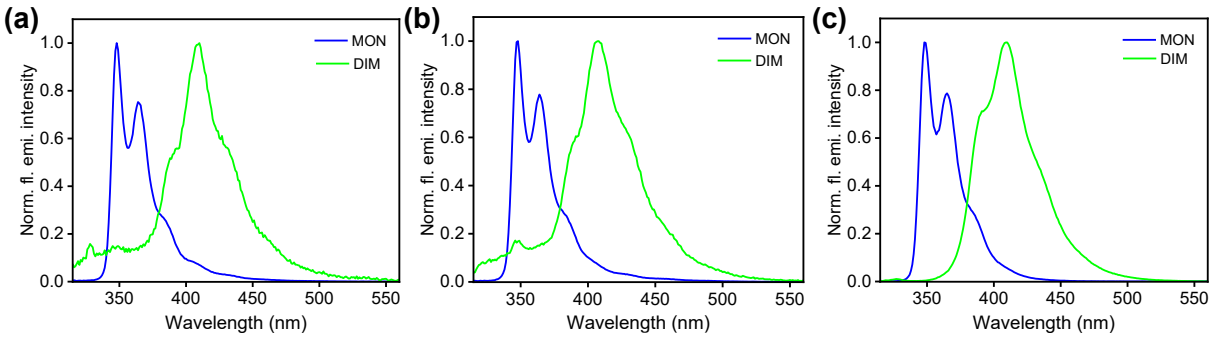

Figure A3.8: A comparison of fluorescence emission spectra of monomer, N-hexyl Cz and C-C D in (a) TOL, (b) THF and (c) ACN.

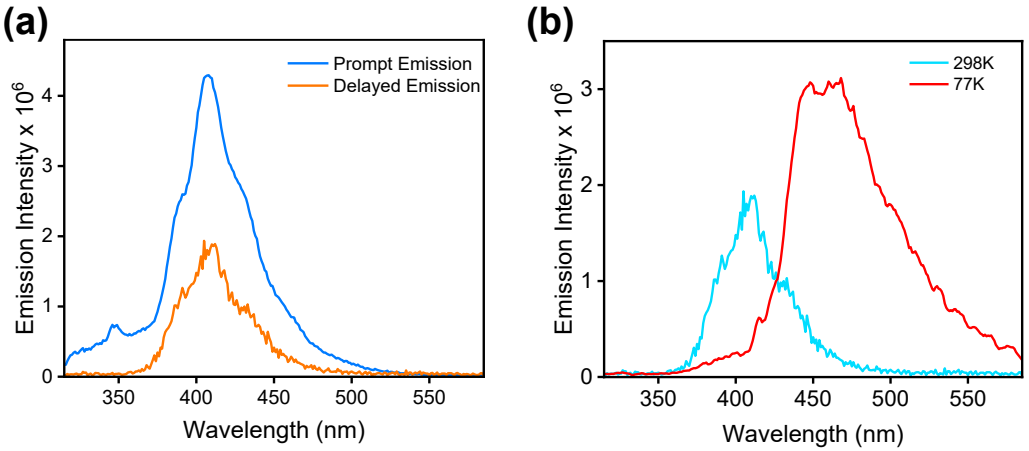

Figure A3.9: (a) Prompt and delayed emission of C-C D in THF at 298 K and (b) Delayed emission of C-C D in THF at 298 K and 77 K.

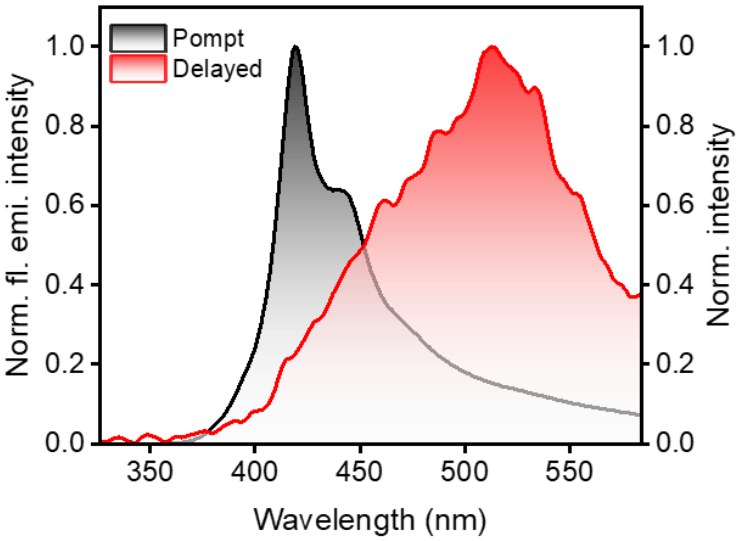

Figure A3.10. Prompt and delayed emission of C-C D in crystalline state at 298 K.

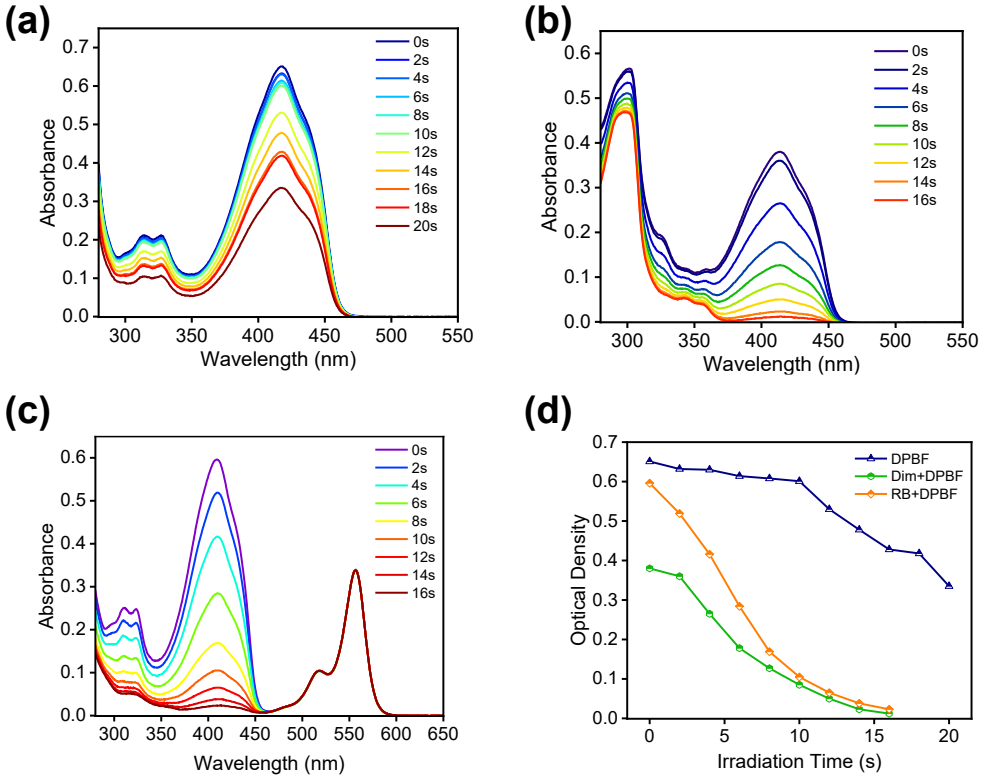

Figure A3.11: (a) Absorption and emission spectra of DPBF in DMF, (b) Absorption spectra of DPBF and C-C D mixture on different irradiation times, (c) Absorption spectra of DPBF and Rose Bengal on different irradiation times, (d) Absorbance-Time plot of DPBF, DPBF with Rose Bengal, and DPBF with C-C D.

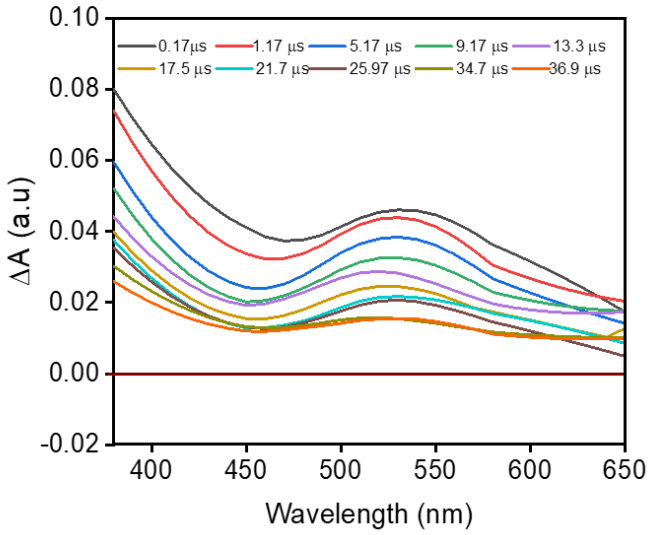

Figure A3.12: The nsTA spectra of (a) C-C D in N_2 purged THF solution.

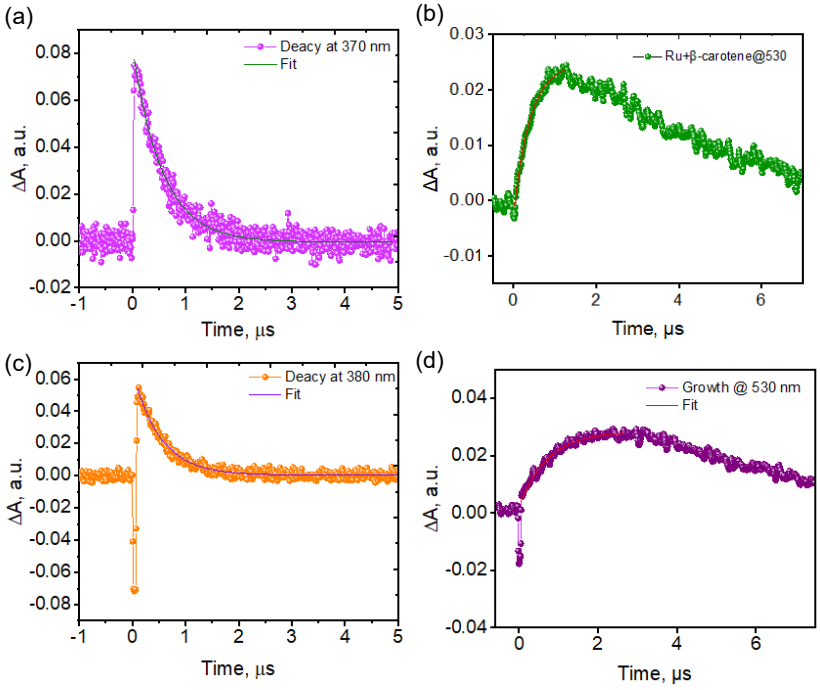

Figure A3.13: (a). The nsTA of $[Ru(bpy)_3]^{2+}$ showing its triplet decay at 370 nm, (b) The triplet growth of a mixture of β-carotene and $[Ru(bpy)_3]^{2+}$ in methanol, confirming the TTET from $[Ru(bpy)_3]^{2+}$ to β-carotene, (c) The triplet decay profile of C-C D at 380 nm and (d) the triplet growth of a mixture of C-C dimer and β-carotene in THF.

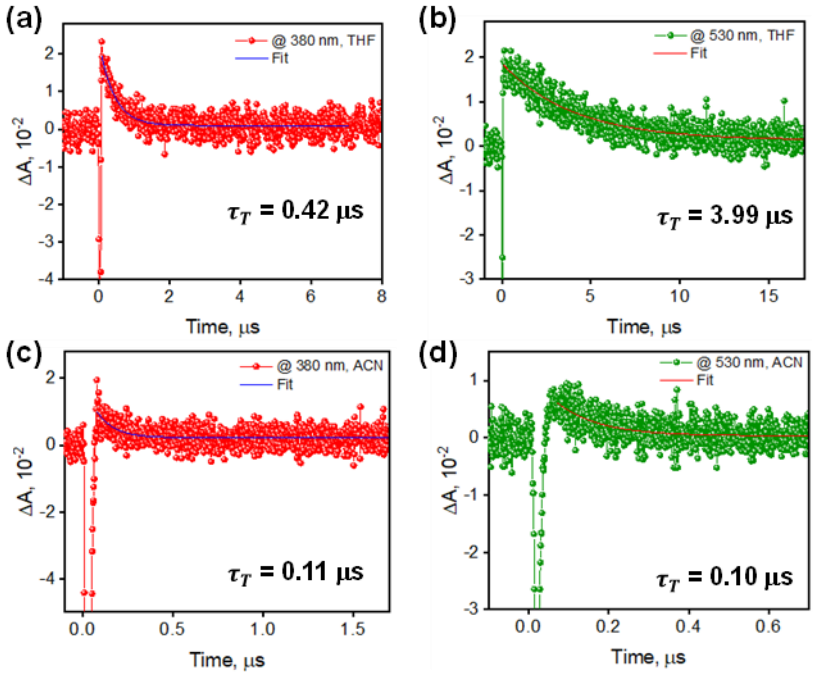

Figure A3.14: Decay profile of C-C D in N_2-purged solution of THF (a) at 380 nm, (b) at 530 nm and in ACN (c) at 380 nm and (d) at 530 nm.

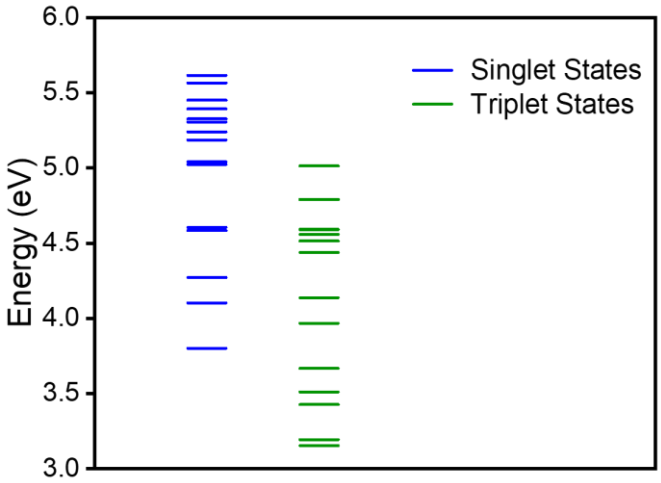

Figure A3.15: Vertical excitation energies of C-C D at CAMB3LYP-D3/6-311g++(d,p) level of theory.

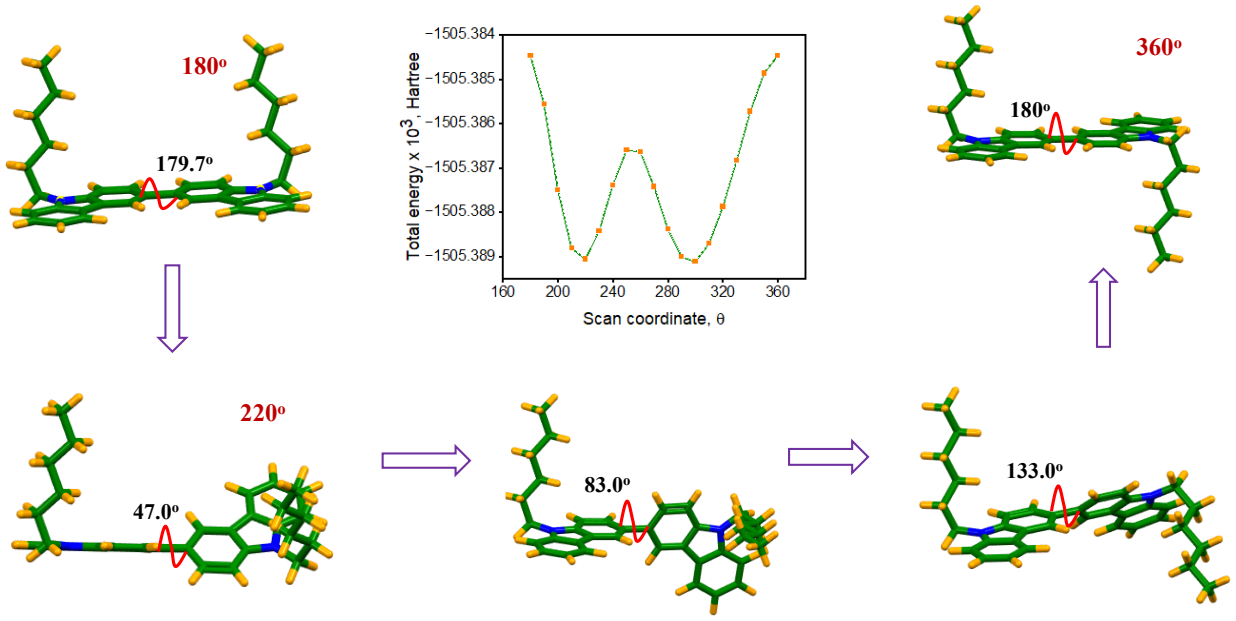

Figure A3.16: The Potential energy scan analysis of C-C D.

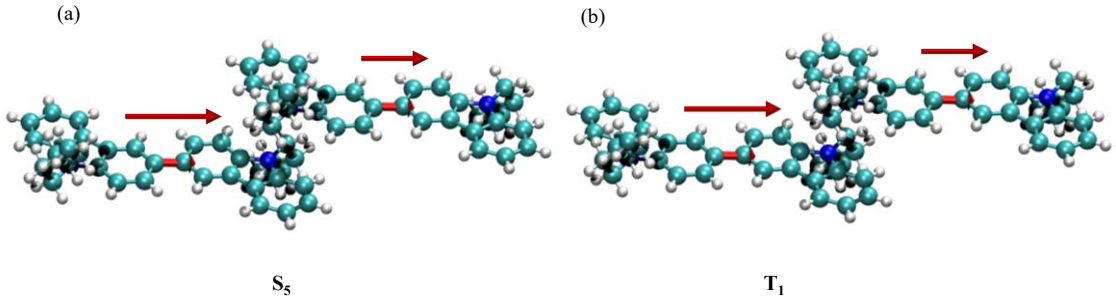

Figure A3.17: Transition dipole moment (TDM) vector aligned in a similar magnitude and direction for the (a) S5 and (b) T1 states of the crystal aggregate of CD at 298 K coordinates.

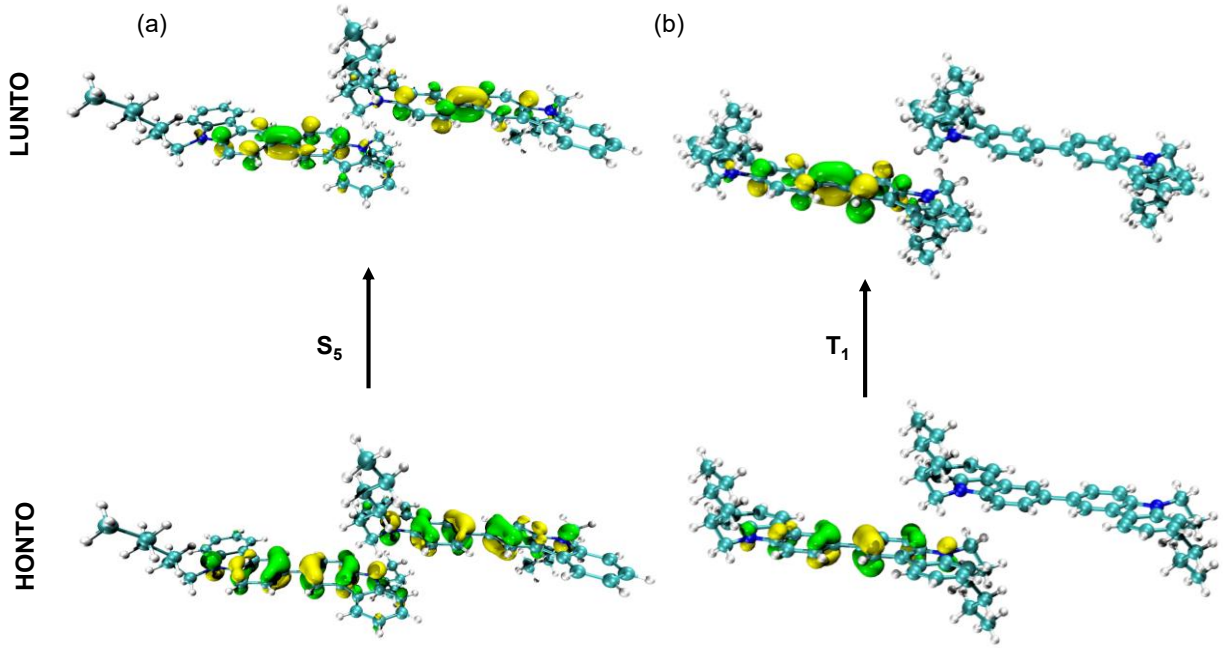

Figure A3.18: The NTO analysis of C-C D for (a) S5 and (b) T1 state.

Table A3.1: Unit cell analysis of C-C D at 298 K

298 K	
Space group	*P2₁/c*
Cell lengths	a = 9.50 Å b = 13.73 Å c = 11.12 Å

Cell angles	α = 90.00° β = 97.90° γ = 90.00°
Cell volume	1437.21 Å³

Table A3.2: Unit cell analysis of C-C D at 77 K.

77 K	
Space group	*P2₁/c*
Cell lengths	a = 9.10 Å b = 14.84 Å c = 11.98 Å
Cell angles	α = 90.00° β = 98.63° γ = 90.00°
Cell volume	1384.06 Å³

Table A3.3: Isolated dimers used for SAPT(0) calculations.

Geometry	Electrostatic Energy (KJ/mol)	Exchange Energy (KJ/mol)	Induction Energy (KJ/mol)	Dispersion Energy (KJ/mol)	Total Energy (KJ/mol)
Dimer 1	-15.847	37.161	-4.857	-78.237	-61.780
Dimer 2	-2.809	7.334	-0.554	-11.128	-7.158

Table A3.4: Vertical excitation energies computed at the ground-state optimized geometry of **C-C D** (CAM-B3LYP-D3/6-311G+(d,p) level of theory) in vacuum.

Singlet State	Energy (eV)	Oscillator Strength (f)
S_1	3.80	0.00
S_2	4.10	0.07
S_3	4.27	0.62
S_4	4.58	0.00
S_5	4.60	1.41
S_6	5.02	0.00
S_7	5.04	0.00
S_8	5.18	0.03
S_9	5.24	0.00
S_{10}	5.30	0.20
S_{11}	5.33	0.11
S_{12}	5.39	0.004
S_{13}	5.45	0.00
S_{14}	5.56	0.36
S_{15}	5.61	0.00

Table A3.5: Vertical excitation energies computed at the ground-state optimised geometry of **C-C D** (TDA-CAM-B3LYP-D3/6-311G+(d,p) level of theory) in vacuum.

Triplet State	Energy (eV)
T_1	3.15
T_2	3.19
T_3	3.43
T_4	3.51

T_5	3.67
T_6	3.97
T_7	4.14
T_8	4.44
T_9	4.51
T_{10}	4.56
T_{11}	4.589
T_{12}	4.59
T_{13}	4.789
T_{14}	4.79
T_{15}	5.01

Table A3.6: S_1-optimised SOC calculation of C-C D at CAMB3LYP-D3/6-311-G+(d,p) level of theory.

C-C D	
$\langle S_0\|Hso\|T_1\rangle$	0.1575
$\langle S_0\|Hso\|T_2\rangle$	0.0543
$\langle S_0\|Hso\|T_3\rangle$	0.5518
$\langle S_0\|Hso\|T_4\rangle$	0.4657
$\langle S_0\|Hso\|T_5\rangle$	0.4690
$\langle S_0\|Hso\|T_6\rangle$	0.4136
$\langle S_0\|Hso\|T_7\rangle$	0.4637
$\langle S_0\|Hso\|T_8\rangle$	0.3029
$\langle S_0\|Hso\|T_9\rangle$	1.0865
$\langle S_0\|Hso\|T_{10}\rangle$	0.7723

$\langle S_1\|Hso\|T_1\rangle$	0.0315
$\langle S_1\|Hso\|T_2\rangle$	0.0152
$\langle S_1\|Hso\|T_3\rangle$	0.1023
$\langle S_1\|Hso\|T_4\rangle$	0.4787
$\langle S_1\|Hso\|T_5\rangle$	0.5713
$\langle S_1\|Hso\|T_6\rangle$	0.1129
$\langle S_1\|Hso\|T_7\rangle$	0.0103
$\langle S_1\|Hso\|T_8\rangle$	0.0300
$\langle S_1\|Hso\|T_9\rangle$	0.0063
$\langle S_1\|Hso\|T_{10}\rangle$	0.0090

3.6. Appendix

3.6.1. Materials and Methods

Detailed information regarding the materials and methods used is given in section 2.6.1.

3.6.2. X-ray Crystallography

High-quality crystals of **C-C D** with appropriate dimensions were selected for the X-ray diffraction experiments. The crystallographic data collected are presented in the Supporting Information, Table S1. A single crystal was mounted using oil (Infineum V8512) on a glass fibre. All measurements were made using a CCD area detector with graphite-monochromated Mo Kα radiation. The data was collected using a Bruker APEXII detector and processed using APEX2 from Bruker. The structure was solved by the direct method and expanded using the Fourier technique. The non-hydrogen atoms were refined anisotropically. Hydrogen atoms were included in idealised positions, but not refined. Their positions were constrained relative to their parent atom using the appropriate HFIX command in SHELX-97.3. All programs used during the crystal structure analysis are incorporated in the WINGX software. 4, 5 The full validation of the CIF and structure factor was performed using the checkCIF utility and found to be free of major alert levels.

3D structure visualisation and the exploration of the crystal packing were carried out using Mercury 3.10.1.

We also performed temperature-dependent crystallographic analysis, and the observations are as follows.

Arithmetic & simple metrics

V (298 K) = 1437 Å³ → V (77 K) = 1387 Å³

Absolute change ΔV = 1437 − 1387 = 50 Å³.

Fractional change = 50 / 1437 = 0.0348 = 3.48% volume decrease.

Temperature change ΔT = 77 − 298 = −221 K.

Volumetric thermal expansion coefficient (approximate, using average V):

$$\beta = \frac{\Delta V}{V\,\Delta T}$$

$$= \text{-}50/1437 \text{ x } (\text{-}221)$$

$$= 1.60 \text{ x } 10^{-4}\ K^{-1}$$

Convert to an effective linear thermal expansion (≈ β/3):

$$\propto_{linear} = \frac{\beta}{3} = 5.3 \text{ x } 10^{-5}$$

3.6.4. Computational Analysis

All the computational investigations were carried out in the Gaussian 16 software package.[162] Ground-state geometry optimisation in vacuum and solvents (IEFPCM model) and rigid PES scan was performed at B3LYP-D3/6-311+G(d,p) level of theory. The FMOs were obtained from the generated cube files of energy calculations. Vertical excitation energies along with oscillator strengths were obtained using time-dependent density functional theory (TDDFT) calculations at the CAM-B3LYP-D3/6-311+G(d,p) level. Geometry optimisation of the first singlet excited state (S1) was carried out using the CAM-B3LYP-D3 functional and the 6-31G basis set (a smaller basis set was employed to reduce computational cost and avoid convergence failure).

3.6.4. Femtosecond Transient Absorption (fsTA) Measurement

The detailed fsTA instrumentation and experimental methods are provided in Section *2.6.9.*

3.6.5. Nanosecond Transient Absorption (nsTA) Measurement

An Applied Photophysics Model LKS-60 laser kinetic spectrometer was used for the nanosecond laser flash photolysis experiments in THF and ACN. The fundamental pulse of 710 nm from the Quanta Ray INDI-40-10 series pulsed Nd:YAG laser was converted into its second harmonic (355 nm, pulse duration ≈approximately 10 ns) and used to excite the samples.

3.6.6. Global Analysis

Global analysis of the fsTA data was performed using Glotaran software and is detailed in Section *2.6.10.*

3.6.7. Triplet Quantum Yield (ϕ_T) Measurements

To determine the triplet quantum yield (ϕ_T) of **PDI-T**, a method involving triplet-triplet energy transfer to β-carotene was employed, using $[Ru(bpy)_3]^{2+}$ as a reference compound with a known ϕ_T of approximately 1, as reported in the literature.[119] Equal volumes of β-carotene dissolved in $CHCl_3$ were added to optically matched solutions of $[Ru(bpy)_3]^{2+}$ in methanol and **PDI-T** in TOL, THF, and ACE, each adjusted to have an absorbance between 0.1 and 0.2 at 532 nm. Upon excitation, both $[Ru(bpy)_3]^{2+}$ and **PDI-T** were capable of transferring triplet energy to β-carotene, leading to the formation of its triplet excited state, which was monitored at 530 nm. The triplet quantum yields for **PDI-T** were calculated using a standard equation, where the superscripts "Sam" and "Ref" refer to the sample (**PDI-T**) and the reference ($[Ru(bpy)_3]^{2+}$), respectively. Here, k_{obs} represents the pseudo-first-order rate constant for β-carotene triplet growth, while k_0 denotes the decay constant of the donor triplet state in the absence of β-carotene, with both measurements taken from solutions having identical absorbance.

$$\phi_T^{Sam} = \phi_T^{Ref} \times \frac{\Delta A^{Sam}}{\Delta A^{Ref}} \times \frac{k_{obs}^{Sam}}{k_{obs}^{Sam} - k_0^{Sam}} \times \frac{k_{obs}^{Ref} - k_0^{Ref}}{k_{obs}^{Ref}} \quad \text{(Eq 3.1)}$$

3.6.8. NMR Analysis

Solid-state ^{13}C cross-polarisation magic-angle spinning (CP-MAS) NMR and ^{1}H MAS NMR spectra were recorded using a Bruker NEO solid-state NMR spectrometer operating at a magnetic field strength corresponding to a ^{1}H Larmor frequency of 500 MHz. Measurements

were carried out using a 3.2 mm double-resonance MAS probe at two different sample temperatures, approximately 25 °C and −25 °C, to examine temperature-dependent changes in the local electronic environment.

Magic-angle spinning was performed at 12 kHz to efficiently average anisotropic interactions and improve spectral resolution. Cross-polarisation was employed for 13C detection to enhance signal sensitivity through polarisation transfer from abundant ^{1}H nuclei. Chemical shifts (δ) are reported in parts per million (ppm), referenced according to standard conventions.

Chapter 4

3D Electron Diffraction Reveals the Structural Origin of Delayed Dual Emission in a Heavy-Atom-Free Carbazole Hexamer

Abstract

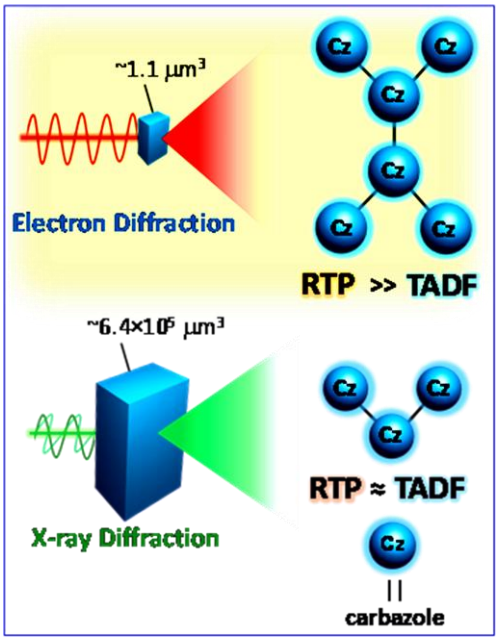

The coexistence of TADF and RTP offers a powerful yet rarely realised strategy for harvesting triplet excitons in purely organic materials. However, the understanding of the structural factors governing such delayed dual emission remains limited. Here, we unveil the structure-property correlation in a spacer- and heavy-atom-free carbazole hexamer (**Cz-H**) by utilising three-dimensional electron diffraction and ultrafast time-resolved spectroscopy. Remarkably, in solid-state **Cz-H** exhibits a phosphorescence-dominated delayed dual emission, in contrast to its reference trimer (Cz-T), which displays an equitable TADF-RTP. Despite its micro-crystalline nature (~5.7×10^5 times smaller crystal volume than Cz-T) arising from a nonplanar aromatic framework, the molecular packing of **Cz-H** was successfully resolved using 3D ED. The analysis reveals a rigid supramolecular network reinforced by C-H···π interactions, which likely suppresses nonradiative decay, facilitating triplet generation. Femtosecond and nanosecond transient absorption spectroscopy confirm enhanced ISC in **Cz-H** ($k_{ISC}^{Cz-H} > k_{ISC}^{Cz-T}$). Quantum-chemical calculations further indicate a 7.8-fold increase in spin-orbit coupling in Cz-H compared to Cz-T, with a significant reduction in ΔE_{ST} from 22.6 meV (Cz-T) to 8.5 meV (**Cz-H**). These findings demonstrate that 3D ED provides direct structural insights, enabling the correlation between molecular packing-induced supramolecular rigidity and triplet generation in organic emitters.

4.1. Introduction

A precise understanding of molecular structure is crucial for deciphering the excited-state properties of organic chromophores and advancing the design of next-generation photofunctional materials. The spatial arrangement of molecules and their intermolecular interactions often dictates the excited-state dynamics, thereby governing processes such as fluorescence,[179] phosphorescence,[50] and thermally activated delayed fluorescence (TADF).[180] Pioneering contributions by Adachi and co-workers have established diverse chromophoric systems that exhibit remarkable emissive behaviours, enabling efficient organic light-emitting diodes (OLEDs).[181–183] However, establishing a direct and quantitative correlation between molecular packing, electronic structure, and the resulting optical and excited-state phenomena remains a major challenge. The observed challenge is further intensified when moving from simple monomeric units to larger, more complex chromophoric assemblies.[184,185] As molecular size, nonplanarity, and conformational flexibility increase, obtaining high-quality single crystals suitable for conventional single-crystal X-ray diffraction (SCXRD) becomes increasingly difficult, thereby limiting structural insights. In such cases, 3D ED has emerged as a powerful alternative technique, capable of resolving atomic-level structures from micro-crystalline samples.[186–189] The 3D ED enables a detailed exploration of structure-property relationships even for systems that elude conventional crystallographic approaches.[190]

From a photophysical perspective, efficient triplet harvesting remains one of the most critical and intriguing goals in organic optoelectronics.[3] Owing to spin statistics, charge recombination in OLED yields 25% singlet and 75% triplet excitons,[35,112] making the utilisation of the triplet manifold essential for achieving high device efficiencies.[45] Traditionally, this has been accomplished either by incorporating heavy atoms to promote intersystem crossing (ISC)[113,114] or by engineering donor-acceptor (D-A) architectures to facilitate reverse intersystem crossing (RISC).[65,67,191] However, such approaches often complicate the synthesis and may compromise material stability.

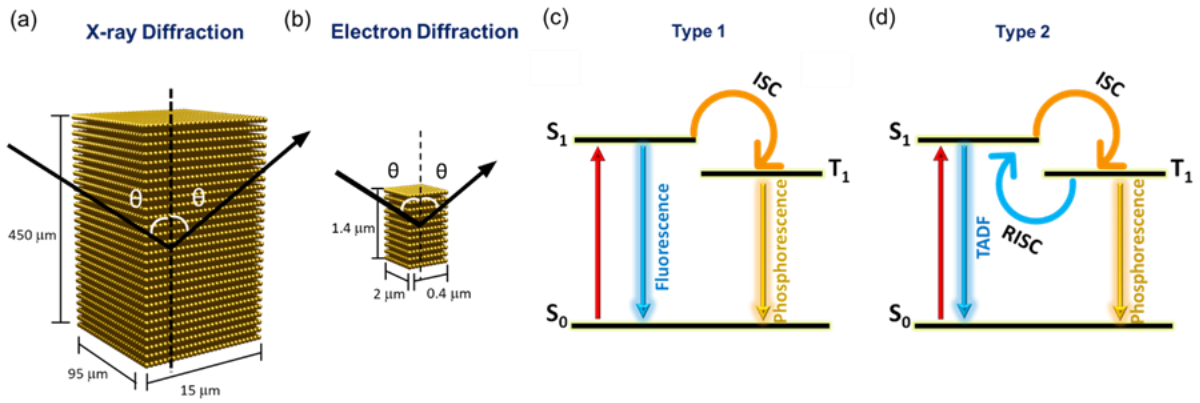

Scheme 4.1: Schematic representation of: (a) X-ray diffraction of Cz-T showing the crystal dimensions used for SCXRD; (b) Electron diffraction of Cz-H illustrating the crystal dimensions used for 3D ED; and Jablonski diagrams depicting two distinct dual-emission pathways in purely organic systems: (c) conventional fluorescence with phosphorescence, and (d) coexistence of TADF and RTP.

Recent research has increasingly focused on purely organic systems that exhibit dual delayed emission, characterised by the concurrent emission from both singlet and triplet excited states (Scheme 4.1).[191] Depending on the mechanism, dual emission can manifest as (i) fluorescence couples with phosphorescence or (ii) TADF coexisting with RTP.[192] While the former is relatively common, the latter remains rare because achieving both efficient RISC and prolonged RTP within a single molecular framework poses a formidable design challenge. Several pioneering contributions have addressed this particular challenge, achieving the dual emission from different molecular systems.[88,193,194] Notably, Lu and co-workers recently demonstrated a heavy-atom (Ag)-based D-A system combining triphenylamine and phenanthroline units, achieving simultaneous TADF and ultralong RTP.[84]

Herein, we report a unique example of dual delayed emission in a carbazole hexamer (Cz-H), exhibiting both TADF and RTP in a single organic chromophore devoid of heavy atoms, D-A character, or spacers. The molecular structure, elucidated through advanced 3D ED analysis, reveals how subtle packing and intermolecular interactions of the Cz-H govern the excited-state dynamics. Remarkably, the successful crystallographic resolution of hexamer (Cz-H), comprising six carbazole units linked directly, represents a significant advancement in understanding organic solid-state optical behaviour. The ability to obtain well-defined crystals of such a flexible and π-rich system underscores the supramolecular rigidity imparted by intermolecular interactions, which in turn enables efficient triplet generation and balanced dual emission.[45,102] Overall, this

work introduces a novel approach for generating triplets in purely organic frameworks, which has significant implications for guiding the rational design of high-performance optoelectronic materials.

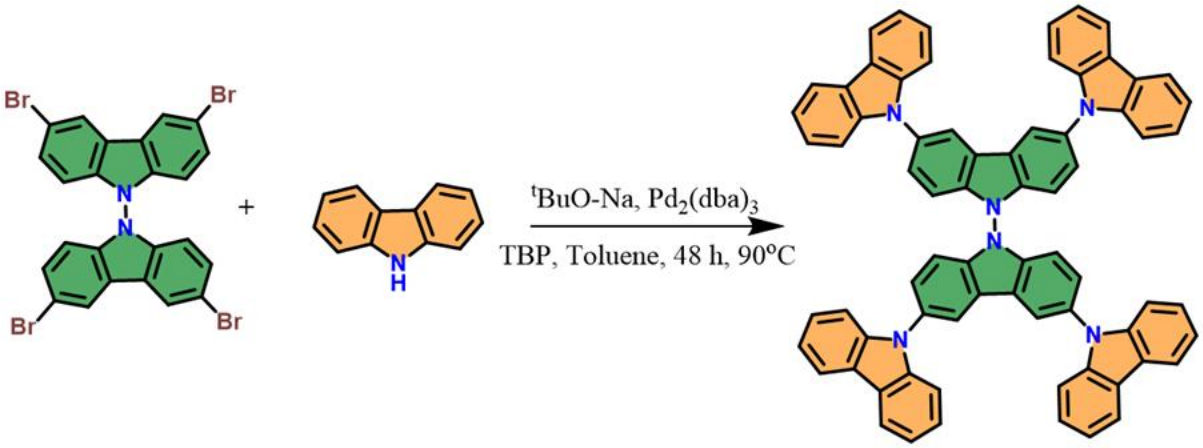

Scheme 4.2: Synthesis scheme of **Cz-H**.

4.2. Results and Discussion

4.2.1. Elucidating the molecular structure through 3D ED analysis

The synthesis of a novel carbazole hexamer (**Cz-H**), together with its trimeric reference compound (**Cz-T**), was accomplished following a modified literature protocol (Schemes 4.2 and A4.1).[195] Structurally, **Cz-H** can be regarded as a dimeric extension of **Cz-T** with N-N connectivity. High-quality single crystals of **Cz-T** were obtained through slow evaporation of a chloroform-hexane mixture at ambient temperature (Table A4.1). SCXRD analysis confirmed that **Cz-T** crystallises in the monoclinic space group $P2_1/c$ with cell parameters a = 17.59 Å, b = 20.13 Å, c = 8.88 Å, α = γ = 90.0°, β = 101.2° (Crystal size, mm^3: *15×95×450*, CCDC no. 2498405). Slow evaporation of a dichloromethane-hexane binary solvent mixture at ambient temperature yields micro-crystalline **Cz-H** (Table A4.2). The morphology of **Cz-H** was analysed by transmission electron microscopy (TEM, Figure S4), revealing a needle-like plate morphology with dimensions in the micrometre scale (Crystal size, mm^3: *2×1.4×0.4*, Table A4.3, Figure A4.7).

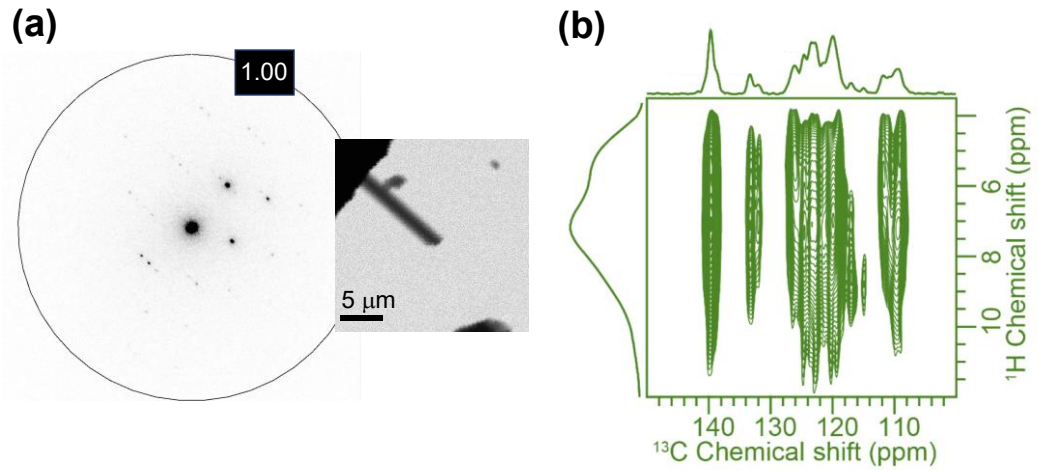

Figure 4.1: (a) The electron diffraction pattern obtained for Cz-H with the TEM image used for 3D ED measurement, and (b) The 2D $^{13}C\{^{1}H\}$ cross-polarisation heteronuclear correlation (CP HETCOR) NMR spectrum of Cz-H in solid-state obtained at a spinning rate of 60 kHz and a magnetic field of B_o = 14.1 T, utilizing natural isotopic abundance with a contact time of 5 ms.

Unlike the Cz-T, which readily afforded high-quality crystals suitable for SCXRD, the Cz-H could only be obtained as microcrystals, approximately 5.7 × 10^5 times smaller in volume, thereby hindering the use of conventional SCXRD techniques. To overcome this limitation, we employed 3D ED, which enables structural elucidation from crystals as small as a few hundred nanometers (Figure 4.1). Data collected on an ELDICO ED-1 diffractometer enabled the unambiguous resolution of both the molecular conformation and packing arrangement of Cz-H (CCDC no. 2493775). Cz-H crystallises in the monoclinic space group $P2_1/c$ with cell parameters a = 9.46 Å, b = 21.22 Å, c = 28.41 Å, α = γ = 90.0°, β = 95.17°. The asymmetric unit contains a single symmetrically independent molecule (Z′ = 1), corresponding to four molecules per unit cell (Z = 4). The molecular framework adopts an "X-like" geometry, in which two trimeric carbazole subunits are joined via a central N-N bond (torsional angle 70.39°). Within each trimeric subunit, the carbazole groups at the C-N junction exhibit torsional angles of 47.97°, 54.72°, 39.53°, and 54.99°. These values indicate a relatively rigid conformation compared to Cz-T, where the corresponding torsional deviations are larger

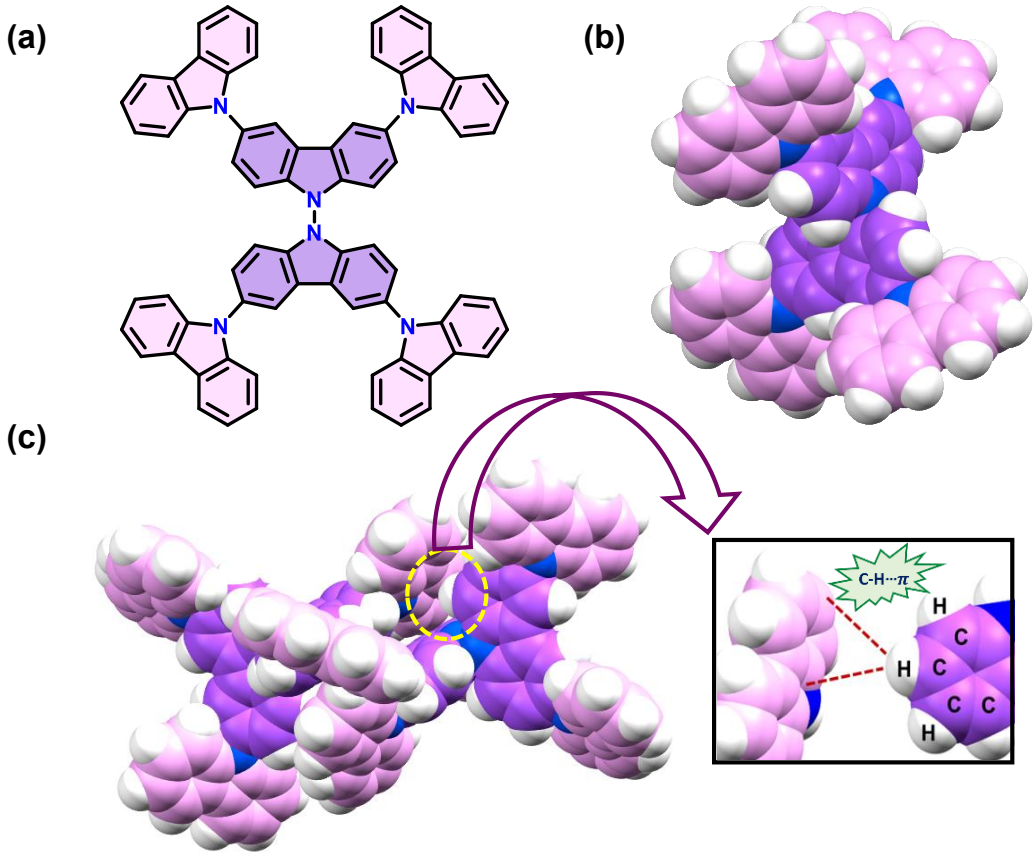

Figure 4.2: (a) Molecular structure of **Cz-H**, (b) Crystal structure of **Cz-H** in space-filled model, (c) Crystal packing of **Cz-H** with C-H···π interaction in a dimeric arrangement.

(57.41° and 69.05°, Figure S2a). Thus, Cz-H can be regarded as structurally more constrained, with reduced rotational freedom imposed by steric crowding at the C-N linkages. The root-mean-square deviation (RMSD) between the calculated and experimental solid-state NMR chemical shifts can be used as a primary metric for assessing the accuracy of the Cz-H structure. To address this, the Cz-H sample was further characterised by solid-state NMR as described below. The solid-state ^{1}H-^{13}C heteronuclear correlation (HETCOR) NMR spectrum of the carbazole hexamer, Cz-H, is shown in Figure 4.1b. All the protonated carbon atoms are observed in the ^{1}H-^{13}C HETCOR spectrum collected at the short contact time. The ^{13}C chemical shift assignments were made with the aid of the solution-state NMR spectra (Table A4.4 and Appendix 4.6.4).[196] From both solution and solid-state NMR data, it is evident that twelve distinguishable carbon sites are present. The chemical shifts of C1, C2, C3, C4, C4a, and C8b are observed at 110 ppm, 127 ppm, 132 ppm, 120 ppm, 122 ppm, and 141 ppm, respectively. In addition, the resonances corresponding to C9, C10, C11, C12, C12a, and C16b appear at 109 ppm, 127 ppm,

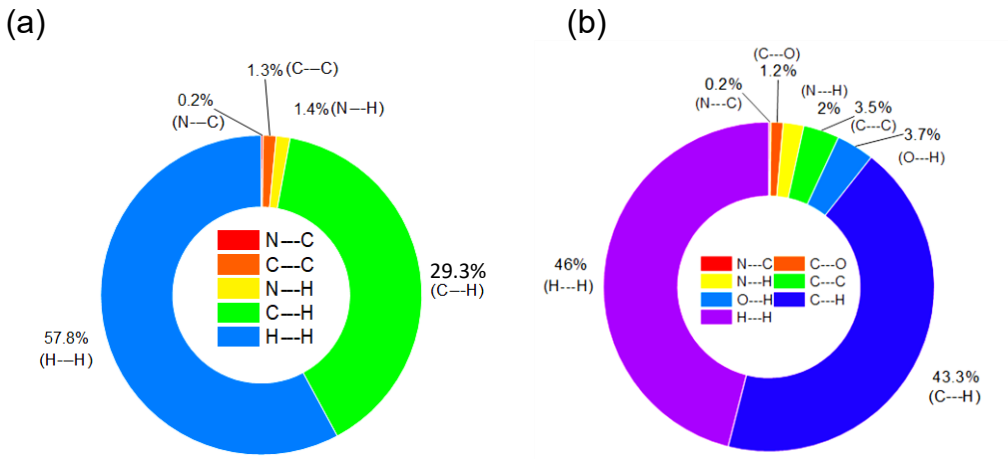

Figure 4.3: Quantified intermolecular interaction in (a) Cz-T and (b) Cz-H using Hirshfeld surface analysis.

120 ppm, 120 ppm, 123 ppm and 139 ppm, respectively (Table S4). Castep calculations were performed on the structure obtained from the 3D ED to predict the ^{13}C chemical shifts.[197–200] The RMSD between the calculated and experimental chemical shifts is 2.05 ppm, which is consistent with the values reported in the literature for the 3D ED NMR crystallography approach.[201,202] Packing analysis of Cz-H revealed limited but distinct π–π contacts, along with a network of weaker intermolecular interactions that stabilise the crystal lattice. Hirshfeld surface analysis provided a quantitative comparison of intermolecular interactions. For Cz-T, H···H contacts dominate (57.9%), followed by C-H···π contacts (39.3%, Figure A4.10), whereas Cz-H exhibits fewer H···H contacts (46%) and an increased proportion of C-H···π contacts (43.3%,). The observed redistribution reflects a denser and more heterogeneous packing environment in Cz-H, consistent with its more rigid C-N-linked architecture.[203–205] The enhanced rigidity and dense packing of Cz-H suppress non-radiative relaxation pathways, opening a more efficient triplet channel and thereby favouring RTP.[60]

4.2.2. Decoding the optical behaviour

The steady-state photophysical properties of the **Cz-H** were investigated in toluene (TOL, ε = 0.38) and compared with those of its reference trimer, **Cz-T.** The corresponding UV-vis absorption spectra are shown in Figure 4.4 (Table A4.5). **Cz-H** and its half-analogue **Cz-T** exhibited a distinct absorption band with maxima at λ_{max}^{Abs}= 341 nm and 344 nm, respectively. The low-energy band is attributed to an n → p* electronic transition, which is characteristically weak in intensity owing to its low oscillator strength. Additionally, a more intense high-energy

absorption band centred around 294 nm is observed for both **Cz-H** and **Cz-T**, corresponding to a p → p* transition associated with the conjugated carbazole framework.[19] The marginal blue shift observed for **Cz-H** is indicative of minimal electronic coupling between

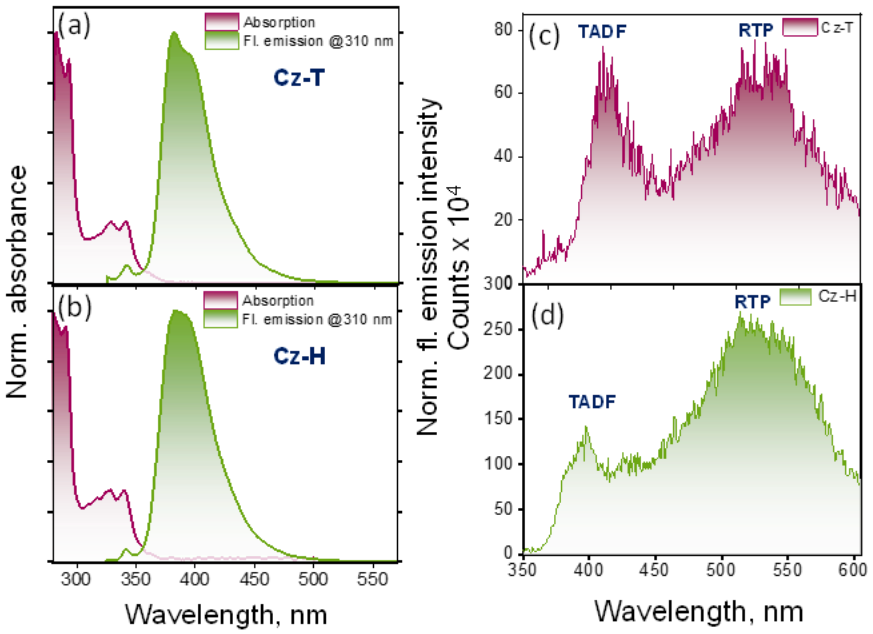

Figure 4.4: Normalised UV-vis absorption and fluorescence emission spectra of (a) Cz-T and (b) **Cz-H** in TOL, Solid-state delayed emission spectra of (c) Cz-T and (d) **Cz-H** at ambient temperature.

the trimeric units across the N-N linkage. These observations suggest that the N-N bond acts as an electronically insulating bridge, preventing effective p-conjugation extension and thereby preserving the localised electronic structure of each trimeric segment.[206,207] Furthermore, both **Cz-T** and **Cz-H** showed negligible solvatochromism in their absorption spectra across solvents of different polarities (Figure A4.11), suggesting that the ground-state electronic transitions are predominantly localised and minimally influenced by the surrounding dielectric environment.

Fluorescence emission spectra recorded at room temperature (RT) revealed pronounced differences between the **Cz-H** and its reference compound, **Cz-T**. Both **Cz-T** and **Cz-H** exhibited emission maxima at approximately λ_{max1}^{Fl} = 386 nm in TOL, indicating similar singlet excited-state energies. The fluorescence quantum yield (φ_{Fl}) of **Cz-T** in TOL, determined via the relative method, is φ_{Fl} = 33.3%, while **Cz-H** shows a lower value of φ_{Fl} = 16.0% under identical conditions. Additionally, **Cz-H** exhibits reduced vibronic resolution in its emission spectrum compared to **Cz-T** in TOL, suggesting greater conformational freedom or stronger excited-state

relaxation effects in **Cz-H** in its monomeric state/solution state.[208] The fluorescence quantum yield for both **Cz-H** and **Cz-T** systematically decreases with different solvent polarities, while the emission maxima remain essentially unchanged. The observed behaviour suggests that solvent polarity primarily modulates non-radiative decay rates, without significantly affecting the nature or energy of the emissive singlet state.[137,138] The negligible solvatochromism supports the conclusion that emission arises from a locally excited (LE) state.[19]

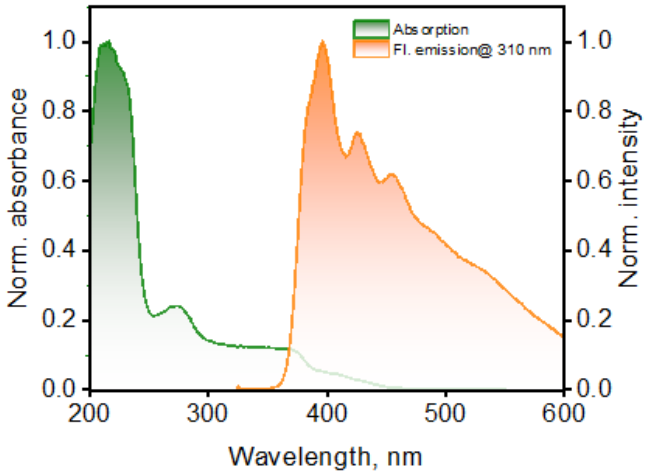

Figure 4.5: UV-vis absorption and fluorescence emission spectra in solid-state.

The UV-vis absorption and fluorescence emission properties of the **Cz-H** and the parent **Cz-T** were further examined in the solid state (Figure 4.5). Kubelka-Munk-transformed diffuse reflectance spectra displayed broad absorption features extending into the visible region for both **Cz-T** and **Cz-H**. The spectral broadening is indicative of enhanced vibronic coupling and possible intermolecular excitonic interactions in the solid phase, likely arising from close molecular packing and extended p-p interactions.[114] Compared to their solution-phase behaviour, the steady-state fluorescence emission spectra of the solid samples exhibited red-shifted maxima, with λ_{max}^{Fl}= 395 nm observed for both **Cz-T** and **Cz-H**. Notably, **Cz-H** displayed a significantly broader emission band in the solid state, a feature absent in both its solution-phase and the solid-state fluorescence emission spectra of **Cz-T** (Figures S11 and S12). The observed spectral broadening may be attributed to a distribution of emissive states (*vide infra*) arising from interchromophoric interactions within the hexameric framework in the solid matrix.[209] The absolute quantum yield of **Cz-H** was measured in the solid state, and a substantially lower value of 1.3% was observed. The pronounced difference in fluorescence quantum yields between the solution and solid states suggests possibly an efficient population transfer from the singlet to the triplet manifold in the

solid state. This process is likely facilitated by close molecular packing and intermolecular interactions that promote ISC.[210–212]

To probe the triplet-state contributions to the emission behaviour of **Cz-H** and its monomeric part **Cz-T**, steady-state delayed emission measurements were conducted under both ambient (Figures A4.12) and cryogenic conditions (Figures A4.13 and A4.14). Delayed photoluminescence arises from the population of triplet excitons, either via RISC, as TADF, or through direct radiative decay from the triplet state, characteristic of phosphorescence.[2,4] The delayed emission measurements provided direct insight into the participation of triplet states in the emission process.[4] At RT, both **Cz-H** and **Cz-T** exhibited delayed emission bands in TOL and in the crystalline state that closely mirrored their respective prompt fluorescence spectra, with maxima at λ_{max}^{Dl} = 397 nm. The experimentally determined singlet-triplet energy gaps ($DE_{S1\text{-}T1}$ of 0.51 eV for **Cz-H** and 0.42 eV for **Cz-T**) indicate a more efficient RISC process in **Cz-T** compared to **Cz-H**.[76,213–215] To rule out triplet-triplet annihilation (TTA) processes, delayed emission lifetimes were recorded at systematically varied excitation fluences. The observed dependence of the delayed emission lifetime on excitation intensity corroborates the assignment of the component to a monomolecular RISC process. In addition to the TADF band, the solid samples of both **Cz-H** and **Cz-T** displayed a broad, red-shifted delayed emission feature centred at ~543 nm and ~550 nm, respectively. These emissions extended up to ~650 nm for **Cz-H** and ~600 nm for **Cz-T**, and are attributed to RTP. The presence of both emission types confirms the existence of dual triplet-generating pathways in the solid state. Notably, **Cz-T** exhibits an equitable contribution from TADF and RTP (I_{RTP}:I_{TADF} = 0.98 ± 0.01, Figure 3c and Figure S16). At the same time, **Cz-H** shows dual emission with a dominant RTP component (I_{RTP}:I_{TADF} = 1.71 ± 0.20), suggesting that molecular rigidity in **Cz-H** enhances radiative decay from the lowest triplet state (Figure 3d and S17).

To further elucidate the origin of the triplet emissions, delayed emission spectra were recorded at 77 K in the solid state (Figures A4. 13 and A4.14). At cryogenic temperatures, the high-energy delayed emission (~400 nm) is completely quenched, as the lack of thermal energy suppresses RISC, thereby eliminating TADF (Figures S20). However, the broad, low-energy emission persisted in both **Cz-T** (λ_{max}^{Dl} ≈ 540 nm) and **Cz-H** (λ_{max}^{Dl}≈ 550 nm), unequivocally confirming its phosphorescent origin. Additionally, the phosphorescence lifetimes of **Cz-H** and **Cz-T** in the solid-state were measured, which support these findings. **Cz-T** showed a modest increase from τ_P = 530 µs (298 K) to τ_P = 650 µs (77 K, Table S7), whereas **Cz-H** exhibited a more pronounced increase from τ_P = 226 µs (298 K) to τ_P = 575 µs (77 K). These findings establish that both **Cz-T** and **Cz-H** display dual emissions characteristic of TADF and RTP at ambient conditions. The

transition from nearly equivalent TADF and RTP contributions in **Cz-T** to RTP-dominated emission in **Cz-H** likely originates from increased molecular rigidity induced by strong C–H···p interactions and efficient triplet-state stabilisation in the hexameric framework (*vide supra*). The activation energy for the RISC process in **Cz-T** and **Cz-H** was evaluated using the Arrhenius equation (Equation 4.1).[216–218] Based on the delayed emission intensities measured at 298 K and 77 K, the calculated activation energies are E_a = 12 meV for **Cz-T** and E_a = 39 meV for **Cz-H**. The lower activation energy for **Cz-T** suggested a more thermally accessible RISC process, supporting its comparable contributions from TADF and RTP pathways. In contrast, the higher energy barrier in **Cz-H** indicated a less efficient RISC pathway, consistent with its dominant role in RTP.

$$E_a = -k_B \cdot \frac{\left[ln\frac{I_2}{I_1}\right]}{\left[\frac{1}{T_1} - \frac{1}{T_2}\right]} \qquad \text{Equation 4.1}$$

4.2.3. Femtosecond Transient Absorption Measurements of Cz-T and Cz-H

To gain insights into the excited-state dynamics underlying the dual delayed emission behaviour of **Cz-H** and compare it with that of its reference compound **Cz-T**, femtosecond transient absorption (fsTA) spectroscopy was performed in TOL (Figure 4.6). Upon excitation at 330 nm with a 100-fs pump pulse, **Cz-T** displayed a broad, positive excited-state absorption (ESA) spanning 426-700 nm, with a maximum at 592 nm. The spectral profile is characteristic of singlet excited-state absorption in carbazole-based systems.[219] A gradual blue shift of the ESA maximum to 573 nm was observed over a few picoseconds, after which the signal remained nearly unchanged throughout the 3.5 ns temporal window. Global analysis of the fsTA data using a sequential A → B → GS (GS-ground state) model yielded evolution-associated spectra (EAS) with two distinct kinetic components (Figure 4.6b). The first component (A), assigned to the vibrationally hot singlet excited state, decayed with a lifetime of 7.8 ± 0.02 ps. The second component (B), attributed to the relaxed singlet excited state, exhibited a decay time that extended beyond the experimental window of 3.5 ns (Figure 4.6c), consistent with the fluorescence lifetime of **Cz-T** (4.8 ns).

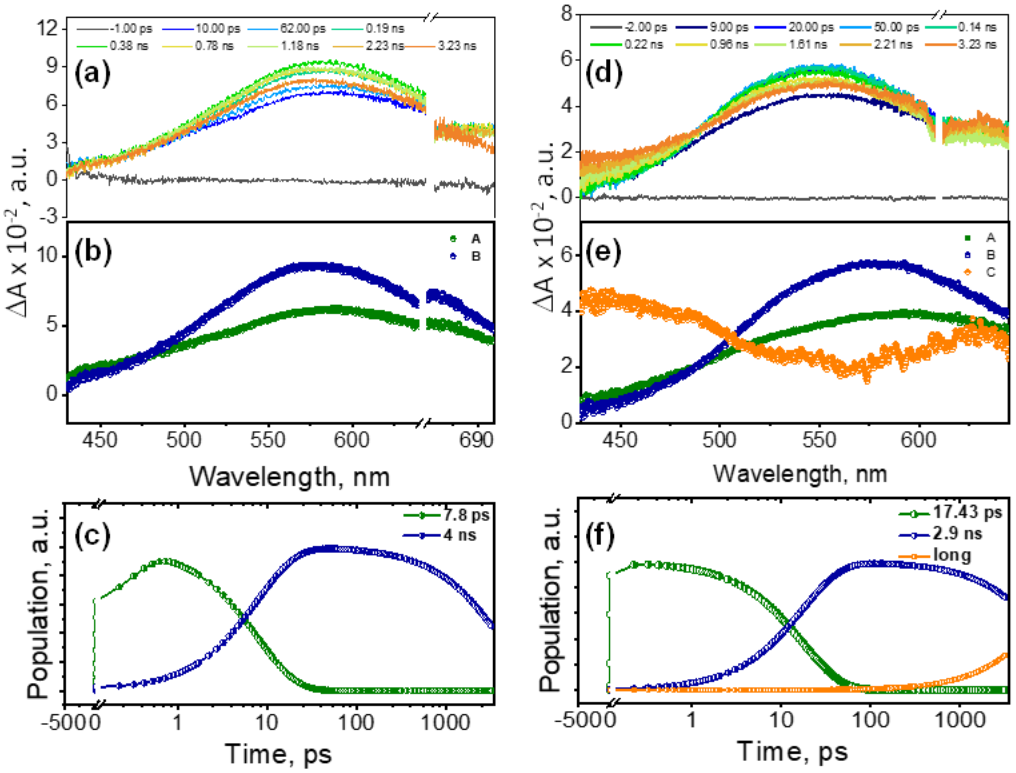

Figure 4.6: (a) Femtosecond transient absorption spectra of Cz-T in TOL, (b) Evolution associated spectra (EAS) of Cz-T obtained using the sequential A→B→GS model of Cz-T in TOL, (c) Kinetic evolution of EAS for Cz-H in TOL, (d) Femtosecond transient absorption spectra of Cz-H in TOL, (e) Evolution associated spectra (EAS) of Cz-H obtained using the sequential A→B→C→GS model of Cz-H in TOL, and (f) Kinetic evolution of EAS for Cz-H in TOL.

In contrast, **Cz-H** exhibited markedly different excited-state behaviour, evidenced by the appearance of a new species evolving over longer timescales. Upon identical excitation at 330 nm, the ESA spectrum of **Cz-H** initially resembled that of reference compound **Cz-T**, with a broad band from 426 to 700 nm and a maximum at 593 nm, which blue-shifted to 574 nm within a few picoseconds. Within a few nanoseconds, a significant growth at 420 nm could be observed in **Cz-H**, indicating the population of an additional excited state species, which remained populated throughout the experimental time window of 3.5 ns (Figure 4.6d). Global fitting using a sequential A → B → C → GS model revealed three kinetic components in **Cz-H**. The initial component (A), representing the vibrationally hot singlet state, relaxed to component B (the relaxed singlet state) with a lifetime of 17.4 ± 0.02 ps. The relaxed singlet state decays within 2.9 ± 0.03 ns, generating a long-lived species (component C) with a formation rate constant of k_{ISC} = 3.4 × 10^8 s^{-1}, which persists throughout the 3.5 ns time window (Figures 4.6e, 4.6f). The emergence of the new species, along with its spectral signature in the 420 nm region, is consistent with the formation of a triplet

excited state, as corroborated by previous analysis on carbazole derivatives.[108,152] The absence of the triplet feature at the fsTA window indicates a relatively slow intersystem crossing rate (k_{ISC}) in the reference compound **Cz-T**.

4.2.4. Unravelling the long-lived excited states through nanosecond transient absorption measurements

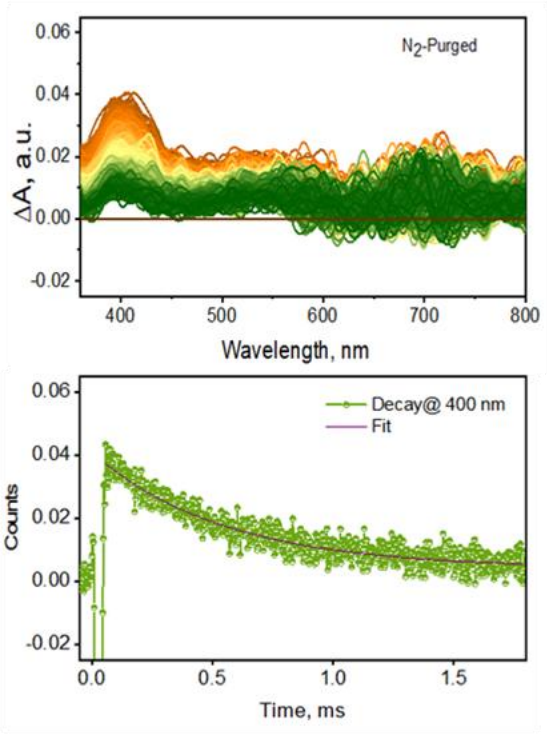

Figure 4.7: The nsTA (λ_{ex} = 355 nm) spectra (top), and the relative population profiles of the triplet excited state (bottom) of **Cz-H** in TOL.

Nanosecond transient absorption (nsTA) spectroscopy was used to investigate the long-lived excited-state species associated with the triplet manifold in **Cz-H** and compared with those of its monomer analogue **Cz-T** (Figure 4.7). Measurements were conducted in TOL at a concentration of 20 μM using 355 nm excitation with a pulse duration of ~10 ns. Under nitrogen-purged conditions, both **Cz-T** and **Cz-H** exhibited a prominent ESA band centred at 420 nm, which is assigned to the $T_1 \rightarrow T_n$ transition of the carbazole triplet state (Figure A4.15).[108] The triplet nature of the absorption band was confirmed through quenching experiments under oxygen-saturated conditions, where the 420 nm ESA band decayed rapidly due to efficient deactivation by molecular oxygen. Monoexponential fitting of the decay kinetics at 420 nm revealed triplet-state lifetimes of τ_T = 1.27 μs for **Cz-T** and τ_T = 0.67 μs for **Cz-H** (Figure A4.16). The shorter triplet

lifetime in **Cz-H**, despite its stronger RTP emission, may reflect a more efficient triplet-generating process facilitated by enhanced ISC and faster radiative decay from the triplet state.

4.2.5. Elucidating the excited-state landscape through quantum-chemical calculations

Quantum chemical calculations were performed using DFT at CAM-B3LYP-D3/6-311++G(d,p) level of theory to understand the ISC behaviour in **Cz-H** and its half analogue **Cz-T** in vacuum. Vertical excitation energies (VEEs) at the same level of theory reveal a significantly higher number of triplet states (T_1-T_{14}) below the lowest singlet excited state (S_1) in **Cz-H** (Tables A4.6-A4-9, n=14 states) compared to **Cz-T** (T_1-T_7, n=7 states), indicating a higher triplet density of states (DOS) in the hexamer (Appendix 4.6.12 1.12, Figure A4.17,). The elevated DOS is attributed to the increased electronic complexity of the larger conjugated framework in **Cz-H**. Although direct quantification of ISC rates based solely on triplet density is limited, Fermi's Golden Rule suggests that the ISC rate depends on both the spin-orbit coupling magnitude (V_{SOC}) and the Franck-Condon-weighted density of accessible triplet states.[220–223] In p-conjugated systems, higher triplet DOS and enhanced vibronic coupling are known to promote ISC efficiency. Therefore, an increase in the number of triplet manifolds in **Cz-H** implies a greater number of ISC channels, leading to an increased ISC rate (k_{ISC}), and consequently, more efficient non-radiative deactivation from S_1 via ISC compared to **Cz-T**. The dense triplet manifold can suppress prompt fluorescence but may also facilitate TADF via RISC with thermal energy. Thus, while a high triplet DOS often suggests stronger non-radiative decay (ISC), it may also enable delayed emission pathways under favourable energetic conditions.

$$\eta_{ISC} \propto \frac{|SOC|^2}{Exp\ (\Delta E_{ST})^2} \qquad \text{Equation 4.2}$$

Spin-orbit coupling (SOC) calculations were performed to further probe the influence of electronic coupling at the CAM-B3LYP-D3/6-311++G(d,p) level of theory (Tables A4. 11 and A4.12). In **Cz-T**, the nearly isoenergetic states S_1 (3.977 eV) and T_7 (3.9548 eV) exhibit a small singlet-triplet energy gap (ΔE_{ST} = 0.023 eV) and a moderate SOC value of V_{SOC} = 0.205 cm^{-1}. In **Cz-H**, the closest triplet (T_{14}) lies at ΔE_{ST} = 0.008 eV from S_1, but the corresponding SOC is higher at 1.601 cm^{-1}. The relative ISC efficiency descriptor η_{ISC}, calculated using Equation 4.2, were found to be 0.042 for **Cz-T** and 2.563 for **Cz-H**. The significantly higher η_{ISC} the **Cz-H** data reflect a more

efficient and rapid triplet population, consistent with the fsTA data, which show clear triplet-related features within the femtosecond time window. In contrast, the substantially lower η_{ISC} of **Cz-T** indicates a significantly slower ISC process, confirming the absence of observable triplet signatures in its fsTA spectrum. The disparity highlights the distinct ISC efficiencies in the two systems, likely arising from differences in SOC or energetic alignment between singlet and triplet states. Following ISC, RISC from the lower triplet (T_1) states becomes feasible in the reference compound **Cz-T**. Quantum chemically computed singlet-triplet energy gap (ΔE_{ST}) was found to be 0.72 eV (S_1-T_1) for **Cz-H**, whereas it was 0.58 eV (S_1-T_1) for **Cz-T**. In **Cz-H**. The presence of 14 closely packed triplet states below S_1 may promote efficient internal conversion (The Energy gap law),[224] to T_1, which can subsequently enable RTP-dominant delayed dual emission. In contrast, **Cz-T** is expected to exhibit more efficient RISC owing to its smaller $\Delta E_{S1\text{-}T1}$, which facilitates faster back conversion from T_1 to S_1.[159] Additionally, the SOC between T_1 and S_0 supports the observed RTP in both **Cz-H** and the reference compound **Cz-T**. The SOC values for $T_1 \rightarrow S_0$ transitions are V_{SOC} = 0.349 cm^{-1} for **Cz-T** and V_{SOC} = 0.987 cm^{-1} for **Cz-H**, consistent with the radiative decay from the triplet manifold (RTP). Hence, **Cz-T** has equitable contributions from TADF and RTP, while **Cz-H** favours RTP as a consequence of stronger SOC and the prominent C-H$\cdots\pi$ interactions in the molecular packing (I_{RTP}:I_{TADF} = 1.71 ± 0.20).

4.2.6. Proposed Jablonski Diagram

Figure 4.7 presents the schematic excited-state energetics of **Cz-H** and its control unit, Cz-T. Upon photoexcitation, **Cz-H** and Cz-T undergo ISC from their respective S_1 states to higher triplet states (T_{14} for **Cz-H** and T_7 for Cz-T). In **Cz-H**, the increased molecular rigidity promotes efficient internal conversion to T_1, thereby enhancing the contribution from RTP. In contrast, Cz-T exhibits a smaller S_1–T_1 energy gap, which facilitates efficient reverse intersystem crossing from T_1 back to S_1, resulting in comparable contributions from both delayed fluorescence and RTP (Figure 4.8).

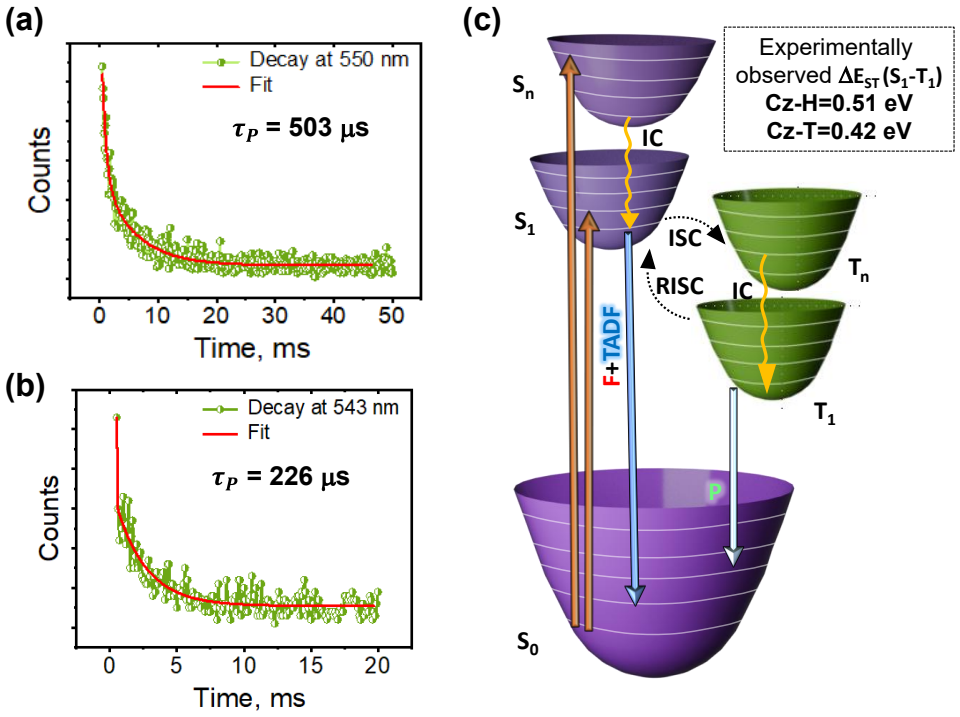

Figure 4.8: (a) Decay profile of delayed emission of **Cz-T** at RT, (b) Decay profile of delayed emission of **Cz-H** at RT, and (c) Jablonski diagram illustrating the possible excited-state relaxation pathways in **Cz-T** and **Cz-H**. Pathways include prompt fluorescence (F), ISC, RISC, IC, and phosphorescence (P, representing RTP) with experimentally observed S_1-T_1 energy difference.

4.3. Conclusion

In summary, we establish an experimentally validated connection between the molecular architecture and excited-state dynamics in purely organic, donor-acceptor-free, and spacer-free delayed dual-emissive systems. By combining advanced structural elucidation through 3D ED with ultrafast spectroscopic and computational investigations, we reveal how supramolecular rigidity and specific C–H···π intermolecular interactions facilitate efficient triplet harvesting in Cz-H.[225] The ability of 3D ED to resolve complex micro-crystalline frameworks such as Cz-H beyond the reach of conventional crystallography demonstrates its unique power to decode structure-property relationships in complex organic materials. The solid-state NMR analysis further corroborates the well-defined crystalline assembly of Cz-H. The complementary spectroscopic and computational findings collectively show that subtle variations in molecular packing can steer triplet formation, intersystem crossing rates, and emission properties in heavy-atom-free systems. Looking forward, the synergy between 3D ED and time-resolved spectroscopic characterisation offers a powerful blueprint for designing next-generation dual-emissive

chromophores. Expanding this integrative approach to broader molecular scaffolds and hybrid systems could enable predictive control of excited-state processes, ultimately advancing the rational design of efficient optoelectronic materials.

4.4. Experimental Section

4.4.1. Syntheses and Characterisation

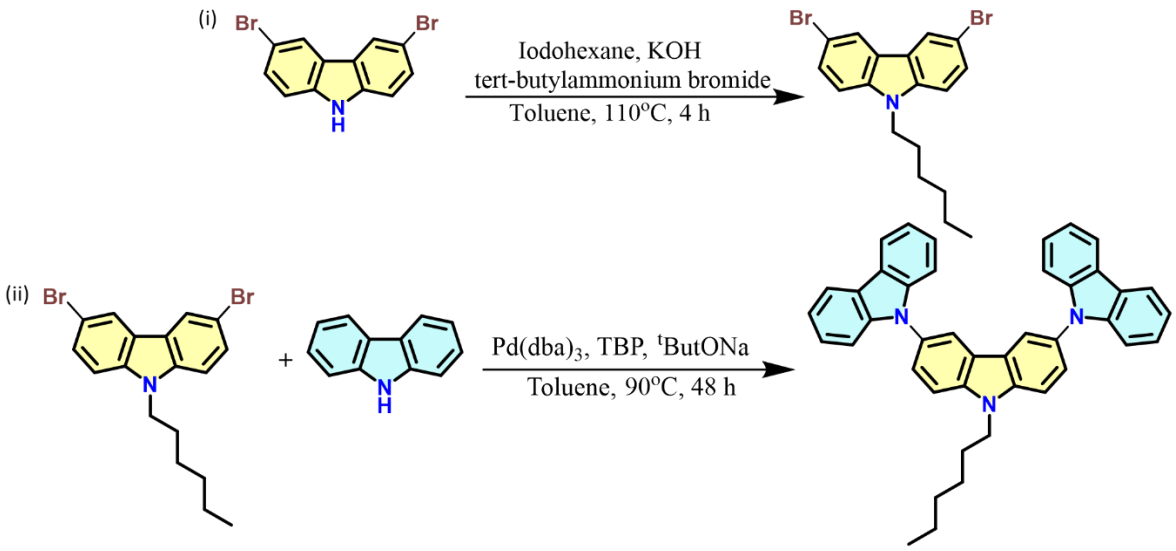

Scheme A4.1: Synthesis of 3,6-dibromo-9-hexylcarbazole and Cz-T.

Synthesis of 3,6-dibromo-9-hexylcarbazole: 3,6-dibromocarbazole (500 mg, 1.54 mmol) and 1-iodohexane (0.27mL, 1.85mmol) were dissolved in toluene (50 mL). To this, a solution of KOH (233mg, 4.16 mmol) and tetrabutylammonium bromide (49 mg, 0.154 mmol) in water (45 mL) was added. This mixture was stirred at 110 °C for 4 hours. After cooling the mixture, extraction was done with CHCl3. It is then dried over MgSO4 and recrystallised from ethyl ether, producing white crystals (yield of 85%).

Synthesis of Cz-T: $Pd(dba)_3$ (0.1 mol%) and tri-tert-butyl phosphine (0.3 mL) were stirred under an argon atmosphere in 20 mL of dry toluene for 10 minutes at room temperature. To this solution, a mixture of the N-hezyl-2,7-dibromocarbazole (250 mg, 0.77 mmol), carbazole (308.7 mg, 1.85 mmol), and sodium tert-butoxide (147.8 mg, 1.54 mmol) in 50 mL of dry toluene was added. The reaction mixture was then stirred for 48 hours at 90 °C. After cooling, the mixture was diluted with ethyl acetate, and the organic phase was washed with water and brine. The crude was then

purified by column chromatography (Yield of 21%).

^{1}H NMR *(500 MHz, 298K, CDCl3): δ 8.15 (d, 2H), 8.9 (d, 4H), 7.62-7.57 (m, 4H), 7.32-7.2 (m, 12H), 4.42 (t, 2H), 1.98 (t, 2H), 1.39-1.31 (m, 6H), 0.87 (t, 3H).*

Synthesis of Cz-H: $Pd(dba)_3$ (0.165 g, 0.18 mmol) and tri-tert-butyl phosphine (TBP, 0.04g, 0.18 mmol) were dissolved under nitrogen in 20 ml of dry toluene and stirred for 10 min at room temperature. Then the mixture of 3,6-dibromocarbazole dimer (2g, 3.08 mmol), carbazole (1.61 g, 9.6 mmol), and sodium tert-butoxide in 50 ml of dry toluene was added. The reaction mixture was heated at 90°C for 48 hours. After cooling, the reaction mixture was diluted with ethyl acetate, and the organic phase was washed with water and brine. The residue was purified by column chromatography (yield of 28%).

4.5. Additional Figures and Tables

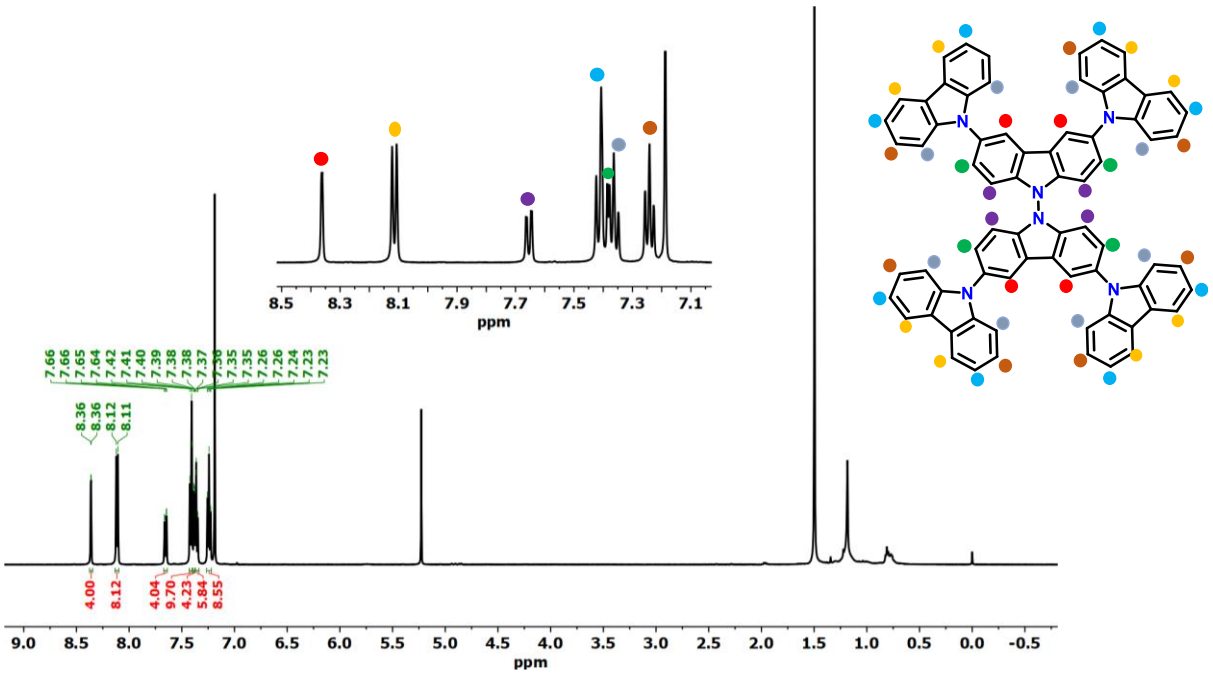

Figure A4.1: ^{1}H-NMR spectrum of **Cz-H** in $CDCl_3$.

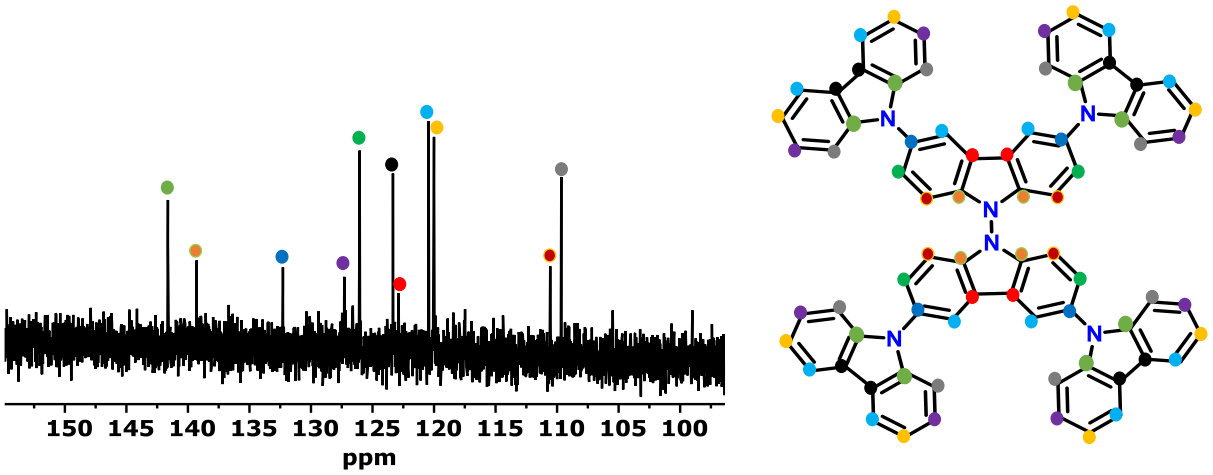

Figure A4.2: ^{13}C-NMR spectrum of **Cz-H** in $CDCl_3$.

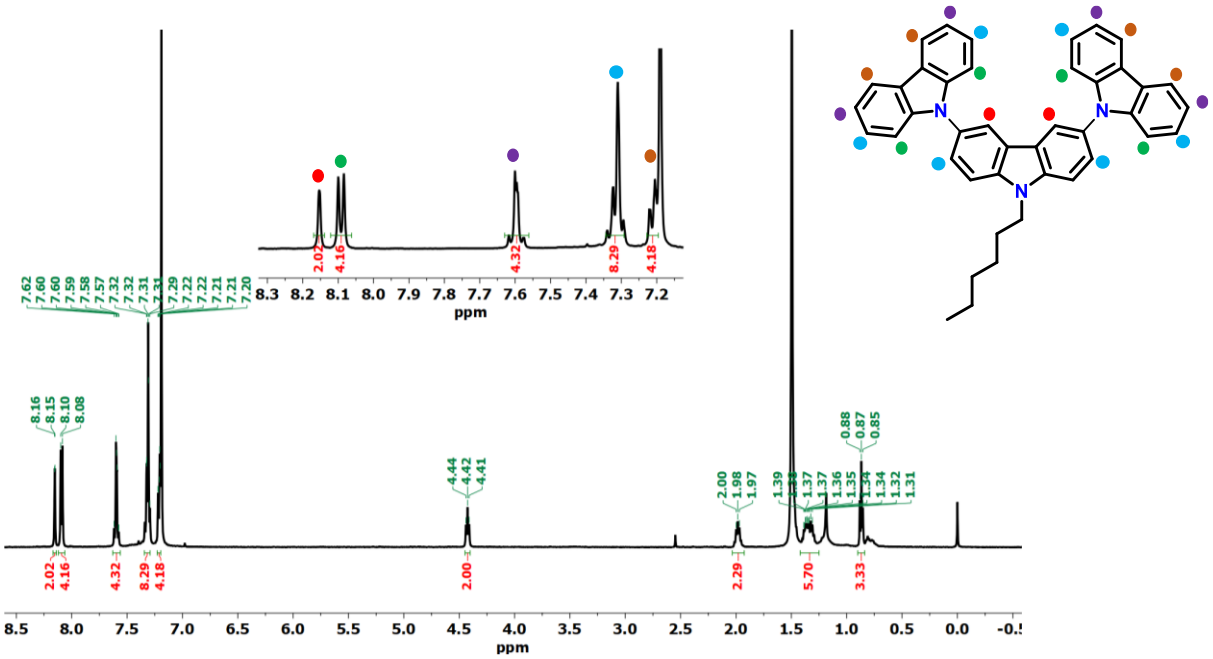

Figure A4.3: ^{1}H-NMR spectrum of **Cz-T** in $CDCl_3$.

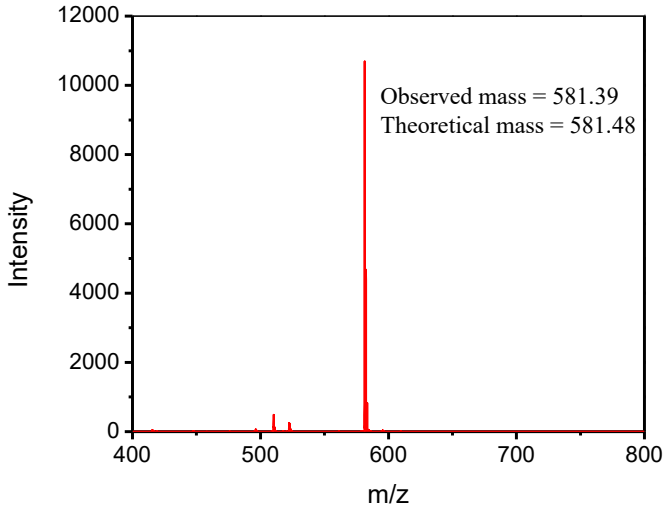

Figure A4.4: a) MALDI-TOF analysis of **Cz-T.**

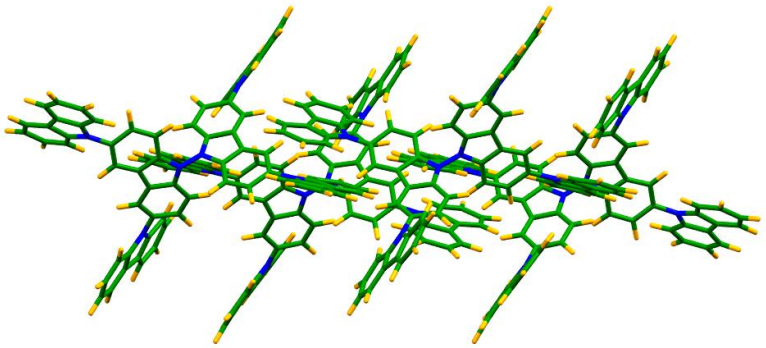

Figure A4.5: Crystal packing of **Cz-H.**

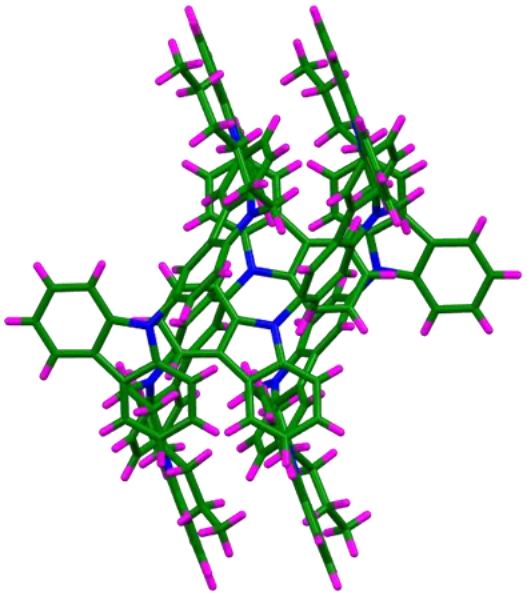

Figure A4.6: Crystal packing of **Cz-T.**

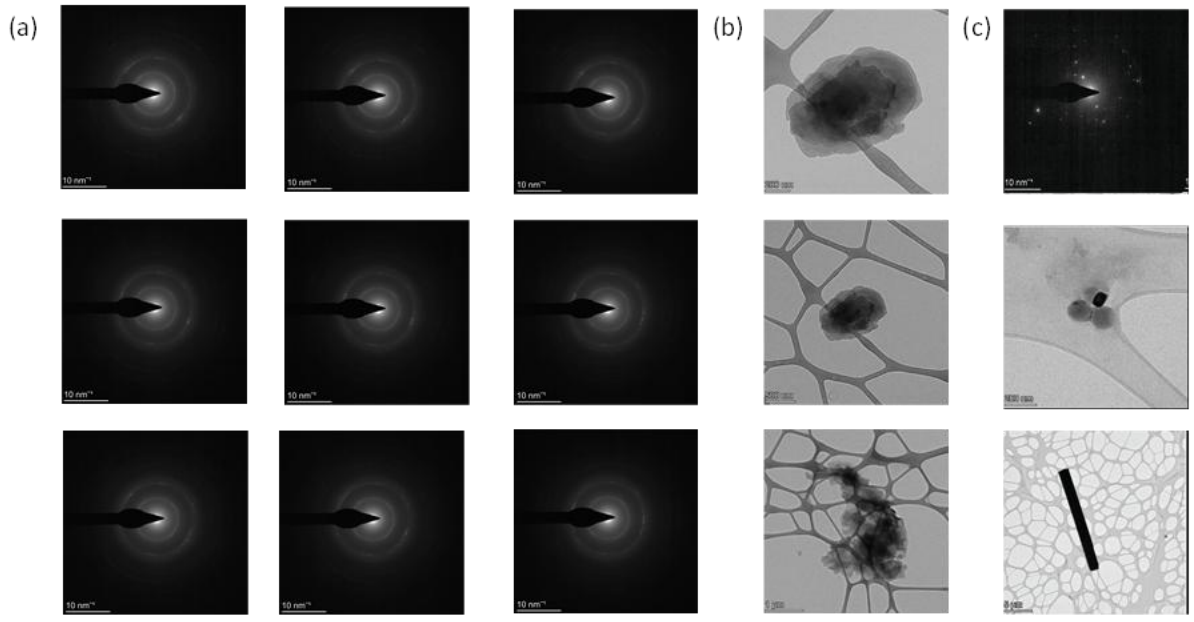

Figure A4.7: (a) Diffraction pattern of Cz-H in different tilt angles from -1 ° to -9 °, (b) TEM images of amorphous Cz-H, and (c) the diffraction pattern and TEM images of micro-crystalline Cz-H.

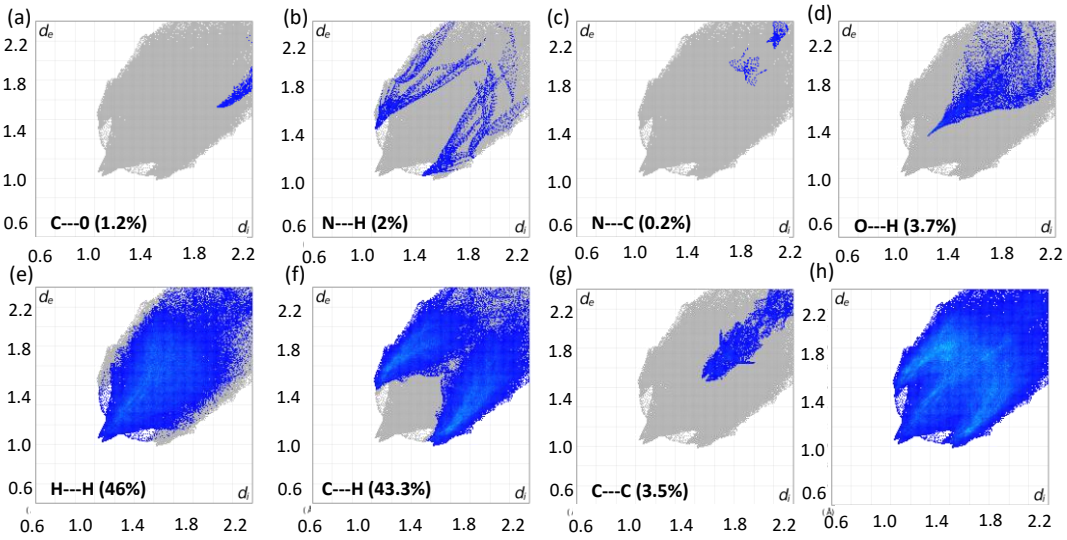

Figure A4.8: Hirshfeld 2D fingerprint plots for Cz-H showing (a) C-O, (b) N-H, (c) N-C, (d) O-H, (e) H-H, (f) C-H, (g) C-C, and (h) total interactions.

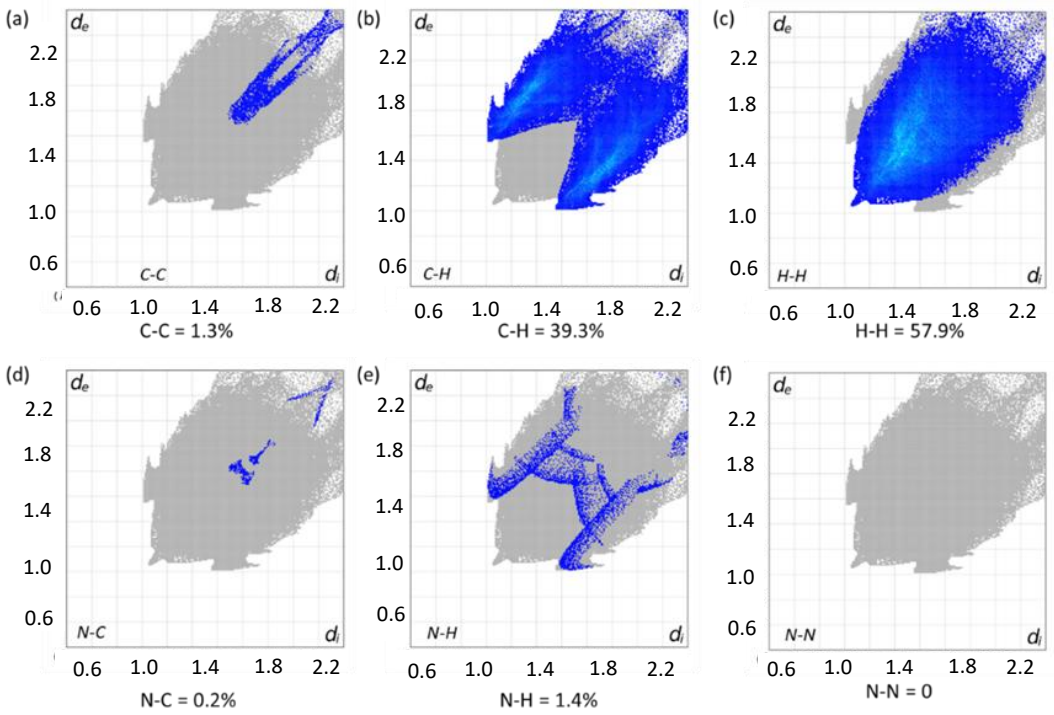

Figure A4.9: Hirshfeld 2D fingerprint plots for Cz-T showing (a) C-C, (b) C-H, (c) H-H, (d) N-C, (e) N-H, and (f) N-N interactions.

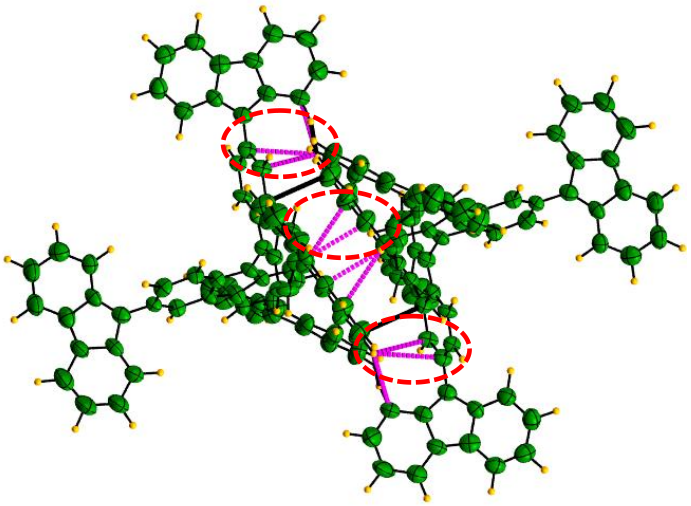

Figure A4.10: The crystal packing of Cz-H, highlighting the C-H---π interactions in red circles.

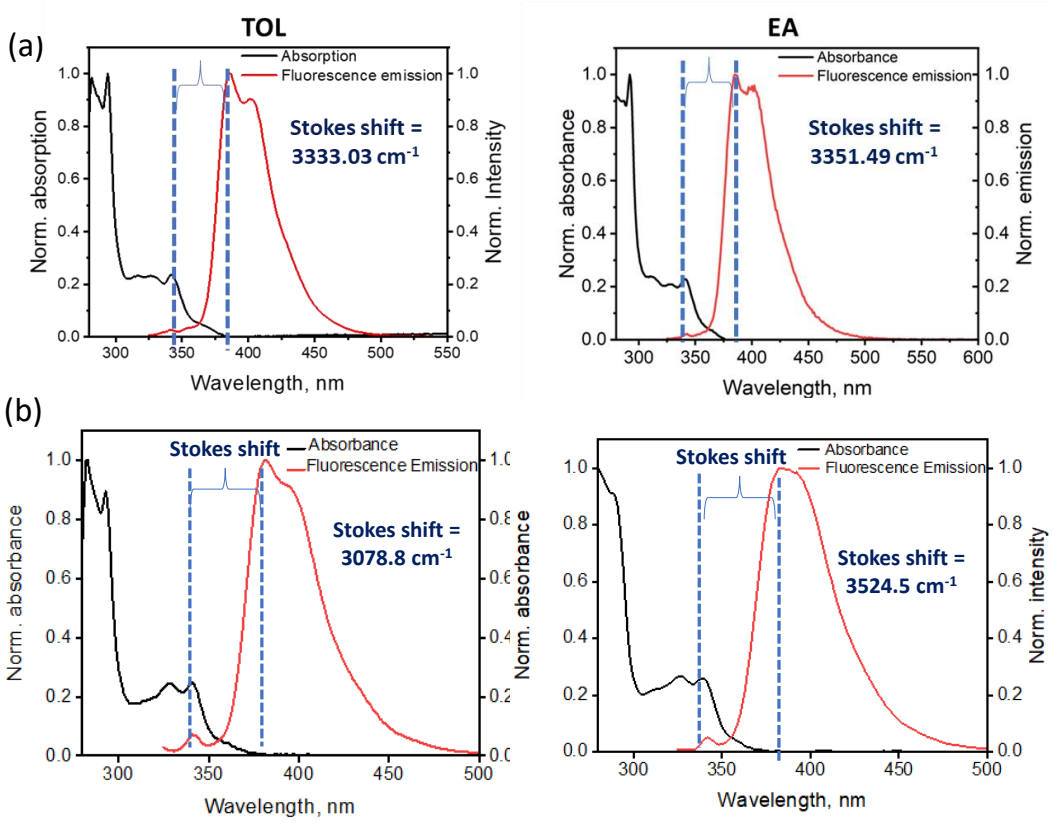

Figure A4.11. Steady-state UV-vis absorption spectra and fluorescence emission spectra of (a) Cz-T and Cz-H in TOL and EA with Stokes' shift.

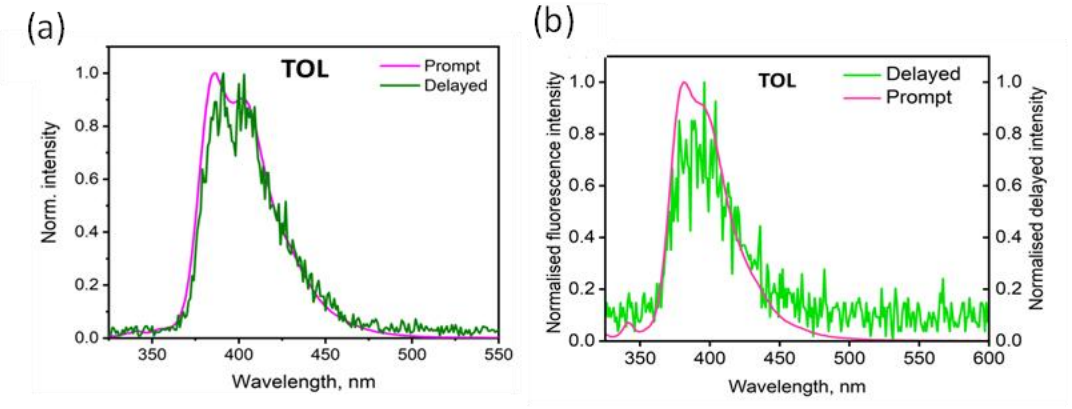

Figure A4.12: Prompt and delayed emission spectra of (a) Cz-T and (b) Cz-H in TOL.

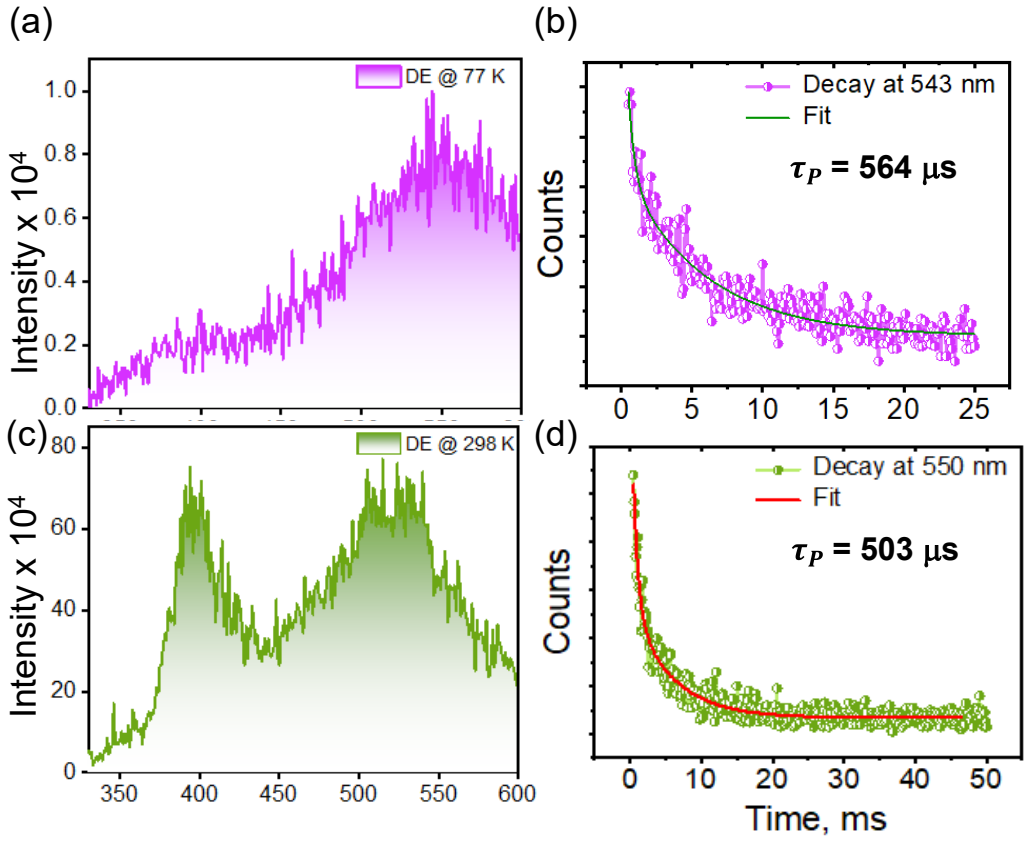

Figure A4.13: Delayed emission measurements of Cz-T at (a) 77 K, (c) 298 K, and decay profile of Cz-T at (b) 77 K and (d) 298 K.

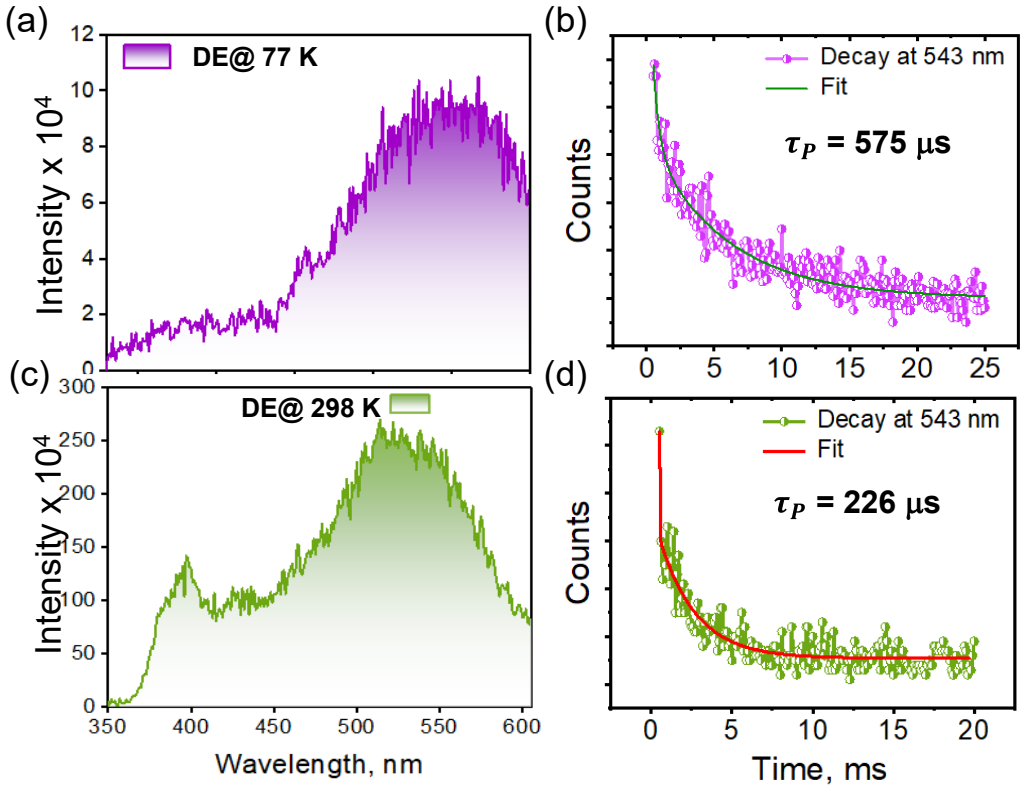

Figure A4.14: Delayed emission measurements of Cz-H at (a) 77 K, (c) 298 K, and decay profile of Cz-T at (b) 77 K and (d) 298 K.

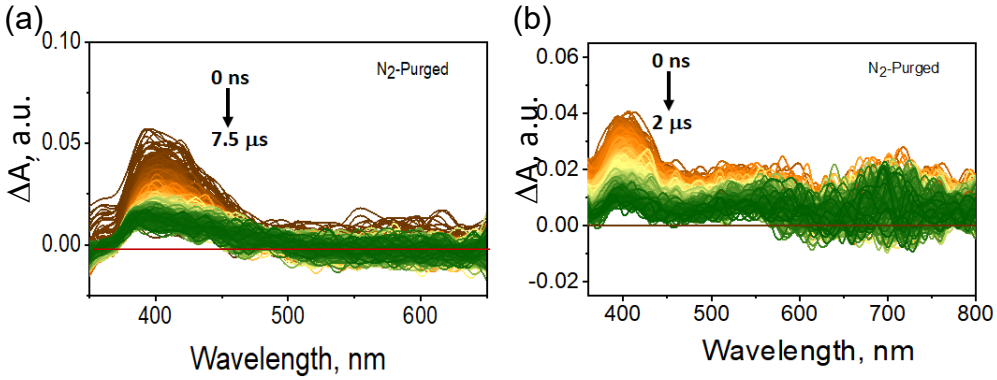

Figure A4.15: The nsTA spectra of (a) Cz-T and (b) Cz-H in N2 purged TOL solution.

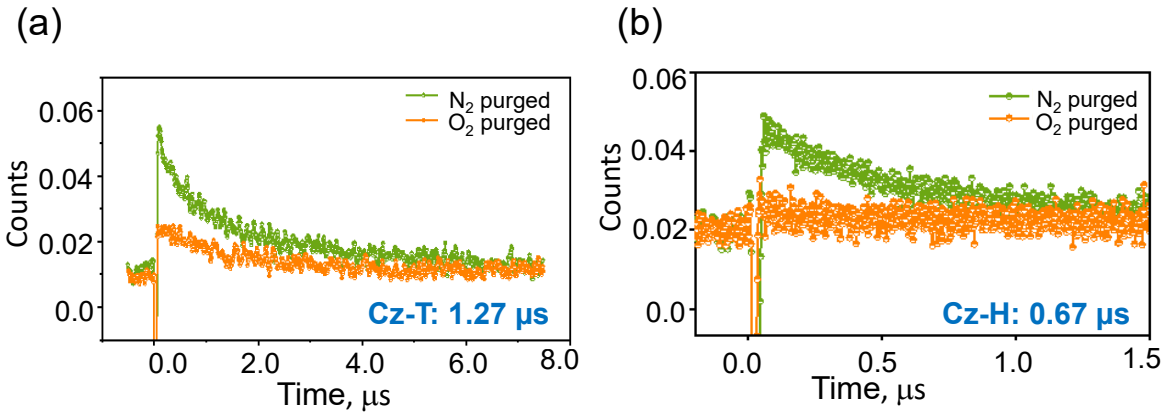

Figure A4.16: The nsTA decay profile of N_2 and O_2 purged solution of (a) Cz-T and (b) Cz-H.

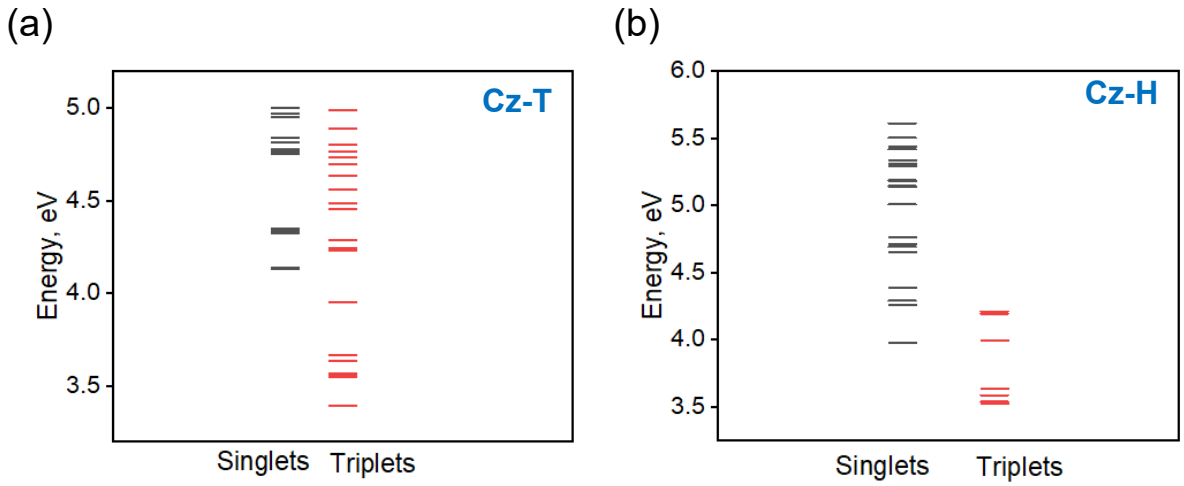

Figure A4.17: Vertical excitation energies of (a) Cz-T and (b) Cz-H at CAMB3LYP-D3/6-311g++(d,p) level of theory.

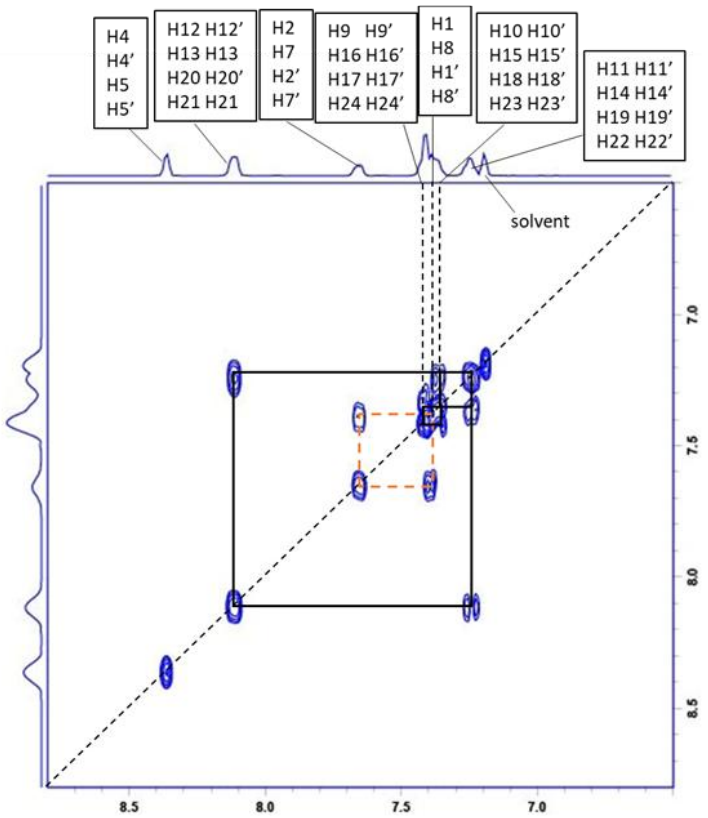

Figure A4.18: COSY spectrum of **Cz-H** in $CDCl_3$ (500 MHz).

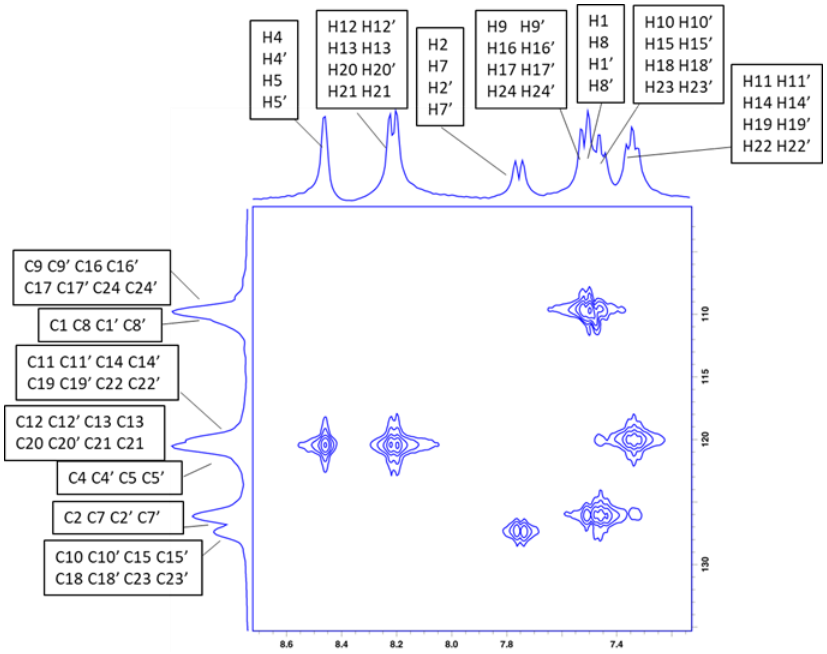

Figure A4.19: HSQC spectrum of **Cz-H** in CDCl3 (500 MHz).

Table A4.1: Crystallographic data and refinement parameters for Cz-T.

Parameters	Cz-T
Formula	$C_{42}H_{35}N_3$
Formula weight	581.73
Space group	$P2_1/c$
Crystal system	Monoclinic
a (Å)	17.589
b (Å)	20.133
c (Å)	8.8766
α (°)	90
β (°)	101.195
γ (°)	90
V (Å^3)	3083.6
R factor	7.39
Goodness of fit	0.973
CCDC deposition no.	2498405

Table A4.2: Crystallographic data and refinement parameters for Cz-H.

Parameters	Cz-H
Formula	$C_{72}H_{43}N_6$
Formula weight	581.73
Space group	$P2_1/c$
Crystal system	Monoclinic
a (Å)	9.46
b (Å)	21.22
c (Å)	28.41
α (°)	90
β (°)	95.17
γ (°)	90
Resolution (Å)	0.95
R_{int}	24.84
Goodness of fit	1.17
CCDC deposition no.	2493775

Table A4.3: 3D ED data collection details for the Cz-H crystals used in refinement.

Crystal no.	Approximate size [µm]	Angular range [°]	Rotation per frame [°]	Exposure time [s]	Total exposure [s]	Frames measured	Frames used
1	>5 x 1.0 x 0.8	−50 to +30	0.5	0.5	80	160	21 to 140
2	>5 x >5 x 0.5	−20 to +60	0.5	0.5	80	160	1 to 120
3	2.0 x 1.4 x 0.4	−60 to +60	0.5	0.5	120	240	1 to 160
4	3.8 x 1.5 x 0.4	−30 to +50	0.5	0.5	80	160	1 to 80
5	>5 x 2.1 x 0.5	−30 to +50	0.5	0.5	80	160	1 to 120
6	2.1 x 1.0 x 0.4	−70 to +60	0.5	0.5	130	260	51 to 200

Table A4.4: NMR experimental and CASTEP predicted chemical shifts for Cz-H.

Numbering	Solution-state NMR chemical shift (ppm)	Solid-state NMR chemical shift (ppm)	CASTEP Calculation		
			Chemical shielding (ppm)	Predicted NMR shift (ppm)[a]	Difference
C8a, C8b, C8a', C8b'	141.63	141	28.86	138.10	3.53
		141	28.33	138.59	3.04
		141	27.81	139.06	2.57
		141	28.27	138.64	3.00
C1, C8, C1', C8'	110.56	110	56.01	113.12	-2.56
		110	55.30	113.77	-3.21
		110	57.60	111.66	-1.10
		110	54.42	114.58	-4.02
C2, C7, C2', C7'	127.30	127	40.78	127.13	0.17
		127	40.21	127.66	-0.36
		127	40.16	127.70	-0.40
		127	44.4	123.80	3.50
C3, C6, C3', C6'	132.28	132	34.18	133.20	-0.92
		132	34.2	133.19	-0.90
		132	33.88	133.48	-1.20
		132	33.61	133.73	-1.45
C4, C5, C4', C5'	120.44	120	50.52	118.17	2.27
		120	49.03	119.54	0.90
		120	51.93	116.87	3.57
		120	52.39	116.45	4.00
C12, C13, C20, C21, C12', C13', C20', C21'	120.44	120	47.58	120.88	-0.44
		120	46.33	122.03	-1.59
		120	47.15	121.27	-0.83
		120	46.05	122.28	-1.84
		120	41.00	126.93	-6.49
		120	45.71	122.60	-2.17
		120	46.25	122.10	-1.66
		120	46.98	121.43	-1.00
	122.88	122	43.78	124.37	-1.49

C4a, C4b, C4a', C4b'		122	44.31	123.88	-1.00
		122	42.91	125.17	-2.29
		122	43.31	124.80	-1.93
C9, C16, C24, C17, C9', C16', C24', C17'	109.66	109	57.94	111.35	-1.69
		109	59.69	109.74	-0.08
		109	58.52	110.81	-1.15
		109	57.70	111.57	-1.91
		109	59.44	109.97	-0.31
		109	59.24	110.15	-0.49
		109	59.63	109.79	-0.13
		109	58.26	111.05	-1.39
C10, C15, C18, C23, C10', C15', C18', C23'	127.29	127	41.28	126.67	0.62
		127	42.46	125.59	1.70
		127	41.98	126.02	1.26
		127	38.78	128.97	-1.68
		127	41.59	126.38	0.90
		127	43.36	124.76	2.53
		127	39.46	128.35	-1.06
		127	42.2	125.83	1.46
C11, C14, C22, C19, C11', C14', C22', C19'	120.00	120	45.91	122.41	-2.41
		120	45.96	122.37	-2.37
		120	47.34	121.10	-1.10
		120	44.25	123.94	-3.94
		120	46.70	121.69	-1.69
		120	45.29	122.98	-2.98
		120	46.11	122.23	-2.23
		120	46.58	121.80	-1.80
C12a, C12b, C20a, C20b, C12a', C12b', C20a', C20b'	123.34	123	43.08	125.02	-1.70
		123	44.31	123.88	-0.55
		123	45.36	122.92	0.42
		123	42.89	125.19	-1.85
		123	43.55	124.58	-1.24
		123	43.17	124.94	-1.59
		123	43.17	124.93	-1.59
		123	45.34	122.94	0.40
C16a, C16b, C24a, C24b, C16a', C16b', C24a', C24b'	139.29	139	29.35	137.65	1.64
		139	29.69	137.34	1.95
		139	27.84	139.04	0.25
		139	27.68	139.18	0.11
		139	27.64	139.22	0.07
		139	28.82	138.14	1.15
		139	30.29	136.78	2.51
		139	30.31	136.77	2.52
			RMSD = 2.05		

[a] *predicted NMR shift = [(Chemical shielding from CASTEP x -0.98) + 171.2]*

Table A4.5: Absorption and fluorescence emission maxima, lifetime, and quantum yield for Cz-T and Cz-H in two different solvents.

Solvents	Cz-T				Cz-H			
	λ_{abs} (nm)	λ_{emi} (nm)	Φ_f (%)	τ (ns)	λ_{abs} (nm)	λ_{emi} (nm)	Φ_f (%)	τ (ns)
TOL	294, 342	386	33.6	4.8	293, 341	382	16	3.6
EA	292, 341	385	7.4	3.0	291, 340	385	1	2.7

Table A4.6 TD-DFT calculated vertical excitation energies and oscillator strength of singlet excited states in Cz-H computed at CAM-B3LYP-D3/6-311++g(d,p) level of theory.

State	Energy (eV)	Oscillator strength (f)
S_1	3.9813	0.0613
S_2	4.0664	0.0391
S_3	4.1419	0.0651
S_4	4.2576	0.1714
S_5	4.3172	0.1908
S_6	4.3753	0.2296
S_7	4.3783	0.0383
S_8	4.4368	0.0819
S_9	4.6485	0.2328
S_{10}	4.6550	0.1670

Table A4.7. TD-DFT calculated vertical excitation energies and oscillator strength of singlet excited states in Cz-T computed at CAM-B3LYP-D3/6-311++g(d,p) level of theory.

State	Energy (eV)	Oscillator strength (f)
S_1	3.9774	0.0281
S_2	4.2572	0.0718
S_3	4.2881	0.0631
S_4	4.3882	0.1504
S_5	4.6530	0.0423

S_6	4.6916	0.1045
S_7	4.7111	0.2352
S_8	4.7643	0.1185
S_9	5.0067	0.7064
S_{10}	5.1412	0.0553

Table A4.8. TDA calculated vertical excitation energies of triplet excited states in Cz-H computed at CAM-B3LYP/6-311++g(d,p) level of theory

State	Energy (eV)
T_1	3.2567
T_2	3.3875
T_3	3.4024
T_4	3.4248
T_5	3.4560
T_6	3.5277
T_7	3.5609
T_8	3.5645
T_9	3.5700
T_{10}	3.6526
T_{11}	3.6971
T_{12}	3.7996
T_{13}	3.8230
T_{14}	3.9728
T_{15}	3.9962
T_{16}	4.0920
T_{17}	4.1240
T_{18}	4.1597
T_{19}	4.1958
T_{20}	4.2803

Table A4.9. TDA calculated vertical excitation energies of triplet excited states in Cz-T computed at CAM-B3LYP/6-311++g(d,p) level of theory

State	Energy (eV)
T_1	3.3925
T_2	3.5449
T_3	3.5609
T_4	3.5650
T_5	3.6343
T_6	3.6623
T_7	3.9548
T_8	4.2309
T_9	4.2468
T_{10}	4.2860
T_{11}	4.4557
T_{12}	4.4895
T_{13}	4.5597
T_{14}	4.6341
T_{15}	4.7014
T_{16}	4.7346
T_{17}	4.7683
T_{18}	4.8065
T_{19}	4.8937
T_{20}	4.9928

Table A4.10. Solid-state Phosphorescence lifetime obtained with 310 nm excitation wavelength

	298 K	77 K
Cz-T	530 ms	650 ms
Cz-H	226 ms	575 ms

Table A4.11. SOC values in (cm-1) for Cz-H

Cz-H			
$\langle S_0\|Hso\|T_1\rangle$	0.89710	$\langle S_3\|Hso\|T_1\rangle$	0.18152

$\langle S_0\|Hso\|T_2\rangle$	0.32704	$\langle S_3\|Hso\|T_2\rangle$	0.00023
$\langle S_0\|Hso\|T_3\rangle$	0.10646	$\langle S_3\|Hso\|T_3\rangle$	0.54440
$\langle S_0\|Hso\|T_4\rangle$	0.09904	$\langle S_3\|Hso\|T_4\rangle$	0.51407
$\langle S_0\|Hso\|T_5\rangle$	0.06249	$\langle S_3\|Hso\|T_5\rangle$	0.44571
$\langle S_0\|Hso\|T_6\rangle$	0.06316	$\langle S_3\|Hso\|T_6\rangle$	0.44518
$\langle S_0\|Hso\|T_7\rangle$	1.42461	$\langle S_3\|Hso\|T_7\rangle$	0.02886
$\langle S_0\|Hso\|T_8\rangle$	0.02471	$\langle S_3\|Hso\|T_8\rangle$	0.38801
$\langle S_0\|Hso\|T_9\rangle$	0.18787	$\langle S_3\|Hso\|T_9\rangle$	0.01463
$\langle S_0\|Hso\|T_{10}\rangle$	0.17840	$\langle S_3\|Hso\|T_{10}\rangle$	0.01318
$\langle S_0\|Hso\|T_{11}\rangle$	0.12609	$\langle S_3\|Hso\|T_{11}\rangle$	0.06155
$\langle S_0\|Hso\|T_{12}\rangle$	0.00103	$\langle S_3\|Hso\|T_{12}\rangle$	0.05413
$\langle S_0\|Hso\|T_{13}\rangle$	0.57897	$\langle S_3\|Hso\|T_{13}\rangle$	0.05055
$\langle S_0\|Hso\|T_{14}\rangle$	1.04720	$\langle S_3\|Hso\|T_{14}\rangle$	0.00105
$\langle S_0\|Hso\|T_{15}\rangle$	0.00162	$\langle S_3\|Hso\|T_{15}\rangle$	0.05333
$\langle S_1\|Hso\|T_1\rangle$	0.81901	$\langle S_4\|Hso\|T_1\rangle$	0.00019
$\langle S_1\|Hso\|T_2\rangle$	0.28437	$\langle S_4\|Hso\|T_2\rangle$	0.17325
$\langle S_1\|Hso\|T_3\rangle$	0.01815	$\langle S_4\|Hso\|T_3\rangle$	0.52052
$\langle S_1\|Hso\|T_4\rangle$	0.01935	$\langle S_4\|Hso\|T_4\rangle$	0.55117
$\langle S_1\|Hso\|T_5\rangle$	0.02568	$\langle S_4\|Hso\|T_5\rangle$	0.45068
$\langle S_1\|Hso\|T_6\rangle$	0.02576	$\langle S_4\|Hso\|T_6\rangle$	0.45120
$\langle S_1\|Hso\|T_7\rangle$	0.00308	$\langle S_4\|Hso\|T_7\rangle$	0.37193
$\langle S_1\|Hso\|T_8\rangle$	0.15449	$\langle S_4\|Hso\|T_8\rangle$	0.02008
$\langle S_1\|Hso\|T_9\rangle$	0.09979	$\langle S_4\|Hso\|T_9\rangle$	0.01008
$\langle S_1\|Hso\|T_{10}\rangle$	0.09610	$\langle S_4\|Hso\|T_{10}\rangle$	0.01123
$\langle S_1\|Hso\|T_{11}\rangle$	0.00044	$\langle S_4\|Hso\|T_{11}\rangle$	0.05264
$\langle S_1\|Hso\|T_{12}\rangle$	0.12943	$\langle S_4\|Hso\|T_{12}\rangle$	0.05830
$\langle S_1\|Hso\|T_{13}\rangle$	0.11841	$\langle S_4\|Hso\|T_{13}\rangle$	0.00045
$\langle S_1\|Hso\|T_{14}\rangle$	1.60023	$\langle S_4\|Hso\|T_{14}\rangle$	0.02600
$\langle S_1\|Hso\|T_{15}\rangle$	0.20742	$\langle S_4\|Hso\|T_{15}\rangle$	0.18032
$\langle S_2\|Hso\|T_1\rangle$	0.28477	$\langle S_5\|Hso\|T_1\rangle$	0.03676
$\langle S_2\|Hso\|T_2\rangle$	0.71828	$\langle S_5\|Hso\|T_2\rangle$	0.08831
$\langle S_2\|Hso\|T_3\rangle$	0.00917	$\langle S_5\|Hso\|T_3\rangle$	0.47670
$\langle S_2\|Hso\|T_4\rangle$	0.00859	$\langle S_5\|Hso\|T_4\rangle$	0.50906
$\langle S_2\|Hso\|T_5\rangle$	0.01964	$\langle S_5\|Hso\|T_5\rangle$	0.58226
$\langle S_2\|Hso\|T_6\rangle$	0.01957	$\langle S_5\|Hso\|T_6\rangle$	0.58356
$\langle S_2\|Hso\|T_7\rangle$	0.16559	$\langle S_5\|Hso\|T_7\rangle$	0.00114
$\langle S_2\|Hso\|T_8\rangle$	0.00335	$\langle S_5\|Hso\|T_8\rangle$	0.04879
$\langle S_2\|Hso\|T_9\rangle$	0.09707	$\langle S_5\|Hso\|T_9\rangle$	0.01512
$\langle S_2\|Hso\|T_{10}\rangle$	0.10007	$\langle S_5\|Hso\|T_{10}\rangle$	0.01369
$\langle S_2\|Hso\|T_{11}\rangle$	0.13583	$\langle S_5\|Hso\|T_{11}\rangle$	0.00021
$\langle S_2\|Hso\|T_{12}\rangle$	0.00045	$\langle S_5\|Hso\|T_{12}\rangle$	0.01779
$\langle S_2\|Hso\|T_{13}\rangle$	0.05274	$\langle S_5\|Hso\|T_{13}\rangle$	0.07057
$\langle S_2\|Hso\|T_{14}\rangle$	0.11980	$\langle S_5\|Hso\|T_{14}\rangle$	0.14298
$\langle S_2\|Hso\|T_{15}\rangle$	0.00069	$\langle S_5\|Hso\|T_{15}\rangle$	0.14082

Table A4.12. SOC values in (cm-1) for Cz-T

Cz-T			
$\langle S_0\|Hso\|T_1\rangle$	0.34946	$\langle S_3\|Hso\|T_1\rangle$	0.09057
$\langle S_0\|Hso\|T_2\rangle$	0.04321	$\langle S_3\|Hso\|T_2\rangle$	1.09199
$\langle S_0\|Hso\|T_3\rangle$	0.13221	$\langle S_3\|Hso\|T_3\rangle$	0.13731
$\langle S_0\|Hso\|T_4\rangle$	0.82193	$\langle S_3\|Hso\|T_4\rangle$	0.06259
$\langle S_0\|Hso\|T_5\rangle$	0.10322	$\langle S_3\|Hso\|T_5\rangle$	0.08842
$\langle S_0\|Hso\|T_6\rangle$	0.25689	$\langle S_3\|Hso\|T_6\rangle$	0.02060
$\langle S_0\|Hso\|T_7\rangle$	0.48657	$\langle S_3\|Hso\|T_7\rangle$	0.07875
$\langle S_0\|Hso\|T_8\rangle$	0.72070	$\langle S_3\|Hso\|T_8\rangle$	0.09465
$\langle S_0\|Hso\|T_9\rangle$	0.70907	$\langle S_3\|Hso\|T_9\rangle$	0.05606
$\langle S_0\|Hso\|T_{10}\rangle$	1.20374	$\langle S_3\|Hso\|T_{10}\rangle$	0.21536
$\langle S_1\|Hso\|T_1\rangle$	0.86937	$\langle S_4\|Hso\|T_1\rangle$	0.30684
$\langle S_1\|Hso\|T_2\rangle$	0.04012	$\langle S_4\|Hso\|T_2\rangle$	0.07503
$\langle S_1\|Hso\|T_3\rangle$	0.04314	$\langle S_4\|Hso\|T_3\rangle$	0.07563
$\langle S_1\|Hso\|T_4\rangle$	0.12905	$\langle S_4\|Hso\|T_4\rangle$	0.91700
$\langle S_1\|Hso\|T_5\rangle$	0.03634	$\langle S_4\|Hso\|T_5\rangle$	0.11460
$\langle S_1\|Hso\|T_6\rangle$	0.13541	$\langle S_4\|Hso\|T_6\rangle$	0.12248
$\langle S_1\|Hso\|T_7\rangle$	0.20518	$\langle S_4\|Hso\|T_7\rangle$	0.43783
$\langle S_1\|Hso\|T_8\rangle$	0.11622	$\langle S_4\|Hso\|T_8\rangle$	0.33098
$\langle S_1\|Hso\|T_9\rangle$	0.14819	$\langle S_4\|Hso\|T_9\rangle$	0.20039
$\langle S_1\|Hso\|T_{10}\rangle$	0.06935	$\langle S_4\|Hso\|T_{10}\rangle$	0.09471
$\langle S_2\|Hso\|T_1\rangle$	0.09835	$\langle S_5\|Hso\|T_1\rangle$	0.08515
$\langle S_2\|Hso\|T_2\rangle$	0.14012	$\langle S_5\|Hso\|T_2\rangle$	0.13861
$\langle S_2\|Hso\|T_3\rangle$	1.05386	$\langle S_5\|Hso\|T_3\rangle$	0.09643
$\langle S_2\|Hso\|T_4\rangle$	0.15864	$\langle S_5\|Hso\|T_4\rangle$	0.62034
$\langle S_2\|Hso\|T_5\rangle$	0.00970	$\langle S_5\|Hso\|T_5\rangle$	0.49840
$\langle S_2\|Hso\|T_6\rangle$	0.16469	$\langle S_5\|Hso\|T_6\rangle$	0.07133
$\langle S_2\|Hso\|T_7\rangle$	0.15859	$\langle S_5\|Hso\|T_7\rangle$	0.59000
$\langle S_2\|Hso\|T_8\rangle$	0.19844	$\langle S_5\|Hso\|T_8\rangle$	0.15567
$\langle S_2\|Hso\|T_9\rangle$	0.21100	$\langle S_5\|Hso\|T_9\rangle$	0.12197
$\langle S_2\|Hso\|T_{10}\rangle$	0.06763	$\langle S_5\|Hso\|T_{10}\rangle$	0.15504

Table A4.13. The previous reports on dual emission with a conventional strategy.

Sl. No.	Authors	Work	Chromophore architecture	Chromophore
1.	**Jibin Sivanarayanan, Kavya Vinod, Sujitha Suresh, Amalnadh T., Anitta Benoy, Brijith Thomas, and Mahesh Hariharan***	**Current work**	**Heavy atom and Donor-Acceptor Free**	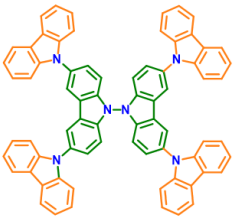
2.	Xian-Bao Cai,ab Dong Liang, a Deng-Chao Zhang,c Ji-Hui Jia,c Xiao-Yuan Wu a and Can-Zhong Lu*	*Chem. Sci*., **2025**, 16, 9802	Donor-Acceptor with heavy atom (**Ag**)	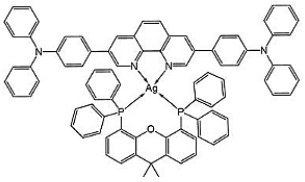
3.	Ping Li, Qixin Lv, Chengxi Sun, Peng Zhang, Xianjie Wang, Chao Yin, Yuyu Pan, * and Runfeng Chen*	*J. Phys. Chem. Lett.* **2024**, 15, 9787−9794	Heavy atom (**Br**)	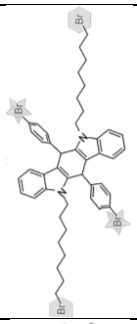
4.	Harsh Bhatia and Debdas Ray*	*Mater. Adv*., **2020**, 1, 1858	Donor-Acceptor	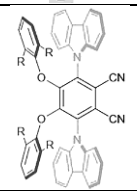
5.	Pengfei Xu, Ryoga Hojo, and Zachary M. Hudson	*Chem. Eur. J.* **2023**, 29, e202203585	Donor-Acceptor	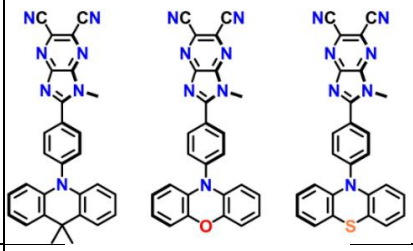
6.	Suvendu Dey, Monirul Hasan, Atul Shukla, Nirmalya Acharya, Manoj Upadhyay, Shih-Chun Lo, Ebinazar B. Namdas, and Debdas Ray*	*J. Phys. Chem. C* **2022**, 126, 5649−5657	Donor- Acceptor	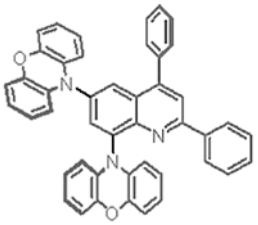

7.	Tian-yi Li, Daniel Sylvinson Muthiah Ravinson, Ralf Haiges, Peter I. Djurovich, and Mark E. Thompson*	*J. Am. Chem. Soc.* **2020**, 142, 6158−6172	Heavy atom (**Au**)	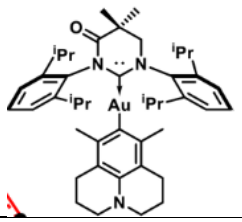
8.	Patrick J. Conaghan, Campbell S. B. Matthews, Florian Chotard, Saul T. E. Jones, Neil C. Greenham, Manfred Bochmann, Dan Credgington & Alexander* S. Romanov*	*Nat. comm*. **2020,** s41467-020-15369-8	Heavy atom (**Au**)	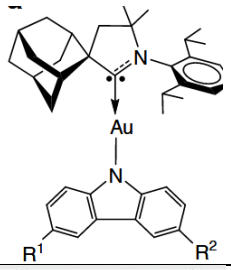
9.	Jiayi Li, Liding Wang, Zifeng Zhao, Xiaoyue Li, Xiao Yu, Peihao Huo, Qionghua Jin, Zhiwei Liu, * Zuqiang Bian, and Chunhui Huang	*Angew. Chem. Int. Ed.* **2020,** 59, 8210 – 8217	Donor-Acceptor with heavy atom (**Cu**)	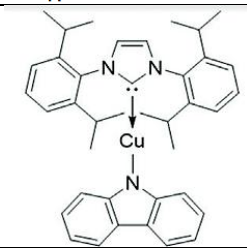
10.	Rasha Hamze, Shuyang Shi, Savannah C. Kapper, Daniel Sylvinson Muthiah Ravinson, Laura Estergreen, Moon-Chul Jung, Abegail C. Tadle, Ralf Haiges, Peter I. Djurovich, Jesse L. Peltier, Rodolphe Jazzar, Guy Bertrand, Stephen E. Bradforth, and Mark E. Thompson*	*J. Am. Chem. Soc.* **2019**, 141, 8616−8626	Heavy atoms (**Cu, Au, and Ag**)	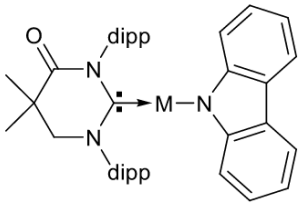

4.6. Appendix

4.6.1. Materials and Methods

Detailed information regarding the materials and methods used is given in section *2.6.1.*

4.6.2. X-ray Crystallography

Detailed information regarding the X-ray crystallography used is given in section *2.6.2.*

4.6.3. 3D Electron Diffraction

Samples of Cz-H were deposited on standard TEM grids (amorphous carbon on Cu) as dry powder after gentle grinding between microscope slides and measured on an ELDICO ED-1 electron diffractometer at room temperature using the software ELDIX. The device is equipped with a

LaB6 electron source operating at an acceleration voltage of 160 kV (λ = 0.02851 Å) and a hybrid-pixel detector (Dectris QUADRO). The grid was screened for suitable crystals in STEM (scanning transmission electron microscopy) mode, and diffraction data were recorded in continuous rotation mode with a pseudo-parallel beam of ca. 750 nm diameter. Parts of the measurements affected by beam damage or shadowing by the grid were omitted. Measurement details for all datasets used are given in Table S3.

Data were processed using the APEX4 software package. Frames were integrated separately for each crystal, then merged, scaled, and corrected for Lorentz effects, scan speed, background, and absorption using SAINT and SADABS. The space group assignment was based on systematic absences, E statistics, and the successful refinement of the structure. The structure was solved using ShelXT and refined with ShelXL in conjunction with ShelXle. Least squares refinements were carried out within the kinematic approximation by minimizing Σw(Fobs2-Fcalc2)2 with the ShelXL weighting scheme and using neutral electron scattering factors. Non-H atoms were refined with anisotropic displacement parameters. Restraints on APDs were used to ensure convergence within physically meaningful limits. The occupancies of the co-crystallised solvent molecules (dichloromethane and water) were refined freely. H atoms were placed in calculated positions based on typical distances for neutron diffraction and refined using riding model with Uiso(H) = 1.2·Ueq(C). The H atoms on the co-crystallised water molecule could not be located and were omitted. Deposition Number 2493775 contains the supplementary crystallographic data for this paper. These data are provided free of charge by the joint Cambridge Crystallographic Data Centre and Fachinformationszentrum Karlsruhe Access Structures service and can be accessed at www.ccdc.cam.ac.uk/structures.

4.6.4. Solid-state NMR

All solid-state NMR experiments were carried out on a Bruker Avance HD spectrometer operating at a magnetic field strength of 14.1 T. The samples were packed in a 1.3 mm ZrO_2 rotor and spun at 60 kHz using a Bruker HXY triple-resonance probe under N_2 gas flow. Proton pulses were calibrated on the sample itself. The ^{1}H NMR chemical shifts were indirectly referenced to tetramethylsilane in $CDCl_3$ using adamantane as a secondary chemical shift standard, based on the previously published relative NMR frequencies. All experiments were conducted at room temperature.

The ^{1}H 90-degree pulse length was 1.3 µs for a nutation frequency of 192 kHz, 16 accumulated NMR-signal transients, and a relaxation delay of 3.0 s. The ^{13}C spectra were recorded by the ^{1}H

→ ^{13}C CP at the double quantum Hartmann-Hahn condition, $n_H + n_c = n_{rf}$, which involved ramped CP of $n_H = 20 \pm 5$kHz for a 1.7 ms 90° ^{1}H pulse and spinal-64 ^{1}H decoupling at $n_H = 150$ kHz. The ^{1}H-^{13}C 2D HETCOR spectra were acquired with a contact time of 5 ms with a recycle delay of 2.5 s.

4.6.5. Kubelka-Munk Transformed Absorption

Detailed information regarding the X-ray crystallography used is given in section *2.6.3.*

4.6.6. Computing Activation Energy for RISC

According to the Arrhenius equation, the rate of RISC is

$$k_{RISC} = A.e^{(^{-E_a}/_{T}k_B)} \qquad \text{Equation A4.1}$$

Where k_{RISC} is the rate of reverse intersystem crossing, A is the pre-exponential factor, E_a (DE_{ST}) is the activation energy, T is the temperature, and k_B is the Boltzmann constant.

$$\ln k_{RISC} = \ln A - \frac{E_a}{Tk_B} \qquad \text{Equation A4.2}$$

At two different temperatures T_1 and T_2, the equation can be modified as,

$$\frac{lnk_2 - lnk_1}{\frac{1}{T_1} - \frac{1}{T_2}} = \frac{-E_a}{k_B} \qquad \text{Equation A4.3}$$

Where k_1 and k_2 are the rates of RISC at T_1 and T_2. Hence, the activation energy for the RISC is,

$$E_a = -k_B.\frac{\ln(^{I_2}/_{I_1})}{(\frac{1}{T_1} - \frac{1}{T_2})} \qquad \text{Equation A4.5}$$

Since the intensity of the TADF (I) is directly influenced by the rate of reverse intersystem crossing (k_{RISC}), under the following assumptions, the TADF intensity (I) can be used as a proxy for k_{RISC}:

- ❖ The TADF intensity is proportional to the rate of RISC (k_{RISC}).
- ❖ Other decay pathways from the triplet state, such as internal conversion (IC), phosphorescence, and non-radiative decay, are either negligible or temperature-independent over the studied range.
- ❖ The prompt fluorescence and intersystem crossing (ISC) rates are not significantly affected by temperature.

4.6.7. Computational Analysis

All calculations are performed using Gaussian 16.[162] DFT is performed using CAM-b3lyp-D3 and 6-311G++(d,p) basis set. Singlet excited states are calculated using TD-DFT with CAM-B3LYP and 6-311G++(d,p) basis set. Triplet excited states are computed using TDA with the WB97XD functional and the 6-311++g(d,p) basis set. Hole-electron analysis and NTO analysis are performed using Multiwfn version 3.7[16] and plotted using the VMD software.[17]

4.6.8. Noncovalent Interaction (NCI) Plot

Detailed information regarding the X-ray crystallography used is given in section *2.6.6.*

4.6.9. Hirshfeld Analyses

Detailed information regarding the X-ray crystallography used is given in section *2.6.7.*

4.6.10. Symmetry Adapted Perturbation Theory (SAPT)

Detailed information regarding the X-ray crystallography used is given in section *2.6.8.*

4.6.11. Femtosecond Transient Absorption Measurements

The detailed fsTA instrumentation and experimental methods are provided in Section *2.6.9.*

4.6.12. Nanosecond Transient Absorption Measurements

An Applied Photophysics Model LKS-60 laser kinetic spectrometer was used for the nanosecond laser flash photolysis experiments in TOL. The fundamental pulse of 710 nm from the Quanta Ray INDI-40-10 series pulsed Nd:YAG laser was converted into its second harmonic (355 nm, pulse duration ≈approximately 10 ns) and used to excite the samples.

4.6.13. Fermi Golden Rule for Intersystem Crossing

$$k_{ISC} = \frac{2\pi}{\hbar} |< \Psi_t|\widehat{H_{SOC}}|\Psi_s|^2 . \rho(E) \qquad \text{Equation A4.6}$$

Where,

- k_{ISC} = Rate constant of intersystem crossing.
- $|< \Psi_t|\widehat{H_{SOC}}|\Psi_s|$ = Spin-orbit coupling matrix element between the singlet and triplet wavefunctions.

❖ H_{SOC} = Spin-orbit coupling Hamiltonian.

❖ $\rho(E)$ = Density of final states (triplet states) at energy E, often treated as a Dirac delta function when discrete transitions are considered.

❖

4.6.14. CASTEP calculation[196,197,200,226]

Geometry optimisations for the CASTEP calculations were performed using the Smart algorithm with a convergence tolerance of 0.0001 kcal mol^{-1} and force of 0.005 kcal $Å^{-1}$ with a maximum of 500 iterations. The plane-wave DFT calculations were performed using the gauge-including projected augmented wave (GIPAW) approach, as implemented in the CASTEP version 2017. Geometry optimisation and NMR properties were calculated using the generalised gradient approximation (GGA) with the exchange-correlation PBESOL functional, with On-the-Fly ultra-Pseudopotential. The Tkatchenko and Scheffler method was employed for dispersion corrections. An energy cutoff of 700 eV, along with a Monkhorst-Pack grid with a k-point spacing of 0.08 $Å^{-1}$, was chosen to maximise calculation efficiency.

The predicted NMR shift = [(*Chemical shielding from CASTEP x -0.98) + 171.2*]

Chapter 5

Conclusion and Outlook

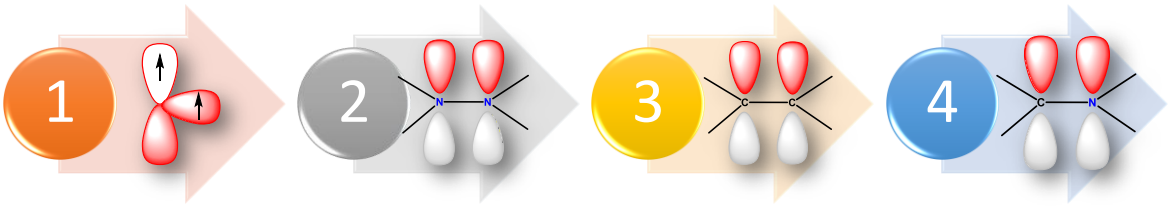

Efficient access to and utilisation of the triplet manifold is a central requirement for the development of next-generation optoelectronic devices, which are expected to dominate future display and lighting technologies. A fundamental understanding of molecular design principles that enable effective triplet generation and harvesting in purely organic systems is therefore crucial. This thesis has systematically addressed this challenge by elucidating how strategic modulation of connectivity and substitution patterns in carbazole-based architectures governs excited-state dynamics and triplet-state accessibility. The research presented herein provides comprehensive insights into triplet-state generation through deliberate variation in the connectivity of carbazole derivatives. By correlating molecular structure with photophysical behaviour, this work demonstrates that subtle changes in linkage topology can profoundly influence intersystem crossing (ISC), reverse intersystem crossing (rISC), and radiative decay pathways.

In Chapter 2, it was demonstrated that TADF can be realised in a donor-only system, challenging the conventional paradigm that relies predominantly on D-A architectures. Furthermore, strategic bromine substitution in N-N-linked carbazole dimers was shown to effectively switch the emission behaviour from TADF in the pristine carbazole dimer to RTP in the crystalline state. This observation underscores the crucial role of halogen engineering in modulating spin-orbit coupling and molecular packing, thereby providing a viable design strategy for triplet harvesting that does not rely on complex D-A frameworks.

In Chapter 3, the emergence of RTP from a purely organic, C-C-connected carbazole dimer was demonstrated in the absence of heavy-atom substitution. This finding underscores the

significance of rigid molecular frameworks and controlled electronic coupling in stabilising triplet excitons and suppressing non-radiative decay pathways, thereby enabling efficient phosphorescence in metal-free systems.

In Chapter 4, carbazole trimers and their corresponding dimers featuring C-N and N-N connectivities were investigated. These systems exhibited dual delayed emission, arising from the coexistence of TADF and RTP, which represents a particularly intriguing photophysical phenomenon. The ability to fine-tune excited-state energetics through connectivity engineering opens new avenues for the rational design of advanced emissive materials tailored for high-performance organic light-emitting diodes (OLEDs).

Overall, this thesis demonstrates that the progressive modulation of connectivity in carbazole-based systems is an effective and versatile strategy for achieving efficient triplet generation and harvesting. The insights gained from this systematic study provide a robust molecular-level understanding that is directly applicable to the design of functional organic optoelectronic materials.

Building on the findings of this thesis, several promising directions for future research can be envisaged. Extending the connectivity-engineering strategy to higher-order carbazole oligomers and polymers may offer enhanced control over exciton diffusion and triplet stabilisation, which are crucial for device-scale applications. Additionally, co-crystallisation and supramolecular assembly approaches could be explored to further manipulate molecular packing and intermolecular interactions, thereby optimising triplet lifetimes and emission efficiencies.

From a device perspective, integrating these carbazole-based emitters into OLED architectures will be an important next step to directly correlate molecular design with electroluminescent performance. Furthermore, time-resolved spectroscopic investigations under operational conditions could provide deeper insights into exciton dynamics relevant to real-world devices. Finally, combining connectivity modulation with subtle heteroatom or isotopic substitution may open new pathways for achieving high-efficiency, metal-free phosphorescent and dual-emissive materials, paving the way for sustainable and cost-effective optoelectronic technologies.

Bibliography

[1] J. D. Kovac, *J. Chem. Educ.* **1998**, *75*, 545.

[2] J. R. Lakowicz, *Principles of fluorescence spectroscopy*, 3rd ed., Springer, New York, **2006**.

[3] D. Sasikumar, A. T. John, J. Sunny, M. Hariharan, *Chem. Soc. Rev.* **2020**, *49*, 6122.

[4] N. J. Turro, *Modern molecular photochemistry*, 2. print, Univ. Science Books, Sausalito, Calif, **1991**.

[5] M. Kasha, *Discuss. Faraday Soc.* **1950**, *9*, 14.

[6] Atkins' Physical Chemistry 11e.pdf - Share - File Browser.

[7] R. Khatri, B. D. Dunietz, *J. Phys. Chem. C* **2025**, *129*, 436.

[8] W. Z. Yuan, X. Y. Shen, H. Zhao, J. W. Y. Lam, L. Tang, P. Lu, C. Wang, Y. Liu, Z. Wang, Q. Zheng, J. Z. Sun, Y. Ma, B. Z. Tang, *J. Phys. Chem. C* **2010**, *114*, 6090.

[9] Q. Zhang, J. Li, K. Shizu, S. Huang, S. Hirata, H. Miyazaki, C. Adachi, *J. Am. Chem. Soc.* **2012**, *134*, 14706.

[10] K. Brunner, A. Van Dijken, H. Börner, J. J. A. M. Bastiaansen, N. M. M. Kiggen, B. M. W. Langeveld, *J. Am. Chem. Soc.* **2004**, *126*, 6035.

[11] M. Jia, J. Kong, H. Zhou, J. Chen, S. Zhang, M. Zhou.

[12] H. P. Pasanen, R. Khan, J. A. Odutola, N. V. Tkachenko, *J. Phys. Chem. C* **2024**, *128*, 6167.

[13] A. O. Lykhin, S. A. Varganov, *Phys. Chem. Chem. Phys.* **2020**, *22*, 5500.

[14] S. W. Atalla, A. K. Maresca, R. T. Branca, *Sci Rep* **2025**, *15*, 38584.

[15] A. J. Redman, G. Moise, S. Richert, E. J. Peterson, W. K. Myers, M. J. Therien, C. R. Timmel, *J. Phys. Chem. C* **2021**, *125*, 11782.

[16] Y. Ooyama, T. Enoki, J. Ohshita, T. Kamimura, S. Ozako, T. Koide, F. Tani, *RSC Advances* **2017**, *7*, 18690.

[17] F. Sadiq, J. Zhao, M. Hussain, Z. Wang, **2018**.

[18] M. Kasha, *J. Chem. Phys.* **1952**, *20*, 71.

[19] J. Sivanarayanan, K. Vinod, A. Benoy, M. Hariharan, *Chemistry – A European Journal* **2025**, *31*, e202500635.

[20] S. K. Rajagopal, N. K, S. Deb, V. Bhat, D. Sasikumar, E. Sebastian, M. Hariharan, *Phys. Chem. Chem. Phys.* **2018**, *20*, 19120.

[21] M. B. Smith, J. Michl, *Chem. Rev.* **2010**, *110*, 6891.

[22] S. D. Jadhav, D. Sasikumar, M. Hariharan, *Phys. Chem. Chem. Phys.* **2022**, *24*, 16193.

[23] F. S. Conrad-Burton, T. Liu, F. Geyer, R. Costantini, A. P. Schlaus, M. S. Spencer, J. Wang, R. H. Sánchez, B. Zhang, Q. Xu, M. L. Steigerwald, S. Xiao, H. Li, C. P. Nuckolls, X. Zhu, *J. Am. Chem. Soc.* **2019**, *141*, 13143.

[24] E. A. Margulies, C. E. Miller, Y. Wu, L. Ma, G. C. Schatz, R. M. Young, M. R. Wasielewski, *Nature Chem* **2016**, *8*, 1120.

[25] Y. Dong, A. A. Sukhanov, J. Zhao, A. Elmali, X. Li, B. Dick, A. Karatay, V. K. Voronkova, *J. Phys. Chem. C* **2019**, *123*, 22793.

[26] Y. Hou, X. Zhang, K. Chen, D. Liu, Z. Wang, Q. Liu, J. Zhao, A. Barbon, *J. Mater. Chem. C* **2019**, *7*, 12048.

[27] Y. Hou, T. Biskup, S. Rein, Z. Wang, L. Bussotti, N. Russo, P. Foggi, J. Zhao, M. Di Donato, G. Mazzone, S. Weber, *J. Phys. Chem. C* **2018**, *122*, 27850.

[28] A. Mazumder, K. Vinod, P. D. Maret, P. P. Das, M. Hariharan, *J. Phys. Chem. Lett.* **2024**, *15*, 5896.

[29] K. Nagarajan, A. R. Mallia, K. Muraleedharan, M. Hariharan, *Chem. Sci.* **2017**, *8*, 1776.

[30] Y. Liu, M. Lin, Y. Zhao, *J. Phys. Chem. A* **2017**, *121*, 1145.

[31] P. C. Y. Chow, S. Albert-Seifried, S. Gélinas, R. H. Friend, *Advanced Materials* **2014**, *26*, 4851.

[32] H. Chang, L. Tang, Y. Wang, J. Jiang, J. Li, *Anal. Chem.* **2010**, *82*, 2341.

[33] L. Zhao, R. Grande-Aztatzi, C. Foroutan-Nejad, J. M. Ugalde, G. Frenking, *ChemistrySelect* **2017**, *2*, 863.

[34] Y. M. Sung, M.-C. Yoon, J. M. Lim, H. Rath, K. Naoda, A. Osuka, D. Kim, *Nature Chem* **2015**, *7*, 418.

[35] M. A. Baldo, D. F. O'Brien, Y. You, A. Shoustikov, S. Sibley, M. E. Thompson, S. R. Forrest, *Nature* **1998**, *395*, 151.

[36] M. A. El-Sayed, *Acc. Chem. Res.* **1968**, *1*, 8.

[37] B. Valeur, M. N. Berberan-Santos, *J. Chem. Educ.* **2011**, *88*, 731.

[38] C. W. Tang, S. A. VanSlyke, C. H. Chen, *J. Appl. Phys.* **1989**, *65*, 3610.

[39] C. W. Tang, S. A. VanSlyke, *Appl. Phys. Lett.* **1987**, *51*, 913.

[40] G. Hong, X. Gan, C. Leonhardt, Z. Zhang, J. Seibert, J. M. Busch, S. Bräse, *Advanced Materials* **2021**, *33*, 2005630.

[41] C. Adachi, M. A. Baldo, S. R. Forrest, S. Lamansky, M. E. Thompson, R. C. Kwong, *Appl. Phys. Lett.* **2001**, *78*, 1622.

[42] D. Volz, M. Wallesch, C. Fléchon, M. Danz, A. Verma, J. M. Navarro, D. M. Zink, S. Bräse, T. Baumann, *Green Chem.* **2015**, *17*, 1988.

[43] C. A. Parker, C. G. Hatchard, *Trans. Faraday Soc.* **1961**, *57*, 1894.

[44] H. Wang, Y. Yuan, Z. Wang, Y. Wang, *ACS Appl. Eng. Mater.* **2024**, *2*, 781.

[45] H. Uoyama, K. Goushi, K. Shizu, H. Nomura, C. Adachi, *Nature* **2012**, *492*, 234.

[46] P. Keerthika, V. Nutalapati, R. K. Konidena, *J. Mater. Chem. C* **2025**, *13*, 17416.

[47] D. B. Clapp, *J. Am. Chem. Soc.* **1939**, *61*, 523.

[48] C. S. Bilen, N. Harrison, D. J. Morantz, *Nature* **1978**, *271*, 235.

[49] R. Kabe, C. Adachi, *Nature* **2017**, *550*, 384.

[50] O. Bolton, K. Lee, H.-J. Kim, K. Y. Lin, J. Kim, *Nature Chem* **2011**, *3*, 205.

[51] S. Jena, J. Eyyathiyil, S. K. Behera, M. Kitahara, Y. Imai, P. Thilagar, *Chem. Sci.* **2022**, *13*, 5893.

[52] M. Shimizu, A. Kimura, H. Sakaguchi, *European Journal of Organic Chemistry* **2016**, *2016*, 467.

[53] G. Lu, J. Tan, H. Wang, Y. Man, S. Chen, J. Zhang, C. Duan, C. Han, H. Xu, *Nat Commun* **2024**, *15*, 3705.

[54] Y. Zhao, J. Yang, C. Liang, Z. Wang, Y. Zhang, G. Li, J. Qu, X. Wang, Y. Zhang, P. Sun, J. Shi, B. Tong, H.-Y. Xie, Z. Cai, Y. Dong, *Angewandte Chemie International Edition* **2024**, *63*, e202317431.

[55] I. Sánchez-Barragán, J. M. Costa-Fernández, A. Sanz-Medel, M. Valledor, J. C. Campo, *TrAC Trends in Analytical Chemistry* **2006**, *25*, 958.

[56] Y. Meng, W. Liu, Z. Liu, M. Gao, M. Fang, J. Yang, D. Ma, Z. Li, *ACS Appl. Mater. Interfaces* **2024**, *16*, 60658.

[57] J. Zeng, S. Song, Y. Fu, X. Peng, B. Z. Tang, Z. Zhao, *Science Advances* **2025**, *11*, eadt7899.

[58] G. Sgouros, L. Bodei, M. R. McDevitt, J. R. Nedrow, *Nat Rev Drug Discov* **2020**, *19*, 589.

[59] V. Ferraro, C. Bizzarri, S. Bräse, *Advanced Science* **2024**, *11*, 2404866.

[60] D. K. A. Phan Huu, S. Saseendran, R. Dhali, L. G. Franca, K. Stavrou, A. Monkman, A. Painelli, *J. Am. Chem. Soc.* **2022**, *144*, 15211.

[61] R. Dhali, D. K. A. P. Huu, F. Bertocchi, C. Sissa, F. Terenziani, A. Painelli, *Physical Chemistry Chemical Physics* **2021**, *23*, 378.

[62] D. K. A. P. Huu, S. Saseendran, A. Painelli, **2022**.

[63] F. D. Maiolo, D. K. A. P. Huu, D. Giavazzi, A. Landi, O. Racchi, A. Painelli, *Chemical Science* **2024**, *15*, 5434.

[64] C.-Y. Chan, Y.-T. Lee, M. Mamada, K. Goushi, Y. Tsuchiya, H. Nakanotani, C. Adachi, *Chem. Sci.* **2022**, *13*, 7821.

[65] T. Hosokai, H. Matsuzaki, H. Nakanotani, K. Tokumaru, T. Tsutsui, A. Furube, K. Nasu, H. Nomura, M. Yahiro, C. Adachi, *Science Advances* **2017**, *3*, e1603282.

[66] B. Madushani, M. Mamada, K. Goushi, H. Katagiri, H. Nakanotani, T. Hatakeyama, C. Adachi, *Advanced Materials* **2024**, *36*, 2402275.

[67] A. L. Schleper, K. Goushi, C. Bannwarth, B. Haehnle, P. J. Welscher, C. Adachi, A. J. C. Kuehne, *Nat Commun* **2021**, *12*, 6179.

[68] H. Noda, H. Nakanotani, C. Adachi, *Sci Adv* **2018**, *4*, eaao6910.

[69] M. K. Etherington, J. Gibson, H. F. Higginbotham, T. J. Penfold, A. P. Monkman, *Nat Commun* **2016**, *7*, 13680.

[70] J. Gibson, A. P. Monkman, T. J. Penfold, *ChemPhysChem* **2016**, *17*, 2956.

[71] J. S. Ward, R. S. Nobuyasu, A. S. Batsanov, P. Data, A. P. Monkman, F. B. Dias, M. R. Bryce, *Chem. Commun.* **2016**, *52*, 2612.

[72] M. Hempe, N. A. Kukhta, A. Danos, M. A. Fox, A. S. Batsanov, A. P. Monkman, M. R. Bryce, *Chem. Mater.* **2021**, *33*, 3066.

[73] I. A. Wright, M. K. Etherington, A. S. Batsanov, A. P. Monkman, M. R. Bryce, *Chemistry A European J* **2023**, *29*, e202300428.

[74] J. Eng, T. J. Penfold, *Commun Chem* **2021**, *4*, 91.

[75] E. Ullah Mughal, S. Fariha Kainat, A. M. Almohyawi, N. Naeem, E. M. Hussein, A. Sadiq, A. Abd-El-Aziz, N. Ma, A. S. Abd-El-Aziz, A. Timoumi, Z. Moussa, N. Saeed Abbas, S. A. Ahmed, **2025**.

[76] M. K. Etherington, F. Franchello, J. Gibson, T. Northey, J. Santos, J. S. Ward, H. F. Higginbotham, P. Data, A. Kurowska, P. L. Dos Santos, D. R. Graves, A. S. Batsanov, F. B. Dias, M. R. Bryce, T. J. Penfold, A. P. Monkman, *Nat Commun* **2017**, *8*, 14987.

[77] J. U. Kim, I. S. Park, C.-Y. Chan, M. Tanaka, Y. Tsuchiya, H. Nakanotani, C. Adachi, *Nat Commun* **2020**, *11*, 1765.

[78] R. P. Steer, *Photochem. Photobiol. Sci.* **2014**, *13*, 1117.

[79] M. Wilms, D. Tibben, I. Lyskov, S. P. Russo, J. van Embden, E. Della Gaspera, T. U. Connell, D. E. Gómez, *J. Phys. Chem. C* **2024**, *128*, 15041.

[80] G. A. Schick, *Thin Solid Films* **1989**, *179*, 521.

[81] D. Dunlop, L. Ludvíková, A. Banerjee, H. Ottosson, T. Slanina, *J. Am. Chem. Soc.* **2023**, *145*, 21569.

[82] D. Huppert, J. Jortner, P. M. Rentzepis, *Chemical Physics Letters* **1972**, *13*, 225.

[83] J. Li, L. Wang, Z. Zhao, X. Li, X. Yu, P. Huo, Q. Jin, Z. Liu, Z. Bian, C. Huang, *Angewandte Chemie International Edition* **2020**, *59*, 8210.

[84] X.-B. Cai, D. Liang, D.-C. Zhang, J.-H. Jia, X.-Y. Wu, C.-Z. Lu, *Chem. Sci.* **2025**, *16*, 9802.

[85] N. A. Kukhta, M. R. Bryce, *Mater. Horiz.* **2021**, *8*, 33.

[86] P. J. Conaghan, C. S. B. Matthews, F. Chotard, S. T. E. Jones, N. C. Greenham, M. Bochmann, D. Credgington, A. S. Romanov, *Nat Commun* **2020**, *11*, 1758.

[87] S. Shi, M. C. Jung, C. Coburn, A. Tadle, D. Sylvinson M. R., P. I. Djurovich, S. R. Forrest, M. E. Thompson, *J. Am. Chem. Soc.* **2019**, *141*, 3576.

[88] T. Li, D. S. Muthiah Ravinson, R. Haiges, P. I. Djurovich, M. E. Thompson, *J. Am. Chem. Soc.* **2020**, *142*, 6158.

[89] Carbazole - an overview | ScienceDirect Topics, .

[90] K. Radhakrishna, S. B. Manjunath, D. Devadiga, R. Chetri, A. T. Nagaraja, *ACS Appl. Energy Mater.* **2023**, *6*, 3635.

[91] P. S. Waghmare, A. R. Chabukswar, K. G. Raut, P. T. Giri, *Chirality* **2025**, *37*, e70021.

[92] S. Oner, M. R. Bryce, *Mater. Chem. Front.* **2023**, *7*, 4304.

[93] Q. Ullah, A. Rahman, M. Arifuddin, I. Khan, N. H. Ansari, P. A. Ali Khan, *J Fluoresc* **2025**, *35*, 7475.

[94] K. Panthi, R. M. Adhikari, T. H. Kinstle, *J. Phys. Chem. A* **2010**, *114*, 4550.

[95] D. P. Chakraborty, B. K. Barman, P. K. Bose, *Tetrahedron* **1965**, *21*, 681.

[96] P. Ledwon, *Organic Electronics* **2019**, *75*, 105422.

[97] K. Ivaniuk, P. Stakhira, I. Yaremchuk, S. Kutsiy, T. Bulavinets, D. Volyniuk, I. Klymenko, G. Sych, N. Karaush-Karmazin, A. Ali, A. Vaitusionak, S. V. Kostjuk, J. V. Grazulevicius, G. V. Baryshnikov, *ACS Appl. Electron. Mater.* **2023**, *5*, 2156.

[98] Sanyam, N. Tejiyan, A. Mondal, *Mater. Adv.* **2025**, *6*, 6978.

[99] S. Oner, M. R. Bryce, *Mater. Chem. Front.* **2023**, *7*, 4304.

[100] G. Yuan, Y.-C. Wang, Z. Zhang, J.-Y. Liu, Y.-H. He, G.-W. Chen, Y.-Q. Li, J.-X. Tang, *Nat Commun* **2025**, *16*, 10461.

[101] G. Turkoglu, M. E. Cinar, T. Ozturk, *Molecules* **2017**, *22*, 1522.

[102] M. Mamada, S. Yada, M. Hayakawa, R. Uchida, H. Katagiri, T. Hatakeyama, C. Adachi, *Commun Chem* **2024**, *7*, 1.

[103] G. Grybauskaite-Kaminskiene, K. Ivaniuk, G. Bagdziunas, P. Turyk, P. Stakhira, G. Baryshnikov, D. Volyniuk, V. Cherpak, B. Minaev, Z. Hotra, H. Ågren, J. V. Grazulevicius, *J. Mater. Chem. C* **2018**, *6*, 1543.

[104] K. Ivaniuk, V. Cherpak, P. Stakhira, Z. Hotra, B. Minaev, G. Baryshnikov, E. Stromylo, D. Volyniuk, J. V. Grazulevicius, A. Lazauskas, S. Tamulevicius, B. Witulski, M. E. Light, P. Gawrys, R. J. Whitby, G. Wiosna-Salyga, B. Luszczynska, *J. Phys. Chem. C* **2016**, *120*, 6206.

[105] R. Butkute, R. Lygaitis, V. Mimaite, D. Gudeika, D. Volyniuk, G. Sini, J. V. Grazulevicius, *Dyes and Pigments* **2017**, *146*, 425.

[106] F. B. Dias, K. N. Bourdakos, V. Jankus, K. C. Moss, K. T. Kamtekar, V. Bhalla, J. Santos, M. R. Bryce, A. P. Monkman, *Advanced Materials* **2013**, *25*, 3707.

[107] R. M. Adhikari, D. C. Neckers, *J. Phys. Chem. A* **2009**, *113*, 417.

[108] R. Hiyoshi, H. Hiura, Y. Sakamoto, M. Mizuno, M. Sakai, H. Takahashi, *Journal of Molecular Structure* **2003**, *661–662*, 481.

[109] B. Bezgin Carbas, *ACS Appl. Polym. Mater.* **2025**, *7*, 4051.

[110] R. A. Shaukat, S. Ameen, Q. M. Saqib, M. Y. Chougale, J. Kim, S. R. Patil, M. Noman, H. K. Kim, J. Bae, *J. Mater. Chem. A* **2023**, *11*, 14800.

[111] V. Dippold, H. Küçükkeçeci, E. Bosler, J. Schmidt, S. Ghosh, G. Michl, I. E. Khalil, L. Gerland, A. Lange, D. Oberschmidt, A. Thomas, *Advanced Materials* **2025**, *37*, 2506689.

[112] M. A. Baldo, D. F. O'Brien, M. E. Thompson, S. R. Forrest, *Phys. Rev. B* **1999**, *60*, 14422.

[113] J. Sivanarayanan, E. Sebastian, K. Vinod, F. Würthner, M. Hariharan, *J. Phys. Chem. C* **2022**, *126*, 13319.

[114] K. Vinod, S. D. Jadhav, M. Hariharan, *Chemistry – A European Journal* **2024**, *30*, e202400499.

[115] S. K. Behera, S. Y. Park, J. Gierschner, *Angewandte Chemie International Edition* **2021**, *60*, 22624.

[116] C. W. Tang, S. A. VanSlyke, *Applied Physics Letters* **1987**, *51*, 913.

[117] Z. An, C. Zheng, Y. Tao, R. Chen, H. Shi, T. Chen, Z. Wang, H. Li, R. Deng, X. Liu, W. Huang, *Nat Mater* **2015**, *14*, 685.

[118] J. Chan, S. C. Dodani, C. J. Chang, *Nature Chem* **2012**, *4*, 973.

[119] R. Gao, X. Mei, D. Yan, R. Liang, M. Wei, *Nat Commun* **2018**, *9*, 2798.

[120] J. Yang, X. Gao, Z. Xie, Y. Gong, M. Fang, Q. Peng, Z. Chi, Z. Li, *Angewandte Chemie International Edition* **2017**, *56*, 15299.

[121] Q. Liao, Q. Gao, J. Wang, Y. Gong, Q. Peng, Y. Tian, Y. Fan, H. Guo, D. Ding, Q. Li, Z. Li, *Angewandte Chemie International Edition* **2020**, *59*, 9946.

[122] X. Liang, T.-T. Liu, Z.-P. Yan, Y. Zhou, J. Su, X.-F. Luo, Z.-G. Wu, Y. Wang, Y.-X. Zheng, J.-L. Zuo, *Angewandte Chemie International Edition* **2019**, *58*, 17220.

[123] H.-T. Feng, J. Zeng, P.-A. Yin, X.-D. Wang, Q. Peng, Z. Zhao, J. W. Y. Lam, B. Z. Tang, *Nat Commun* **2020**, *11*, 2617.

[124] M. Hariharan, *Crystal Growth & Design* **2022**, *22*, 2046.

[125] M. A. Niyas, R. Ramakrishnan, V. Vijay, E. Sebastian, M. Hariharan, *J. Am. Chem. Soc.* **2019**, *141*, 4536.

[126] A. Tabey, P. Y. Vemuri, F. W. Patureau, *Chemical Science* **2021**, *12*, 14343.

[127] W. H. Perkin, S. H. Tucker, *J. Chem. Soc., Trans.* **1921**, *119*, 216.

[128] K. Szalewicz, *WIREs Computational Molecular Science* **2012**, *2*, 254.

[129] M. A. Spackman, D. Jayatilaka, *CrystEngComm* **2009**, *11*, 19.

[130] L. Loots, L. J. Barbour, *CrystEngComm* **2011**, *14*, 300.

[131] H. A. Abro, T. Zhou, W. Han, T. Xue, T. Wang, *RSC Adv.* **2017**, *7*, 55382.

[132] J. T. Yi, L. Alvarez-Valtierra, D. W. Pratt, *The Journal of Chemical Physics* **2006**, *124*, 244302.

[133] K. M. Knötig, D. Gust, T. Lenzer, K. Oum, *Photochem* **2024**, *4*, 163.

[134] J. Eng, S. Thompson, H. Goodwin, D. Credgington, T. J. Penfold, *Phys. Chem. Chem. Phys.* **2020**, *22*, 4659.

[135] M. Mońka, D. Grzywacz, E. Hoffman, V. Ievtukhov, K. Kozakiewicz, R. Rogowski, A. Kubicki, B. Liberek, P. Bojarski, I. E. Serdiuk, *J. Mater. Chem. C* **2022**, *10*, 11719.

[136] E. Sebastian, M. Hariharan, *Angewandte Chemie International Edition* **2023**, *62*, e202216482.

[137] E. Sebastian, M. Hariharan, *J. Am. Chem. Soc.* **2021**, *143*, 13769.

[138] E. Sebastian, A. M. Philip, A. Benny, M. Hariharan, *Angewandte Chemie International Edition* **2018**, *57*, 15696.

[139] A. Mazumder, K. Vinod, P. D. Maret, P. P. Das, M. Hariharan, *J. Phys. Chem. Lett.* **2024**, *15*, 5896.

[140] N. N. M. Y. Chan, A. Idris, Z. H. Z. Abidin, H. Anuar Tajuddin, Z. Abdullah, *RSC Advances* **2021**, *11*, 13409.

[141] P. Pander, A. Swist, J. Soloducho, F. B. Dias, *Dyes and Pigments* **2017**, *142*, 315.

[142] J. Herbich, A. Kapturkiewicz, J. Nowacki, *Chemical Physics Letters* **1996**, *262*, 633.

[143] J. Yang, X. Zhen, B. Wang, X. Gao, Z. Ren, J. Wang, Y. Xie, J. Li, Q. Peng, K. Pu, Z. Li, *Nat Commun* **2018**, *9*, 840.

[144] J. Wang, C. Wang, Y. Gong, Q. Liao, M. Han, T. Jiang, Q. Dang, Y. Li, Q. Li, Z. Li, *Angewandte Chemie International Edition* **2018**, *57*, 16821.

[145] M. Shimizu, R. Shigitani, M. Nakatani, K. Kuwabara, Y. Miyake, K. Tajima, H. Sakai, T. Hasobe, *J. Phys. Chem. C* **2016**, *120*, 11631.

[146] W. Z. Yuan, X. Y. Shen, H. Zhao, J. W. Y. Lam, L. Tang, P. Lu, C. Wang, Y. Liu, Z. Wang, Q. Zheng, J. Z. Sun, Y. Ma, B. Z. Tang, *J. Phys. Chem. C* **2010**, *114*, 6090.

[147] A. Y. Baranov, A. S. Berezin, D. G. Samsonenko, A. S. Mazur, P. M. Tolstoy, V. F. Plyusnin, I. E. Kolesnikov, A. V. Artem'ev, *Dalton Trans.* **2020**, *49*, 3155.

[148] M. K. Etherington, J. Gibson, H. F. Higginbotham, T. J. Penfold, A. P. Monkman, *Nat Commun* **2016**, *7*, 13680.

[149] J. Gibson, A. P. Monkman, T. J. Penfold, *ChemPhysChem* **2016**, *17*, 2956.

[150] T. J. Penfold, E. Gindensperger, C. Daniel, C. M. Marian, *Chem. Rev.* **2018**, *118*, 6975.

[151] M. Martin, E. Breheret, F. Tfibel, B. Lacourbas, *J. Phys. Chem.* **1980**, *84*, 70.

[152] G. L. Thornton, R. Phelps, A. J. Orr-Ewing, *Phys. Chem. Chem. Phys.* **2021**, *23*, 18378.

[153] X. Wang, L. Martínez-Fernández, Y. Zhang, K. Zhang, R. Improta, B. Kohler, J. Xu, J. Chen, *Chemistry – A European Journal* **2021**, *27*, 10932.

[154] M. Lv, X. Wang, D. Wang, X. Li, Y. Liu, H. Pan, S. Zhang, J. Xu, J. Chen, *Phys. Chem. Chem. Phys.* **2021**, *23*, 25455.

[155] R. L. Martin, *J. Chem. Phys.* **2003**, *118*, 4775.

[156] F. Plasser, *J. Chem. Phys.* **2020**, *152*.

[157] F. Plasser, H. Lischka, *J. Chem. Theory Comput.* **2012**, *8*, 2777.

[158] T. Serevičius, S. Tumkevičius, J. Dodonova-Vaitkūnienė, S. Juršėnas, *J. Phys. Chem. Lett.* **2025**, *16*, 3100.

[159] F. B. Dias, K. N. Bourdakos, V. Jankus, K. C. Moss, K. T. Kamtekar, V. Bhalla, J. Santos, M. R. Bryce, A. P. Monkman, *Adv Mater* **2013**, *25*, 3707.

[160] H. Uoyama, K. Goushi, K. Shizu, H. Nomura, C. Adachi, *Nature* **2012**, *492*, 234.

[161] Q. Zhang, J. Li, K. Shizu, S. Huang, S. Hirata, H. Miyazaki, C. Adachi, *J. Am. Chem. Soc.* **2012**, *134*, 14706.

[162] Citation | Gaussian.com, .

[163] J. J. Snellenburg, S. Laptenok, R. Seger, K. M. Mullen, I. H. M. van Stokkum, *Journal of Statistical Software* **2012**, *49*, 1.

[164] A. E. R. Watson, S. Y. Tao, A. Siemiarczuk, P. D. Boyle, P. J. Ragogna, J. B. Gilroy, *Angewandte Chemie* **2025**, *137*, e202414534.

[165] G. Lu, J. Tan, H. Wang, Y. Man, S. Chen, J. Zhang, C. Duan, C. Han, H. Xu, *Nat Commun* **2024**, *15*, 3705.

[166] Carbazole isomers induce ultralong organic phosphorescence | Nature Materials, .

[167] P. S. Waghmare, A. R. Chabukswar, K. G. Raut, P. T. Giri, *Chirality* **2025**, *37*, e70021.

[168] S. M. Kasim, B. M. Al-Dabbagh, Y. F. Mustafa, *Eurasian Chemical Communications* **2022**, *4*, 495.

[169] P. Ledwon, *Organic Electronics* **2019**, *75*, 105422.

[170] P. Naik, K. S. Keremane, M. R. Elmorsy, A. El-Shafei, A. V. Adhikari, *Electrochemical Science Advances* **2022**, *2*, e2100061.

[171] B. Wex, B. R. Kaafarani, *J. Mater. Chem. C* **2017**, *5*, 8622.

[172] ja049883asi20040219_051936-SI.

[173] Y. Sato, T. Taira, *Opt. Mater. Express, OME* **2022**, *12*, 1397.

[174] A. van der Lee, D. G. Dumitrescu, *Chemical Science* **2021**, *12*, 8537.

[175] P. Wen, Z. Gao, R. Zhang, A. Li, F. Zhang, J. Li, J. Xie, Y. Wu, M. Wu, K. Guo, *J. Mater. Chem. C* **2017**, *5*, 6136.

[176] A. T. John, A. Narayanasamy, D. George, M. Hariharan, *J. Phys. Chem. C* **2021**, *125*, 10716.

[177] E. Sebastian, M. Hariharan, *ACS Energy Lett.* **2022**, *7*, 696.

[178] W. E. Ford, H. Hiratsuka, P. V. Kamat, *J. Phys. Chem.* **1989**, *93*, 6692.

[179] H. Wang, C. Gong, P. Jin, C. Guo, D. Wang, G. Xu, Y. Peng, *Chem. Commun.* **2022**, *58*, 9798.

[180] S. Kuila, H. Miranda-Salinas, J. Eng, C. Li, M. R. Bryce, T. J. Penfold, A. P. Monkman, *Nat Commun* **2024**, *15*, 9611.

[181] M. Mamada, K. Inada, T. Komino, W. J. Jr. Potscavage, H. Nakanotani, C. Adachi, *ACS Cent. Sci.* **2017**, *3*, 769.

[182] H. Nakanotani, K. Masui, J. Nishide, T. Shibata, C. Adachi, *Sci Rep* **2013**, *3*, 2127.

[183] Q. Zhang, B. Li, S. Huang, H. Nomura, H. Tanaka, C. Adachi, *Nature Photon* **2014**, *8*, 326.

[184] O. D. Bernardinelli, S. M. Cassemiro, L. A. O. Nunes, T. D. Z. Atvars, L. Akcelrud, E. R. deAzevedo, *J. Phys. Chem. B* **2012**, *116*, 5993.

[185] F. N. Castellano, *Acc. Chem. Res.* **2015**, *48*, 828.

[186] M. Gemmi, E. Mugnaioli, T. E. Gorelik, U. Kolb, L. Palatinus, P. Boullay, S. Hovmöller, J. P. Abrahams, *ACS Cent. Sci.* **2019**, *5*, 1315.

[187] D. L. Dorset, *Acta Crystallographica Section B* **1996**, *52*, 753.

[188] Electron crystallography - Dorset - 1996 - Acta Crystallographica Section B - Wiley Online Library, .

[189] T. Gruene, J. J. Holstein, G. H. Clever, B. Keppler, *Nat Rev Chem* **2021**, *5*, 660.

[190] Y. Luo, B. Wang, S. Smeets, J. Sun, W. Yang, X. Zou, *Nat. Chem.* **2023**, *15*, 483.

[191] G. Yang, S. Hao, Z. Zhang, W. Z. Yuan, M.-D. Li, L. Dang, *Nat Commun* **2025**, *16*, 8927.

[192] N. A. Kukhta, M. R. Bryce, *Mater. Horiz.* **2021**, *8*, 33.

[193] S. Dey, M. Hasan, A. Shukla, N. Acharya, M. Upadhyay, S.-C. Lo, E. B. Namdas, D. Ray, *J. Phys. Chem. C* **2022**, *126*, 5649.

[194] R. Hamze, S. Shi, S. C. Kapper, D. S. Muthiah Ravinson, L. Estergreen, M.-C. Jung, A. C. Tadle, R. Haiges, P. I. Djurovich, J. L. Peltier, R. Jazzar, G. Bertrand, S. E. Bradforth, M. E. Thompson, *J. Am. Chem. Soc.* **2019**, *141*, 8616.

[195] K. Brunner, A. van Dijken, H. Börner, J. J. A. M. Bastiaansen, N. M. M. Kiggen, B. M. W. Langeveld, *J. Am. Chem. Soc.* **2004**, *126*, 6035.

[196] F. Mauri, *Phys. Rev. Lett.* **1996**, *77*, 5300.

[197] S. J. Clark, M. D. Segall, C. J. Pickard, P. J. Hasnip, M. I. J. Probert, K. Refson, M. C. Payne, *Zeitschrift für Kristallographie - Crystalline Materials* **2005**, *220*, 567.

[198] J. R. Yates, C. J. Pickard, F. Mauri, *Phys. Rev. B* **2007**, *76*, 024401.

[199] A. Tkatchenko, M. Scheffler, *Phys. Rev. Lett.* **2009**, *102*, 073005.

[200] J. P. Perdew, A. Ruzsinszky, G. I. Csonka, O. A. Vydrov, G. E. Scuseria, L. A. Constantin, X. Zhou, K. Burke, *Phys. Rev. Lett.* **2008**, *100*, 136406.

[201] K. Vinod, R. Mathew, C. Jandl, B. Thomas, M. Hariharan, *Chemical Science* **2024**, *15*, 16015.

[202] R. Mathew, A. Mazumder, P. Kumar, J. Matula, S. Mohamed, P. Brazda, M. Hariharan, B. Thomas, *Chemical Science* **2024**, *15*, 490.

[203] J. Wang, L. Yao, *Sci Rep* **2019**, *9*, 20149.

[204] M. Nishio, *CrystEngComm* **2004**, *6*, 130.

[205] J.-N. Li, D. Chen, Y. Wang, J. Li, Y. Chai, X. Xiao, X. Li, J.-P. Xue, *Inorg. Chem.* **2024**, *63*, 8286.

[206] C. Herrmann, *J. Phys. Chem. A* **2019**, *123*, 10205.

[207] M. Woodhouse, C. L. Perkins, M. T. Rawls, R. A. Cormier, Z. Liang, A. M. Nardes, B. A. Gregg, *J. Phys. Chem. C* **2010**, *114*, 6784.

[208] G. Padmanaban, S. Ramakrishnan, *J. Am. Chem. Soc.* **2000**, *122*, 2244.

[209] K. P. Wall, R. Dillon, M. K. Knowles, *Biochemistry and Molecular Biology Education* **2015**, *43*, 52.

[210] Y. Huang, J. Xing, Q. Gong, L.-C. Chen, G. Liu, C. Yao, Z. Wang, H.-L. Zhang, Z. Chen, Q. Zhang, *Nat Commun* **2019**, *10*, 169.

[211] X. Ma, R. Sun, J. Cheng, J. Liu, F. Gou, H. Xiang, X. Zhou, *J. Chem. Educ.* **2016**, *93*, 345.

[212] K. Zhang, J. Liu, Y. Zhang, J. Fan, C.-K. Wang, L. Lin, *J. Phys. Chem. C* **2019**, *123*, 24705.

[213] Q. Xu, A. D. Scully, M. A. Skidmore, H. Ke, X. Wu, J. Li, Z. Zhang, X. Li, K. Ueno, *J. Mater. Chem. C* **2024**, *12*, 15039.

[214] X. Tang, R. Pan, X. Zhao, H. Zhu, Z. Xiong, *J. Phys. Chem. Lett.* **2020**, *11*, 2804.

[215] M. Hagai, N. Inai, T. Yasuda, K. J. Fujimoto, T. Yanai, *Science Advances* **2024**, *10*, eadk3219.

[216] M. Hagai, N. Inai, T. Yasuda, K. J. Fujimoto, T. Yanai, *Science Advances* **2024**, *10*, eadk3219.

[217] T. Serevičius, R. Skaisgiris, D. Gudeika, K. Kazlauskas, S. Juršėnas, **2021**.

[218] L. Zhang, K. W. Cheah, *Sci Rep* **2018**, *8*, 8832.

[219] Y. Yang, Z. Jiang, Y. Liu, T. Guan, Q. Zhang, C. Qin, K. Jiang, Y. Liu, *J. Phys. Chem. Lett.* **2022**, *13*, 9381.

[220] T. Micklitz, *Phys. Rev. Lett.* **2022**, *129*.

[221] A. Landi, D. K. A. Phan Huu, A. Painelli, *J. Phys. Chem. C* **2024**, *128*, 18598.

[222] B. de Souza, F. Neese, R. Izsák, *J. Chem. Phys.* **2018**, *148*, 034104.

[223] Q. Peng, Y. Yi, Z. Shuai, J. Shao, *J. Chem. Phys.* **2007**, *126*, 114302.

[224] Y. R. Poh, S. Pannir-Sivajothi, J. Yuen-Zhou, *J. Phys. Chem. C* **2023**, *127*, 5491.

[225] T. Kim, G. Shin, T. Park, M. Kim, *Advanced Functional Materials* **2025**, *35*, 2412267.

[226] J. R. Yates, C. J. Pickard, F. Mauri, *Phys. Rev. B* **2007**, *76*, 024401.

List of Publications

Published

❖ **Sivanarayanan J**., Vinod K., Benoy A., and Hariharan M.*, Unlocking the Room Temperature Phosphorescence through Halogen Engineering in Carbazole Dimer, Chem. Eur. J., 2025, 31: e202500635.

❖ **Sivanarayanan J.**, Sebastian E., Vinod K., Wüthner F., and Hariharan M.*, Ultrafast Intersystem Crossing in Selenium-Annulated Perylene Bisimide, J. Phys. Chem. C 2022, 126, 31, 13319–13326.

Submitted

❖ **Sivanarayanan J.**, Suresh S. Vinod K., and Hariharan M.*, Topological Control of Excited-State Dynamics in Carbazole Trimers (Submitted).

❖ **Sivanarayanan J.**, Vinod K., Suresh S. Tharamel. A., Thomas B., and Hariharan M.*, 3D Electron Diffraction Reveals the Structural Origin of Delayed Dual Emission in a Heavy-Atom-Free Carbazole Hexamer (Submitted).

❖ **Sivanarayanan J.**, Saji S., Bhatt V. and Hariharan M.*, Halogen-Mediated Switching of Emission Pathways in Carbazole–Pentafluoro-benzaldehyde Co-crystals: From TADF to RTP (Under preparation).

❖ **Sivanarayanan J**., Muralidharanan A., Tharamel A., and Hariharan M., Structural Planarization in Carbazole Dimer Enables Room Temperature Phosphorescence, (Under preparation).

❖ Patra S., **Sivanarayanan J.**, Bhat V., Maret P. D., Bhattacharyya A., Ghosh S., Hariharan M.*, Tiwari V.* (Submitted).

Workshops and Conferences

1. Presented a poster in the **32nd International Conference on Photochemistry 2025 (ICP 2025)** at Aachen, Germany (July 13-18, 2025)

2. Invited talk in Julius-Maximilians-Universität Würzburg, Germany (July 22, 2025)

3. Participated in the **International Research Training Group (IRTG) 2991 Startup Meeting** at IISER Thiruvananthapuram, India (February 25-28, 2025)

4. Participated in the **12th International Symposium on Dynamic Exciton (ISDyEx 2024)**, Thiruvananthapuram, India (December 14-15, 2024).

5. Participated in the **ChemSci 2024 LITF Symposium**, IISER Thiruvananthapuram, India (December 9-11, 2024).

6. Presented a poster in the **National Workshop on Fluorescence and Raman Spectroscopy (FCS XIV)**, IISER Mohali, India (December 09-15, 2023).

7. Facilitator at **Yusuf Hamied Chemistry Camp**, IISER Thiruvananthapuram, India (July 19-21, 2023).

8. Presented a poster in the **3rd Edition of the Annual Symposium, Frontier Symposium in Chemistry 2023 (FS-CHM 2023)**, IISER Thiruvananthapuram, India (January 13-15, 2023).

9. Presented a poster in the **13th National workshop on Fluorescence and Raman Spectroscopy (FCSXIII)**, Fluorescence Chemical Society, IISER Thiruvananthapuram and RGCB, India (January 06-11, 2023).

10. Presented a poster in the **9th Theme meeting on Ultrafast Sciences (UFS 2022)**, IISER Thiruvananthapuram, India (November 03-05, 2022).

11. Presented a poster in the **2nd Edition of the Annual Symposium, Frontier Symposium in Chemistry 2022 (FS-CHM 2022)**, IISER Thiruvananthapuram, India (April 08-10, 2022).

12. Participated in the **12th National workshop on Fluorescence and Raman Spectroscopy (FCS 2021)**, Fluorescence Chemical Society, IISER Thiruvananthapuram and RGCB, India (November 29-December 4, 2021).

13. Participated in the **Virtual Chemistry Course "Functional π-Systems – Organic Materials Design by Molecular and Supramolecular Engineering"**, Department of Chemistry & Pharmacy at the Julius-Maximilians-Universität Würzburg,

Germany (July 19- 23, 2021).

14. Participated in the **International Conference on Ultrafast Spectroscopy (ICUS 2020)**, IISER TVM, Kerala, India February 21-22, 2020).

15. Participated in the **IISERTVM-RSC Symposium on Advances in Chemical Sciences**, IISER TVM, Kerala, India (February 4, 2020).

Achievements in Workshops and Conferences

1. **Opportunity to present my work at** Julius-Maximilians-Universität Würzburg, Germany (July 22, 2025)

2. Best Poster Award at **Ultrafast Sciences (UFS 2022),** IISER Thiruvananthapuram, India (November 03-05, 2022).

Copyrights and Permissions

Order Details

1. Physical chemistry chemical physics

Article: Extending the scope of the carbonyl facilitated triplet excited state towards visible light excitation.

Billing Status: Open

Print License

Order License ID	1682261-1	**Type of Use**	Republish in a thesis/dissert...
Order detail status	Completed	**Publisher**	ROYAL SOCIETY OF CHEMIS...
ISSN	1463-9084	**Portion**	Chart/graph/table/figure

0.00 USD

Republication Permission

Hide Details

LICENSED CONTENT

Publication Title	Physical chemistry chemical ...	**Publication Type**	e-Journal
Article Title	Extending the scope of the c...	**Start Page**	19120
Author / Editor	Royal Society of Chemistry (...	**End Page**	19128
Date	01/01/1999	**Issue**	28
Language	English	**Volume**	20
Country	United Kingdom of Great Bri...	**URL**	http://firstsearch.oclc.org/jo...
Rightsholder	Royal Society of Chemistry		

REQUEST DETAILS

Portion Type	Chart/graph/table/figure	**Distribution**	Worldwide
Number of Charts / Graphs / Tables / Figures Requested	1	**Translation**	Original language of publica...
		Copies for the Disabled?	No
Format (select all that apply)	Electronic	**Minor Editing Privileges?**	No
Who Will Republish the Content?	Academic institution	**Incidental Promotional Use?**	Yes
Duration of Use	Current edition and up to 5 ...	**Currency**	USD
Lifetime Unit Quantity	Up to 499		
Rights Requested	Main product		

NEW WORK DETAILS

Title	Structural Modulation of Ca...	**Institution Name**	IISER Thiruvananthapuram
Instructor Name	Prof. Mahesh Hariharan	**Expected Presentation Date**	2026-02-26

ADDITIONAL DETAILS

The Requesting Person / Organization to Appear on the License	Jibin Sivanarayanan, IISER T...

REQUESTED CONTENT DETAILS

Title, Description or Numeric Reference of the Portion(s)	Jablonski diagrams for (a) Py...	**Title of the Article / Chapter the Portion Is From**	Extending the scope of the c...
		Author of Portion(s)	Bhat, Vinayak; Deb, Somadri...
Editor of Portion(s)	Bhat, Vinayak; Deb, Somadri...	**Issue, if Republishing an Article From a Serial**	28
Volume / Edition	20		
Page or Page Range of Portion	19120-19128	**Publication Date of Portion**	2018-07-18

Enhanced intersystem crossing in core-twisted aromatics

K. Nagarajan, A. R. Mallia, K. Muraleedharan and M. Hariharan, *Chem. Sci.*, 2017, **8**, 1776 **DOI:** 10.1039/C6SC05126J

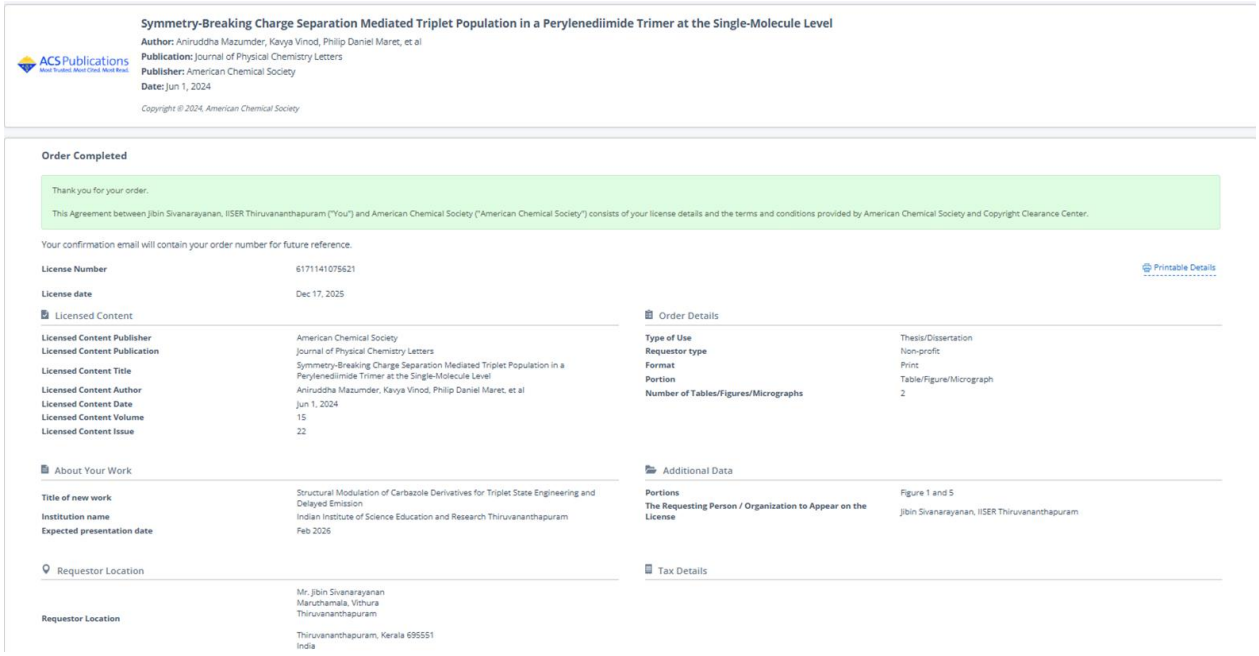

Symmetry-Breaking Charge Separation Mediated Triplet Population in a Perylenediimide Trimer at the Single-Molecule Level

Author: Aniruddha Mazumder, Kavya Vinod, Philip Daniel Maret, et al
Publication: Journal of Physical Chemistry Letters
Publisher: American Chemical Society
Date: Jun 1, 2024

Copyright © 2024, American Chemical Society

Order Completed

Thank you for your order.

This Agreement between Jibin Sivanarayanan, IISER Thiruvananthapuram ("You") and American Chemical Society ("American Chemical Society") consists of your license details and the terms and conditions provided by American Chemical Society and Copyright Clearance Center.

Your confirmation email will contain your order number for future reference.

Printable Details

License Number	6171141075621
License date	Dec 17, 2025

Licensed Content

Licensed Content Publisher	American Chemical Society
Licensed Content Publication	Journal of Physical Chemistry Letters
Licensed Content Title	Symmetry-Breaking Charge Separation Mediated Triplet Population in a Perylenediimide Trimer at the Single-Molecule Level
Licensed Content Author	Aniruddha Mazumder, Kavya Vinod, Philip Daniel Maret, et al
Licensed Content Date	Jun 1, 2024
Licensed Content Volume	15
Licensed Content Issue	22

Order Details

Type of Use	Thesis/Dissertation
Requestor type	Non-profit
Format	Print
Portion	Table/Figure/Micrograph
Number of Tables/Figures/Micrographs	2

About Your Work

Title of new work	Structural Modulation of Carbazole Derivatives for Triplet State Engineering and Delayed Emission
Institution name	Indian Institute of Science Education and Research Thiruvananthapuram
Expected presentation date	Feb 2026

Additional Data

Portions	Figure 1 and 5
The Requesting Person / Organization to Appear on the License	Jibin Sivanarayanan, IISER Thiruvananthapuram

Requestor Location

Requestor Location	Mr. Jibin Sivanarayanan Maruthamala, Vithura Thiruvananthapuram Thiruvananthapuram, Kerala 695551 India

Tax Details

SPRINGER NATURE

Reversal of Hückel (anti)aromaticity in the lowest triplet states of hexaphyrins and spectroscopic evidence for Baird's rule

Author: Young Mo Sung et al
Publication: Nature Chemistry
Publisher: Springer Nature
Date: Apr 13, 2015

Order Completed

Thank you for your order.

This Agreement between Jibin Sivanarayanan, IISER Thiruvananthapuram ("You") and Springer Nature ("Springer Nature") consists of your license details and the terms and conditions provided by Springer Nature and Copyright Clearance Center.

Your confirmation email will contain your order number for future reference.

Printable Details

License Number	6171140809932
License date	Dec 17, 2025

Licensed Content

Licensed Content Publisher	Springer Nature
Licensed Content Publication	Nature Chemistry
Licensed Content Title	Reversal of Hückel (anti)aromaticity in the lowest triplet states of hexaphyrins and spectroscopic evidence for Baird's rule
Licensed Content Author	Young Mo Sung et al
Licensed Content Date	Apr 13, 2015

Order Details

Type of Use	Thesis/Dissertation
Requestor Type	academic/university or research institute
Format	print and electronic
Portion	figures/tables/illustrations
Number of figures/tables/illustrations	1
Would you like a high resolution image with your order?	no
Will you be translating?	no
Circulation/distribution	1 - 29
Author of this Springer Nature content	no

About Your Work

Title of new work	Structural Modulation of Carbazole Derivatives for Triplet State Engineering and Delayed Emission
Institution name	Indian Institute of Science Education and Research Thiruvananthapuram
Expected presentation date	Feb 2026

Additional Data

Portions	Figure 3
The Requesting Person / Organization to Appear on the License	Jibin Sivanarayanan, IISER Thiruvananthapuram

Requestor Location

Requestor Location	Mr. Jibin Sivanarayanan Maruthamala, Vithura Thiruvananthapuram

Tax Details

SPRINGER NATURE

Activating efficient phosphorescence from purely organic materials by crystal design

Author: Onas Bolton et al
Publication: Nature Chemistry
Publisher: Springer Nature
Date: Feb 13, 2011

Order Completed

Thank you for your order.

This Agreement between Jibin Sivanarayanan, IISER Thiruvananthapuram ("You") and Springer Nature ("Springer Nature") consists of your license details and the terms and conditions provided by Springer Nature and Copyright Clearance Center.

Your confirmation email will contain your order number for future reference.

Printable Details

License Number	6171110530692
License date	Dec 16, 2025

Licensed Content

Licensed Content Publisher	Springer Nature
Licensed Content Publication	Nature Chemistry
Licensed Content Title	Activating efficient phosphorescence from purely organic materials by crystal design
Licensed Content Author	Onas Bolton et al
Licensed Content Date	Feb 13, 2011

Order Details

Type of Use	Thesis/Dissertation
Requestor Type	academic/university or research institute
Format	print and electronic
Portion	figures/tables/illustrations
Number of figures/tables/illustrations	1
Would you like a high resolution image with your order?	no
Will you be translating?	no
Circulation/distribution	1 - 29
Author of this Springer Nature content	no

About Your Work

Title of new work	Structural Modulation of Carbazole Derivatives for Triplet State Engineering and Delayed Emission
Institution name	Indian Institute of Science Education and Research Thiruvananthapuram
Expected presentation date	Feb 2026

Additional Data

Portions	Figure 1
The Requesting Person / Organization to Appear on the License	Jibin Sivanarayanan, IISER Thiruvananthapuram

Requestor Location

Requestor Location	Mr. Jibin Sivanarayanan Maruthamala, Vithura Thiruvananthapuram Thiruvananthapuram, Kerala 695551 India

Tax Details

Room-Temperature Phosphorescence of Crystalline 1,4-Bis(aroyl)-2,5-dibromobenzenes

Author: Masaki Shimizu, Akinori Kimura, Hiroshi Sakaguchi
Publication: European Journal of Organic Chemistry
Publisher: John Wiley and Sons
Date: Jan 5, 2016

Order Completed

Thank you for your order.

This Agreement between Jibin Sivanarayanan, IISER Thiruvananthapuram ("You") and John Wiley and Sons ("John Wiley and Sons") consists of your license details and the terms and conditions provided by John Wiley and Sons and Copyright Clearance Center.

Your confirmation email will contain your order number for future reference.

Printable Details

License Number	6171111293686
License date	Dec 16, 2025

Licensed Content

Licensed Content Publisher	John Wiley and Sons
Licensed Content Publication	European Journal of Organic Chemistry
Licensed Content Title	Room-Temperature Phosphorescence of Crystalline 1,4-Bis(aroyl)-2,5-dibromobenzenes
Licensed Content Author	Masaki Shimizu, Akinori Kimura, Hiroshi Sakaguchi
Licensed Content Date	Jan 5, 2016
Licensed Content Volume	2016
Licensed Content Issue	3
Licensed Content Pages	7

Order Details

Type of use	Dissertation/Thesis
Requestor type	University/Academic
Format	Print and electronic
Portion	Figure/table
Number of figures/tables	1
Will you be translating?	No

About Your Work

Title of new work	Structural Modulation of Carbazole Derivatives for Triplet State Engineering and Delayed Emission
Institution name	Indian Institute of Science Education and Research Thiruvananthapuram
Expected presentation date	Feb 2026

Additional Data

Portions	Abstract Figure (Table of Content)
The Requesting Person / Organization to Appear on the License	Jibin Sivanarayanan, IISER Thiruvananthapuram

Requestor Location

Requestor Location
Mr. Jibin Sivanarayanan
Maruthamala, Vithura
Thiruvananthapuram

Tax Details

CCC RightsLink

SPRINGER NATURE

Delayed room temperature phosphorescence enabled by phosphines

Author: Guang Lu et al
Publication: Nature Communications
Publisher: Springer Nature
Date: May 2, 2024

Creative Commons

Crystallization induced room-temperature phosphorescence and chiral photoluminescence properties of phosphoramides

S. Jena, J. Eyyathiyil, S. K. Behera, M. Kitahara, Y. Imai and P. Thilagar, *Chem. Sci.*, 2022, **13**, 5893 **DOI:** 10.1039/D2SC00990K

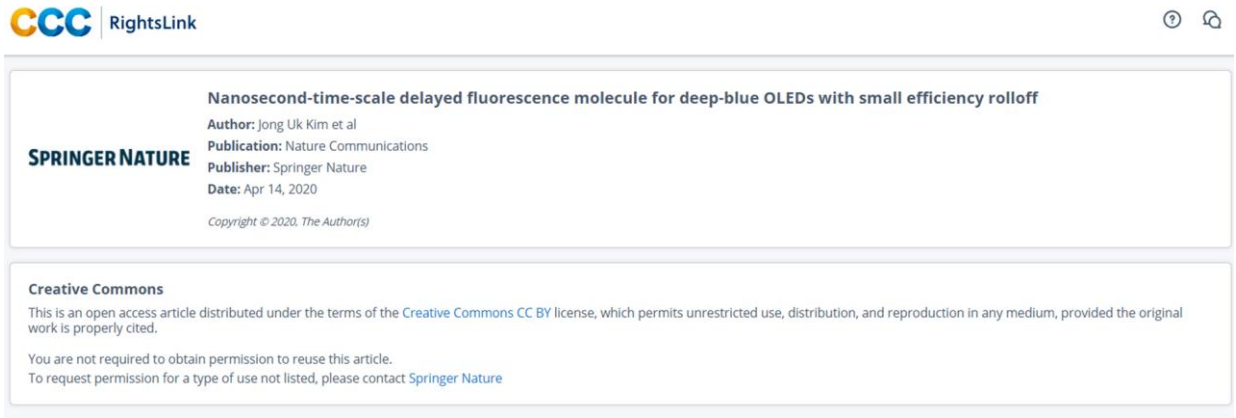

Achieving dual emission of thermally activated delayed fluorescence and ultralong room-temperature phosphorescence by controlling excited state dynamics through metal coordination

X. Cai, D. Liang, D. Zhang, J. Jia, X. Wu and C. Lu, *Chem. Sci.*, 2025, **16**, 9802 **DOI:** 10.1039/D5SC00555H